
Electronic Thesis and Dissertation Repository

8-23-2013 12:00 AM

PIV-based Investigation of Hemodynamic Factors in Diseased Carotid Artery Bifurcations with Varying Plaque Geometries

Sarah Kefayati
The University of Western Ontario

Supervisor
Dr. Tamie L. Poepping
The University of Western Ontario

Graduate Program in Physics
A thesis submitted in partial fulfillment of the requirements for the degree in Doctor of Philosophy
© Sarah Kefayati 2013

Follow this and additional works at: <https://ir.lib.uwo.ca/etd>



Part of the [Bioimaging and Biomedical Optics Commons](#), [Biomedical Devices and Instrumentation Commons](#), and the [Fluid Dynamics Commons](#)

Recommended Citation

Kefayati, Sarah, "PIV-based Investigation of Hemodynamic Factors in Diseased Carotid Artery Bifurcations with Varying Plaque Geometries" (2013). *Electronic Thesis and Dissertation Repository*. 1547.
<https://ir.lib.uwo.ca/etd/1547>

This Dissertation/Thesis is brought to you for free and open access by Scholarship@Western. It has been accepted for inclusion in Electronic Thesis and Dissertation Repository by an authorized administrator of Scholarship@Western. For more information, please contact wlsadmin@uwo.ca.

PIV-based Investigation of Hemodynamic Factors in Diseased Carotid Artery Bifurcations with Varying Plaque Geometries

(Thesis format: Integrated Article)

by

Sarah Kefayati

Graduate Program in Physics

A thesis submitted in partial fulfillment
of the requirements for the degree of
Doctor of Philosophy

The School of Graduate and Postdoctoral Studies
The University of Western Ontario
London, Ontario, Canada

© Sarah Kefayati 2013

Abstract

Ischemic stroke is often a consequence of complications due to clot formation (i.e. thrombosis) at the site of an atherosclerotic plaque developed in the internal carotid artery. Hemodynamic factors, such as shear-stress forces and flow disturbances, can facilitate the key mechanisms of thrombosis. Atherosclerotic plaques can differ in the severity of stenosis (narrowing), in eccentricity (symmetry), as well as inclusion of ulceration (wall roughness). Therefore, in terms of clinical significance, it is important to investigate how the local hemodynamics of the carotid artery is mediated by the geometry of plaque. Knowledge of thrombosis-associated hemodynamics may provide a basis to introduce advanced clinical diagnostic indices that reflect the increased probability of thrombosis and thus assist with better estimation of stroke risk, which is otherwise primarily assessed based on the degree of narrowing of the lumen.

A stereoscopic particle image velocimetry (stereo-PIV) system was configured to obtain instantaneous full-field velocity measurements in life-sized carotid artery models. Extraction of the central-plane and volumetric features of the flow revealed the complexity of the stenotic carotid flow, which increased with increasing stenosis severity and changed with the symmetry of the plaque. Evaluation of the energy content of two models of the stenosed carotid bifurcation provided insight on the expected level of flow instabilities with potential clinical implications. Studies in a comprehensive family of eight models ranging from disease-free to severely stenosed (30%, 50%, 70% diameter reduction) and with two types of plaque symmetry (concentric or eccentric), as well as a single ulcerated stenosed model, clearly demonstrated the significance of plaque geometry in marked alteration of the levels and patterns of downstream flow disturbances and shear stress. Plaque eccentricity and ulceration resulted in enhanced flow disturbances. In addition, shear-stress patterns in those models with eccentric stenosis were suggestive of increased thrombosis potential at the post-stenotic recirculation zone compared to their concentric counterpart plaques.

Keywords: Atherosclerosis, thrombosis, carotid artery, turbulence, particle image velocimetry, shear stress, proper orthogonal decomposition, stenosis, plaque eccentricity, ulceration

Co-Authorship Statement

This thesis contains materials that have been published in, submitted to, or prepared for peer-reviewed journals. Permission to reproduce the published manuscript appears in Appendix E.

Chapter 3 presents material from an article entitled “Transitional flow analysis in the carotid artery bifurcation by proper orthogonal decomposition and particle image velocimetry,” which has been published in *Medical Engineering and Physics*. This article was co-authored by Sarah Kefayati and Tamie L. Poepping. S. Kefayati designed and performed the experiments, analyzed the data, and wrote the manuscript. T. L. Poepping reviewed the results and manuscript prior to submission.

Chapter 4 presents material from an article entitled “Turbulence intensity measurements using particle image velocimetry in diseased carotid artery models: effect of stenosis severity, plaque eccentricity, and ulceration,” which has been submitted to *Journal of Biomechanics* and is under revision for resubmission. This article is co-authored by Sarah Kefayati, David W. Holdsworth, and Tamie L. Poepping. S. Kefayati designed and performed the experiments, analyzed the data, and wrote the manuscript. D. W. Holdsworth and T. L. Poepping reviewed the results and manuscript prior to submission.

Chapter 5 presents material from an article entitled “Effects of plaque geometry on *in vitro* shear stress measurements in a family of carotid artery models using particle image velocimetry,” which is prepared for submission to *PLOS ONE*. This article is co-authored by Sarah Kefayati, Jaques S. Milner, David W. Holdsworth, and Tamie L. Poepping. S. Kefayati designed and performed the experiments, analyzed the data, and wrote the manuscript. J. S. Milner performed the processing steps required for visualization of wall shear stress and reviewed the manuscript. D. W. Holdsworth and T. L. Poepping reviewed the results and manuscript.

Dedication

To Milad, my love,

for making my reality dreamier than my dreams

Acknowledgments

During the formation of this thesis, I have had the pleasure of meeting and the opportunity to work with many amazing people to whom I am very thankful.

First and foremost, I am deeply grateful to my supervisor, Dr. Tamie Poepping, for giving me this opportunity. Tamie, thank you for your boundless generosity, for all the encouragement, and professional guidance. It has been a great honour to know you and work with you.

I am also very thankful to Dr. David Holdsworth and Dr. Kamran Siddiqui for their helpful advice and encouragement and for sharing their experiences with me. A great measure of thanks to Dr. Maria Drangova for her generous help with many research-related matters. Gratitude to Hristo Nikolov for fabricating perhaps the most important tool of my research, my phantoms. Thanks to Jaques Milner and Dr. William Handler for sharing their technical expertise when needed. For all those times when I ran anxiously to Frank Van Sas and Brian Dalrymple after a failed equipment, thanks for all their machining assistance and also helping me build my experimental setup.

My love and appreciation for my parents Nezhat and Nosrat. Thanks and love to my little sister, Hadis, who has waited patiently for my long days of experimenting and writing to be finally over so that we can have our long sisterly conversations; I very much look forward to it! To Hamed, my big brother, thank you for all your love and kindness. And to my dear husband, Milad, thank you for being so perfectly understanding and so lovingly supportive.

Table of Contents

Abstract.....	ii
Co-Authorship Statement	iii
Dedication	iv
Acknowledgments	v
Table of Contents	vi
List of Tables	x
List of Figures.....	xi
List of Symbols and Abbreviations	xix
Chapter 1	1
1 Introduction.....	1
1.1 Ischemic Stroke, Atherosclerosis, and the Carotid Artery Bifurcation	1
1.1.1 Diagnosis based on degree of stenosis severity	2
1.1.2 Atherothrombotic stroke and the need for better predictors	5
1.1.3 Contribution of hemodynamic factors to atherosclerosis and thrombosis..	6
1.1.4 Plaque geometry: stenosis severity, eccentricity, and ulceration.....	9
1.2 Full-field Flow Characterization.....	12
1.2.1 Doppler ultrasound (DUS).....	13
1.2.2 Magnetic resonance imaging (MRI)	15
1.2.3 Numerical methods	16
1.3 Particle Image Velocimetry (PIV)	19
1.3.1 Working principles of the classical PIV technique.....	20
1.3.2 PIV application for hemodynamic studies.....	21
1.3.3 Previous PIV studies of carotid artery bifurcation models	23

1.4 Research Objectives and Thesis Outline.....	25
1.5 References.....	27
Chapter 2	41
2 Methods.....	41
2.1 Flow Components	41
2.1.1 PIV-compatible phantoms	41
2.1.2 Blood-mimicking fluid.....	42
2.1.3 Carotid-artery flowrate waveform	43
2.2 Stereoscopic PIV.....	45
2.2.1 Stereoscopic PIV arrangements	45
2.2.2 Calibration.....	47
2.2.3 Image acquisition.....	48
2.2.4 Self-calibration.....	49
2.2.5 Velocity evaluation	52
2.3 References.....	53
Chapter 3	55
3 Transitional Flow Analysis in the Carotid Artery Bifurcation by Proper Orthogonal Decomposition and Particle Image Velocimetry	55
3.1 Introduction.....	55
3.2 Methods.....	57
3.2.1 Flow experiment set-up.....	57
3.2.2 PIV system.....	58
3.2.3 PIV data acquisition and analysis	60
3.2.4 POD experiment.....	61
3.3 Results.....	63
3.3.1 General features of flow.....	63

3.3.2	Stenosis severity effect via POD analysis.....	66
3.3.3	POD analysis of multiple planes in 70% stenosed model.....	71
3.3.4	Temporal resolution effect.....	71
3.4	Discussion.....	73
3.5	Conclusion	79
3.6	References.....	79
Chapter 4	84
4	Turbulence Intensity Measurements Using Particle Image Velocimetry in Diseased Carotid Artery Models: Effect of Stenosis Severity, Plaque Eccentricity, and Ulceration.....	84
4.1	Introduction.....	84
4.2	Methods.....	86
4.2.1	Flow set-up.....	86
4.2.2	Data acquisition and analysis.....	87
4.2.3	Turbulence intensity (TI) estimation	88
4.2.4	Convergence test for TI estimation.....	89
4.3	Results.....	91
4.3.1	Combined effect of stenosis severity and eccentricity on turbulence intensity.....	91
4.3.2	Effect of ulceration on turbulence intensity.....	100
4.4	Discussion.....	102
4.5	Conclusion	104
4.6	References.....	105
Chapter 5	110
5	Effects of Plaque Geometry on <i>In Vitro</i> Shear Stress Measurements in a Family of Carotid Artery Models Using Particle Image Velocimetry.....	110
5.1	Introduction.....	110
5.2	Methods.....	112

5.2.1	Experimental set-up	112
5.3	Data Acquisition and Analysis.....	113
5.4	Results.....	116
5.4.1	Laminar shear stress.....	116
5.4.2	Turbulent shear stress	125
5.5	Discussion	131
5.6	Conclusion	133
5.7	References.....	134
Chapter 6	139
6	Summary, Conclusion, and Future Work.....	139
6.1	Summary of Studies.....	139
6.1.1	Summary of Chapter 3.....	139
6.1.2	Summary of Chapter 4.....	140
6.1.3	Summary of Chapter 5.....	141
6.2	Conclusion	142
6.3	Future Directions	145
6.3.1	Turbulence quantification using high-frame-rate DUS	145
6.3.2	Compliant carotid artery models.....	147
6.3.3	Numerical simulations	150
6.4	References.....	151
Appendix A	154
Appendix B	158
Appendix C	160
Appendix D	168
Appendix E	174
Curriculum Vitae	178

List of Tables

Table 3.1: Comparison of the POD relative eigenvalues for five different temporal resolutions shown for first four modes of flow in the 70%-stenosed model.	73
Table 4.1: Cycle-averaged turbulence intensity (m/s). Values from all 8 models are given as mean \pm SD of ROI – TI averaged over the 87 cardiac-cycle time points shown in Figure 4.8.	99
Table C.1: Uncertainty and measured values at peak systole time point for the specified variables. Values are mean and standard deviation over the range of values present in the corresponding branch of bifurcation.	165
Table C.2: Uncertainty and measured values at end diastole time point for the specified variables. Values are mean and standard deviation over the range of values present in the corresponding branch of bifurcation.	166

List of Figures

Figure 1.1: A schematic showing the right carotid artery extending from the neck upward. At the bifurcation apex located in the neck, the common carotid artery branches into the external and internal carotid arteries.....	2
Figure 2.1: A silicone phantom incorporating a 50% stenosis with eccentric plaque formation. The direction of the flow is from the common carotid artery (CCA) towards the two outlet branches of the internal carotid artery (ICA) and external carotid artery (ECA)..	42
Figure 2.2: Silicone phantoms filled with (left to right) air, water, and blood-mimicking fluid (BMF). The matched refractive index between the phantom and the BMF can be recognized via visual elimination of the phantom boundaries with the absence of optical distortions. ...	43
Figure 2.3: Measured carotid-artery flowrate waveform at the inlet of CCA and outlets of ICA and ECA.....	44
Figure 2.4: Schematic of (one camera) of a stereoscopic arrangement with Scheimpflug condition satisfied through the angled arrangement of the lens relative to the camera and a viewing prism placed on top of the test object to achieve orthogonal incidence.	46
Figure 2.5: Calibration set-up including the two-leveled calibration target immersed in blood-mimicking fluid with the orthogonal-viewing prism secured at the top of the fluid level.	48
Figure 2.6: Volumetric acquisition of the velocity field via multiple planes of data. Shown here are the central-plane of measurement and two off-center planes inside the lumen (grey) volume.....	49
Figure 2.7: RMS differences between corresponding vectors in maps processed using the central-plane and plane-associated calibration parameters. Error bars represent standard deviation from the mean of five repeated measurements.	51
Figure 2.8: Velocity-vector maps from 1.5 mm below the central plane in a 50% eccentrically stenosed model derived using two different calibration sets: a) central-plane calibration and b) plane-associated calibration.....	52

Figure 3.1: A life-sized normal (disease-free) phantom cast in transparent silicone (a), schematic of the 50% and 70% concentrically stenosed models superimposed on the geometry of the normal model (b), and flow rate measurements in the 50%-stenosed phantom at the inlet of the CCA and outlets of the ICA and ECA (c). Each waveform is the ensemble average across 10 consecutive cardiac cycles..... 57

Figure 3.2: PIV experimental flow set-up depicting the two CMOS cameras (labeled 1 & 2), silicone prism (3), phantom (4), ECA and ICA flow resistors (5 & 6), and 1.5-mm thick laser sheet illuminating an x-y plane through the phantom..... 59

Figure 3.3: Visualization of the flow patterns in the normal (a, d), 50% (b, e) and 70% models (c, f) at peak systole of the cardiac cycle. Sparse representations of the volumetric streamlines are shown across the top row (a, b, c), along with a detailed cross-sectional slice of the velocity vector map corresponding to the position indicated by the colored slice in the ICA. Projections of the 3D streamlines superimposed onto the color-encoded map of the central-plane velocity magnitude are shown along the bottom row (d, e, f). The boxed areas of the ICA indicate the regions detailed in Figure 3.4 and Figure 3.5..... 64

Figure 3.4: Vector-velocity fields at five different time points of the cardiac cycles superimposed on color maps of the swirling strength in the normal (top row), 50% (middle row), and 70% models (bottom row). The color bar was customized to emphasize variation between -1000 and $+1000 \text{ s}^{-1}$ to enable visualization of the details across all three models. The minimum and maximum values present in the 70% model at the peak systole were -1550 s^{-1} and 1474 s^{-1} respectively..... 65

Figure 3.5: Color maps of swirling strength generated for the spatial modes 1, 2, 10, 20, and 40 in the normal (top row), 50% (middle row), and 70% models (bottom row). The color bar was customized to emphasize variation between -1500 and $+1500 \text{ s}^{-1}$ to enable visualization of the details across all three models. The actual maximum strengths present in the first mode of each of the 50% and 70% models are -1550 and -3150 s^{-1} respectively, where the negative indicates clockwise swirl. Contour lines represent $|200| \text{ s}^{-1}$ increments, starting from -100 and $+100 \text{ s}^{-1}$ for negative and positive rotation respectively. 67

Figure 3.6: POD energy plots using a total mode number (N) of 460 and full FOV for each of the three models: (a) Double logarithmic plot of fractional energy spectra as a function of mode number, (b) cumulative energy distribution showing cumulative eigenvalues as a function of normalized mode number (n/N).	68
Figure 3.7: POD (N=460) temporal modes 1, 2, 10, 40, 70, and 100 for normal (blue plots in each set), 50% (red), and 70% (black) models, showing the temporal coefficients, $-a(t)$, as a function of the cardiac cycle.	70
Figure 3.8: Double-logarithmic plot of POD (N=460) fractional energy spectra as a function of mode number, using the smaller ICA FOV for four selected planes in the 70%-stenosed model, corresponding to central plane, plus 1-, 2-, and 3-mm offset planes parallel to the central plane.	72
Figure 3.9: Double-logarithmic plot of POD fractional energy spectra derived from snapshot ensemble of 5 different frame rates (a), and entropy as a function of frame rate (b) in the 70%-stenosed model.	74
Figure 4.1: Geometry of the carotid artery bifurcation phantoms: (a) PIV compatible silicone phantom incorporating the normal (disease-free) geometry shown in (b); (c) outlines of the geometries with various stenosis severity superimposed on the normal geometry for the grey region indicated in (b) and for concentric, eccentric, and ulcerated plaques.	87
Figure 4.2: Dependency of turbulence intensity on the size of the ROI and on the number and sequencing of cardiac cycles incorporated in the ensemble averaging. Values are mean \pm SD based on 6 repeated measures of each TI map using a fixed ROI of $1.2 \times 1.2 \text{ mm}^2$ (upper set of lines, 1) or $5 \times 5.5 \text{ mm}^2$ (lower set of lines, 2) during systolic deceleration.	91
Figure 4.3: Flow pattern visualization at peak systole in carotid models with 50% concentric stenosis (a, d), 50% eccentric stenosis (b, e), and 50% eccentric stenosis with ulceration (c, f). Color-coded, central-plane, ensemble-averaged velocity maps (generated using 15 cardiac cycles) with imposed cross-sectional slices (set 6 mm apart) are shown in the top row (a-c) along with a vector map of the cross-sectional slice at 13 mm distal to the bifurcation apex (slice indicated by the arrow). Central-plane ensemble-averaged velocity maps, superimposed with sparse volumetric streamlines, are shown in the bottom row (d-f).	92

Figure 4.4: Profiles of velocity components (left to right V_x , V_y , and V_z) from 50% concentric stenosed carotid model. Values are mean \pm SD calculated based on 15 cardiac cycles and were extracted along three lateral lines (X_1 , X_2 , and X_3 shown in Figure 4.3e) located in the ICA at approximately 1, 2, and 3 CCA diameters, respectively, downstream from the bifurcation apex. The five time points (from top to bottom) correspond to 30 ms prior to peak systole, peak systole, and 40, 150, and 670 ms post peak systole..... 94

Figure 4.5: Profiles of velocity components (left to right V_x , V_y , and V_z) from 50% eccentric stenosed carotid model. Values are mean \pm SD calculated based on 15 cardiac cycles and were extracted along three lateral lines (X_1 , X_2 , and X_3 shown in Figure 4.3e) located in the ICA at approximately 1, 2, and 3 CCA diameters, respectively, downstream from the bifurcation apex. The five time points (from top to bottom) correspond to 30 ms prior to peak systole, peak systole, and 40, 150, and 670 ms post peak systole. 95

Figure 4.6: Profiles of velocity components (left to right V_x , V_y , and V_z) from 50% ulcerated eccentric model. Values are mean \pm SD calculated based on 15 cardiac cycles and were extracted along three lateral lines (X_1 , X_2 , and X_3 shown in Figure 4.3e) located in the ICA at approximately 1, 2, and 3 CCA diameters, respectively, downstream from the bifurcation apex. The five time points (from top to bottom) correspond to 30 ms prior to peak systole, peak systole, and 40, 150, and 670 ms post peak systole. 96

Figure 4.7: Turbulence intensity maps in the ICA of all 8 models at the time point of ROI – TImax in the cardiac cycle. Cross-sectional slices are shown for the 3 specified locations set 4 mm apart. Boxed area shows the selected ROI, from which an additional 4 shifted ROIs were generated for calculation of ROI – TI. For the normal model, shown in the top right enclosure, a later time point and a color bar with smaller dynamic range were applied..... 97

Figure 4.8: Cardiac-cycle evolution of turbulence intensity for all 8 carotid models. Values are ROI – TI calculated based on five repositioned $5 \times 5.5\text{-mm}^2$ ROIs extracted from ensemble-averaged central-plane TI map generated using an ensemble of 15 sequential cardiac cycles. Error bars represent SD shown, for clarity, in one direction and for selected time points (30 ms, time point of ROI – TI_{Max}, 340 ms, and 840 ms) during the cardiac

cycle. For cardiac-cycle phase reference, a scaled profile of the measured CCA flow-rate waveform is shown as the grey-shaded background..... 99

Figure 4.9: Maximum TI as a function of stenosis severity obtained from the central-plane (left) and volumetric (right) ROI. Values are mean \pm SD of ROI – TI calculated based on five repositioned 5x5.5-mm² ROIs. The time points of maximum were selected based on the central-plane ROI – TI values for each model (Figure 4.8) and carried over for volumetric values. 100

Figure 4.10: Cardiac-cycle evolution of turbulence intensity in the non-ulcerated and ulcerated models with 50% eccentric stenosis. For each model, mean \pm SD values were calculated based on 5 repeated measures of the TI maps each using an ensemble of six non-sequential iterations. 101

Figure 4.11: Distribution of values in the central-plane (left) and volumetric (right) TI maps for the ulcerated and non-ulcerated carotid models with 50% eccentric stenosis. For a specific TI value, the vertical axis corresponds to the total number of units in each TI map of the ICA branch and accumulated over the systolic deceleration phase (180-340 ms). For each model, the temporally and spatially accumulated TI units were normalized by the total number of non-zero units in the central-plane or volumetric TI map. 102

Figure 5.1: Color maps of ensemble-averaged velocity magnitudes shown for peak systole in a family of eight carotid models. Three cross-sectional slices are shown alongside the ICA lumen, for each stenosed model, at the locations indicated by the black lines at approximately 1, 2, and 3 CCA diameters downstream (i.e. \sim 8, 16, 24 mm). For scale, note the downstream ICA diameter is 5.5 mm. Note the range-appropriate color bar for each row of models. 117

Figure 5.2: Color maps of the laminar shear stress shown for peak systole in a family of eight carotid models. Three cross-sectional slices are shown alongside the ICA lumen, for each stenosed model, at the locations indicated by the black lines at approximately 1, 2, and 3 CCA diameters downstream (i.e. \sim 8, 16, 24 mm). Note the bottom right color bar represents the 7 stenosed models and a separate color bar is used for the normal model shown in the enclosed box..... 119

Figure 5.3: Spatial and temporal distribution of the maximum free (i.e. non wall) shear stress in a family of eight carotid models. For each time point, maximum FSS values were extracted across the entire ICA lumen along the 25-mm analyzed length. Data are shown for the 180-ms window, incorporating peak systole (PS), as shown on the reference cardiac-cycle waveform. Note the range-appropriate color bar associated with each row of models and the 1-Pa isocontour increments used for all maps. 120

Figure 5.4: Ensemble-averaged wall shear stress shown for peak systole in a family of eight carotid models. For optimal display, the ICA is shown from 2 different perspectives, as indicated by the orientation schematic in the bottom right corner. The color bar represents all the models including the normal. For improved accommodation, the dynamic range of the color bar is reduced to a maximum of 30 Pa. 122

Figure 5.5: Spatial and temporal distribution of the wall shear stress along the inner wall (a) and outer wall (b) in a family of eight carotid models. For each time point, wall-bounded values were extracted along the 25-mm analyzed length. The analyzed 180-ms window (with peak systole denoted as PS) is highlighted on the reference cardiac-cycle waveform. Note the range-appropriate color bar associated with each row of the models and the 4-Pa contour level used for all the maps. 124

Figure 5.6: Reynolds shear stress $\overline{u'v'}$ shown as a function of time for the set of three 50%-stenosed models. Maps are shown at three time points: 20 ms before peak systole (top row), 20 ms after peak systole (middle), and 20 ms before the diastolic notch (bottom). Three cross-sectional slices are shown alongside the ICA lumen at the locations indicated by the black lines at approximately 2, 2.5, and 3 CCA diameters downstream (i.e. $\sim 16, 20, 24$ mm). Note the separate color bar used for the bottom row with the same zero-value color as for the upper rows..... 126

Figure 5.7: Color-encoded maps of orientation-dependent swirling strength (ω_z) shown for the ICA central plane in each of the set of three 50%-stenosed models at time points similar to those applied to Figure 5.6. Swirling strength maps were obtained from x and y components of the ensemble-averaged (left ICA of each column pair) and instantaneous

(right ICA of each column pair) velocity maps. Note the different limits of the color bar used for the bottom row. 128

Figure 5.8: Color-encoded maps of total shear stress for the time point of maximum TSS in each of eight carotid models. Note the bottom right color bar (set to the maximum of 150 Pa) and indicated time point of maximum TSS (20 ± 10 ms post peak systole) represents the seven stenosed models; those associated with the normal model are shown in the enclosed box..... 129

Figure 5.9: Combined spatial and temporal occurrence frequency of total shear stress values. The analyzed region extended wall-to-wall laterally and 35 mm distal to the apex in the ICA branch calculated both for the central-plane (left column) and volumetrically (right column). Values were accumulated over the systolic time window (180 ms). Horizontal axes are presented in log 2. Also, note the different range for the vertical axis of the plot associated with the normal model. 130

Figure 6.1: DUS-simulated POD energy spectra derived from PIV velocity measurements. Comparison of (a) PIV and DUS-simulated energy spectra obtained in a 70% concentric model of the carotid artery, and (b) DUS-simulated POD energy spectra using two different temporal resolutions and two different sample volumes in the same carotid artery model.. 148

Figure C.1: Color-coded maps of instantaneous (a) and ensemble-averaged (c) velocity magnitude, alongside the corresponding maps for uncertainty bandwidth (b, d) for the time point of peak systole. The respective color bars are shown between the relevant panels. ... 162

Figure C.2: Color-coded maps of instantaneous (a) and ensemble-averaged (c) velocity magnitude, alongside the corresponding maps for uncertainty bandwidth (b, d) for the time point of end diastole. The respective color bars are shown between the relevant panels. 163

Figure D.1: Profiles of velocity components (left to right V_x , V_y , and V_z) for normal model. 169

Figure D.2: Profiles of velocity components (left to right V_x , V_y , and V_z) for 30% concentric model..... 170

Figure D.3: Profiles of velocity components (left to right V_x , V_y , and V_z) for 30% eccentric model.....	171
Figure D.4: Profiles of velocity components (left to right V_x , V_y , and V_z) for 70% concentric model.....	172
Figure D.5: Profiles of velocity components (left to right V_x , V_y , and V_z) for 70% eccentric model.....	173

List of Symbols and Abbreviations

Alphanumeric:

N	sample size
p	p -value
Re	Reynolds number
t	time point
u	instantaneous velocity component in x direction
v	instantaneous velocity component in y direction
w	instantaneous velocity component in z direction
U	phase-averaged velocity component in x direction
V	phase-averaged velocity component in y direction
W	phase-averaged velocity component in z direction
u'	component of velocity fluctuation in x direction
v'	component of velocity fluctuation in y direction
w'	component of velocity fluctuation in z direction

Greek:

λ_{ci}	swirling strength
μ	dynamic viscosity
ρ	density
τ	shear stress
τ_{turb}	turbulent shear stress
ϕ	spatial mode
ω_z	in-plane vorticity

Abbreviations:

2D	two-dimensional
2D-2C	two-dimensional two-component
2D-3C	two-dimensional three-component
3D	three-dimensional
3D-3C	three-dimensional three-component
ANOVA	a one-way analysis of variance
BMF	blood mimicking fluid
CCA	common carotid artery
CFD	computational fluid dynamics
CTA	computerized tomographic angiography
D_{distal}	inner diameter of internal carotid artery at upstream location

$D_{stenosis}$	inner diameter of internal carotid artery at the maximum stenosis
DNS	direct numerical simulation
DUS	Doppler ultrasound
ECA	external carotid artery
ECG	electrocardiogram
ECST	European Carotid Surgery Trial
FOV	field of view
FSS	free shear stress
ICA	internal carotid artery
LDA	laser Doppler anemometry
LSS	laminar shear stress
MRA	magnetic resonance angiography
MRI	magnetic resonance imaging
NASCET	North American Symptomatic Carotid Endarterectomy Trial
PC-MRI	phase-contrast magnetic resonance imaging
PIV	particle image velocimetry
POD	proper orthogonal decomposition
RANS	Reynolds-averaged Navier-Stokes
RMS	root-mean-square
ROI	region of interest
ROI – TI	ROI-averaged TI
$\overline{ROI - TI}$	mean over multiple ROI – TI values
$\overline{ROI - TI}_{Max}$	maximum $\overline{ROI - TI}$ during cardiac cycle
RSS	Reynolds shear stress
SD	standard deviation
Stereo	stereoscopic
TI	turbulence intensity
TIA	transient ischemic attack
TKE	turbulence kinetic energy
Tomo	tomographic
TSS	total shear stress
WSS	wall shear stress

Chapter 1

1 Introduction

1.1 Ischemic Stroke, Atherosclerosis, and the Carotid Artery Bifurcation

Around the world, stroke causes 9% of all deaths and is the second leading cause of death [1]. According to the World Health Organization, 15 million people suffer stroke worldwide annually, and of these, 5 million die and another 5 million are permanently disabled. In the United States, stroke is the third leading cause of death, affecting 795,000 cases annually. In Canada, stroke accounted for 7% of all deaths in 2000, and in Europe, nearly 650,000 stroke deaths occur per year [2, 3]. Ischemic stroke, occurring due to insufficient blood supply to the brain, accounts for the largest number of strokes (88%), followed by intracerebral hemorrhage (9%) and subarachnoid hemorrhage (3%) [4, 5].

The primary cause of ischemic stroke is atherosclerosis, which is a long-term inflammatory disease beginning at the adluminal surface and causing endothelial abnormalities. It results in thickening and hardening of the vessel wall, eventually producing atherosclerotic plaques, which are essentially composed of lipid, fibrous tissue, and inflammatory cells [6]. Progression of the plaque can lead to a narrowing of the lumen, i.e. stenosis. The main arteries supplying blood to the head and neck are the two common carotid arteries (CCA), which each bifurcate to form the two branches of internal carotid artery (ICA) and external carotid artery (ECA), the latter supplying blood to the face, neck, and exterior of the head as shown in Figure 1.1. The ICA branch, which supplies blood to the brain, is one the most common sites of atherosclerotic plaque accounting for 15% to 20% of all ischemic strokes [7].

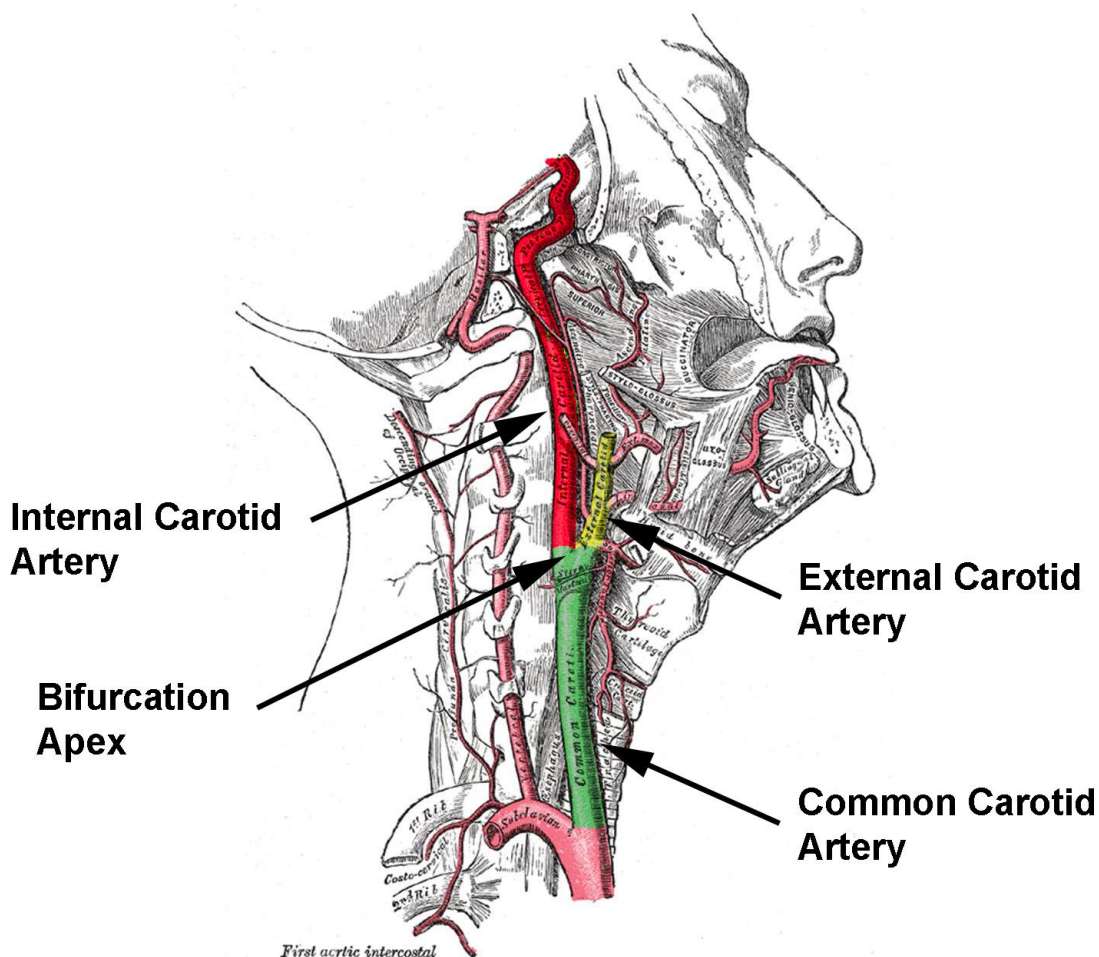


Figure 1.1: A schematic showing the right carotid artery extending from the neck upward. At the bifurcation apex located in the neck, the common carotid artery branches into the external and internal carotid arteries.*

1.1.1 Diagnosis based on degree of stenosis severity

The discovery of association between the internal carotid artery and stroke can be traced back to 1856 by Savory [9], and many reports then followed that emphasized the importance of internal carotid artery occlusion for assessing the risk of stroke. The degree of occlusion or stenosis severity reflects high correlation with stroke risk and thus is considered the main indication for selecting the appropriate treatment strategy. Major

* Adapted from Gray's Anatomy of the human body [8]

clinical trials, including the North American Symptomatic Carotid Endarterectomy Trial (NASCET) [10] and the European Carotid Surgery Trial (ECST) [11], grouped patients based on the degree of stenosis severity and assessed the benefit-risk ratio of surgical removal of plaque known as endarterectomy. The NASCET criterion for grading the degree of stenosis severity is based on the diameter reduction in the ICA branch comparing the inner diameter at the maximum stenosis ($D_{stenosis}$) to the inner diameter at a distal location in the ICA (D_{distal}) as follows:

$$\% \text{ stenosis} = (D_{distal} - D_{stenosis}) / D_{distal} \times 100\% \quad (1.1)$$

It is important to distinguish between the stenosis severity calculated based on diameter reduction (above) and area reduction, which is calculated using squared values of the corresponding diameters; for instance, a stenosis severity of 50% by diameter reduction equals that of 75% by area reduction [12]. The NASCET criteria are the primary clinical guidelines for measuring the degree of stenosis severity. The degrees of stenosis severity incorporated in our carotid-artery models were graded based on the NASCET criterion of diameter reduction. Throughout the thesis, any literature values of stenosis severities graded by area reduction are noted as such.

In summary, the results from these major clinical trials, along with the follow-up meta-analysis study by Rothwell *et al.* [13] showed that in patients with mild stenosis (<50%) the benefit of endarterectomy was outweighed by the risks incurred during the procedure, and patients with moderate stenosis (50-69%) still benefited from endarterectomy but with considerably less gain compared to patients with severe stenosis (>70%), who benefited significantly from surgery.

The main clinical diagnostic techniques for measuring the degree of stenosis severity are x-ray angiography, magnetic resonance angiography (MRA), computerized tomographic angiography (CTA), and duplex ultrasound. X-ray angiography has widely been considered the gold standard technique, perhaps due to being the technique of choice in the NASCET and ECST studies. However, with inherent risks due to invasiveness of this technique, it is gradually being replaced by the aforementioned non-invasive (or minimal-invasive) techniques each with its own advantages and disadvantages [14, 15].

MRA is commonly performed using time-of-flight imaging to image the magnetized blood and can provide a three-dimensional rendition of the carotid artery. Studies suggest in some cases using magnetic resonance imaging (MRI) for imaging the lumen can yield better accuracy compared to MRA [16]. Cost can be considered the main disadvantage of this method, along with some imposed technical limitations such as signal dropout in case of severe stenosis where turbulent flow is expected. CTA is a minimally invasive technique that has multiple advantages over MRA, with the main ones being better accuracy and availability. Duplex ultrasound grades the stenosis severity based on the increased jet velocities induced by stenosis [17]. Various peak-systole velocity thresholds have been proposed previously a classification of which can be found in the literature [18, 19]; in summary, peak-systole velocity less than 1.25 m/s corresponds to a normal ICA when no plaque is visible and it corresponds to mild stenosis with visible plaque. Moderate stenosis (50-69%) is identified with peak-systole velocity 1.25-2.30 m/s with visible plaque, and severe stenosis ($\geq 70\%$) is associated with peak-systole velocity greater than 2.30 m/s and visible plaque. Considering ultrasound's cost effectiveness and high accuracy for severe stenoses (90%), this technique is normally considered the first-line diagnostic tool [20].

Measurement of the degree of stenosis severity remains the main predictor for stroke risk and determinant for therapy selection [21]. However, there is increasing evidence that stenosis severity alone is not a sensitive predictor of stroke and may result in misidentifying patients who have a significant risk of ischemic attack but categorized as mild or moderate stenoses [22-24]. Also, based on stenosis severity alone, management of asymptomatic patients remains debatable with minimal reduced annual risk reported for those patients with $>60\%$ stenosis undergoing endarterectomy [25]. The extracranial cerebral mechanisms leading to ischemic stroke and transient ischemic attack (TIA) can be categorized into five major mechanisms as follows: artery-to-artery embolism of thrombus formed at the site of atherosclerotic plaque, embolism of other atheromatous debris (e.g. cholesterol crystals), acute occlusion from thrombus at the site of ruptured plaque, disintegration of the arterial wall structure as a result of dissection or subintimal hematoma, and lastly the presence of critical stenosis or occlusive plaque combined with insufficient collateral perfusion [5, 21]. With increasing evidence from clinical episodes,

it becomes clear that other indications are required beside the degree of stenosis severity for better risk stratification.

1.1.2 Atherothrombotic stroke and the need for better predictors

A main complication of atherosclerosis is thrombosis (i.e. clot formation), which is a complex multilevel process mainly involving activation and subsequent aggregation of platelets [26]. Superimposed thrombus at the site of atherosclerotic plaque can lead to local occlusion and potentially distal embolism, and it is commonly found in many autopsy studies [27]. It is estimated that large-artery athero-thromboembolism accounts for 20% of all strokes and about 50% of all ischemic strokes in Caucasian populations [13, 28].

Thrombosis can be promoted by ruptured plaque, which can expose the blood to the highly thrombogenic contents of the plaque. The complications of abrupt plaque rupture with subsequent thrombus or debris embolism results in ischemic stroke even in patients with moderate stenosis [29]. By definition, plaques that are prone to rupture are considered vulnerable plaques, which are characterized as plaques with a large lipid core, thin fibrous cap, active inflammation, intraplaque hemorrhage, and neovascularization of the vasa vasorum [30, 31].

Vulnerable plaques can be detected non-invasively with various imaging techniques using a set of morphological and pathological markers associated with plaque vulnerability [31, 32]. Many studies have reported the association of vulnerable plaques with an increased number of cerebrovascular events. For instance, a clinical study by Takaya *et al.* [33] on asymptomatic patients with stenosis severity ranging from moderate to severe showed certain MRI plaque characteristics, including a thin or ruptured fibrous cap, intraplaque hemorrhage, larger lipid-rich necrotic core, and larger maximum wall thickness, were all associated with subsequent cerebrovascular events.

It is now well established that thrombosis indicators can assist with more sensitive assessment of stroke risk and better therapy selection for patients with intermediate carotid stenosis or asymptomatic patients that show sudden onset of symptoms [34].

Hemodynamic parameters uniquely induced by stenosis can also play a major role in the thrombosis process, and thus are of potential significance for identifying an increased likelihood of thrombosis.

1.1.3 Contribution of hemodynamic factors to atherosclerosis and thrombosis

Hemodynamic factors play a major role in atherosclerosis pathology and the association of hemodynamic factors on the early formation and localization of atherosclerotic plaques has been demonstrated [35-37]. In the carotid artery bifurcation, unique flow phenomena, including recirculating flow in the bulb creating low and high oscillatory wall shear stress (WSS), can result in dysfunction of endothelial cells and induce activation of a number of atherogenic genes in them [38, 39]. Once formed, atherosclerotic plaque results in local hemodynamic alterations that can subsequently result in increased plaque growth or plaque rupture [40]. While shear stress is of the order of 1-2 Pa in healthy arteries, shear stresses higher than 30 Pa are expected within the stenosis throat of a diseased lumen [40].

Hemodynamics are linked to thrombosis through damaging the plaque surface – either superficially (involving endothelial and subendothelial layers) or deeper (resulting in plaque rupture and ulceration), both of which can increase the tendency to thrombosis at the site of a plaque [41]. Beside the mechanical damage, findings suggest that hemodynamic parameters can be more involved in various aspects of thrombosis and facilitate essential stages of activation, adhesion, and aggregation of platelets [42, 43].

1.1.3.1 Shear-induced thrombosis

Shear stress characterizes the mechanical force resultant from the spatial gradients of velocity (i.e. shear rates) and fluid viscosity. Platelet activation and aggregation are key functions in thrombosis and both can be influenced by hemodynamic parameters. Platelet activation can be triggered by either chemical agonists or by the mechanical forces of shear stress [44]. Aggregation of platelets is also mediated by shear stress ranges that mediate the primary binding factors [45]. In activation and aggregation of platelets both shear-stress level and exposure time are the key factors and early experimental studies

demonstrated the interrelation between these two factors [46, 47]. According to the threshold known as Hellums criterion [48], an accumulated shear-stress level of 3.5 Pa is required for platelet activation. Platelets can be activated when exposed to high levels of pathological shear stress for as short as a few milliseconds [49].

Furthermore, shear stress seems to be the governing mechanism for enhanced accumulation of platelets, and various observations have been reported; *ex vivo* experiments with collagen-coated stenotic surfaces reported the maximum accumulation at the apex of the stenosis [50], and other studies in smooth artificial surfaces reported the maximum accumulation at the immediate post-stenotic region speculating that high wall shear stress at the apex washes away the potentially adherent platelets resulting in low accumulation [51]. Recently, Nesbitt *et al.* [52] demonstrated that spatial gradients, instead of level, of wall shear stress can promote platelet aggregation at the immediate post-stenotic region where the spatial shear gradient (i.e. shear drop off) is highest. These aggregates were directly regulated by hemodynamic changes and were at a low level of platelet activation at the time of aggregation.

Beside characteristically high wall shear stress in the stenosed lumen, intraluminal shear stress layers (i.e. free shear stress) exist at the intersecting layer of the fast jet and the flow separation regions. Platelets that come into contact with these high-shear layers are susceptible to activation and aggregation, and they can potentially form free emboli by being entrapped in and convected by the vortices shedding along this shear layer [51, 53].

1.1.3.2 Effect of flow disturbances and turbulence

Turbulence refers to chaotic and unstable behavior of flow with random fluctuations of local velocities. The presence of plaque in the carotid artery can induce flow instabilities changing periodically with flow pulsatility and reaching the highest level during the deceleration phase of systole [54]. Many studies, some of which are discussed, have been conducted experimentally and numerically to characterize flow behavior and transition to turbulence in stenosed models under both steady and pulsatile flow conditions using both time and frequency domain analyses. It should be noted that, compared to steady inlet conditions, pulsatility results in a lower critical Reynolds number (Re) for transition to

turbulence. Young and Tsai [55, 56] reported a critical $Re = 1000$ in their pulsatile-flow study of a severely stenosed tube and a higher critical Reynolds number in their steady-flow study. A numerical study by Sherwin and Blackburn [57] in an axisymmetric 75% stenosis (i.e. 50% diameter reduction) reported transition to turbulence at a $Re = 535$ under pulsatile conditions, while under steady conditions, flow transitioned to turbulence at a $Re = 722$.

With regards to pathological effects, turbulence can be involved in several mechanisms that can eventually lead to ischemic stroke. For stenosis severity greater than 50%, turbulence can be a major limiting factor of blood flow by inducing significant pressure losses [45]. By generating high temporal shear gradients (i.e. transitions), turbulence can play a role in acute damage to the endothelial layer [58]. Larger spatial shear gradients associated with turbulence can promote convective mass transport to the arterial wall and facilitate the formation of atherosclerotic plaque or its weakening and rupture [59].

Close association of turbulence and thrombosis was demonstrated in the study by Stein and Sabbah [60] in which a high level of turbulence intensity was directly correlated with greater thrombi weight generated on the arterial surfaces of the shunt inserted into an animal vein. Unsteady conditions initially generated by pulsatility has been shown to enhance the platelet activation through enhancing the level of shear stress and the platelet collision rates [51]. Given an even higher level of instability expected in stenotic flow, a further increased level of platelet activation can be speculated.

1.1.3.3 Recirculation zones and thrombosis

Flow characteristics such as separation, recirculation, stagnation, and reattachment have been recognized for their significant role in thrombosis. *In vitro* studies have demonstrated the increased level of platelet deposition in the post-stenotic recirculation region [50]; the involved mechanism is considered to be enhanced convective transport of platelets and blood cells towards the vessel walls along locally curved streamlines with velocity components perpendicular to the wall. The platelets that have already been exposed to high levels of shear stress at the throat become entrapped in the recirculation zone with the convection pattern along the curved streamlines bringing them to the vessel

wall. Recirculation zones further favor the thrombosis process by providing a prolonged residence time for platelets and thrombogenic materials, with an increased collision rate of platelets thus promoting platelet-platelet binding, and the characteristically low wall-shear stress in these regions that further helps with adhesion of platelets to the wall.

1.1.4 Plaque geometry: stenosis severity, eccentricity, and ulceration

The interrelationship between hemodynamic factors and thrombosis activity is mediated by alterations in the local hemodynamics of stenotic flow that are influenced by both the morphology and the geometry of plaques. Three key geometrical factors that have been identified as having significant impact on local flow patterns are stenosis severity, eccentricity and ulceration.

The presence of stenosis results in the narrowing of the passage through which a jet forms. Patterns and mechanical characteristics of stenotic flow under either steady or pulsatile conditions have been extensively studied since the early 1970s, and a good overview can be found in several review articles [40, 45, 61]. The main stenotic flow features can be summarized as flow separation and reattachment, recirculation zones, shear layers created between the high-velocity jet and the recirculation zones, vortex shedding along the jet, and downstream flow instabilities.

As the stenosis severity increases, the jet is expected to become faster and narrower thus impacting the post-stenotic flow patterns and resulting levels of shear stress and turbulence. Early experimental studies using hot-film probes and laser Doppler anemometry (LDA) have clearly demonstrated the effect of increasing stenosis severity (under both steady and pulsatile flow) on the elevation of downstream flow instabilities [54-56, 62-69]. A LDA study by Khalifa and Giddens [68] in a set of three tubular models of stenosis with area reductions of 25%, 50%, and 75% was conducted under pulsatile conditions with peak Reynolds number similar to that of dog aorta. The critical Reynolds number was reported to fall rapidly for stenoses greater than 25%, and turbulence was observed for both 50% and 75% stenoses. In the same stenosed tubes, Ahmed and Giddens [64] compared flow under pulsatile conditions using a sinusoidal

waveform with mean Reynolds number of 600, providing a range similar to that of a human carotid artery, and reported turbulence with only the 75% stenosis (50% diameter reduction). The effect of carotid stenosis severity previously was visualized experimentally through digital particle imaging [70]; marked differences were noted between a 30% and 70% stenosed model of the carotid artery with the latter being associated with increased downstream flow disturbance and complexity. In a numerical study, Birchall *et al.* [71] simulated flow in nine patient-specific models of the carotid artery bifurcation, of which eight included stenoses ranging from mild to severe. They demonstrated the different flow patterns in these models with increasing WSS at the stenosis due to increasing stenosis severity

Independent of stenosis severity, plaque eccentricity (symmetry) can impact the local flow patterns. Plaque can form with varying symmetries; a symmetric (or concentric) plaque is considered a plaque that has obstructed the lumen equally from opposite walls. An asymmetric (or eccentric) plaque refers to the type that expands into the lumen preferentially from one side over the other. In the ICA, an eccentric plaque expands from the outer wall towards the inner wall (i.e. the flow-divider wall or wall intersecting with the bifurcation apex). Eccentric formation of plaque is reportedly more common [72].

Clinical significance of eccentricity is reflected in the trial study by Ohara *et al.* [73] where eccentric plaques were found to be associated with increased cerebrovascular events independent of other stroke risk factors. The association of eccentric plaque and more adverse symptoms has also been reported in the coronary arteries [74, 75].

Previous *in vitro* flow dynamic studies by Loree *et al.* [76], Young *et al.* [56], and Tang *et al.* [77], performed under the simplified condition of steady flow in stenotic tubes assessed the impact of stenosis eccentricity, and they collectively reported higher turbulent pressure fluctuations, higher pressure drops, higher shear-stress levels, and larger flow separation regions associated with an eccentric constriction as opposed to concentric. Under pulsatile flow conditions, marked differences were also detected in the flow patterns of concentric versus eccentric constrictions with the latter having stronger effects on the post-stenotic flow [78]. Stenosis eccentricity has also been shown to trigger

earlier transition to turbulence in severe stenosis [79]. These findings collectively signify the independent effect of stenosis eccentricity in the alteration of the local dynamics of stenotic flow.

Ulceration is a commonly developed morphological feature of atherosclerotic plaques that is formed as an excavated necrotic core following a ruptured or eroded fibrous cap [4]. By exposing the thrombogenic contents of the plaque, ulcerations can lead to greater thrombotic potential as reported previously [80, 81]. An examination of the control group of the NASCET trial demonstrated that patients with high-grade carotid stenosis in the absence of angiographic evidence of ulceration had a two-year stroke rate of 17%, which increased to a two-year stroke rate of 30% when ulceration was present with similar degrees of stenosis [82]. In another control study by Rothwell *et al.* [83] using ECST pooled data, plaque irregularities elevated the two-year risk of stroke for all groups of stenosis grade resulting in approximately equal risk for smooth plaque with severe stenosis and irregular plaques with moderate stenosis. In a recent study correlating risk factors to plaque morphology using a large series of carotid endarterectomy specimens collected from both symptomatic and asymptomatic patients ulcerated lesions were the most common finding, irrespective of clinical status [84]. The American Heart Association guidelines for endarterectomy [85] recommend surgery for patients with single or multiple TIAs and ipsilateral carotid stenosis $\geq 70\%$ stenosis or for symptomatic patients with stenosis $\geq 50\%$ in the presence of ulceration with no other source of emboli.

Reportedly ulceration occurs proximal to the stenotic plaque at regions of high WSS in plaque [86, 87]; it is postulated that high WSS generated at the plaque results in destabilization of the cap through various signaling pathways making the plaque prone to rupture [88]. It must be noted that the occurrence of ulceration is not only hemodynamically mediated but can also be regulated by physiological factors, perhaps explaining ulceration in mild and moderate stenoses [83]. Regardless of the underlying cause, once developed, ulceration itself leads to further hemodynamic alterations; Wong *et al.* [89] conducted a Doppler ultrasound study to investigate the effect of ulceration (in various sizes and shapes) in a group 50% eccentrically stenosed models and reported an

increased level of downstream flow disturbances compared to the matched non-ulcerated model.

1.2 Full-field Flow Characterization

The proven role and significance of hemodynamics in promoting cerebrovascular events has motivated many flow studies in carotid artery bifurcations. Early flow visualization in healthy carotid bifurcation models were performed using particle imaging, hydrogen bubbles, dye streaklines, photochromic lines, and dye washout [61]. Early quantitative measurements of carotid-artery flow were mainly conducted using LDA, which is a non-intrusive optical technique providing excellent spatial and temporal resolution (i.e. $\sim 10\ \mu\text{m}$, $\sim 100\ \text{kHz}$) [90]. The majority of carotid flow studies were performed in the healthy models [91-95] with few stenosed model studies. For instance, Gijsen *et al.* [96] conducted a LDA study in a healthy and a mildly stenosed (25%) models of carotid artery and reported no distinguishable differences for the compared large-scale flow features. Due to the advantages of high temporal and spatial resolution, this technique has been used previously as the validation platform for both experimental [97] and numerical flow studies [98]. However, in its original form, LDA only enables single-point measurement, thus, for spatial distribution of velocity information, multiple probe measurements need to be repeated which makes it a tedious task, as well as introducing velocity discontinuity. For instance, in order to provide cross-sectional flow information in models of a carotid artery, Liepsch *et al.* [99] measured 69 points in each cross-section located at various locations along the lumen length. Although in recent advanced LDA methods [100], such as multi-probe or scanning LDA, the single-point measurement is not a limit and full-field measurements can be achieved, these techniques only provide one component of velocity thus still limiting the full quantification of flow.

Full-field velocity quantifications – enabling measurement of instantaneous and gradient-based features of flow – in the carotid artery bifurcation models are possible through a variety of techniques including clinical, bench-top, and numerical methods.

1.2.1 Doppler ultrasound (DUS)

Doppler ultrasound (DUS) works based on the principle of a Doppler shift in frequency between a transmitted pulse and the returning echoes reflected from the moving structures (e.g. red blood cells). The returned (i.e. received) frequency increases as the red blood cell moves towards the transducer probe and decreases as it moves away from the transducer. Knowing the transmitted-pulse frequency and direction, the measured frequency shift can then be converted to the single-component velocity estimation along the beam direction [101].

Spectral and color DUS are two routinely implemented ultrasound techniques in clinical vascular-flow assessments. In pulsed-wave spectral DUS, short bursts of pulses are transmitted with a predefined interval (i.e. pulse repetition frequency) and returned echoes are received and analyzed from a specified “sample volume”. In the demodulation stage, the Doppler shift is obtained by comparing the frequency of the received signal to that of the transmitted in order to derive their difference. Spectral analysis of the Doppler shift spectrum can provide quantitative information of flow such as peak, mean, and minimum velocity in the assessed sample volume. Limited insight to the dynamics of the flow can be obtained through spectral analysis, such as the presence of downstream turbulence through broadening of the frequency spectrum [102-104].

To circumvent the limitation imposed by single-point measurements, multi-gate DUS was introduced in which simultaneous Doppler spectra are extracted from a series of gates (i.e sample volumes) spread along the ultrasound beam line thus providing a velocity profile measurement across the lumen along with superimposed spectral information (i.e. broadening). Based on the capability of profiling velocities across the lumen, previous *in vivo* studies have demonstrated flow patterns in the common carotid artery and measured axial WSS [105, 106].

In order to investigate more comprehensive flow visualization and quantification using DUS, Poepping *et al.* [107] introduced an *in vitro* set-up in which the sample volume was raster scanned over the region of interest with each measurement synchronized to the intended phase of the cardiac cycle via a synchronization signal provided by the flow

pump. In the examined 30% concentrically stenosed model, large-scale features of the flow such as jet path and region of recirculation were detected. The level of complex flow was quantified using phase-averaged fluctuations (i.e. turbulence intensity) and spectral width (i.e. spectral broadening index) over an ensemble of 10 cardiac cycles which were shown to be related to flow disturbances and recirculation.

Color DUS enables real-time flow visualization enabling overall understanding of the flow such as flow direction (i.e. forward and reverse) and the presence of large recirculation zones. In color DUS, similarly the Doppler shift yields velocity information. However, unlike spectral DUS, an entire scan line is processed for the stream of received echoes; through autocorrelation processing, streams of echoes received from an ensemble of transmitted pulses (e.g. eight pulses) yield an average Doppler shift which is transformed to velocity information. The scan line is then repeated laterally to build up a two-dimensional (2D) flow image. Several studies have applied this technique to visualize stenotic flow: Polak *et al.* [108] applied color DUS *in vitro* to a model of a normal carotid artery and were able to measure the size of the recirculation zone in the sinus bulb; Rittgers *et al.* [109] characterized stenotic flow *in vitro* in a series of tubes with asymmetric stenosis severity ranging from 0 to 80% and reported close correspondence of flow features compared to hydrogen-bubble visualization. Although conventional color DUS can assist with flow visualization, quantifiable hemodynamic assessments are limited due to the low temporal resolution (low frame rate).

With recent hardware and the capability of parallel computing, an entirely new class of ultrafast ultrasound imaging has been introduced in which high-frame rate acquisition in order of kilohertz are feasible increasing the frame rate of conventional color Doppler by five to 10 times [110]. Bercoff *et al.* [111] applied plane-wave emission for color flow imaging, where instead of transmission of the focused beam successively line-by-line, the entire field of view (FOV) is insonified sequentially by several plane waves each transmitted at a different angle. The summation of the received backscattered signals is then used to yield a compounded high-temporal resolution 2D image.

Cross-beam vector Doppler and speckle-tracking techniques are among the Doppler techniques developed for 2D-2C (i.e. in-plane) velocity vector measurements [112, 113]. In vector Doppler, a velocity vector is yielded by simultaneous measurement of two differently directed velocity components made possible by two different transmit angles (i.e. crossed beams) [114, 115]. Speckle tracking derives in-plane velocity vectors by correlating sequential images depicting the speckle patterns created by constructive and destructive interference of backscattered ultrasound waves from blood [116]. The ultrafast approach has also been applied to the ultrasound vector method; Udesen *et al.* [117] proposed the use of plane-wave excitation for the speckle-tracking method and presented preliminary *in vivo* measurements in a healthy human carotid bifurcation. Although studies have reported promising results for future clinical implementation, recent high-frame-rate ultrasound techniques are mostly in the developmental stage.

1.2.2 Magnetic resonance imaging (MRI)

The first exploitation of magnetic resonance for blood flow measurements was suggested by Singer in 1959 for nuclear magnetic resonance (NMR) based on the time-of-flight effect of flowing blood [118]. As described earlier, this method provides angiographic estimation of the degree of stenosis severity.

Quantified flow measurements via velocity maps are accomplished using phase-contrast MRI (PC-MRI). The magnetization vector of the molecular spins bears both magnitude and phase information. By measuring the phase shifts of the moving spins (i.e. protons) in blood, velocity and directional information can be obtained for the plane perpendicular to the blood flow direction. The first *in vivo* applications of the velocity maps were in the early 1980s.

Although real-time measurements are possible, for improved quality of signal, without the loss of spatial resolution, data acquisition is split over multiple cardiac cycles with each acquisition synchronized to the cardiac cycle by means of electrocardiogram (ECG) gating. From the combined signal for each cardiac time point, a series of time-resolved ('CINE') images are generated, which represents the flow dynamics over the course of the cardiac cycle.

Traditionally, PC-MRI methods were used to resolve single-direction velocity measurements in 2D planes. By acquisition of orthogonal planes, all three components of velocity can be resolved [119]. Recent developments permit the comprehensive time-resolved acquisition with full volumetric coverage yielding three-component velocity-vector maps. The capability of this method – popularly referred to as 4D (flow) MRI – in resolving and visualizing time-evolving complex flow features has been applied towards many hemodynamic studies. For instance, Frydrychowicz *et al.* [120] reported flow visualization and WSS measurements in patients with aortic coarctation (i.e. constriction). Most recently, Dyverfeldt *et al.* [121] applied this method for *in vivo* measurements of turbulence kinetic energy (TKE) and pressure loss in aortic stenosis. Further technical details and various hemodynamic applications are discussed in the review article by Markl *et al.* [122].

1.2.3 Numerical methods

Stenotic flow has been studied extensively using computational fluid dynamics (CFD) methods. The conventional CFD method is based on the Reynolds-averaged Navier-Stokes (RANS), which provides a low-cost approach to describe the unsteady flows. The governing equations of the RANS models include the ensemble-averaged velocities thus only describing the largest flow structures and do not include the smaller scales. In order to model turbulent flow, the component of velocity fluctuations appearing as Reynolds shear stress in the RANS equation must be solved to close the system. There are a variety of approaches for RANS-based turbulent models including zero-, one- and two- equation models in which the eddy viscosity is assumed to be isotropic which may not be the case in flows with larger separations. The conventional RANS models are designed for either laminar or classical high- Re turbulence. This imposes another limitation on predicting flows with low Re in which transitional behaviors are expected. Therefore, for transitional flows, a specific class of RANS designed for low- Re models may be more appropriate. For pulsatile flow conditions with transitional behaviors, the RANS approach incorporating two-equation low- Re turbulent models has been employed in both a simple stenotic tube [123] and patient-specific carotid artery models [124]. Later, it was clarified that there are inherent limitations associated with RANS when applied to

pulsatile flow simulations as the governing equations of this method are ensemble-averaged [125].

A well-suited method to transitional regimes is the direct numerical simulation (DNS) method, in which all turbulence scales are fully resolved. Fisher *et al.* [126] introduced the application of this method to flow predictions in a stenosed carotid artery bifurcation. They evaluated the simulation requirements in terms of the adequate number of grid points, which was reported to about 2-4 millions points. Energy spectra of velocity fluctuations revealed the presence of high-frequency flow variations in the post-stenotic region and indicated evidence of high spatio-temporal resolution requirements for transitional flows, as opposed to large-scale structures in laminar flows. Lee *et al.* [127] employed this evaluated DNS method to study the transitional flow characteristic in a patient-specific mildly stenosed carotid artery. Flow characteristics during the systolic phase, including high-frequency vortex shedding and strong Dean-type vortices downstream of the stenosis, were reported, where the transitional state of the flow was demonstrated through both time and frequency analyses. Grinberg *et al.* [128] also employed the DNS approach to analyze the transient turbulent flow in a patient-specific model of a carotid artery bifurcation incorporating 77% stenosis (by area reduction, equals $\sim 52\%$ diameter reduction) and reported detailed features of the flow such as helical swirling motion downstream of the stenosis.

Despite the advantage of DNS in temporally and spatially resolving the flow characteristics, the computational expense of this method may impose some limitations. In this case, the large-eddy simulation (LES) method, in which only the large or filtered scales are resolved, may be considered the method of choice. Mittal *et al.* [129] applied this method to model the flow in a 50%-stenosed tube and depicted vortex shedding along the shear layer. Flow was transitional immediately downstream of the stenosis and fully turbulent further downstream. In a comparative study, Rayz *et al.* [130] applied the LES technique to detect transitional flow in a severely stenosed model of the carotid artery bifurcation under steady inlet flow with Reynolds number of 410. The focus of this investigation was to assess the effect of computational-grid resolution, which in the case of insufficiency resulted in no notable differences from the laminar flow solution. By

increasing the resolution, transitional features of the flow, such as vortex shedding downstream of the stenosis, appeared. They concluded that LES successfully simulates arterial flow at moderately high Reynolds numbers.

CFD modeling can resolve the complex features of the flow in a time and cost-effective way. However, in order to gain full confidence in CFD predictions, validation with experimental measurements is required. Perhaps MRI has been the main assisting platform for CFD modeling providing model geometries [131], boundary conditions of flow (MRI-based CFD) [132], and velocity-based validation. Milner *et al.* [133] extracted the MRI-based geometry of the carotid artery bifurcations of two healthy subjects and compared the CFD results with an idealized model of the carotid artery. WSS patterns were compared among the three models and, based on the observed inter-subject variations, it was postulated that development and progression of atherosclerotic plaque can be mediated by individualized characteristics of the carotid artery. Long *et al.* [78] conducted an *in vivo* MRI study and measured velocities in a healthy carotid artery as a validation base for the CFD predictions in the same model. For most of the cardiac cycle, good qualitative and quantitative agreements between the flow patterns were reported; however, discrepancies were observed during the systolic deceleration phase in which skew pattern was observed for the measured CCA flow different from more circular pattern predicted by CFD. Botnar *et al.* [134] conducted *in vitro* study under pulsatile flow inlet in a healthy replica of carotid artery bifurcation and compared their result to those of CFD. In general MRI and numerical results agreed well, however, variation was observed in secondary flow patterns in the form of developed vortices. Marshall *et al.* [135] studied flow in two idealized models of normal and 30%-stenosed carotid artery and compared simulated results with MRI measurements. The qualitative comparison revealed relatively good agreement in central-plane flow pattern; however, in the secondary-flow region, MRI-based WSS extraction was unreliable due to difficulty in measuring low-velocity ranges in secondary flow region in the stenosed model.

As described, the majority of MRI-based CFD validations in the carotid artery are performed in the healthy models. In the stenosed models where dynamic range of velocities is wide, MRI can show deficiencies if both high and low velocities are to be

measured [136]. Moreover, in the stenosed models in which onset of instabilities and turbulence is expected, high velocity fluctuations can result in dispersion and loss of signal (i.e. intravoxel dephasing) proving challenging for flow quantification in these models and requiring validation itself [122]. Due to current limitations of clinical techniques, either DUS or MRI, in some cases the role is reversed and numerical simulation are used as validation [137].

Non-clinical experimental techniques can also provide validation for CFD; several cardiovascular flow studies have validated their CFD predictions with LDA measurements; Tan *et al.* [124], and Banks and Bressloff [138] validated their turbulent model developed for stenotic flows based on LDA measurements provided by Ahmed and Giddens [64] for selected velocity profiles in a simple tube with 75% stenosis (area reduction, equals 50% diameter reduction). Followed by the conclusion of good agreement, both studies have applied their method to simulate flow in stenosed carotid models.

To date, particle image velocimetry is considered the gold-standard experimental technique providing full-field vectoral velocity quantifications that can be applied to validate measurements from both clinical modalities and numerical simulations. As the technique of choice in this thesis, the following section is dedicated to an overall overview of this technique followed by its adaptation and application in hemodynamic studies.

1.3 Particle Image Velocimetry (PIV)

Particle image velocimetry (PIV) refers to the class of optical velocimetry techniques that provides instantaneous velocity measurements based on recorded images of displaced tracer particles seeded in the flow media. The flexibility and expandability of PIV to specific applications makes this technique a suitable candidate for a variety of fluid mechanics studies ranging from aerodynamics to biology, and from large-scale industrial to small-scale laboratory set-ups. From motion characterizations in the atmosphere to within boundaries of nanostructured surfaces [139], the PIV technique has been evolving over the past three decades, and many developments are still ongoing. Extensive details

on the developmental history, components, systematic arrangements, applications of PIV, and future directions can be found in the book by Raffel *et al.* [140], as well as the most recent review by Westerweel *et al.* [141]. Regardless of their complexity level, PIV techniques mainly follow similar underlying working principles that will be discussed in the following section.

1.3.1 Working principles of the classical PIV technique

A PIV system fundamentally is composed of an illumination source, tracer particles, and recording camera(s). Pulsed lasers (e.g. Nd:YAG lasers) are the standard PIV light source and are equipped with light-sheet optics to generate a thin planar illumination through the flow field, which is seeded with tracer particles. For the specified field of view (FOV), the camera records at least two sequential frames separated by a time interval adjusted according to the flow conditions. A timing unit synchronizes shuttering of the camera and laser pulses.

Modern cameras considered for PIV applications include charged-coupled device (CCD) or complementary metal-oxide semiconductor (CMOS) sensors (usually with megapixel resolution capacity), with the latter enabling high sensitivity and high-speed recording in the hundreds of kilohertz to megahertz range [140].

Analysis of the recorded images includes subdividing the image area into small interrogation windows with the assumption that particles within each window move homogeneously. Velocity evaluation is most often performed by cross correlating the corresponding windows in the first and second frames in order to estimate the displacement of the particles [142]. To reduce the computational time, instead of applying the direct cross-correlation scheme, the standard procedure is to apply the correlation theorem and calculate the inverse-Fourier transform of the complex conjugate Fourier transform of the intensity images. From the estimated displacement, the planar two-component (2D-2C) velocity vectors are then calculated for the whole FOV by taking into account the time delay between the two illuminations and the magnification factor between the image and object planes.

In the design of the PIV experiment and prior to data acquisition, careful considerations are required accounting for the flow media and conditions. For instance, *a priori* optimization ensures the suitability of tracer particles, which are expected to faithfully follow the flow and appear with adequate diameter (i.e. more than one-pixel size) in the recorded images. Other optimizations include adjusting the seeding density of the particles, for which at least three pairs per interrogation window are recommended [143], and adjusting the time interval between the two illumination pulses in order to allow adequate particle displacement while avoiding to have particles leaving the illuminated plane.

With recent advances in evaluation algorithms, high-repetition rate hardware, and computing capacities, the boundaries of conventional PIV have been pushed, and an entirely new class of PIV techniques has been introduced. Currently, two of the major ongoing developments are time-resolved PIV, founded on the high-repetition-rate pulsed lasers and high-frame-rate cameras, and tomographic PIV, which is a multi-camera system enabling volumetric three-component (3D-3C) measurements [144, 145].

One of the extensions of classical PIV is stereoscopic PIV [146], that in its planar form enables three-component (2D-3C) velocity measurements. According to Westerweel *et al.* [141], “planar stereoscopic PIV is the current standard system, providing a major tool for understanding complex and turbulent flows, especially instantaneous flow structures”. In the present work, a stereoscopic PIV system was applied for flow characterizations. An overview of stereoscopic PIV along with the required arrangements are given in Chapter 2 – Methods.

1.3.2 PIV application for hemodynamic studies

Ideally, hemodynamic measurements are performed with clinically applicable flow-measurement modalities, such as DUS and MRI, as described earlier. However, the main limitation of these techniques is imposed by their insufficiencies in temporal and spatial resolution or the trade-off between the two. The typical temporal resolution for MRI is estimated between 20 to 50 ms; however, since improved signal is obtained from the combination of signals of multiple cardiac cycles, the acquisition time can be expanded to

minutes for 3D and three-directional velocity coverage. For instance, it is estimated that cardiac blood flow can currently be measured with 3-mm spatial resolution and 50-ms temporal resolution from a 20-minute data acquisition time [136]. Color DUS can provide real-time flow visualization with temporal resolution of 4-20 ms in 2D [136]. Although high-frame rate DUS techniques promise significantly higher temporal resolutions, in general, the accuracy of DUS flow measurements in resolving smaller unsteady features is tampered by spatial and temporal averaging in post-processing of the raw Doppler signals.

PIV is a non-intrusive technique allowing flow to be measured without the interference of measurement probes. An important advantage of PIV is the ability for full-field measurement of instantaneous velocities with high spatial resolution and high temporal resolution, extending down to the micron range with high-speed frame rates on the order of kilohertz [140].

With its capability in resolving details of spatially and temporally evolving flows, PIV has been adopted for *in vitro* hemodynamic studies in cardiovascular or cardiovascular-assisting device models. The first cardiovascular application of PIV can most likely be traced back to as early as 1995 to investigate flow-related thrombotic complications in mechanical heart valves, which are perhaps some of the most studied models using PIV [147]. Application of PIV has also been expanded to flow studies in replicas of aneurysm models [148] and bifurcating structures [149], among other models [150-152]. PIV has also provided baseline understanding of stenotic flows applied to simple stenosed tubes. For instance, in study by Vetel *et al.* [153], stereo-PIV was applied to characterize transitional-turbulent flow regimes in an axisymmetric stenotic tube with 75% area reduction (i.e. 50% diameter reduction). The applied inlet flow was steady with Reynolds number ranging from 100 to 1100. A critical Reynolds number of 400 was recognized beyond which post-stenotic flow became highly unsteady and intermittent. Once the Reynolds number was increased beyond 900, the oscillation phenomena generated by large-scale unstable features (i.e. recirculation zone) disappeared and flow become stationary turbulent. Karri and Vlachos [154] investigated the effect of phase angle between the pressure and flow in two models of compliant stenosed tubes under various

pulsatile flow inlets. Several studies have also applied PIV to investigate the effect of stenting on downstream flow patterns in stenotic tubes [155, 156].

The efficiency of PIV has inspired a generation of new velocimetry techniques with *in vivo* implications including ultrasonic PIV (echo-PIV), micro-PIV (μ PIV), micro ultrasound PIV, and x-ray PIV, all of which employ the principle of velocimetry based on tracer particles. A review on these PIV-inspired techniques can be found elsewhere [157]. Echo-PIV has gained much interest recently and has been fast improving over the past decade [158, 159]. This technique is based on the synthesis of PIV and brightness-mode (B-mode) ultrasound imaging techniques. Contrast microbubbles are used as the tracer particles providing an enhanced level of ultrasound backscatter. Similar to optical PIV, the two sequential frames (i.e. B-mode images) are subdivided into interrogation regions and are subject to cross-correlation, resulting in a 2D-2C velocity vector map. The clinical potential of echo-PIV has also recently been demonstrated; Zhang *et al.* [160] conducted a comparative study between the echo-PIV *in vivo* velocity profiles of human CCA flow and PC-MRI measurements and *in vitro* results to optical PIV. A good agreement with both validations was reported concluding the *in vivo* feasibility of echo-PIV with high temporal (~ 0.7 ms) and spatial (~ 0.5 mm) resolution. Niu *et al.* [161] proposed a method of simultaneously measuring velocity and arterial wall strain and tested their method *in vitro* and *in vivo* (mouse CCA) with validation based on DUS velocity measurements.

1.3.3 Previous PIV studies of carotid artery bifurcation models

To date, only three PIV studies (excluding echo-PIV studies) in carotid artery models have been reported, all of which were conducted under steady inlet-flow assumptions. Bale-Glickman *et al.* [162] applied conventional 2D PIV to two optically transparent silicone phantoms incorporating patient-specific geometries – one with a moderate-to-severe ICA stenosis of 70% (area reduction) and the other one with severe ($>70\%$) stenosis. The working fluid was composed of isopropyl alcohol (70%) and glycerol (30%), which gave lower values of density and dynamic viscosity compared to those of blood, in order to match the refractive index of the silicone. Images were acquired with a

maximum of 30-Hz frame rate, and the time interval between the sequential frames was set to 3 ms. Flow was input at three levels of Reynolds number with the maximum of 410. In-plane velocity streamlines visualized governing features of flow, such as regions of flow separation and recirculations, and revealed the unsteady state of the flow at highest Reynolds number for both models.

Vetel *et al.* [163] studied flow in a scaled-up patient-specific model of a healthy carotid artery using stereo-PIV equipped with Scheimpflug adapters. To enable an orthogonal viewing condition, normally achieved by using a prism as described earlier, they assembled the phantom in an octagonal tank with cameras viewing the test section through the sides. The tank was filled with the same working fluid as for the phantom perfusion – a water-glycerol (40:60 ratio by weight) solution that matched the refractive index of the silicone material of the phantom. In their study, coherent structures of the flow were visualized using finite-time Lyapunov exponent. A physiologically relevant Reynolds number of 340 was first applied, and coherent structures – such as regions of flow reversal and recirculation – were highlighted. Interestingly, for a high Reynolds number (850, 1000, 1200), an unusual transitional behavior was revealed in the CCA before the bifurcation apex. This observation was postulated to be driven by the presence of physiologically realistic curvatures in the CCA of the model, which is different from the normally studied straight and circular cross-section CCA models. This finding can be recognized when applying boundary conditions for simulation studies in which, normally, a fully developed inlet flow is assumed.

Buchmann *et al.* [164] employed both tomographic and stereoscopic PIV in an exact replica of a healthy carotid artery model. The working fluid was an aqueous mixture of glycerin (61% by weight) which matched the refractive index of their silicone phantom. The working fluid, however, had significantly higher (approximately three-fold) dynamic viscosity compared to that of blood. Steady flow was input at a Reynolds number of 339 (corresponding to average physiological flow). Although unrealistic, the use of steady flow conditions suited the scope of their study in which the feasibility of tomographic PIV was demonstrated and validated via measurement-error comparison to stereo-PIV. In general, excellent agreement was reported between the instantaneous velocity maps

measured with both tomographic and stereo-PIV. WSS was computed via interpolation of principal shear stress values on the vessel-wall boundaries and yielded acceptable agreement, with some differences in magnitude between the two techniques.

1.4 Research Objectives and Thesis Outline

The role of hemodynamics in thrombosis and the subsequent complication of ischemic events is now well recognized and has motivated many cardiovascular hemodynamic studies. In particular, stenotic flow has been extensively studied and characterized through various stenotic models (albeit the majority of them in tubular models), inlet flow conditions, and measurement techniques. As described in Section 1.1.4, the local geometry of plaque can influence the flow patterns downstream of a stenosis. The degree of stenosis severity is recognized as an important variable, and as described earlier, forms the current clinical diagnosis by being graded either directly based on local diameters or using DUS-based clinical diagnosis of measuring the stenosis-induced jet flow. However, this current diagnosis will not encourage distinguishing between plaques with different symmetries, as well as plaques with irregular surfaces and ulceration.

More sensitive stroke risk estimations are expected when the level of thrombotic activity is assessed. Although, the possible association of a higher level of thrombotic activity with increased stenosis severity can perhaps be recognized in stroke statistics (which show a higher risk of stroke for patients with more severe stenosis), it is not clear how the local geometry of the plaque affects the thrombotic-associated hemodynamic factors. Once this association is understood, quantifiable metrics reflecting hemodynamic factors, such as the level of flow instabilities and disturbances, may assist with the long-term goal of improved diagnosis of pathological plaques prone to thrombosis.

The overall objectives of this thesis were to: 1) investigate the thrombosis-associated hemodynamics of the carotid artery bifurcation under the effect of plaque geometry and ulceration, and 2) investigate quantitative metrics that can reflect the change in flow complexity and the disturbance induced by changes in plaque features. A stereoscopic PIV system, as the current gold standard technique providing full-field flow measurement, was the technique of choice in this thesis. PIV-compatible blood-

mimicking fluid and carotid artery phantoms were developed previously in our laboratory and implemented for this thesis. To achieve the above objectives, the primary goals of this thesis can be broken down as follows: 1) configure and optimize the stereoscopic PIV for instantaneous velocity measurements in the life-sized carotid phantoms, 2) investigate instantaneous and phased-averaged (coherent) flow features from the central-plane of measurement in carotid bifurcation models, 3) extract the volumetric large coherent structures via reconstruction of the lumen volume, 4) investigate the effect of plaque geometry on the level of flow complexity and disturbances, 5) investigate clinically applicable quantitative metrics indicative of the level of flow disturbances, and 6) evaluate the level and pattern of shear stress affected by changing plaque geometry.

These goals were achieved in the three studies detailed in this thesis. Detailed extraction and analysis of the flow features in individual carotid bifurcations will be provided collectively in all three studies each with an additional specific focus. The study described in Chapter 3 will specifically aim at assessing the transitional flow regime and the change in the energy content of the flow due to the presence of stenosis and with increasing stenosis severity from a moderate to a severe stenosis. This chapter will also introduce two quantitative metrics to address the fifth goal above. Chapter 4 will focus on a comparative evaluation of flow disturbances downstream of a stenosis in a comprehensive family of carotid bifurcations spanning the full range of disease progression with varying plaque symmetry, as well as the presence of plaque ulceration. This chapter also will address the fifth goal by demonstrating the capability of statistically based metrics of turbulence measurement in reflecting the effect of plaque geometry. Chapter 5 will focus specifically on shear-stress evaluation in the same family of models employed in the previous chapter. Finally, Chapter 6 will provide a summary of the described studies and address the future directions of the current work.

The overall hypothesis of this thesis is that certain geometrical factors of carotid artery plaque, including increasing stenosis severity, plaque eccentricity, and the presence of plaque ulceration will result in alterations and enhancement of the flow disturbances and shear-stress levels. It is hypothesized that these alterations can be captured and quantified via PIV measurements in life-sized carotid artery models under pulsatile flow conditions.

1.5 References

- [1] G. A. Donnan, M. Fisher, M. Macleod, *et al.* (2008), Stroke. *Lancet*, vol. 371, pp. 1612-1623.
- [2] A. S. Go, D. Mozaffarian, V. L. Roger, *et al.* (2013), Heart disease and stroke statistics-2013 update a report from the american heart association. *Circulation*, vol. 127, pp. E6-E245.
- [3] Heart and Stroke Fundation of Canada (2003), *The growing burden of heart disease and stroke in canada*. Available online at: <http://www.cvdinfobase.ca/cvdbook/En/>
- [4] F. D. Kolodgie, G. Nakazawa, G. Sangiorgi, *et al.* (2007), Pathology of atherosclerosis and stenting. *Neuroimaging Clinics of North America*, vol. 17, pp. 285-vii.
- [5] P. Vilela and A. Goulao (2005), Ischemic stroke: Carotid and vertebral artery disease. *European Radiology*, vol. 15, pp. 427-433.
- [6] J. Gallego, E. Martinez Vila, and R. Munoz (2007), Patients at high risk for ischemic stroke: Identification and actions. *Cerebrovascular Diseases*, vol. 24, pp. 49-63.
- [7] S. Chaturvedi, A. Bruno, T. Feasby, *et al.* (2005), Carotid endarterectomy - an evidence-based review - report of the therapeutics and technology assessment subcommittee of the american academy of neurology. *Neurology*, vol. 65, pp. 794-801.
- [8] H. Gray and W. H. Lewis (1918), *Anatomy of the human body*. Lea & Febiger. Available online at: <http://www.bartleby.com/107/>
- [9] W. S. Savory (1856), Case of a young woman in whom the main arteries of both upper extremities and of the left side of the neck were throughout completely obliterated. *Medico-chirurgical transactions*, vol. 39, pp. 205-19.
- [10] North american symptomatic carotid endarterectomy trial (NASCET) investigators. (1991). Benefit of carotid endarterectomy for patients with high-grade stenosis of the internal carotid artery, *Stroke*, vol. 22, pp. 816-7.
- [11] B. Farrell, A. Fraser, P. Sandercock, *et al.* (1998), Randomised trial of endarterectomy for recently symptomatic carotid stenosis: Final results of the mrc european carotid surgery trial (ECST). *Lancet*, vol. 351, pp. 1379-1387.

- [12] A. J. Fox (1993), How to measure carotid stenosis. *Radiology*, vol. 186, pp. 316-318.
- [13] P. M. Rothwell, M. Eliasziw, S. A. Gutnikov, *et al.* (2003), Analysis of pooled data from the randomised controlled trials of endarterectomy for symptomatic carotid stenosis. *Lancet*, vol. 361, pp. 107-116.
- [14] M. R. Jaff, G. V. Goldmakher, M. H. Lev, *et al.* (2008), Imaging of the carotid arteries: The role of duplex ultrasonography, magnetic resonance arteriography, and computerized tomographic arteriography. *Vascular Medicine*, vol. 13, pp. 281-292.
- [15] J. M. Wardlaw, F. M. Chappell, J. J. K. Best, *et al.* (2006), Non-invasive imaging compared with intra-arterial angiography in the diagnosis of symptomatic carotid stenosis: A meta-analysis. *Lancet*, vol. 367, pp. 1503-1512.
- [16] S. S. Berr, N. S. Hurt, C. R. Ayers, *et al.* (1995), Assessment of the reliability of the determination of carotid-artery lumen sizes by quantitative image-processing of magnetic-resonance angiograms and images. *Magnetic Resonance Imaging*, vol. 13, pp. 827-835.
- [17] G. Fell, D. J. Phillips, P. M. Chikos, *et al.* (1981), Ultrasonic duplex scanning for disease of the carotid-artery. *Circulation*, vol. 64, pp. 1191-1195.
- [18] G.-M. von Reutern, M.-W. Goertler, N. M. Bornstein, *et al.* (2012), Grading carotid stenosis using ultrasonic methods. *Stroke*, vol. 43, pp. 916-921.
- [19] E. G. Grant, C. B. Benson, G. L. Moneta, *et al.* (2003), Carotid artery stenosis: Gray-scale and Doppler US diagnosis - society of radiologists in ultrasound consensus conference. *Radiology*, vol. 229, pp. 340-346.
- [20] L. B. Goldstein, C. C. D. Bushnell, R. J. Adams, *et al.* (2011), Guidelines for the primary prevention of stroke a guideline for healthcare professionals from the american heart association/american stroke association. *Stroke*, vol. 42, pp. 517-584.
- [21] T. G. Brott, J. L. Halperin, S. Abbara, *et al.* (2011), 2011 ASA/ACCF/AHA/AANN/AANS/ACR/ASNR/CNS/SAIP/SCAI/SIR/SNIS/SVM/SVS guideline on the management of patients with extracranial carotid and vertebral artery disease: Executive summary. *Journal of the American College of Cardiology*, vol. 57, pp. 1002-1044.
- [22] B. A. Wasserman, R. J. Wityk, H. H. Trout, *et al.* (2005), Low-grade carotid stenosis - looking beyond the lumen with MRI. *Stroke*, vol. 36, pp. 2504-2513.
- [23] B. G. Brown, C. A. Gallery, R. S. Badger, *et al.* (1986), Incomplete lysis of thrombus in the moderate underlying atherosclerotic lesion during intracoronary

infusion of streptokinase for acute myocardial-infarction - quantitative angiographic observations. *Circulation*, vol. 73, pp. 653-661.

- [24] M. J. Davies (1990), A macro and micro view of coronary vascular insult in ischemic-heart-disease. *Circulation*, vol. 82, pp. 38-46.
- [25] P. M. Rothwell and L. B. Goldstein (2004), Carotid endarterectomy for asymptomatic carotid stenosis - asymptomatic carotid surgery trial. *Stroke*, vol. 35, pp. 2425-2427.
- [26] B. Furie and B. C. Furie (2007), In vivo thrombus formation. *Journal of Thrombosis and Haemostasis*, vol. 5, pp. 12-17.
- [27] P. Constantinides (1990), Cause of thrombosis in human atherosclerotic arteries. *American Journal of Cardiology*, vol. 66, pp. G37-G40.
- [28] D. Leys (2001), Atherothrombosis: A major health burden. *Cerebrovascular Diseases*, vol. 11, pp. 1-4.
- [29] V. Fuster, B. Stein, J. A. Ambrose, *et al.* (1990), Atherosclerotic plaque rupture and thrombosis - evolving concepts. *Circulation*, vol. 82, pp. 47-59.
- [30] A. V. Finn, M. Nakano, J. Narula, *et al.* (2010), Concept of vulnerable/unstable plaque. *Arteriosclerosis Thrombosis and Vascular Biology*, vol. 30, pp. 1282-1292.
- [31] N. Nighoghossian, L. Derex, and P. Douek (2005), The vulnerable carotid artery plaque - current imaging methods and new perspectives. *Stroke*, vol. 36, pp. 2764-2772.
- [32] G. L. ten Kate, E. J. Sijbrands, D. Staub, *et al.* (2010), Noninvasive imaging of the vulnerable atherosclerotic plaque. *Current Problems in Cardiology*, vol. 35, pp. 556-591.
- [33] N. Takaya, C. Yuan, B. C. Chu, *et al.* (2006), Association between carotid plaque characteristics and subsequent ischemic cerebrovascular events - a prospective assessment with MRI - initial results. *Stroke*, vol. 37, pp. 818-823.
- [34] L. G. Spagnoli, A. Mauriello, G. Sangiorgi, *et al.* (2004), Extracranial thrombotically active carotid plaque as a risk factor for ischemic stroke. *Journal of the American Medical Association*, vol. 292, pp. 1845-1852.
- [35] C. K. Zarins and C. A. Taylor (2002), "Hemodynamic factors in atherosclerosis," in *Vascular surgery: A comprehensive review*. W.B. Saunders Company, Philadelphia, PA, pp. 105-118.

- [36] D. P. Giddens, C. K. Zarins, and S. Glagov (1993), The role of fluid-mechanics in the localization and detection of atherosclerosis. *Journal of Biomechanical Engineering*, vol. 115, pp. 588-594.
- [37] G. C. Makris, A. N. Nicolaides, X. Y. Xu, *et al.* (2010), Introduction to the biomechanics of carotid plaque pathogenesis and rupture: Review of the clinical evidence. *British Journal of Radiology*, vol. 83, pp. 729-735.
- [38] P. F. Davies (2009), Hemodynamic shear stress and the endothelium in cardiovascular pathophysiology. *Nature Clinical Practice Cardiovascular Medicine*, vol. 6, pp. 16-26.
- [39] J.-J. Chiu and S. Chien (2011), Effects of disturbed flow on vascular endothelium: Pathophysiological basis and clinical perspectives. *Physiological Reviews*, vol. 91, pp. 327-387.
- [40] S. A. Berger and L. D. Jou (2000), Flows in stenotic vessels. *Annual Review of Fluid Mechanics*, vol. 32, pp. 347-382.
- [41] V. Fuster, P. M. Steele, and J. H. Chesebro (1985), Role of platelets and thrombosis in coronary atherosclerotic disease and sudden-death. *Journal of the American College of Cardiology*, vol. 5, pp. B175-B184.
- [42] S. P. Jackson, W. S. Nesbitt, and E. Westein (2009), Dynamics of platelet thrombus formation. *Journal of Thrombosis and Haemostasis*, vol. 7, pp. 17-20.
- [43] W. S. Nesbitt, P. Mangin, H. H. Salem, *et al.* (2006), The impact of blood rheology on the molecular and cellular events underlying arterial thrombosis. *Journal of Molecular Medicine*, vol. 84, pp. 989-995.
- [44] J. D. Hellums (1994), 1993 Whitaker lecture - biorheology in thrombosis research. *Annals of Biomedical Engineering*, vol. 22, pp. 445-455.
- [45] D. M. Wootton and D. N. Ku (1999), Fluid mechanics of vascular systems, diseases, and thrombosis. *Annual Review of Biomedical Engineering*, vol. 1, pp. 299-329.
- [46] Y. Miyazaki, S. Nomura, T. Miyake, *et al.* (1996), High shear stress can initiate both platelet aggregation and shedding of procoagulant containing microparticles. *Blood*, vol. 88, pp. 3456-3464.
- [47] P. A. Holme, U. Orvim, M. Hamers, *et al.* (1997), Shear-induced platelet activation and platelet microparticle formation at blood flow conditions as in arteries with a severe stenosis. *Arteriosclerosis Thrombosis and Vascular Biology*, vol. 17, pp. 646-653.

- [48] J. D. Hellums, D. M. Peterson, N. A. Stathopoulos, *et al.* (1987), "Studies on the mechanisms of shear-induced platelet activation," in *Cerebral ischemia and hemorheology*. Springer Berlin Heidelberg, pp. 80-89.
- [49] L. J. Wurzinger, R. Opitz, P. Blasberg, *et al.* (1985), Platelet and coagulation parameters following millisecond exposure to laminar shear-stress. *Thrombosis and Haemostasis*, vol. 54, pp. 381-386.
- [50] L. Badimon, J. J. Badimon, A. Galvez, *et al.* (1986), Influence of arterial damage and wall shear rate on platelet deposition - ex vivo study in a swine model. *Arteriosclerosis*, vol. 6, pp. 312-320.
- [51] D. Bluestein, L. J. Niu, R. T. Schoephoerster, *et al.* (1997), Fluid mechanics of arterial stenosis: Relationship to the development of mural thrombus. *Annals of Biomedical Engineering*, vol. 25, pp. 344-356.
- [52] W. S. Nesbitt, E. Westein, F. J. Tovar-Lopez, *et al.* (2009), A shear gradient-dependent platelet aggregation mechanism drives thrombus formation. *Nature Medicine*, vol. 15, pp. 665-U146.
- [53] D. Bluestein, E. Rambod, and M. Gharib (2000), Vortex shedding as a mechanism for free emboli formation in mechanical heart valves. *Journal of Biomechanical Engineering*, vol. 122, pp. 125-134.
- [54] R. M. Nerem and W. A. Seed (1972), In-vivo study of aortic flow disturbances. *Cardiovascular Research*, vol. 6, pp. 1-&.
- [55] D. F. Young and F. Y. Tsai (1973), Flow characteristics in models of arterial stenoses .2. Unsteady flow. *Journal of Biomechanics*, vol. 6, pp. 547-559.
- [56] D. F. Young and F. Y. Tsai (1973), Flow characteristics in models of arterial stenoses .1. Steady flow. *Journal of Biomechanics*, vol. 6, pp. 395-&.
- [57] S. J. Sherwin and H. M. Blackburn (2005), Three-dimensional instabilities and transition of steady and pulsatile axisymmetric stenotic flows. *Journal of Fluid Mechanics*, vol. 533, pp. 297-327.
- [58] C. R. White, M. Haidekker, X. Bao, *et al.* (2001), Temporal gradients in shear, but not spatial gradients, stimulate endothelial cell proliferation. *Circulation*, vol. 103, pp. 2508-13.
- [59] N. Depaola, M. A. Gimbrone, P. F. Davies, *et al.* (1992), Vascular endothelium responds to fluid shear-stress gradients. *Arteriosclerosis and Thrombosis*, vol. 12, pp. 1254-1257.
- [60] P. D. Stein and H. N. Sabbah (1974), Measured turbulence and its effect on thrombus formation. *Circulation Research*, vol. 35, pp. 608-614.

- [61] D. N. Ku (1997), Blood flow in arteries. *Annual Review of Fluid Mechanics*, vol. 29, pp. 399-434.
- [62] R. A. Cassanova and D. P. Giddens (1978), Disorder distal to modeled stenoses in steady and pulsatile flow. *Journal of Biomechanics*, vol. 11, pp. 441-453.
- [63] D. P. Giddens, R. F. Mabon, and R. A. Cassanova (1976), Measurements of disordered flows distal to subtotal vascular stenoses in thoracic aortas of dogs. *Circulation Research*, vol. 39, pp. 112-119.
- [64] S. A. Ahmed and D. P. Giddens (1984), Pulsatile poststenotic flow studies with laser Doppler anemometry. *Journal of Biomechanics*, vol. 17, pp. 695-&.
- [65] S. A. Ahmed and D. P. Giddens (1983), Velocity-measurements in steady flow through axisymmetric stenoses at moderate Reynolds-numbers. *Journal of Biomechanics*, vol. 16, pp. 505-&.
- [66] S. A. Ahmed and D. P. Giddens (1983), Flow disturbance measurements through a constricted tube at moderate Reynolds-numbers. *Journal of Biomechanics*, vol. 16, pp. 955-963.
- [67] W. Yongchareon and D. F. Young (1979), Initiation of turbulence in models of arterial stenoses. *Journal of Biomechanics*, vol. 12, pp. 185-196.
- [68] A. M. A. Khalifa and D. P. Giddens (1981), Characterization and evolution of post-stenotic flow disturbances. *Journal of Biomechanics*, vol. 14, pp. 279-296.
- [69] A. M. A. Khalifa and D. P. Giddens (1978), Analysis of disorder in pulsatile flows with application to post-stenotic blood velocity-measurement in dogs. *Journal of Biomechanics*, vol. 11, pp. 129-141.
- [70] T. L. Poepping, R. N. Rankin, and D. W. Holdsworth (2010), Flow patterns in carotid bifurcation models using pulsed Doppler ultrasound: Effect of concentric vs. Eccentric stenosis on turbulence and recirculation. *Ultrasound in Medicine and Biology*, vol. 36, pp. 1125-1134.
- [71] D. Birchall, A. Zaman, J. Hacker, *et al.* (2006), Analysis of haemodynamic disturbance in the atherosclerotic carotid artery using computational fluid dynamics. *European Radiology*, vol. 16, pp. 1074-1083.
- [72] D. A. Steinman, T. L. Poepping, M. Tambasco, *et al.* (2000), Flow patterns at the stenosed carotid bifurcation: Effect of concentric versus eccentric stenosis. *Annals of Biomedical Engineering*, vol. 28, pp. 415-423.
- [73] T. Ohara, K. Toyoda, R. Otsubo, *et al.* (2008), Eccentric stenosis of the carotid artery associated with ipsilateral cerebrovascular events. *American Journal of Neuroradiology*, vol. 29, pp. 1200-1203.

- [74] S. Ellis, E. L. Alderman, K. Cain, *et al.* (1989), Morphology of left anterior descending coronary territory lesions as a predictor of anterior myocardial-infarction - a cass registry study. *Journal of the American College of Cardiology*, vol. 13, pp. 1481-1491.
- [75] D. Tousoulis, G. Davies, T. Crake, *et al.* (1998), Angiographic characteristics of infarct-related and non-infarct-related stenoses in patients in whom stable angina progressed to acute myocardial infarction. *American Heart Journal*, vol. 136, pp. 382-388.
- [76] H. M. Loree, R. D. Kamm, C. M. Atkinson, *et al.* (1991), Turbulent pressure-fluctuations on surface of model vascular stenoses. *American Journal of Physiology*, vol. 261, pp. H644-H650.
- [77] D. L. Tang, C. Yang, S. Kobayasi, *et al.* (2003), Effect of stenosis asymmetry on blood flow and artery compression: A three-dimensional fluid-structure interaction model. *Annals of Biomedical Engineering*, vol. 31, pp. 1182-1193.
- [78] Q. Long, X. Y. Xu, K. V. Ramnarine, *et al.* (2001), Numerical investigation of physiologically realistic pulsatile flow through arterial stenosis. *Journal of Biomechanics*, vol. 34, pp. 1229-1242.
- [79] S. S. Varghese, S. H. Frankel, and P. F. Fischer (2007), Direct numerical simulation of stenotic flows. Part 2. Pulsatile flow. *Journal of Fluid Mechanics*, vol. 582, pp. 281-318.
- [80] M. Fisher, A. Paganini-Hill, A. Martin, *et al.* (2005), Carotid plaque pathology - thrombosis, ulceration, and stroke pathogenesis. *Stroke*, vol. 36, pp. 253-257.
- [81] M. Sitzler, M. Siebler, G. Rose, *et al.* (1995), Cerebral microembolism in atherosclerotic carotid artery disease: Facts and perspectives. *Functional Neurology*, vol. 10, pp. 251-258.
- [82] M. Eliasziw, J. Y. Streifler, A. J. Fox, *et al.* (1994), Significance of plaque ulceration in symptomatic patients with high-grade carotid stenosis. *Stroke*, vol. 25, pp. 304-308.
- [83] P. M. Rothwell, R. Gibson, C. P. Warlow, *et al.* (2000), Interrelation between plaque surface morphology and degree of stenosis on carotid angiograms and the risk of ischemic stroke in patients with symptomatic carotid stenosis. *Stroke*, vol. 31, pp. 615-621.
- [84] A. Mauriello, G. M. Sangiorgi, R. Virmani, *et al.* (2010), A pathobiologic link between risk factors profile and morphological markers of carotid instability. *Atherosclerosis*, vol. 208, pp. 572-580.

- [85] W. S. Moore, H. J. M. Barnett, H. G. Beebe, *et al.* (1995), Guidelines for carotid endarterectomy - a multidisciplinary consensus statement from the ad-hoc-committee, american-heart-association. *Stroke*, vol. 26, pp. 188-201.
- [86] H. C. Groen, F. J. H. Gijssen, A. van der Lugt, *et al.* (2007), Plaque rupture in the carotid artery is localized at the high shear stress region - a case report. *Stroke*, vol. 38, pp. 2379-2381.
- [87] J. K. Lovett and P. M. Rothwell (2003), Site of carotid plaque ulceration in relation to direction of blood flow: An angiographic and pathological study. *Cerebrovascular Diseases*, vol. 16, pp. 369-375.
- [88] C. J. Slager, J. J. Wentzel, F. J. H. Gijssen, *et al.* (2005), The role of shear stress in the destabilization of vulnerable plaques and related therapeutic implications. *Nature Clinical Practice Cardiovascular Medicine*, vol. 2, pp. 456-464.
- [89] E. Y. Wong, H. N. Nikolov, M. L. Thorne, *et al.* (2009), Clinical Doppler ultrasound for the assessment of plaque ulceration in the stenosed carotid bifurcation by detection of distal turbulence intensity: A matched model study. *European Radiology*, vol. 19, pp. 2739-2749.
- [90] C. Tropea (1995), Laser-Doppler anemometry - recent developments and future challenges. *Measurement Science & Technology*, vol. 6, pp. 605-619.
- [91] B. K. Bharadvaj, R. F. Mabon, and D. P. Giddens (1982), Steady flow in a model of the human carotid bifurcation .1. Flow visualization. *Journal of Biomechanics*, vol. 15, pp. 349-362.
- [92] M. Motomiya and T. Karino (1984), Flow patterns in the human carotid-artery bifurcation. *Stroke*, vol. 15, pp. 50-56.
- [93] C. C. M. Rindt and A. A. vonSteenhoven (1996), Unsteady flow in a rigid 3-d model of the carotid artery bifurcation. *Journal of Biomechanical Engineering-Transactions of the ASME*, vol. 118, pp. 90-96.
- [94] D. N. Ku and D. P. Giddens (1987), Laser Doppler anemometer measurements of pulsatile flow in a model carotid bifurcation. *Journal of Biomechanics*, vol. 20, pp. 407-421.
- [95] C. K. Zarins, D. P. Giddens, B. K. Bharadvaj, *et al.* (1983), Carotid bifurcation atherosclerosis quantitative correlation of plaque localization with flow velocity profiles and wall shear-stress. *Circulation Research*, vol. 53, pp. 502-514.
- [96] F. J. H. Gijssen, D. E. M. Palmen, M. H. E. vanderBeek, *et al.* (1996), Analysis of the axial flow field in stenosed carotid artery bifurcation models - lda experiments. *Journal of Biomechanics*, vol. 29, pp. 1483-1489.

- [97] L. M. Valdescruz, A. P. Yoganathan, T. Tamura, *et al.* (1986), Studies invitro of the relationship between ultrasound and laser Doppler velocimetry and applicability of the simplified bernoulli relationship. *Circulation*, vol. 73, pp. 300-308.
- [98] K. Perktold, M. Hofer, G. Rappitsch, *et al.* (1998), Validated computation of physiologic flow in a realistic coronary artery branch. *Journal of Biomechanics*, vol. 31, pp. 217-228.
- [99] D. Liepsch, G. Pflugbeil, T. Matsuo, *et al.* (1998), Flow visualization and 1- and 3-D laser-Doppler-anemometer measurements in models of human carotid arteries. *Clinical Hemorheology and Microcirculation*, vol. 18, pp. 1-30.
- [100] P. Vennemann, R. Lindken, and J. Westerweel (2007), In vivo whole-field blood velocity measurement techniques. *Experiments in Fluids*, vol. 42, pp. 495-511.
- [101] P. N. Burns (1987), The physical principles of Doppler and spectral-analysis. *Journal of Clinical Ultrasound*, vol. 15, pp. 567-590.
- [102] P. E. Zuech, R. S. C. Cobbold, K. W. Johnston, *et al.* (1984), Spectral-analysis of Doppler flow velocity signals - assessment of objectives, methods, and interpretation. *Annals of Biomedical Engineering*, vol. 12, pp. 103-116.
- [103] K. J. Hutchison and E. Karpinski (1985), Invivo demonstration of flow recirculation and turbulence downstream of graded stenoses in canine arteries. *Journal of Biomechanics*, vol. 18, pp. 285-296.
- [104] K. J. Hutchison (1995), Doppler ultrasound spectral shape downstream of significant arterial-stenosis in-vivo. *Ultrasound in Medicine and Biology*, vol. 21, pp. 447-458.
- [105] P. J. Brands, A. P. G. Hoeks, L. Hofstra, *et al.* (1995), A noninvasive method to estimate wall shear rate using ultrasound. *Ultrasound in Medicine and Biology*, vol. 21, pp. 171-185.
- [106] P. Tortoli, T. Morganti, G. Bambi, *et al.* (2006), Noninvasive simultaneous assessment of wall shear rate and wall distension in carotid arteries. *Ultrasound in Medicine and Biology*, vol. 32, pp. 1661-1670.
- [107] T. L. Poepping, H. N. Nikolov, R. N. Rankin, *et al.* (2002), An in vitro system for Doppler ultrasound flow studies in the stenosed carotid artery bifurcation. *Ultrasound in Medicine and Biology*, vol. 28, pp. 495-506.
- [108] J. F. Polak, D. H. O'leary, W. C. Quist, *et al.* (1990), Pulsed and color Doppler analysis of normal carotid bifurcation flow dynamics using an invitro model. *Angiology*, vol. 41, pp. 241-247.

- [109] S. E. Rittgers and M. C. S. Shu (1990), Doppler color-flow images from a stenosed arterial model - interpretation of flow patterns. *Journal of Vascular Surgery*, vol. 12, pp. 511-522.
- [110] J. Bercoff (2012), The leap from Doppler to ultrafast Doppler. *Radiology Management*, vol. 34, pp. 25-9; quiz 30-1.
- [111] J. Bercoff, G. Montaldo, T. Loupas, *et al.* (2011), Ultrafast compound Doppler imaging: Providing full blood flow characterization. *IEEE Transactions on Ultrasonics Ferroelectrics and Frequency Control*, vol. 58, pp. 134-147.
- [112] A. Swillens, P. Segers, H. Torp, *et al.* (2010), Two-dimensional blood velocity estimation with ultrasound: Speckle tracking versus crossed-beam vector Doppler based on flow simulations in a carotid bifurcation model. *IEEE Transactions on Ultrasonics Ferroelectrics and Frequency Control*, vol. 57, pp. 327-339.
- [113] D. H. Evans, J. A. Jensen, and M. B. Nielsen (2011), Ultrasonic colour Doppler imaging. *Interface Focus*, vol. 1, pp. 490-502.
- [114] M. D. Fox (1978), Multiple crossed-beam ultrasound Doppler velocimetry. *Ieee Transactions on Sonics and Ultrasonics*, vol. 25, pp. 281-286.
- [115] B. Dunmire, K. W. Beach, K. H. Labs, *et al.* (2000), Cross-beam vector Doppler ultrasound for angle-independent velocity measurements. *Ultrasound in Medicine and Biology*, vol. 26, pp. 1213-1235.
- [116] G. E. Trahey, J. W. Allison, and O. T. Vonramm (1987), Angle independent ultrasonic-detection of blood-flow. *IEEE Transactions on Biomedical Engineering*, vol. 34, pp. 965-967.
- [117] J. Udesen, F. Gran, K. L. Hansen, *et al.* (2008), High frame-rate blood vector velocity imaging using plane waves: Simulations and preliminary experiments. *IEEE Transactions on Ultrasonics Ferroelectrics and Frequency Control*, vol. 55, pp. 1729-1743.
- [118] T. Geva (2006), Magnetic resonance imaging: Historical perspective. *Journal of Cardiovascular Magnetic Resonance*, vol. 8, pp. 573-580.
- [119] P. J. Kilner, G. Z. Yang, R. H. Mohiaddin, *et al.* (1993), Helical and retrograde secondary flow patterns in the aortic-arch studied by 3-directional magnetic-resonance velocity mapping. *Circulation*, vol. 88, pp. 2235-2247.
- [120] A. Frydrychowicz, R. Arnold, D. Hirtler, *et al.* (2008), Multidirectional flow analysis by cardiovascular magnetic resonance in aneurysm development following repair of aortic coarctation. *Journal of Cardiovascular Magnetic Resonance*, vol. 10,

- [121] P. Dyverfeldt, M. D. Hope, E. E. Tseng, *et al.* (2013), Magnetic resonance measurement of turbulent kinetic energy for the estimation of irreversible pressure loss in aortic stenosis. *JACC-Cardiovascular Imaging*, vol. 6, pp. 64-71.
- [122] M. Markl, A. Frydrychowicz, S. Kozerke, *et al.* (2012), 4D flow MRI. *Journal of Magnetic Resonance Imaging*, vol. 36, pp. 1015-1036.
- [123] F. Ghalichi, X. Y. Deng, A. De Champlain, *et al.* (1998), Low Reynolds number turbulence modeling of blood flow in arterial stenoses. *Biorheology*, vol. 35, pp. 281-294.
- [124] F. P. P. Tan, G. Soloperto, S. Bashford, *et al.* (2008), Analysis of flow disturbance in a stenosed carotid artery bifurcation using two-equation transitional and turbulence models. *Journal of Biomechanical Engineering*, vol. 130,
- [125] A. Scotti and U. Piomelli (2002), Turbulence models in pulsating flows. *AIAA Journal*, vol. 40, pp. 537-544.
- [126] P. F. Fischer, F. Loth, S. E. Lee, *et al.* (2007), Simulation of high-Reynolds number vascular flows. *Computer Methods in Applied Mechanics and Engineering*, vol. 196, pp. 3049-3060.
- [127] S. E. Lee, S.-W. Lee, P. F. Fischer, *et al.* (2008), Direct numerical simulation of transitional flow in a stenosed carotid bifurcation. *Journal of Biomechanics*, vol. 41, pp. 2551-2561.
- [128] L. Grinberg, A. Yakhot, and G. E. Karniadakis (2009), Analyzing transient turbulence in a stenosed carotid artery by proper orthogonal decomposition. *Annals of Biomedical Engineering*, vol. 37, pp. 2200-2217.
- [129] R. Mittal, S. P. Simmons, and H. S. Udaykumar (2001), Application of large-eddy simulation to the study of pulsatile flow in a modeled arterial stenosis. *Journal of Biomechanical Engineering*, vol. 123, pp. 325-332.
- [130] V. L. Rayz, S. A. Berger, and D. Saloner (2007), Transitional flows in arterial fluid dynamics. *Computer Methods in Applied Mechanics and Engineering*, vol. 196, pp. 3043-3048.
- [131] C. A. Taylor and D. A. Steinman (2010), Image-based modeling of blood flow and vessel wall dynamics: Applications, methods and future directions. *Annals of Biomedical Engineering*, vol. 38, pp. 1188-1203.
- [132] H. C. Groen, L. Simons, Q. J. A. van den Bouwhuijsen, *et al.* (2010), MRI-based quantification of outflow boundary conditions for computational fluid dynamics of stenosed human carotid arteries. *Journal of Biomechanics*, vol. 43, pp. 2332-2338.

- [133] J. S. Milner, J. A. Moore, B. K. Rutt, *et al.* (1998), Hemodynamics of human carotid artery bifurcations: Computational studies with models reconstructed from magnetic resonance imaging of normal subjects. *Journal of Vascular Surgery*, vol. 28, pp. 143-156.
- [134] R. Botnar, G. Rappitsch, M. B. Scheidegger, *et al.* (2000), Hemodynamics in the carotid artery bifurcation: A comparison between numerical simulations and in vitro MRI measurements. *Journal of Biomechanics*, vol. 33, pp. 137-144.
- [135] I. Marshall, S. Z. Zhao, P. Papathanasopoulou, *et al.* (2004), MRI and CFD studies of pulsatile flow in healthy and stenosed carotid bifurcation models. *Journal of Biomechanics*, vol. 37, pp. 679-687.
- [136] P. P. Sengupta, G. Pedrizzetti, P. J. Kilner, *et al.* (2012), Emerging trends in cv flow visualization. *JACC-Cardiovascular Imaging*, vol. 5, pp. 305-316.
- [137] H. Hassani-Ardekani, F. Ghalichi, H. Niroomand-Oscuii, *et al.* (2012), Comparison of blood flow velocity through the internal carotid artery based on Doppler ultrasound and numerical simulation. *Australasian Physical and Engineering Sciences in Medicine*, vol. 35, pp. 413-422.
- [138] J. Banks and N. W. Bressloff (2007), Turbulence modeling in three-dimensional stenosed arterial bifurcations. *Journal of Biomechanical Engineering*, vol. 129, pp. 40-50.
- [139] H. F. Li and M. Yoda (2008), Multilayer nano-particle image velocimetry (mnPIV) in microscale poiseuille flows. *Measurement Science & Technology*, vol. 19,
- [140] M. Raffel, C. E. Willert, S. T. Wereley, *et al.* (2007), *Particle image velocimetry: A practical guide*. Springer-Verlag Berlin Heidelberg.
- [141] J. Westerweel, G. E. Elsinga, and R. J. Adrian (2013), "Particle image velocimetry for complex and turbulent flows," in *Annual review of fluid mechanics*. vol. 45, pp. 409-436.
- [142] A. K. Prasad (2000), Particle image velocimetry. *Current Science*, vol. 79, pp. 51-60.
- [143] R. D. Keane and R. J. Adrian (1992), Theory of cross-correlation analysis of PIV images. *Applied Scientific Research*, vol. 49, pp. 191-215.
- [144] G. E. Elsinga, F. Scarano, B. Wieneke, *et al.* (2006), Tomographic particle image velocimetry. *Experiments in Fluids*, vol. 41, pp. 933-947.
- [145] F. Scarano (2013), Tomographic PIV: Principles and practice. *Measurement Science & Technology*, vol. 24,

- [146] A. K. Prasad (2000), Stereoscopic particle image velocimetry. *Experiments in Fluids*, vol. 29, pp. 103-116.
- [147] R. Kaminsky, S. Kallweit, M. Rossi, *et al.* (2008), PIV measurements of flows in artificial heart valves. *Particle Image Velocimetry: New Developments and Recent Applications*, vol. 112, pp. 55-72.
- [148] T. Yagi, A. Sato, M. Shinke, *et al.* (2013), Experimental insights into flow impingement in cerebral aneurysm by stereoscopic particle image velocimetry: Transition from a laminar regime. *Journal of the Royal Society Interface*, vol. 10,
- [149] M. Lara, C.-Y. Chen, P. Mannor, *et al.* (2011), Hemodynamics of the hepatic venous three-vessel confluences using particle image velocimetry. *Annals of Biomedical Engineering*, vol. 39, pp. 2398-2416.
- [150] M. Heise, S. Schmidt, U. Kruger, *et al.* (2004), Flow pattern and shear stress distribution of distal end-to-side anastomoses. A comparison of the instantaneous velocity fields obtained by particle image velocimetry. *Journal of Biomechanics*, vol. 37, pp. 1043-1051.
- [151] Y. Knapp and E. Bertrand (2005), Particle imaging velocimetry measurements in a heart simulator. *Journal of Visualization*, vol. 8, pp. 217-224.
- [152] C. J. T. Spence, N. A. Buchmann, and M. C. Jermy (2012), Unsteady flow in the nasal cavity with high flow therapy measured by stereoscopic PIV. *Experiments in Fluids*, vol. 52, pp. 569-579.
- [153] J. Vetel, A. Garon, D. Pelletier, *et al.* (2008), Asymmetry and transition to turbulence in a smooth axisymmetric constriction. *Journal of Fluid Mechanics*, vol. 607, pp. 351-386.
- [154] S. Karri and P. P. Vlachos (2010), Time-resolved DPIV investigation of pulsatile flow in symmetric stenotic arteries effects of phase angle. *Journal of Biomechanical Engineering*, vol. 132,
- [155] J. Charonko, S. Karri, J. Schmieg, *et al.* (2010), In vitro comparison of the effect of stent configuration on wall shear stress using time-resolved particle image velocimetry. *Annals of Biomedical Engineering*, vol. 38, pp. 889-902.
- [156] A. M. Walker, C. R. Johnston, and D. E. Rival (2012), The quantification of hemodynamic parameters downstream of a gianturco zenith stent wire using newtonian and non-newtonian analog fluids in a pulsatile flow environment. *Journal of Biomechanical Engineering*, vol. 134,
- [157] A. Fouras, J. Dusting, J. Sheridan, *et al.* (2009), Engineering imaging: Using particle image velocimetry to see physiology in a new light. *Clinical and Experimental Pharmacology and Physiology*, vol. 36, pp. 238-247.

- [158] H. B. Kim, J. R. Hertzberg, and R. Shandas (2004), Development and validation of echo PIV. *Experiments in Fluids*, vol. 36, pp. 455-462.
- [159] H. R. Zheng, L. L. Liu, L. Williams, *et al.* (2006), Real time multicomponent echo particle image velocimetry technique for opaque flow imaging. *Applied Physics Letters*, vol. 88,
- [160] F. Zhang, C. Lanning, L. Mazzaro, *et al.* (2011), In vitro and preliminary in vivo validation of echo particle image velocimetry in carotid vascular imaging. *Ultrasound in Medicine and Biology*, vol. 37, pp. 450-464.
- [161] L. Niu, M. Qian, R. Song, *et al.* (2012), A 2d non-invasive ultrasonic method for simultaneous measurement of arterial strain and flow pattern. *Clinical Physiology and Functional Imaging*, vol. 32, pp. 323-329.
- [162] J. Bale-Glickman, K. Selby, D. Saloner, *et al.* (2003), Experimental flow studies in exact-replica phantoms of atherosclerotic carotid bifurcations under steady input conditions. *Journal of Biomechanical Engineering-Transactions of the ASME*, vol. 125, pp. 38-48.
- [163] J. Vetel, A. Garon, and D. Pelletier (2009), Lagrangian coherent structures in the human carotid artery bifurcation. *Experiments in Fluids*, vol. 46, pp. 1067-1079.
- [164] N. A. Buchmann, C. Atkinson, M. C. Jeremy, *et al.* (2011), Tomographic particle image velocimetry investigation of the flow in a modeled human carotid artery bifurcation. *Experiments in Fluids*, vol. 50, pp. 1131-1151.

Chapter 2

2 Methods

For this thesis work, a PIV-based *in vitro* flow measurement system was constructed and implemented, including a family of life-sized carotid artery geometries incorporated in a series of PIV-compatible flow phantoms, which were perfused with a physiologically realistic flow-rate waveform. The work included the design and implementation of a stereoscopic PIV system for measurements of the velocity fields. The overall design and methodology are described below.

2.1 Flow Components

2.1.1 PIV-compatible phantoms

Optically transparent, life-sized carotid artery phantoms were manufactured using a lost-core casting technique, as previously described [1, 2]. The phantoms were cast in silicone elastomer (Sylgard® 184, Dow Corning Canada, Inc.; refractive index 1.41–1.43). The geometries were based on the *in vivo* study by Smith *et al.* [3] incorporating a common carotid artery (CCA), internal carotid artery (ICA), and external carotid artery (ECA) with inner diameters of 8 mm (CCA inlet), 5.52 mm (ICA outlet), 4.62 mm (ECA outlet), respectively. In addition to the normal (disease-free) model, carotid artery models can incorporate diseased features representing various geometrical plaque parameters, namely stenosis severity, plaque eccentricity (symmetry), and ulceration. The degree of stenosis severity (Equation (1.1)) represents the amount of lumen obstruction which, based on NASCET criteria [4], can fall within mild (30-49%), moderate (50-69%), and severe ($\geq 70\%$) classification. An atherosclerotic plaque can form concentrically (i.e. expanding into the lumen equally from opposing walls) or eccentrically (with preferential expansion from one side, in this case the non-flow-divider or outer wall). Plaque ulceration, defined as an excavated necrotic core under a ruptured fibrous cap, can form in various shapes and sizes as previously categorized [5]. Figure 2.1 shows an example of a silicone phantom incorporating a 50% stenosis with eccentric or asymmetric plaque formation.



Figure 2.1: A silicone phantom incorporating a 50% stenosis with eccentric plaque formation. The direction of the flow is from the common carotid artery (CCA) towards the two outlet branches of the internal carotid artery (ICA) and external carotid artery (ECA).

2.1.2 Blood-mimicking fluid

The blood-mimicking fluid (BMF) was a custom-developed fluid composed of water (47.38% by weight), glycerol (36.94% by weight), and sodium iodide (15.68% by weight) [6]. This fluid has a refractive index of 1.4140 ± 0.0008 , matching that of the fabricated silicone phantoms to avoid optical distortion at the wall, and an appropriate dynamic viscosity ($\mu = 4.31 \pm 0.03$ cP) matching that of blood. Figure 2.2 illustrates the quality of refractive-index matching between the blood-mimicking fluid and the silicone phantom.

The fluid was seeded with Rhodamine B-encapsulated microspheres (FLUOSTAR®, EBM Corp., Tokyo, Japan) with mean diameter of $15 \mu\text{m}$, excitation peak of 550 nm, and emission peak of 580 nm. The PIV-imaging magnification factor was adjusted in order to ensure that the apparent size of the imaged particles is larger than one pixel – a necessary caution to avoid the phase-locking problem [7]. The mean diameter of the imaged particles was ~ 3.5 pixels with a minimum of 2 pixels. Also, the density of the seeded particles was sufficient to ensure accuracy of cross-correlation based on the minimum recommendations of four pairs per interrogation window. The particles were distributed with a density not less than 100 particles per 32×32 pixel² region.

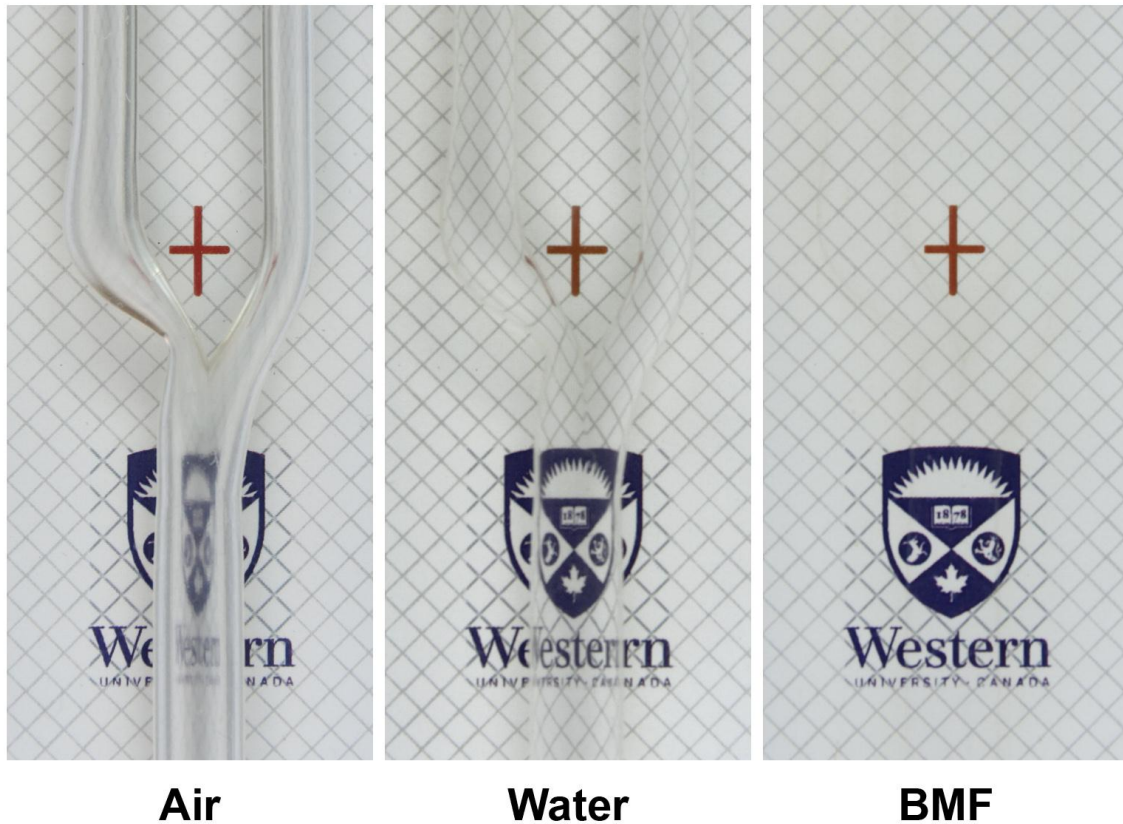


Figure 2.2: Silicone phantoms filled with (left to right) air, water, and blood-mimicking fluid (BMF). The matched refractive index between the phantom and the BMF can be recognized via visual elimination of the phantom boundaries with the absence of optical distortions.

2.1.3 Carotid-artery flowrate waveform

A computer-controlled pump [8] (CompuFlow 1000, Shelley Medical Imaging Technologies, London, ON, Canada) was used to generate physiologically relevant flow waveforms. The pump generates an electrocardiogram (ECG)-simulating signal enabling synchronized acquisition across multiple cardiac cycles. A realistic common carotid flow-rate waveform, based on the *in vivo* waveforms reported by Holdsworth *et al.* [9], was input, and a pair of downstream flow resistors were connected to the ICA and ECA outlets to achieve an approximate flow division of 60:40 (ICA:ECA). Flow waveforms at the inlet of the CCA and outlets of the ICA and ECA were recorded using in-line electromagnetic flow meters (501D, Carolina Medical Electronics, Inc., East Bend NC, USA). Figure 2.3 shows the measured flow waveform at the CCA inlet and the outlets of

ICA and ECA. The measured waveform (with 10 repeated measures) at the inlet of the CCA had a maximum flow rate of $27.1 \pm 0.3 \text{ ml s}^{-1}$ at peak systole and a mean flow rate of $6.29 \pm 0.09 \text{ ml s}^{-1}$, corresponding to Reynolds numbers ($Re = 4\rho Q/\pi\mu D$) of 1246 and 289 respectively. Peak and mean flow rates at the ECA outlet were measured to be 11.6 ± 0.4 and $2.16 \pm 0.05 \text{ ml s}^{-1}$ respectively, corresponding to Reynolds numbers of 920 and 171. Peak and mean flow rates at the ICA outlet were measured to be 12.2 ± 0.2 and $3.56 \pm 0.02 \text{ ml s}^{-1}$, respectively. Maximum and mean Reynolds numbers calculated based on the narrowest diameter of the ICA stenosis can be estimated to be 1162 and 312 in the 30%-stenosed models, 1627 and 473 in the 50%-stenosed models, and 2712 and 789 in the 70%-stenosed models. The cardiac-cycle period was $T = 920 \text{ ms}$ corresponding to a Womersley number ($0.5D\sqrt{2\pi\rho/\mu T}$) of 5.62 based on the 8-mm CCA diameter and a fluid density of $\rho = 1.244 \text{ g/ml}$.

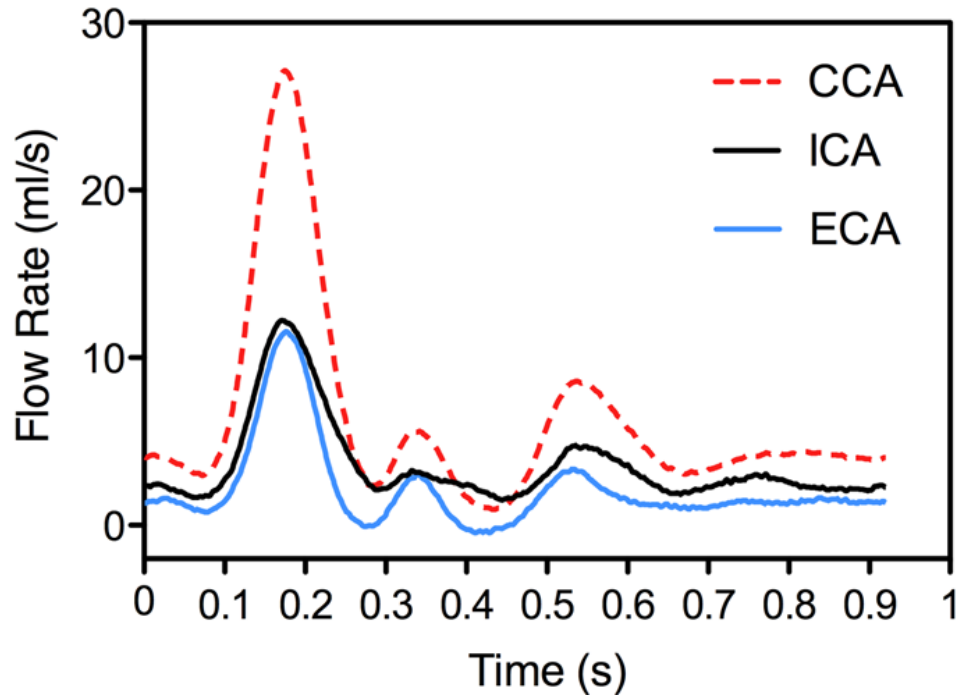


Figure 2.3: Measured carotid-artery flowrate waveform at the inlet of CCA and outlets of ICA and ECA.

2.2 Stereoscopic PIV

With conventional PIV using a single recording camera, 2D-2C velocity-vector measurements are obtained from the projection of velocity vectors onto the plane of illumination. Using stereoscopic PIV (stereo-PIV), three components of a velocity vector can be estimated (2D-3C). The underlying principle of stereo-PIV is similar to human vision, which perceives depth by viewing an object stereoscopically with a pair of eyes. Similarly, two cameras record the same observation of moving particles from different perspectives, and thus, from the two different sets of 2D displacement information, the third component – due to out-of-plane motion – can be reconstructed.

2.2.1 Stereoscopic PIV arrangements

Stereo-PIV systems can be broadly categorized into two main configurations based on transitional (lateral) or angular (rotational) viewing by the cameras. In the transitional arrangement, both cameras view the object plane perpendicularly resulting in parallel planes of object, lens, and image. In an angular arrangement, both cameras – mounted either on the same side or on either side of light sheet – view the object plane at an angle, resulting in an intersection of both image planes with the object plane. The angular configuration can be considered the most common one as it may potentially lead to higher accuracy of out-of-plane components [10].

The stereo-PIV system employed in the present work was a commercial *LaVision* system, which was equipped with acquisition and analysis software of *DaVis 7.2*. The stereoscopic arrangement of cameras was angular with both cameras mounted on the same side of the light sheet. An optimal range of viewing angle for each camera between 30° and 45° is recommended, which minimizes the error in measured velocity components [11, 12]. The viewing angle for each camera was set to 35° .

The oblique viewing by the cameras, however, introduces some level of complexity in the velocity-calculation algorithm, due to non-uniform magnification, requiring a specific calibration protocol. The off-axis viewing also results in aberrations and out-of-focus regions for parts of the illuminated plane. The focusing issue can be suppressed by satisfying the Scheimpflug condition such that the image, lens, and object planes of each

camera intersect in a common line. The designed Scheimpflug adapters, mounted between the camera and objective lens, can be employed to achieve this criterion. Also, due to refraction issue at the interface of the test object and air, radial distortion is expected that can result in transforming circular particles to appear in elliptical shape. Thus, in order to keep the astigmatism minimal, orthogonal viewing of the interface of test object and air should be achieved. This is satisfied by viewing through a prism positioned symmetrically between the two cameras mounted on top of the test section [13]. The prism should be fabricated with matching material (or at least refractive index) to that of the test object, and the bottom corner inclined angle of the prism should match the viewing angle of the camera. For this work, the prism was made with silicone material from which phantoms were fabricated and with the base angle of 35° matching the viewing angles of the cameras. Figure 2.4 shows a schematic of an angular stereoscopic arrangement with applied Scheimpflug condition and viewing prism.

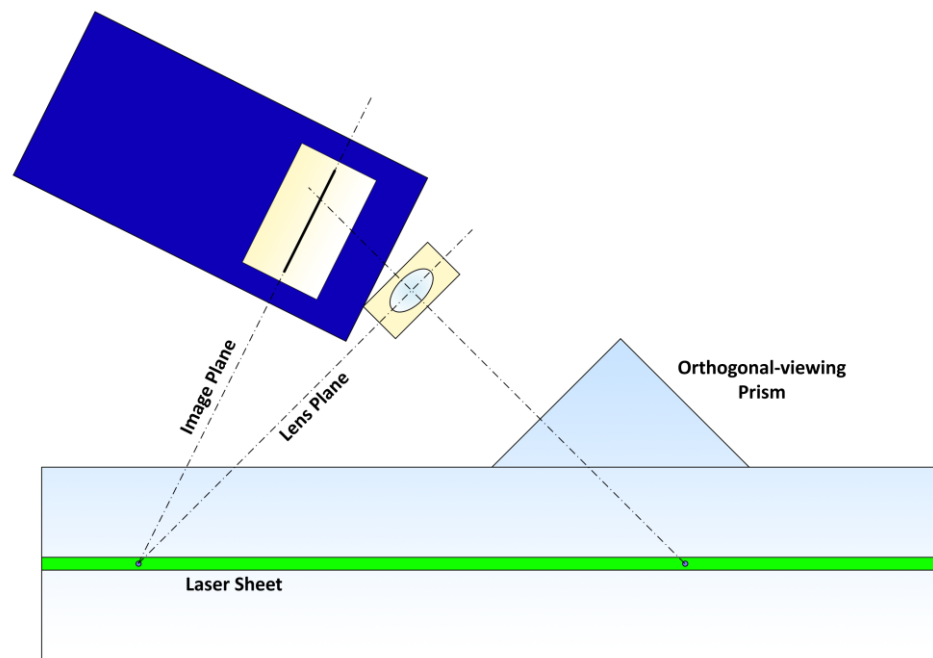


Figure 2.4: Schematic of (one camera) of a stereoscopic arrangement with Scheimpflug condition satisfied through the angled arrangement of the lens relative to the camera and a viewing prism placed on top of the test object to achieve orthogonal incidence.

2.2.2 Calibration

In the stereoscopic arrangement, two cameras are oriented towards the object plane with two different angular views. The calibration procedure allows the two differently oriented images captured by the two cameras to be mapped to a common grid (with corresponding world coordinates), which is required for reconstruction of the out-of-plane velocity component. The correspondence between the object coordinates (x, y, z) and image coordinates (X_1, Y_1) and (X_2, Y_2) of the two cameras needs to be determined based on a mapping function. The coefficients of the mapping function are determined using a calibration procedure, such as done by imaging a multi-level calibration target that bears reference markers arranged on a Cartesian grid and applying a polynomial fitting function [14]. Calibration images are generated using a standard calibration plate of known dimensions and consisting of fiducial marks (e.g. circles) spaced in the form of a grid map. For this work, calibration was performed using a two-leveled *LaVision* standard calibration plate. A mapping function corresponds these imaged marks to their position on the ideal grid map. *DaVis 7* provides the option of mapping using a pinhole fitting function or a third-order polynomial fit. Details on each of these functions can be found in the PIV guidebook by Raffel *et al.* [7] and the *LaVision* Manual [12]. For the present work, third-order polynomial mapping function was used which has proven to be a more robust option compared to the pinhole mapping function.

To ensure identical optical properties, the calibration target was placed in a container filled with BMF to a level 12.5 mm above the target surface, corresponding to the same thickness of silicone above the central-plane of measurement in the flow channel in each phantom. An orthogonal-viewing prism was then placed on top of the fluid resting on two side shelves. This described calibration set-up is shown in Figure 2.5. The top surface of the calibration target was aligned with the level of the laser sheet and a set of images was acquired with both cameras. This was followed by the recommended calibration steps (as specified for *DaVis 7.2*), which included selection of the matched reference marks on images from both cameras by the user. It was ensured that a root-mean-square (RMS) deviation of less than 0.3 pixels between the de-warped marks and ideal grid was always achieved, and typically achieving a value well below 0.3 pixels.

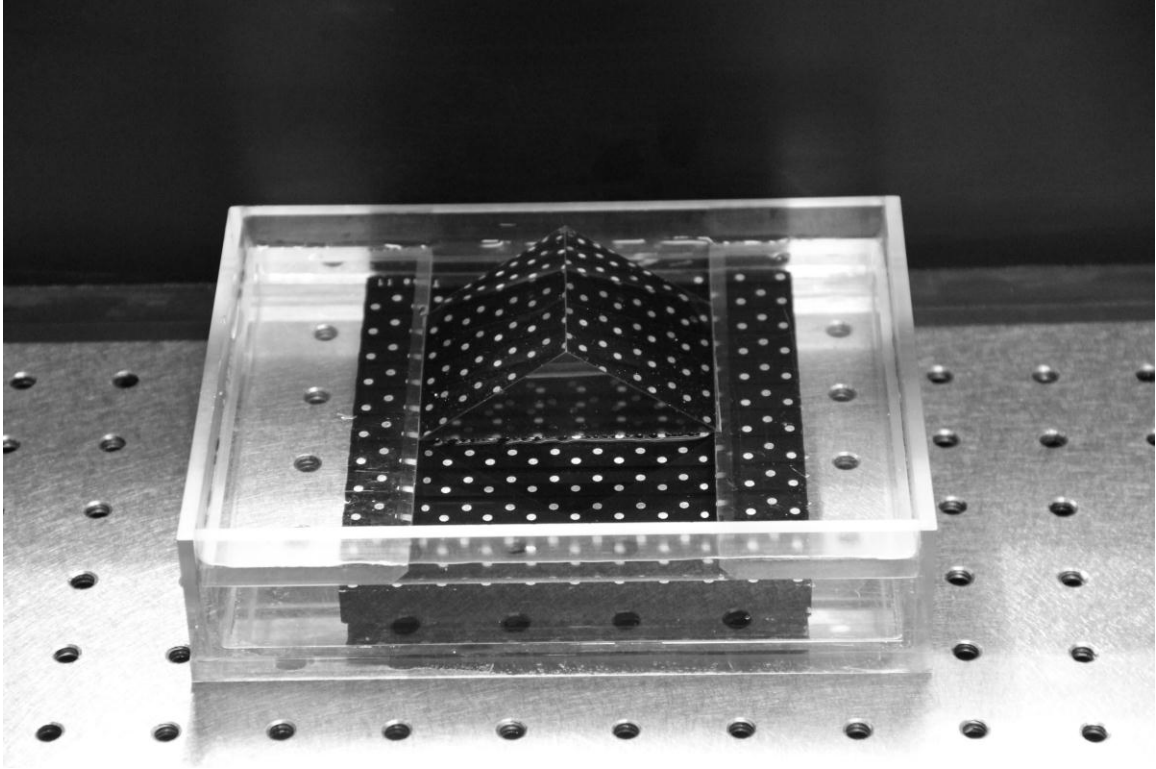


Figure 2.5: Calibration set-up including the two-leveled calibration target immersed in blood-mimicking fluid with the orthogonal-viewing prism secured at the top of the fluid level.

2.2.3 Image acquisition

Once the calibration is performed and the calibration parameters are obtained, the actual particles images can be acquired. The main plane of measurement was the central plane of the phantom, which was located 12.5 mm below the top surface of the phantom with the orientation in the direction of the flow. The FOV was $\sim 45 \times 40 \text{ mm}^2$ capturing 15 mm of the CCA length and 30 mm of the parallel branches of ICA and ECA. Double-frame images were acquired with the time interval between the frames defined based on pilot experiments. The optimal time interval ensures adequate displacement of the particle in order to accurately detect the displacement and is short enough to avoid losing matching particles between cross-correlated windows. The selected time interval ranged from 100 to $400 \mu\text{s}$, as appropriate for the range of velocities present in the most severely (70%) stenosed down to the normal model respectively.

In order to reconstruct the volumetric flow pattern, in addition to the central plane, off-center planes also were acquired throughout the lumen. The off-center planes were acquired by vertically translating the phantom via a precision lab jack (M-EL120, Newport, Corp., Irvine CA, USA) equipped with a dial indicator (Chicago Dial Indicator Co., Inc., Des Plaines, IL). This assured that the relative position of the laser sheet and cameras remained the same, thus only requiring one calibration set acquired with the calibration target. For the stenosed models, a total of 15 planes were imaged, covering both the top and bottom portion of the lumen (i.e. 3.5 mm above and below the central plane). For the normal model, the required number of planes was 19 due to the larger sinus bulb. Figure 2.6 illustrates the central-plane of measurement along with two examples of off-center planes located on the top and bottom portion of the lumen.

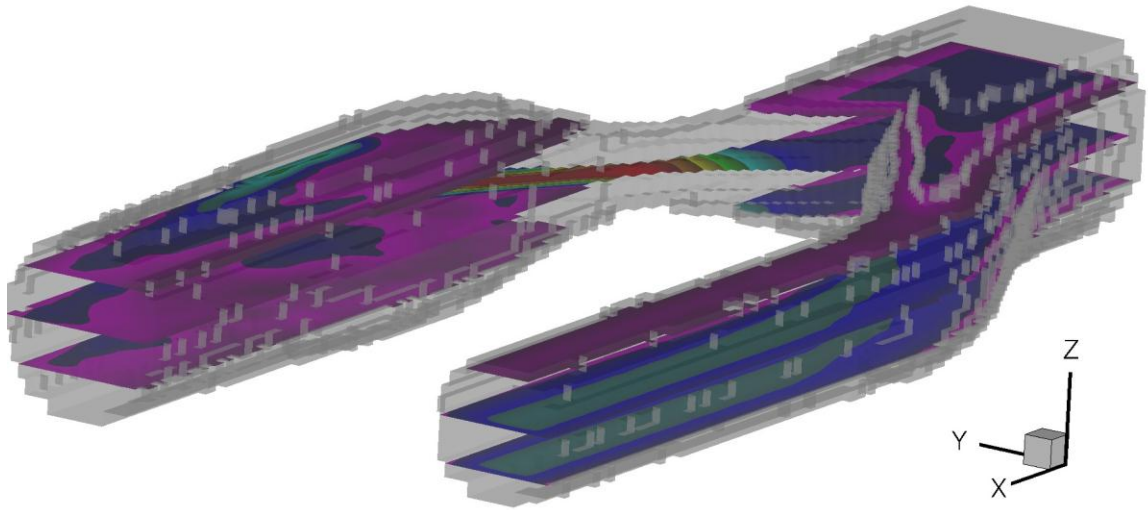


Figure 2.6: Volumetric acquisition of the velocity field via multiple planes of data. Shown here are the central-plane of measurement and two off-center planes inside the lumen (grey) volume.

2.2.4 Self-calibration

As described, the physical calibration is performed outside the lumen volume, thus it is important to ensure that the calibration plate and light-sheet plane (i.e. measurement plane) are aligned. In practice, this alignment can be challenging and misalignments due to elevational or rotational offsets of the light sheet are expected. To address this issue, a

follow-up correction procedure, commonly referred to as self-calibration, is applied using the recorded particle images [15]. Similar to classical PIV, cross-correlation is performed but between a pair of images acquired at the same instance from each camera thus resulting in disparity vectors. As expected, in the absence of misalignments, the disparity map includes null vectors. In the case of misalignments, an iterative algorithm is applied to converge the disparity vectors to null values. By performing the self-calibration procedure, the misalignments are accounted for, and a refined mapping function is calculated.

For each phantom study, self-calibration was performed (using *DaVis 7.2* software) on a series of central-plane particle images (~100 images), which were first de-warped and then masked to remove the non-lumen regions. The disparity map was generated using a sum-of-correlation option with window size of 64x64 (with 50% overlap) and three passes. Based on an iterative calculation of the disparity map, calibration parameters were iteratively refined until no more change was yielded.

As mentioned, central-plane particle images were used to derive the final calibration parameters from the self-calibration procedure. This calibration process potentially should be repeated for each imaging plane and can be a tedious task. Through an *a priori* test, the same calibration set was found to be valid to be applied to the off-center imaging planes, which were acquired up to 3.5 mm above and below the central plane with 0.5-mm incremental steps. Application of the central-plane calibration parameters to the other planes was validated by comparing the resultant velocity vector maps (from the 50%-stenosed model) derived using two different sets of calibration as follows: a) central-plane calibration, where the calibration set obtained by self-calibrating with the central-plane images (as described above) was also applied to all off-center planes, and b) plane-associated calibration, where the calibration set was derived by self-calibrating for each imaging plane and then applying each calibration set to calculate the corresponding velocity vector maps of that plane. Figure 2.7 shows the RMS difference between the two described velocity vector maps of each plane of measurement located from 3 mm below to 3 mm above the central plane.

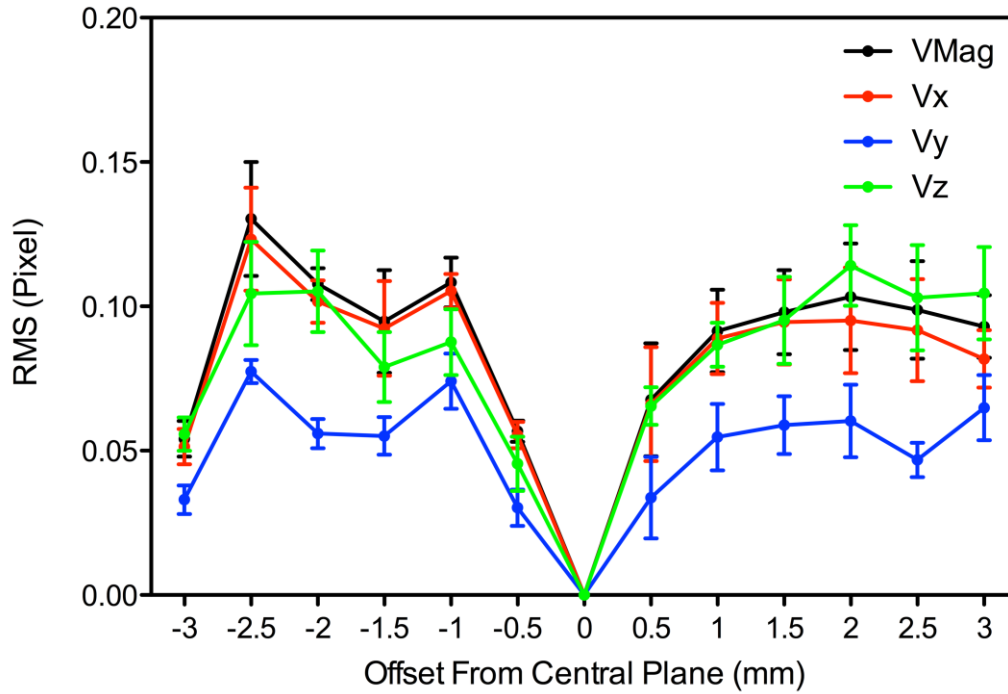


Figure 2.7: RMS differences between corresponding vectors in maps processed using the central-plane and plane-associated calibration parameters. Error bars represent standard deviation from the mean of five repeated measurements.

A trend of increasing RMS with moving further away from the central plane can be observed. However, for the three velocity components, as well as the magnitude of the velocity vector, the RMS did not exceed 0.15 pixels, corresponding to a deviation of less than 9% of the mean pixel displacement in the corresponding map. The good agreement between the two vector maps can also be verified visually in the side-by-side comparison shown in Figure 2.8 for a measurement plane 1.5 mm below the central plane. Given the small differences, the final calibration parameters obtained by self-calibrating the central-plane images were applied to all of the measurement planes throughout the volume for all other studies. The greater-offset planes are not shown simply as they contain only a fraction of the flow lumen and appear disjointed in the area of the neck of the stenosis.

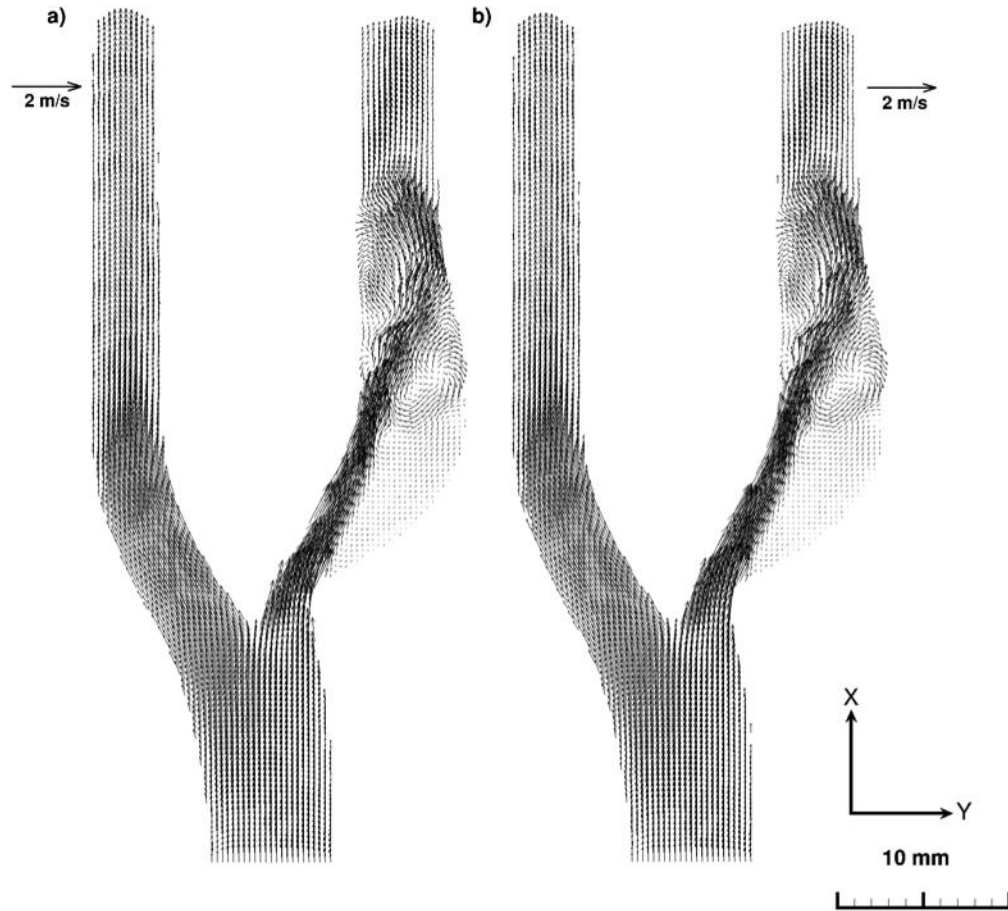


Figure 2.8: Velocity-vector maps from 1.5 mm below the central plane in a 50% eccentric stenosed model derived using two different calibration sets: a) central-plane calibration and b) plane-associated calibration.

2.2.5 Velocity evaluation

Once the mapping function is known, actual images from the tracer particles, now mapped to the global coordinates, are evaluated to obtain two sets of in-plane velocities, which are used in combination to derive the out-of-plane velocity components.

The velocity-evaluation algorithm was a fast-Fourier-transform based cross-correlation analysis, with an adaptive multi-pass processing scheme using decreasing interrogation-window size with no weighting applied to the interrogation windows; the window size ranged from 64 x 64 pixels down to 16 x 16 pixels, with three refinement passes for each window size and 50% overlap throughout. Before the interrogation process, the software deforms the images of each camera to their correct world coordinate. In the adaptive

multi-pass processing, the reference vector field computed for each camera from the previous pass provides an offset estimate to deform and shift the interrogation windows with sub-pixel accuracy. A high-accuracy Whittaker reconstruction [12] was applied for the final pass. The final planar three-component (2D-3C) vector field is reconstructed from the two stereoscopic sets of 2D-2C vector fields and is then subject to further user-defined post-processing. The velocity vector fields were post-processed once with a 3x3-smoothing kernel. The resultant dynamic range of velocities present in the 70%-stenosed model (with the fastest jet compared to the other models) ranged from a minimum of zero in the recirculation zone to a maximum of about 3.5 m/s in the jet.

2.3 References

- [1] R. F. Smith, B. K. Rutt, and D. W. Holdsworth (1999), Anthropomorphic carotid bifurcation phantom for MRI applications. *J Magn Reson Imaging*, vol. 10, pp. 533-44.
- [2] T. L. Poepping, R. N. Rankin, and D. W. Holdsworth (2010), Flow patterns in carotid bifurcation models using pulsed Doppler ultrasound: Effect of concentric vs. Eccentric stenosis on turbulence and recirculation. *Ultrasound in Medicine and Biology*, vol. 36, pp. 1125-1134.
- [3] R. F. Smith, B. K. Rutt, A. J. Fox, *et al.* (1996), Geometric characterization of stenosed human carotid arteries. *Academic Radiology*, vol. 3, pp. 898-911.
- [4] North American Symptomatic Carotid Endarterectomy Trial (NASCET) investigators (1991), Clinical alert: Benefit of carotid endarterectomy for patients with high-grade stenosis of the internal carotid artery. *Stroke*, vol. 22, pp. 816-7.
- [5] E. Y. Wong, H. N. Nikolov, M. L. Thorne, *et al.* (2009), Clinical Doppler ultrasound for the assessment of plaque ulceration in the stenosed carotid bifurcation by detection of distal turbulence intensity: A matched model study. *European Radiology*, vol. 19, pp. 2739-49.
- [6] M. Y. Yousif, D. W. Holdsworth, and T. L. Poepping (2011), A blood-mimicking fluid for particle image velocimetry with silicone vascular models. *Experiments in Fluids*, vol. 50, pp. 769-774.
- [7] M. Raffel, C. E. Willert, S. T. Wereley, *et al.* (2007), *Particle image velocimetry: A practical guide*. Springer-Verlag Berlin Heidelberg.

- [8] D. W. Holdsworth, D. W. Rickey, M. Drangova, *et al.* (1991), Computer-controlled positive displacement pump for physiological flow simulation. *Medical & Biological Engineering & Computing*, vol. 29, pp. 565-570.
- [9] D. W. Holdsworth, C. J. Norley, R. Frayne, *et al.* (1999), Characterization of common carotid artery blood-flow waveforms in normal human subjects. *Physiological Measurement*, vol. 20, pp. 219-40.
- [10] A. K. Prasad (2000), Stereoscopic particle image velocimetry. *Experiments in Fluids*, vol. 29, pp. 103-116.
- [11] K. Parker, K. D. von Ellenrieder, and J. Soria, Stereoscopic PIV measurements of the flow past a circular cylinder at Reynolds number 15000, presented at the *15th Australasian Fluid Mechanics Conference*, Australia, 2004.
- [12] LaVision (2012), *Product manual for davis 8.1*. LaVision GmbH, Göttingen.
- [13] A. K. Prasad and K. Jensen (1995), Scheimpflug stereocamera for particle image velocimetry in liquid flows. *Applied Optics*, vol. 34, pp. 7092-7099.
- [14] S. M. Soloff, R. J. Adrian, and Z. C. Liu (1997), Distortion compensation for generalized stereoscopic particle image velocimetry. *Measurement Science & Technology*, vol. 8, pp. 1441-1454.
- [15] B. Wieneke (2005), Stereo-PIV using self-calibration on particle images. *Experiments in Fluids*, vol. 39, pp. 267-280.

Chapter 3

3 Transitional Flow Analysis in the Carotid Artery Bifurcation by Proper Orthogonal Decomposition and Particle Image Velocimetry*

3.1 Introduction

Atherosclerosis is a major cause of ischemic stroke [1], with the carotid artery bifurcation being one of the most common sites prone to the disease. Plaque buildup at the carotid bifurcation leads to local geometrical changes, which in turn promote hemodynamic changes such as the development of high velocity jets, as well as separation and recirculation zones. Of particular interest is the fact that with high degrees of stenosis, transitional laminar-turbulent regime has been reported during some phases of the cardiac cycle [2-4]. For typical hemodynamic Reynolds numbers, the inertial range scales associated with fully turbulent flow are not expected [5], and therefore the disturbed flow in the stenosed carotid artery might be more accurately described as unstable or transitional flow (i.e. mixed or transitional state of laminar to turbulent flow); however, the literature often oversimplifies this by referring to turbulent flow. The presence of turbulent flow in the carotid bifurcation is of significance because of the high incidence of thromboembolic strokes – clot formation has been highly correlated with the presence of turbulence in past studies [6-8]. This correlation has been attributed to the flow resistance, recirculation zones, vortices, and negative wall-shear stress that result from flow disturbance and turbulence, thereby promoting thrombus formation. In addition, turbulence results in pressure fluctuations and mass transfer to the vessel wall that can weaken the plaque and cause rupture [9, 10] potentially leading to distal embolisms.

* A version of this chapter has been published in *Medical Engineering and Physics* (2013) Volume: 35 pages: 898-909 as an original article entitled “Transitional flow analysis in the carotid artery bifurcation by proper orthogonal decomposition and particle image velocimetry” by S. Kefayati and T. L. Poepping.

Turbulence has been characterized in a number of studies in physical models of stenosed vessels, performed primarily using laser Doppler anemometry (LDA) [11]. In addition, many numerical studies have incorporated turbulent models to characterize flow in symmetric stenoses in straight tubes [8, 12, 13], as well as in patient-specific models [4, 14]. Direct numerical simulation (DNS) has also been employed in stenosed tube [15, 16] and patient-specific models [3]. While DNS is more detailed than numerical turbulent models, all numerical studies require validation with an experimental technique.

Particle image velocimetry (PIV) is an engineering flow measurement tool that provides high temporal and spatial resolution and is one of the gold standard flow-validation techniques. PIV has recently been employed to study flow in stenosed models, but most have been conducted under rather simplified conditions of either stenosis in a straight tube [17, 18] or simplified steady flow through patient-specific models [19, 20]. PIV also provides the required information for assessment of temporally and spatially evolving flow via advanced decomposition methods such as proper orthogonal decomposition (POD). POD is an optimal representation of infinite-dimensional systems, such as dynamic fluid flow, and allows the identification of energetically dominant modes. While PIV enables general characterization of flow structures, further breakdown of the flow into large and small scale structures can be obtained through POD, which uses velocity data to provide the basis functions for modal decomposition. POD was first introduced to the field of turbulence by Lumley [21]. Snapshot POD, suggested by Sirovich [22], enables the identification of flow structures by analyzing an ensemble of uncorrelated realizations (snapshots). In the case of PIV data, each snapshot is represented as an instantaneous velocity field. POD has been applied to many engineering problems but, to our knowledge, only a single study (by Grinberg *et al.* [23]) has applied POD to vascular flow – in a computational fluid dynamics (CFD) simulation of a 77%-stenosed, patient-specific, carotid-bifurcation model.

In the study of this chapter, transitional flow in a family of carotid artery models using a combination of PIV and POD is investigated. An overview of the flow patterns in the set of three models with increasing stenosis severity (normal with no stenosis, 50% concentric stenosis, and 70% concentric stenosis) is first presented. Flow was then further

examined through the calculation of energy spectra, spatial modes, temporal modes, and entropy using POD analysis of the central plane velocity field measured in the set of three carotid bifurcation models. The selection of this set of three models was to ensure capturing the transitional flow stage. Flow at various planes within the 70%-stenosed model was also analyzed, and level of complexity was compared. Moreover, the temporal resolution required to achieve convergence of the POD analysis was examined.

3.2 Methods

3.2.1 Flow experiment set-up

Optically transparent life-sized carotid artery phantoms, with an 8-mm inner diameter common carotid artery (CCA), were manufactured using a lost-core casting technique, as previously described [24, 25]. The phantoms were cast in silicone elastomer (Sylgard[®] 184, Dow Corning Canada, Inc.; refractive index 1.41-1.43). The model geometries were based on the *in vivo* characterization study by Smith *et al.* [26]. The present study was carried out using three phantoms: the normal (disease-free) model as a control, and 50% and 70% concentrically stenosed models (by NASCET [27] criteria). Figure 3.1a depicts a silicone phantom with normal geometry, while Figure 3.1b is a comparison schematic of the three model geometries.

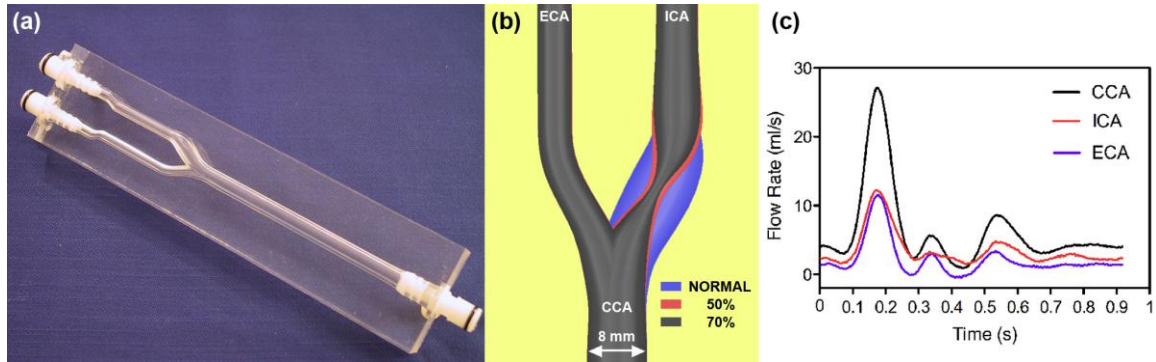


Figure 3.1: A life-sized normal (disease-free) phantom cast in transparent silicone (a), schematic of the 50% and 70% concentrically stenosed models superimposed on the geometry of the normal model (b), and flow rate measurements in the 50%-stenosed phantom at the inlet of the CCA and outlets of the ICA and ECA (c). Each waveform is the ensemble average across 10 consecutive cardiac cycles.

A computer-controlled pump [28] (CompuFlow 1000, Shelley Medical Imaging Technologies, London, ON, Canada) was used to generate physiologically relevant flow waveforms. A pair of flow resistors was connected to the outlets of the internal (ICA) and external (ECA) carotid arteries in order to achieve a downstream flow division between the ICA and ECA of approximately 60:40 [29]. For all experiments, the pump was programmed with a realistic common carotid flow waveform, based on the *in vivo* waveforms reported by Holdsworth *et al.* [30]. The cardiac-cycle period was $T = 920$ ms corresponding to a Womersley number ($0.5D\sqrt{2\pi\rho/\mu T}$) of 5.62 based on the 8-mm CCA diameter and a fluid density of $\rho = 1.244$ g/ml. Flow waveforms at the inlet of the CCA and outlets of the ICA and ECA were digitally recorded using in-line electromagnetic flow meters (501D, Carolina Medical Electronics, Inc, East Bend NC, USA) and are shown in Figure 3.1c. The measured waveform peaked at a flow rate of 27 ml/s with a mean flow rate of 6.3 ml/s. The corresponding Reynolds numbers ($Re = 4\rho Q/\pi\mu D$) for mean and peak flow rates were as follows: for CCA 289 and 1246 respectively, for ECA 171 and 920, locally for ICA stenosis 473 and 1627 in the 50% model, and 789 and 2712 in the 70% model.

To avoid optical distortion in the PIV experiments, the phantoms and BMF must have matched refractive indices; this was achieved using a custom-developed fluid [31] composed of water (47.38% by weight), glycerol (36.94% by weight), and sodium iodide (15.68% by weight), which has a refractive index of 1.4140 ± 0.0008 , matching that of the fabricated silicone phantoms. The fluid also has an appropriate dynamic viscosity (4.31 ± 0.03 cP) to match that of blood. The fluid was seeded with Rhodamine B-encapsulated microspheres (FLUOSTAR[®], EBM Corp., Tokyo, Japan) with mean diameter of 15 μ m, excitation peak of 550 nm, and emission peak of 580 nm.

3.2.2 PIV system

The stereoscopic PIV system (LaVision Inc., Ipsilanti MI, USA) was composed of a continuous-wave Nd:YAG (532 nm, 5.5 W) laser with two high-speed CMOS cameras with sensor matrix size of 1024 x 1024 pixels, and equipped with 60-mm Nikon objective lenses, 550-nm long-pass filters (Bock Optronics Inc., Toronto, ON, Canada), and

Scheimpflug adaptors. The specific stereo-PIV setup is shown in Figure 3.2. Both cameras were installed above the phantom with a viewing angle of 35° relative to the normal. A transparent silicone prism, designed to reduce the stereoscopic perspective distortion, was placed on top of the phantom, midway between the two cameras, with incline angle matching the viewing angle (35°). A precision lab jack (M-EL120, Newport, Corp., Irvine CA, USA) equipped with a dial indicator (Chicago Dial Indicator Co., Inc., Des Plaines, IL) was incorporated to permit reproducible vertical motion of the phantom (to within $\pm 10 \mu\text{m}$) with respect to the laser-camera objective position.

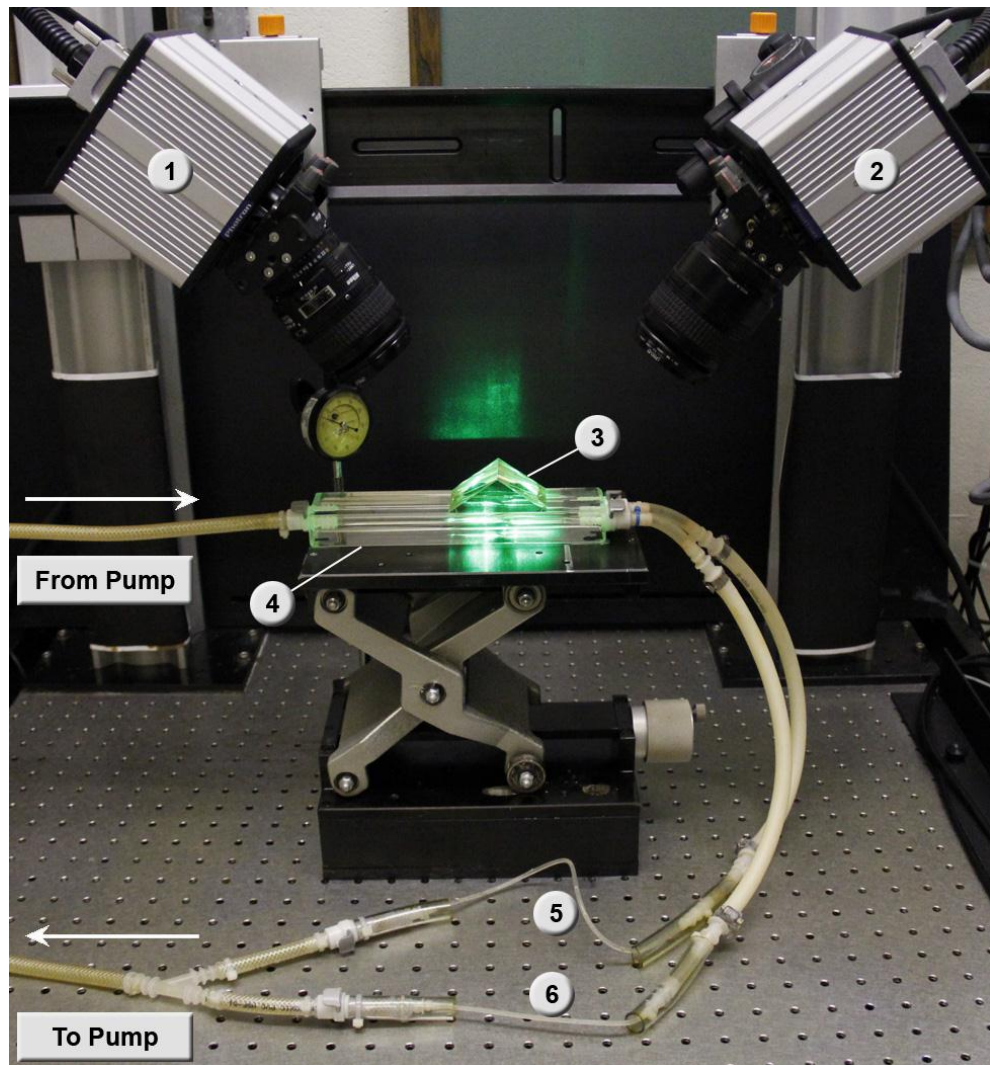


Figure 3.2: PIV experimental flow set-up depicting the two CMOS cameras (labeled 1 & 2), silicone prism (3), phantom (4), ECA and ICA flow resistors (5 & 6), and 1.5-mm thick laser sheet illuminating an x-y plane through the phantom.

Prior to the acquisition of PIV data, geometric calibration of the system was performed, as described in detail in Chapter 2. Briefly, since all PIV experiments were performed in silicone, a specialized calibration setup was developed and implemented. The 3D calibration target was immersed in BMF, and the silicone prism was secured on top of the fluid prior to performing the calibration protocol. The calibrated images had a spatial resolution of $\sim 37 \mu\text{m}/\text{pixel}$ corresponding to a field of view (FOV) of $44 \times 40 \text{ mm}^2$. For volumetric acquisitions, the calibration parameters obtained for the central plane were used for all planes throughout the phantom lumen which was scanned with elevational increments of 0.5 mm covering 3.5 mm above and 3.5 mm below the central plane of symmetry.

3.2.3 PIV data acquisition and analysis

Image acquisition and processing were performed using the commercial system software (DaVis 7.2, LaVision Inc. Ipsilanti MI, USA). Image acquisition was triggered through an ECG-simulation pulse provided by the pump at the start of each waveform cycle. Double-frame images were recorded with time interval settings that varied for each phantom used; these were selected through pilot experiments and ranged from 100 to 400 μs . For each phantom, an algorithmic mask was created using an averaged image, generated by averaging over 460 images, to separate the flow regions of the images from the non-flow regions. Two-dimensional three-component (2D-3C) velocity fields were generated using the fast-Fourier-transform based cross-correlation algorithm, implemented with a multi-pass technique with an adaptive decreasing interrogation window size; the window size ranged from 64×64 pixels down to 16×16 pixels in the last three passes, and a 50% overlap was used for all passes. In the post-processing step, spurious vectors were removed and replaced using a median filter, and velocity fields were then smoothed once with a 3×3 -smoothing kernel.

The 2D-3C velocity fields obtained by the stereo-PIV were then used in snapshot POD analysis. The underlying idea of POD analysis is to decompose the spatio-temporal velocity function of $\vec{u} = (\vec{x}, t)$ to function bases of $\phi^i(\vec{x})$ and their corresponding coefficients of $a_i(t)$:

$$\vec{u}(\vec{x}, t) = \sum_i a_i(t) \phi^i(\vec{x}). \quad (3.1)$$

In Equation (3.1), $\phi^i(\vec{x})$ represent the spatial behavior of the flow and is referred to as spatial modes, and $a_i(t)$ is the series of modal amplitudes corresponding to the change in velocity over time and are referred to as temporal modes. Formulation of snapshot POD and the way it is applied to three-component stereo-PIV velocity fields are described in Appendix A.

Vortex identification was conducted by computing the swirling strength based on the λ_{ci} -criterion [32]. The λ_{ci} -criterion is especially suitable when shear flows are also expected, such as the type of flow present in the stenosed carotid artery models. More details on the λ_{ci} -criterion method and the way it is applied to PIV velocity fields are given in Appendix B.

3.2.4 POD experiment

For each phantom, PIV images were acquired over the entire cardiac cycle (920 ms) at 500 Hz, leading to 460 snapshots for a FOV extending 33 mm distal and 11 mm proximal to the apex of the bifurcation and 40 mm across, and thus encompassing portions of the CCA, ICA, and ECA. POD analysis was performed for the three models over the above-mentioned FOV in order to ensure the same input waveforms (i.e. CCA input) for all the models and avoid the possible differences in ICA waveforms introduced due to the difference in stenosis degree. The 2D-3C velocity fields were computed over the 920-ms of the cardiac cycle, from which the 2D-3C velocity fields of the spatial modes (Equation (A.5)) and the POD coefficient values (Equation (A.7)) were derived. POD data analysis was performed using the commercial *DaVis* 7.2 software. POD formulism were also programmed in MATLAB[®] to verify the consistency of the results generated by the *DaVis* software with the POD theory. The directional swirling strength λ_{ci}^* , (Equation (B.3)) was used for vortex identification and applied on both for the original velocity fields and POD spatial modes. The associated equations for deriving swirling strength are explained in Appendix B.

Further POD analysis was performed for multiple planes in the ICA of the 70%-stenosed phantom to assess the dependence on slice position and FOV selection. The 2D-3C velocity fields of the central plane plus three planes from the top half (considering mirror-image symmetry of the bottom half) were cropped using a digital mask of a smaller rectangular FOV over only the ICA, extending from the bifurcation apex to 33 mm downstream, and applied to the original velocity fields in all the planes.

As described earlier, in the snapshot POD analysis, each eigenvalue contains a decreasing fraction of the total energy of the flow as the mode or eigenvalue number increases; the first modes contain most of the energy as they comprise the dominant features of the flow. In POD analysis, a larger number of snapshots is always preferred, however limitations arising from computing time or experimental apparatus may limit the possible number of snapshots. Therefore, it is important in the present study to test the required number of snapshots per cardiac cycle (i.e. frame rate or temporal resolution) necessary to accurately capture the energy content of the dominant (i.e. first) modes. Previous studies [33, 34] have shown that as Reynolds number is increased or flow becomes more complex, a higher number of modes is required to capture a given fraction of the total energy. Therefore, for comparison studies involving multiple types of flow, it is preferred to perform the convergence test for the most complex flow within the study; in this case, a convergence test was performed on the flow of the 70%-stenosed model.

For the full FOV and cardiac cycle, a maximum frame rate of 500 Hz was possible with the 4-GB onboard camera memory. Data acquisition was conducted at frame rates of 100, 200, 320, 400, and 500 Hz, respectively producing 92, 184, 295, 368, and 460 snapshots per 0.92 s cardiac cycle, with corresponding temporal resolutions of 10, 5, 3.125, 2.5, and 2 ms. Although it is possible to generate subsets of images by down-sampling from the higher frame rates, independent image acquisition were performed for each frame rate, thus allowing independent statistical evaluation and incorporating experimental variations such as cycle-to-cycle variability within the pulsatile flow. A minimum of three iterations was completed for the largest ensemble sizes, and up to 10 iterations for the lowest frame rate. Statistical analysis was performed to test the convergence of the first four energy modes (λ_{1-4}).

3.3 Results

3.3.1 General features of flow

An overview of the complex flow patterns observed using stereo-PIV in the three carotid models is presented in Figure 3.3, which shows the volumetric and central-plane flow patterns of the normal, 50%-stenosed, and 70%-stenosed phantoms at peak systole. The velocity fields shown are phase averages of 15 acquisitions of the same time point in the cardiac cycle. Figure 3.3a and Figure 3.3d show that the flow in the normal model is well organized in the CCA, ICA and ECA. The streamlines throughout the ICA of the 50% and 70% concentrically stenosed models (Figure 3.1e and Figure 3.3f) reveal more complex flow patterns. Helical swirling patterns start immediately distal to the stenosis throat and continue downstream where flow relaminarizes, with a symmetrical pattern above and below the central plane, as evident in the cross-sectional slices shown in Figure 3.3b and Figure 3.3c. A pair of symmetric Dean-type counter-rotating vortices can be seen with the rotational direction from the outer (medial) wall towards the inner (lateral) wall of the ICA. A similar pattern of vortex pairs, although asymmetric, is also reported in the DNS study by Lee *et al.* [3] for a patient-specific 45%-stenosed model (area reduction). At the central plane where these vortices meet, a cross-flow orthogonal to the direction of the high-velocity jet is generated. Reverse flow is seen along the inner wall of the ICA in both of the stenosed models, as evidenced by the streamlines in the central plane in Figure 3.3e and Figure 3.3f.

The flow progression over the cardiac cycle is presented in Figure 3.4, which presents central-plane velocity vector fields overlaid on swirling-strength maps for the three phantoms at five different time points of the cardiac cycle. The highest values of swirling strength are present downstream of the stenosis jet in the 70% model as expected due to larger magnitude of the velocity gradients. Flow in the normal model is very organized, and a recirculation zone – indicated by weak swirling strength – is observed within the bulb only during the deceleration phases. The presence of cross-flow orthogonal to the jet can be observed for the 50% and 70% models at all the time points. At the junction where the cross-flow meets the jet, vortices develop for all the time points and are strongest during systolic deceleration phase. Clockwise vortices also develop on the outer side of

the jet, both immediately distal to the stenosis and when the jet separates from the outer wall. Additional bending and perturbation are observed in the adjacent “jet-free” regions during peak systole and the rapid deceleration phase that follows.

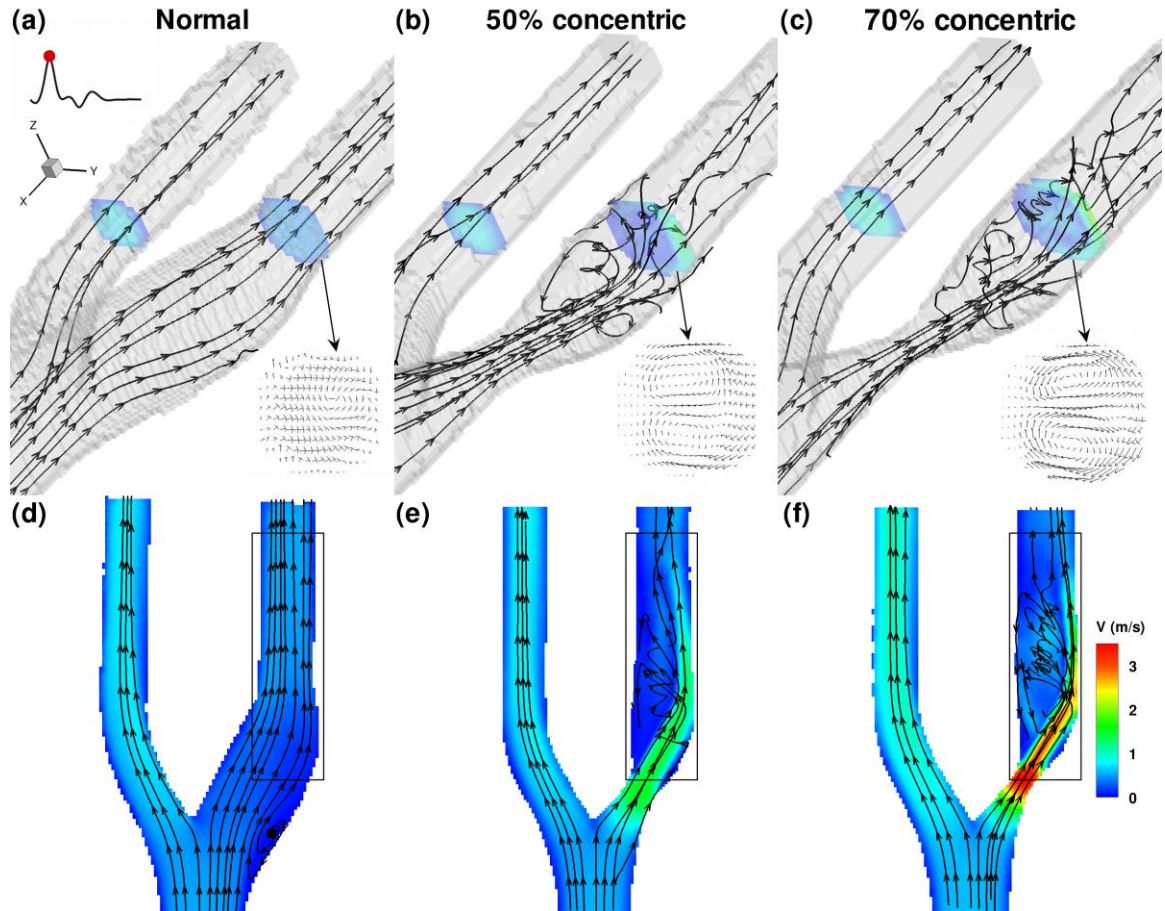


Figure 3.3: Visualization of the flow patterns in the normal (a, d), 50% (b, e) and 70% models (c, f) at peak systole of the cardiac cycle. Sparse representations of the volumetric streamlines are shown across the top row (a, b, c), along with a detailed cross-sectional slice of the velocity vector map corresponding to the position indicated by the colored slice in the ICA. Projections of the 3D streamlines superimposed onto the color-encoded map of the central-plane velocity magnitude are shown along the bottom row (d, e, f). The boxed areas of the ICA indicate the regions detailed in Figure 3.4 and Figure 3.5.

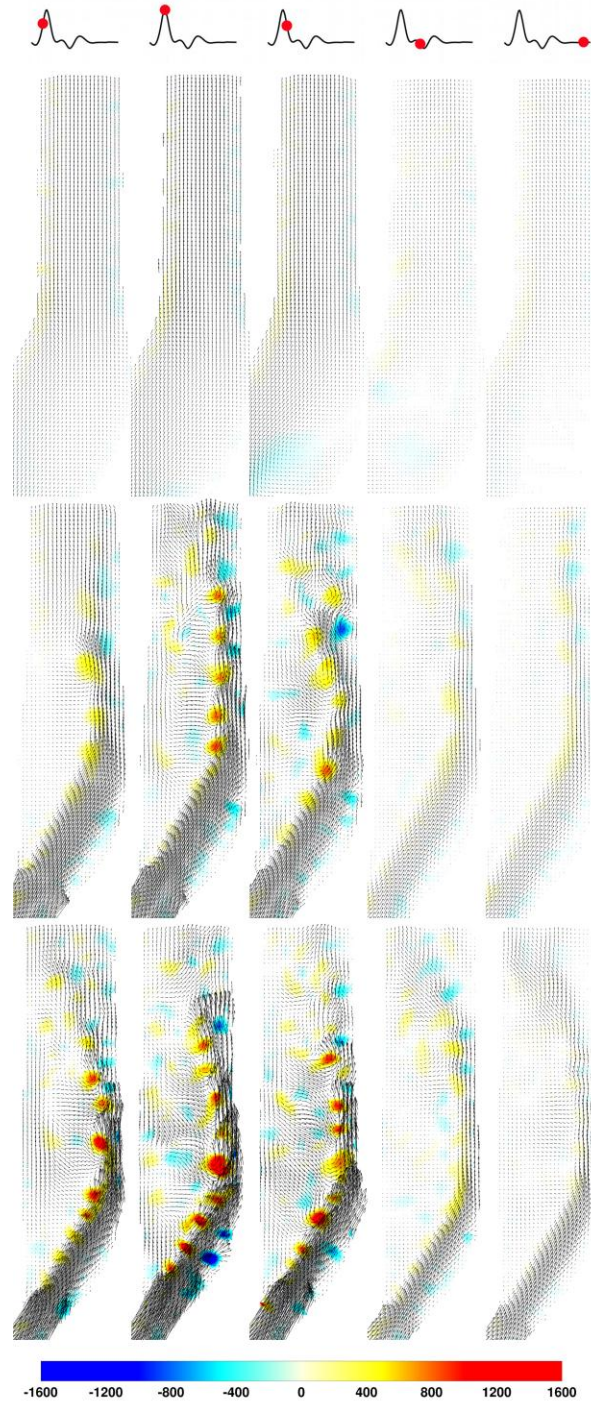


Figure 3.4: Vector-velocity fields at five different time points of the cardiac cycles superimposed on color maps of the swirling strength in the normal (top row), 50% (middle row), and 70% models (bottom row). The color bar was customized to emphasize variation between -1000 and $+1000$ s^{-1} to enable visualization of the details across all three models. The minimum and maximum values present in the 70% model at the peak systole were -1550 s^{-1} and 1474 s^{-1} respectively.

3.3.2 Stenosis severity effect via POD analysis

The swirling-strength maps of five selected POD spatial modes, $\phi^i(\vec{x})$, for each of the three models are shown in Figure 3.5. Recall that the first few modes of the POD analysis are associated with the most dominant features of the flow and carry most of the information of the flow. In Figure 3.5, the first modes of all three models are seen to exhibit large vortices, as demonstrated for example by modes 1, 2, and 10 in the three leftmost columns. A large clockwise (i.e. negative) vortex can be observed in both the 50% model (with maximum center value of about 1550 s^{-1}) and 70% model (maximum of 3150 s^{-1}) and is associated with the interaction of the cross-flow and jet flow (see previous section) generated as a result of the stenosis, in contrast to the normal model. As the spatial mode number increases, the strength and size of the vortices (based on the outermost contour line) decreases, which reflects the characteristic property of higher POD modes being associated with smaller flow structures. The effect of the stenosis on the flow structure can be seen in both the 50% and 70% models: for example, in the intermediate modes of 20 and 40, a concentrated alternating vortex pattern (shown as staggered positive and negative swirling-strength values) is seen downstream in the jet-flow region. Additionally, compared to the 50% model, the 70% model exhibits more swirls that are of larger size and strength. In modes 20 and 40 of the normal model, no structures were detectable of comparable strength to those observed in the 50% and 70% models.

Although POD spatial modes are useful in terms of providing information on the dynamics of the flow, further information such as the different stages of the energy transition can be extracted from the energy spectrum of the flow. The eigenvalues calculated from the auto-correlation matrix of velocity represent the energy content of each spatial mode (Equation (A.4)).

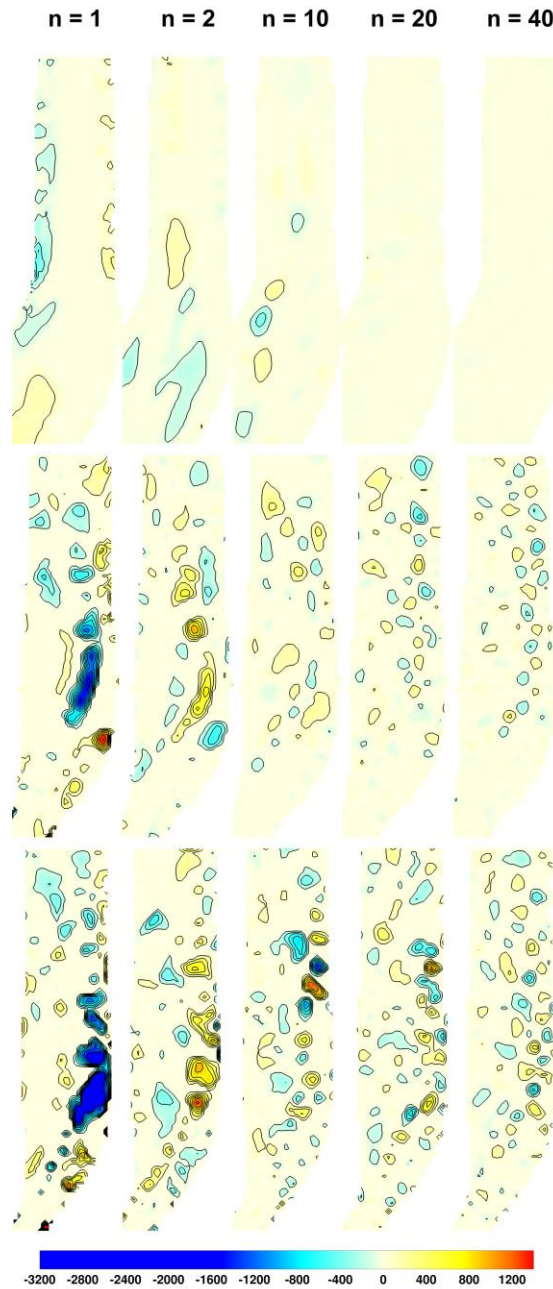


Figure 3.5: Color maps of swirling strength generated for the spatial modes 1, 2, 10, 20, and 40 in the normal (top row), 50% (middle row), and 70% models (bottom row). The color bar was customized to emphasize variation between -1500 and $+1500 \text{ s}^{-1}$ to enable visualization of the details across all three models. The actual maximum strengths present in the first mode of each of the 50% and 70% models are -1550 and -3150 s^{-1} respectively, where the negative indicates clockwise swirl. Contour lines represent $|200| \text{ s}^{-1}$ increments, starting from -100 and $+100 \text{ s}^{-1}$ for negative and positive rotation respectively.

Figure 3.6a shows the double-logarithmic plot of the fractional energy (Equation (A.10)) spectrum as a function of the mode number, with notable differences between the three models. The value for the first-mode energy was 72% for the 70%-stenosed model, 83% for the 50% model, and 86% for the normal model. The energy spectra of the 50% and 70% models exhibit a distinct first zone (consisting of the first three modes) in which the fractional energy content decreases rapidly, as well as a distinct second zone in which energy decays following a power-law slope of -1.34 and -0.91 for the 50% and 70% models respectively. This second zone extends over approximately 35 modes (from around mode 11 to 46) for both models. After this inertial range, a steeper dissipative sub-range is recognizable.

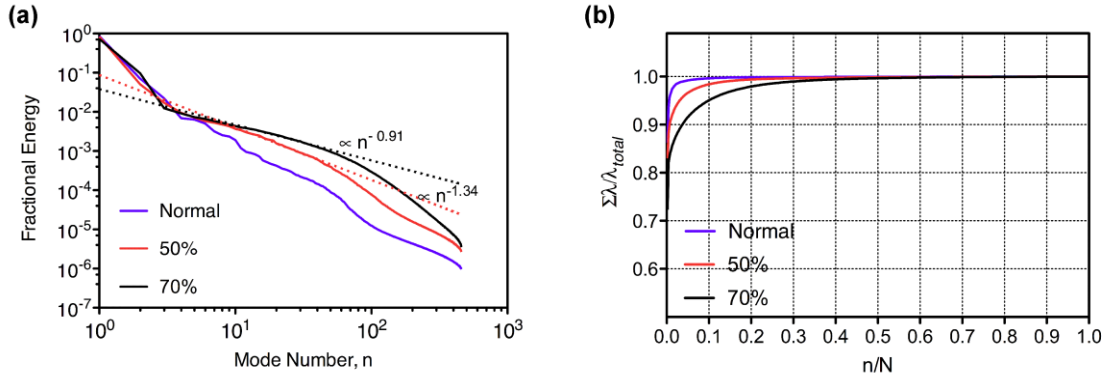


Figure 3.6: POD energy plots using a total mode number (N) of 460 and full FOV for each of the three models: (a) Double logarithmic plot of fractional energy spectra as a function of mode number, (b) cumulative energy distribution showing cumulative eigenvalues as a function of normalized mode number (n/N).

In the energy spectrum of the normal model, a pairwise occurrence of some of the early eigenvalues can be observed; these eigenvalues have almost equal values and therefore produce a stepwise appearance in the energy spectrum. This characteristic pairwise occurrence of eigenvalues has been reported in previous POD studies of periodic flows [34-36] and is associated with the presence of a traveling wave. The spatial modes within each pair are similar but shifted in the stream-wise direction, and likewise the paired temporal modes are phase-shifted in time. The pairwise occurrence vanishes gradually as mode number increases.

The differences observed in the energy spectra and decay rates translate to the cumulative energy distribution presented in Figure 3.6b. The total energy contained within the first 10% (i.e. 46) of the modes is about 100%, 98%, and 95% respectively for the normal, 50% and 70% models, reflecting the slower rate at which the cumulative energy converges toward the total energy content with increasing stenosis severity. The slower convergence rate indicates more spatial modes are needed to reconstruct the velocity fields. To further assess the level of flow instability, the values of global entropy were compared. The entropy value is derived from the mode energy contents as described in Equation (A.11). By increasing flow instabilities, the value of entropy increases reaching a maximum of 1 for the hypothetical flow in which the total energy is fully sustained throughout and is distributed evenly over all the modes. The entropy value further supports the increasing level of flow complexity as it increased from 0.11 in the normal model to 0.17 in the 50% and 0.26 in the 70% model.

POD temporal modes, $a^n(t)$, for 6 selected modes are depicted in Figure 3.7, for each of the three models. For all three models, the first temporal mode essentially reflects the shape of the flow rate waveform input at the CCA inlet (i.e. Figure 3.1c) since this mode reflects the average flow organization. The second mode also reflects the shape of the average cardiac cycle waveform, however, it is slightly time-shifted with a similar but inverted shape. As the mode number increases, the temporal modes start to show more irregular patterns and higher frequencies of fluctuation, as seen from mode 10 and onwards. These disturbances are associated with rapid velocity fluctuations and indicate a transitional turbulent regime. It is interesting to note from mode 10 that the fluctuations start at earlier modes for the 70% model; alternatively the 50% and normal models still show a regular pattern. From mode 40, the cardiac phase during which the velocity fluctuations are exhibited can be determined: in the 50% and 70% models, this duration starts from the mid-systolic acceleration and persists all the way down to the systolic foot. However, for the normal model, the fluctuating region is more confined to mid-acceleration and mid-deceleration. For the 50% and 70% models, small periods of fluctuation are also notable during 0.5 to 0.7 ms, which is the time interval associated with the increased flow right before the diastolic phase in the cardiac cycle waveform

(Figure 3.1c). As the mode number increases, the disturbances become more persistent and more equally spread throughout the cardiac cycle indicating background fluctuations, e.g. due to system noise. The reduction of disturbances, starting in the systolic phase, is first evident in the normal model (as seen by the systolic gap, at 100-250 ms, in mode 70), then in the 50% model (mode 100) and later in the 70% model (approx. mode 200, not shown).

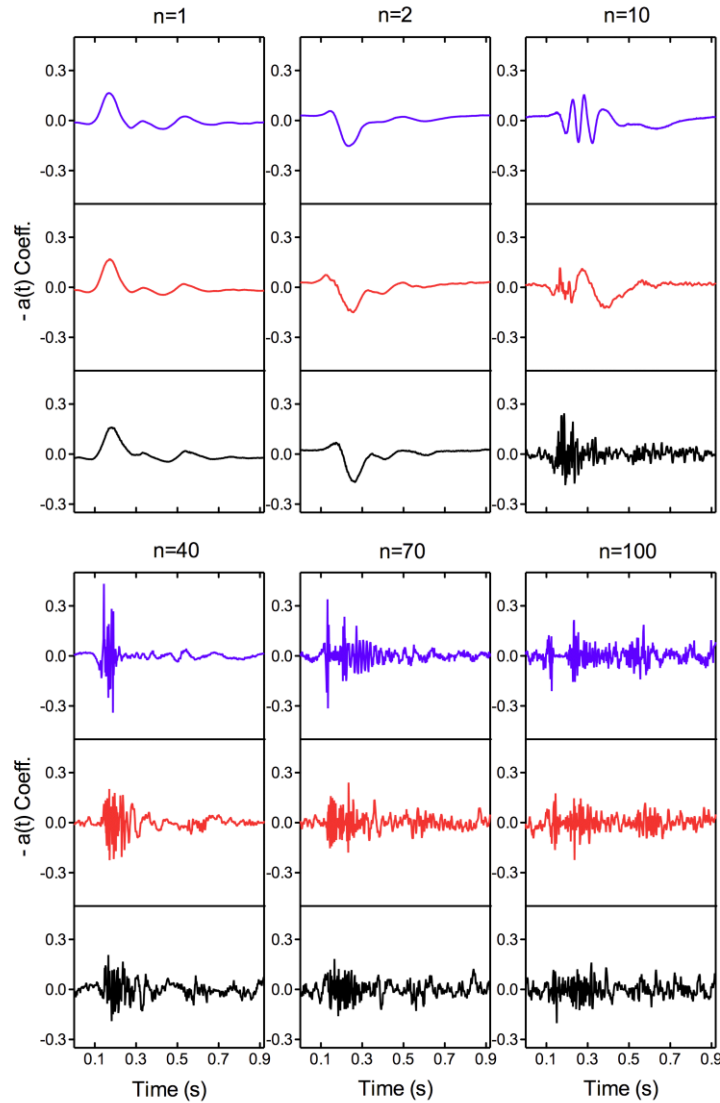


Figure 3.7: POD ($N=460$) temporal modes 1, 2, 10, 40, 70, and 100 for normal (blue plots in each set), 50% (red), and 70% (black) models, showing the temporal coefficients, $-a(t)$, as a function of the cardiac cycle.

3.3.3 POD analysis of multiple planes in 70% stenosed model

Figure 3.8 refers to the POD analysis for the 2D-3C velocity fields of multiple planes from the top half of the 70% phantom using an ICA sub-region FOV. Figure 3.8 shows the double-logarithmic plot of the energy spectra versus the mode number for four selected planes, including the central plane of symmetry. The energy spectra of both the 1-mm and 2-mm offset planes follow the same pattern as that of the central plane, but starting with a smaller first mode energy (of about 47% for both planes) compared to that of the central plane (75%). This suggests the same transitional regime for the flow captured in the offset planes but with a higher level of turbulent energy. This may be associated with a higher level of velocity fluctuations, perhaps due to the contribution of fluctuations from the expected out-of-plane velocity component, as opposed to the more planar flow in the central plane of symmetry. The energy spectrum of the 3-mm offset plane, which had a first-mode energy of approximately 60%, deviates from the energy spectra observed for the central and other offset planes, reflecting a different transitional regime (i.e. different size order of small structures). It should be noted that this plane was adjacent to the upper wall of the lumen and only had a small region of flow in the FOV. The different levels of instabilities and turbulence in the offset planes are also reflected in the different levels of entropy, which are 0.28, 0.50, 0.48, and 0.33 for the central, 1-mm, 2-mm, and 3-mm offset planes respectively.

The dotted line in Figure 3.8 represents the energy spectrum of the 70% model derived from the POD analysis of the full FOV in the central plane, as shown previously in Figure 3.6a. The difference between the energy spectra is primarily due to a drop in the energy of the second eigenfunction from the ICA-FOV analysis as it contributes a lower fraction to the total energy than in the full FOV, corresponding to less of the organized (large-scale coherent) flow when compared to the second mode in the full FOV. The entropy levels are 0.28 and 0.26 for the ICA-FOV and full-FOV respectively.

3.3.4 Temporal resolution effect

From the energy spectrum (Figure 3.6a) and the POD temporal modes for the 70% model (Figure 3.7), it was confirmed that the first and second modes carry the largest portion of

the energy and correspond to large coherent structures and the time-averaged flow. In POD analysis, a standard convergence test refers to the convergence of a mode energy (particularly the first modes) to a uniform value for an increasing number of snapshot ensembles, which here translates to increasing frame rates due to the pulsatile flow over a finite cardiac cycle.

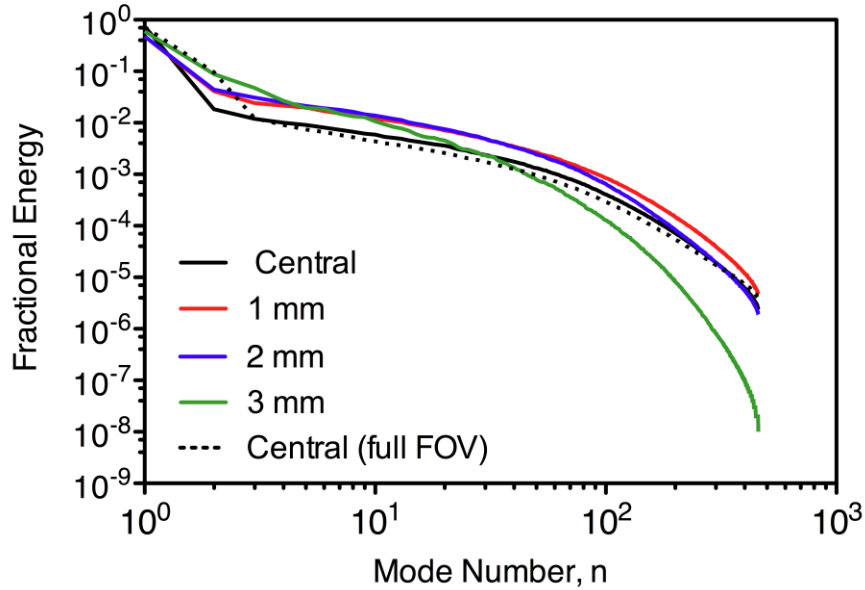


Figure 3.8: Double-logarithmic plot of POD (N=460) fractional energy spectra as a function of mode number, using the smaller ICA FOV for four selected planes in the 70%-stenosed model, corresponding to central plane, plus 1-, 2-, and 3-mm offset planes parallel to the central plane.

Table 3.1 shows the fractional energy of the first four modes for the five different snapshot ensembles (i.e. 92, 184, 295, 368, and 460 per cardiac cycle), corresponding to the five frame rates ranging from 100 to 500 Hz, in the 70% model. The second column shows the average and standard deviation calculated across the means from the different frame rates. It can be noted that the variation across the means is of the same order as variations within the individual ensemble groups. A one-way ANOVA with Bonferroni post-hoc test showed that the mean of the mode-one energy for 400 Hz was significantly different ($P < 0.01$) from 100 and 200 Hz, but for mode two, no significant differences were found between the groups of frame rates. Additionally, further analysis on the

cumulative energy of the first two modes together (corresponding to approximately 82 % of the total energy) showed no significant differences between the means for the different frame-rate groups.

Table 3.1: Comparison of the POD relative eigenvalues for five different temporal resolutions shown for first four modes of flow in the 70%-stenosed model.

Mode Number	$\left(\frac{\lambda_n}{\lambda_{tot}} \right)$	$\frac{\lambda_n}{\lambda_{tot}}$ 100 Hz (92 Snapshots) 10 iterations	$\frac{\lambda_n}{\lambda_{tot}}$ 200 Hz (184 Snapshots) 5 iterations	$\frac{\lambda_n}{\lambda_{tot}}$ 320 Hz (295 Snapshots) 4 iterations	$\frac{\lambda_n}{\lambda_{tot}}$ 400 Hz (368 Snapshots) 4 iterations	$\frac{\lambda_n}{\lambda_{tot}}$ 500 Hz (460 Snapshots) 3 iterations
n = 1	$72.30 \pm 0.61\%$	$71.95 \pm 0.43^{\pi}$	$71.60 \pm 0.68^{\S}$	72.40 ± 0.13	$73.23 \pm 0.43^{\pi, \S}$	72.33 ± 0.51
n = 2	9.56 ± 0.22	9.68 ± 0.35	9.77 ± 0.21	9.36 ± 0.18	9.28 ± 0.11	9.69 ± 0.14
n = 3	1.40 ± 0.20	$1.73 \pm 0.25^{\dagger}$	1.34 ± 0.10	1.38 ± 0.08	1.28 ± 0.13	1.23 ± 0.18
n = 4	1.03 ± 0.17	$1.32 \pm 0.11^{\ddagger}$	1.02 ± 0.09	0.95 ± 0.07	0.94 ± 0.07	0.91 ± 0.10

^{π} Significant difference ($P < 0.01$) between 100 and 400 Hz for mode one;

^{\S} Significant difference ($P < 0.001$) between 200 and 400 Hz for mode one;

^{\dagger} Significant difference ($P < 0.01$) between 100 Hz and all other frame rates for mode three;

^{\ddagger} Significant difference ($P < 0.0001$) between 100 Hz and all other frame rates for mode four;

Figure 3.9a shows the fractional energy spectra corresponding to different frame rates in the 70% model, where each energy spectrum exhibits the distinct zones described previously (Figure 3.6a). However, for frame rates less than 400 Hz, the energy spectra are elevated in the inertial range meaning less relative importance of the first two modes, and thus higher entropy values are expected for this behavior. This is reflected in Figure 3.9b, where the entropy value is higher for the lower frame rates ranging from about 0.32 for 100 Hz down to 0.27 at 300 Hz, and then starts to converge at about 0.26 from 400 Hz onwards. The different entropy values for different temporal resolutions reflect the divergence of the higher modes, as is also revealed through statistical analysis of the energies for modes three and four in Table 3.1 which showed that the values for 100 Hz varied significantly from all the other frame rates.

3.4 Discussion

In the study of this chapter, stereo-PIV measurements in two stenosed carotid artery bifurcation models (with 50% and 70% concentric stenosis), as well as in a normal (disease-free) model as a control, were combined with POD analysis in order to gain more detailed information on the type of the flow observed in the stenosed carotid artery.

Stereo-PIV measurements reveal the complexity of the flow due to the presence of a concentric stenosis. Both 50% and 70% concentrically stenosed models show a region of reverse flow along the inner wall of the ICA, flickering motion of the jet along the outer wall of the ICA, vortices developing along and behind the jet, helical swirling motion in the free-jet region, as well as velocity fluctuations alongside the jet primarily during peak systole and systolic deceleration. Similar features of reverse flow and downstream disturbed flow were previously shown in stenosed models of the same family of geometries using digital particle imaging, Doppler ultrasound, and computational fluid dynamics [25, 37].

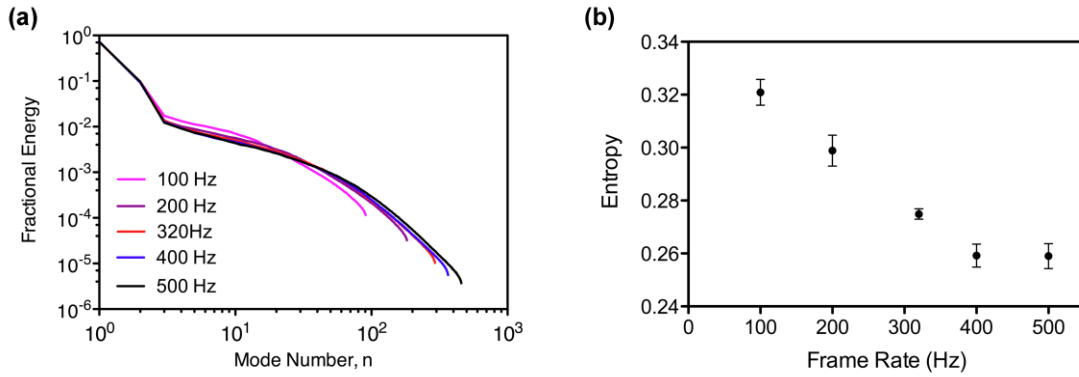


Figure 3.9: Double-logarithmic plot of POD fractional energy spectra derived from snapshot ensemble of 5 different frame rates (a), and entropy as a function of frame rate (b) in the 70%-stenosed model.

POD spatial modes provide insight into these dynamic structures of the flow. While no characteristic flow structure was observed in the higher spatial modes of the normal model, the spatial modes of both the 50% and 70% exhibit smaller coherent structure in the form of an alternating vortex pattern. The generation of this vortex pattern is due to the shedding of the vortices developed along both sides of the free jet with opposite rotational directions.

In the energy spectra from POD analysis, the energy of the first mode represents the energy content of the time-averaged flow and thus the highest value of all modes. The remainder of the energy in each model corresponds by definition to turbulent kinetic energy, with the value being the highest in the 70% model. More uniform distribution of

energy is expected as flow goes through transition to turbulence as more energy-containing small structures develop [33]. Transition to turbulence was seen in the stenosed models as evident from the developed inertial region of the energy spectra, seen as the second distinct zone. However, slower decay of energy, in other words more uniform energy distribution across higher modes, was observed in the 70% model (region with the slope of -0.91), which confirms the higher amount of turbulence with severe stenosis. In the 70% model, the power-law slope appeared to be independent of slice location (i.e. planar offset; Figure 3.8) and temporal resolution (Figure 3.9a). The lack of flow structure in the higher POD spatial modes of the normal model is also reflected in its energy spectrum (Figure 3.6a) in which energy in the higher modes decays quickly with no development of an inertial range (i.e. no evidence of transitional flow), as one might expect.

The POD temporal modes provide the time history for each spatial mode and indicate the cardiac phases for which flow perturbations occur, including in the normal model, although not necessarily transitioning to turbulence. The acceleration and deceleration phases of systole showed the greatest contribution to flow instabilities. This finding is also reported in several previous simulation-based stenosed-carotid artery studies [3, 23, 38] in which time traces of velocity at specified locations in the ICA were obtained. In a time-windowed POD analysis study by Grinberg *et al.* [23], this phase of the cardiac cycle was associated with the slower decay of the energy spectrum compared to the remaining time windows of the cardiac cycle. Wong *et al.* [39] also reported maximum values of the statistical-based turbulence intensity in the post-systolic deceleration phase in an *in vitro* clinical Doppler ultrasound study of ulcerated and non-ulcerated stenosed carotid artery models.

This work provides a comparison-based evaluation of POD analysis in the carotid artery, using a family of models simulating disease progression, showing that the slope of the power-law decay of the energy spectrum can provide a quantitative tool to assess the level of the turbulence in carotid flow. The decay slopes of the POD energy spectrum as a function of mode number may not follow a universal value, but for a known geometry, the slope of the power-law decay can provide a comparative value to quantify the level of

transitional flow and turbulence, such as in the study by Telib *et al.* [34] in which inhomogeneous anisotropic transitional flow in a T-mixer at different Reynolds numbers was quantified. In contrast, Fourier-based decomposition of fully homogeneous isotropic turbulent flows lead to universal energy decay slopes based on Kolmogorov similarity law, but these slopes would not be directly applicable here as flow in the carotid artery is not homogeneous, isotropic, nor fully turbulent. POD studies by Knight and Sirovich [40], Moser [41], and recently Baltzer *et al.* [42], have employed a POD-derived parameter analogous to frequency in order to derive an analogy to Kolmogorov similarity law.

POD analysis also demonstrated that the entropy level could provide a quantitative measure of the flow complexity. Transitional flow leads to a shift of energy from the first mode to the higher modes (i.e. inertial range) leading to higher entropy. Our results showed an increasing entropy level with increasing stenosis severity, ranging from 0.11 in the normal model to 0.17 in the 50% model and 0.26 in the 70%. For comparison, previous studies of turbulence intensity (TI) in this family of geometries showed low TI in 30% and 50% stenosed models, with modest increase due to ulcerations and a very large increase in TI for the 70% stenosed models [25, 39], reflecting the increased complexity and instabilities due to transition to turbulence, as shown here.

POD analysis on a smaller ICA FOV in the 70% model, encompassing only the jet and downstream relaminarization, resulted in a similar entropy level with a difference of only 0.02. Although the same transitional flow regime was observed in the offset planes based on the energy spectra, they showed a higher level of entropy (0.33-0.50), reflecting greater flow complexity due to out-of-plane components and fluctuations. In patient-specific geometries, with more tortuosity and hence out-of-plane flow, higher entropy values may be expected, similar to the offset planes here as opposed to the central plane of symmetry present in our idealized models. For clinical implementation, this would indicate the importance of looking at entropies from multiple planes to sample the full range of levels of instability.

An investigation of the effect of temporal resolution, by imaging a full FOV with increasing frames rates in the 70%-stenosed model, showed the entropy decreasing from ~ 0.32 at 100 Hz and converging at 0.26 for 400 and 500 Hz (Figure 3.9b). From the energy spectra, it was shown that a 100-Hz frame rate would be sufficient for statistical turbulence characterization (e.g. turbulence intensity or fluctuation about the mean velocity), since the fraction of the first mode energy was not significantly different from the energy derived with higher frame rates, based on the convergence test of the first modes. However, the increased energy level of the inertial range relative to the unchanged first-energy mode leads to more even energy distribution and thus higher entropy. This indicated that entropy-based turbulence characterization using an insufficient number of snapshots, or temporal resolution, would result in overestimation of the entropy level.

One of the limitations of the present study lies in the geometry of the models used, which were planar and axisymmetric idealized stenosed models, as opposed to patient-specific or tortuous models. Additionally, the silicone phantoms consist of a hollow carotid flow channel within a silicone block of approximately 50 mm x 25 mm x 210 mm, and thus may not match the physiological compliance of the carotid artery. While the phantom materials and geometries do not exhibit the full complexity of human arteries, the use of a family of matched models with quantified disease progression allows for a careful investigation, of turbulence in this case, in a controlled environment.

In this work, POD analysis provides insight into the flow of the carotid artery and can be used as the knowledge base for statistics-based methods of turbulence quantifications, which are dependent on the measurements of the velocity fluctuations. Based on the present study, it is revealed that the presence of the velocity fluctuations alone are not an indication of transitional flow, and the energy spectrum of the flow is also required in order to distinguish small flow disturbances (such as observed in the normal model) from transitional flow (as seen in the 50% and 70% models).

The work presented in this chapter is aimed at investigating a new method of turbulence quantification for potential application as a clinical diagnostic indicator of increased

stroke risk based on the increased risk of turbulence-induced thrombogenesis. In our previous *in vitro* Doppler ultrasound studies [39], a statistics-based turbulence quantification method of ensemble averaging was implemented. One limitation of such a method is the dependency on ECG gating for synchronizing the ensemble of the collected cardiac cycles; typically Doppler ultrasound exams in the clinical setting do not use ECG gating, thus alternative methods of turbulence quantification were demonstrated [43].

We have demonstrated that POD analysis leading to values of the power-law decay slope or global entropy can provide an alternative quantification method for the level of turbulence in carotid artery bifurcation blood flow. In order to transfer this technique to the clinical stage, certain adjustments with regards to frame rate and velocity components over the conventional methods should be considered. While MRI provides good spatial resolution and all three components of the velocity, the low temporal resolution, typically 20-50 ms, would be insufficient for POD analysis. Color Doppler ultrasound has relatively good temporal resolution (typically 4-20 ms for 2D images), but it only provides one component of the velocity directed to the transducer. However, as discussed in Chapter 1, with the focus of improving the frame rate and capturing more velocity components, many completed and on-going developments in the field of ultrasound-based velocity measurements are reported and more details can be found in the number of excellent reviews [44, 45]. With advanced capabilities of parallel acquisition of pre-beamformed data combined with new approaches such as of plane wave emission, 2D velocity vector maps with frame rates in the range of kilohertz can be expected.

Future work will include investigation of POD analysis on high frame rate Doppler ultrasound velocity maps, as well as further PIV investigations of the effect of plaque eccentricity, ulceration, and vessel compliance. While numerical simulations are frequently used to study large-artery hemodynamics, experimental techniques such as PIV are essential for accurately revealing complex and disturbed flow, and thus also provide valuable data for the validation of numerical turbulence models. In an additional PIV study focused on turbulence intensity, we will provide detailed velocity and turbulence profiles that can be applied towards validation of numerical studies.

3.5 Conclusion

Turbulent and transitional flow in the carotid artery bifurcation is of particular interest due to the known correlation between thrombogenesis and flow disturbances. In this work, we showed the potential of POD for vascular flow applications and have proposed POD-based quantitative measures of instabilities and turbulence in the carotid artery bifurcation. Namely, the energy decay slope and the entropy values provide two complementary metrics for quantifying the levels of transitional flow. Through the POD analysis, transitional flow was detected in both 50%- and 70%-stenosed models. Increased complexity of flow in the 70% model was indicated by the power-law slope of the energy spectrum and the entropy level, particularly in the offset planes with greater out-of-plane flow components. It is also important to ensure adequate temporal resolution for turbulence quantification based on POD-derived parameters, which may require better resolution than indicated by the standard POD convergence test.

3.6 References

- [1] A. De Fabritiis, E. Conti, and S. Coccheri (2002), Management of patients with carotid stenosis. *Pathophysiol. Haemost. Thromb.*, vol. 32, pp. 381-5.
- [2] D. P. Giddens, R. F. Mabon, and R. A. Cassanova (1976), Measurements of disordered flows distal to subtotal vascular stenoses in the thoracic aortas of dogs. *Circulation Research*, vol. 39, pp. 112-9.
- [3] S. E. Lee, S.-W. Lee, P. F. Fischer, *et al.* (2008), Direct numerical simulation of transitional flow in a stenosed carotid bifurcation. *Journal of Biomechanics*, vol. 41, pp. 2551-2561.
- [4] F. P. P. Tan, G. Soloperto, S. Bashford, *et al.* (2008), Analysis of flow disturbance in a stenosed carotid artery bifurcation using two-equation transitional and turbulence models. *Journal of Biomechanical Engineering*, vol. 130, p. 061008.
- [5] A. N. Kolmogorov (1941), The local structure of turbulence in incompressible viscous fluid for very large Reynolds numbers. *Proceedings of the USSR Academy of Sciences*, vol. 30, pp. 299–303.
- [6] P. D. Stein and H. N. Sabbah (1974), Measured turbulence and its effect on thrombus formation. *Circulation Research*, vol. 35, pp. 608-614.

- [7] S. P. Jackson, W. S. Nesbitt, and E. Westein (2009), Dynamics of platelet thrombus formation. *J. Thromb. Haemost.*, vol. 7, pp. 17-20.
- [8] D. Bluestein, C. Gutierrez, M. Londono, *et al.* (1999), Vortex shedding in steady flow through a model of an arterial stenosis and its relevance to mural platelet deposition. *Annals of Biomedical Engineering*, vol. 27, pp. 763-73.
- [9] C. J. Slager, J. K. Wentzel, F. J. H. Gijzen, *et al.* (2005), The role of shear stress in the generation of rupture-prone vulnerable plaques. *Nat. Clin. Pract. Cardiovasc. Med.*, vol. 2, pp. 401-407.
- [10] N. Depaola, M. A. Gimbrone, P. F. Davies, *et al.* (1992), Vascular endothelium responds to fluid shear-stress gradients. *Arteriosclerosis and Thrombosis*, vol. 12, pp. 1254-1257.
- [11] S. A. Ahmed and D. P. Giddens (1984), Pulsatile poststenotic flow studies with laser Doppler anemometry. *Journal of Biomechanics*, vol. 17, pp. 695-705.
- [12] J. Banks and N. W. Bressloff (2007), Turbulence modeling in three-dimensional stenosed arterial bifurcations. *Journal of Biomechanical Engineering*, vol. 129, pp. 40-50.
- [13] J. Ryval, A. G. Straatman, and D. A. Steinman (2004), Two-equation turbulence modeling of pulsatile flow in a stenosed tube. *Journal of Biomechanical Engineering*, vol. 126, pp. 625-35.
- [14] J. S. Stroud, S. A. Berger, and D. Saloner (2002), Numerical analysis of flow through a severely stenotic carotid artery bifurcation. *ASME Journal of Biomechanical Engineering*, vol. 124, pp. 9-20.
- [15] S. J. Sherwin and H. M. Blackburn (2005), Three-dimensional instabilities and transition of steady and pulsatile axisymmetric stenotic flows. *J. Fluid Mech.*, vol. 533, pp. 297-327.
- [16] S. S. Varghese, S. H. Frankel, and P. F. Fischer (2007), Direct numerical simulation of stenotic flows. Part 2. Pulsatile flow. *J. Fluid Mech.*, vol. 582, pp. 281-318.
- [17] S. Karri and P. P. Vlachos (2010), Time-resolved DPIV investigation of pulsatile flow in symmetric stenotic arteries effects of phase angle. *Journal of Biomechanical Engineering-T. ASME*, vol. 132,
- [18] J. Vetel, A. Garon, D. Pelletier, *et al.* (2008), Asymmetry and transition to turbulence in a smooth axisymmetric constriction. *Journal of Fluid Mechanics*, vol. 607, pp. 351-386.

- [19] N. A. Buchmann, C. Atkinson, M. C. Jeremy, *et al.* (2011), Tomographic particle image velocimetry investigation of the flow in a modeled human carotid artery bifurcation. *Exp. Fluids*, vol. 50, pp. 1131-1151.
- [20] J. Vetel, A. Garon, and D. Pelletier (2009), Lagrangian coherent structures in the human carotid artery bifurcation. *Exp. Fluids*, vol. 46, pp. 1067-1079.
- [21] J. L. Lumley (1967), "The structure of inhomogeneous turbulence, in atmospheric turbulence and radio wave propagation," in *Atmospheric turbulence and radio wave propagation*. Nauka, Moscow, pp. 166-178.
- [22] L. Sirovich (1987), Turbulence and the dynamics of coherent structures .1. Coherent structures. *Q. App. Math.*, vol. 45, pp. 561-571.
- [23] L. Grinberg, A. Yakhot, and G. E. Karniadakis (2009), Analyzing transient turbulence in a stenosed carotid artery by proper orthogonal decomposition. *Annals of Biomedical Engineering*, vol. 37, pp. 2200-2217.
- [24] R. F. Smith, B. K. Rutt, and D. W. Holdsworth (1999), Anthropomorphic carotid bifurcation phantom for MRI applications. *Journal of Magnetic Resonance Imaging*, vol. 10, pp. 533-44.
- [25] T. L. Poepping, R. N. Rankin, and D. W. Holdsworth (2010), Flow patterns in carotid bifurcation models using pulsed Doppler ultrasound: Effect of concentric vs. Eccentric stenosis on turbulence and recirculation. *Ultrasound in Medicine and Biology*, vol. 36, pp. 1125-1134.
- [26] R. F. Smith, B. K. Rutt, A. J. Fox, *et al.* (1996), Geometric characterization of stenosed human carotid arteries. *Academic Radiology*, vol. 3, pp. 898-911.
- [27] N. A. S. C. E. T. N. Collaborators (1991), Beneficial effect of carotid endarterectomy in symptomatic patients with high-grade carotid stenosis. North american symptomatic carotid endarterectomy trial collaborators. *The New England journal of medicine*, vol. 325, pp. 445-53.
- [28] D. W. Holdsworth, D. W. Rickey, M. Drangova, *et al.* (1991), Computer-controlled positive displacement pump for physiological flow simulation. *Medical and Biological Engineering and Computing*, vol. 29, pp. 565-70.
- [29] T. L. Poepping, H. N. Nikolov, R. N. Rankin, *et al.* (2002), An in vitro system for Doppler ultrasound flow studies in the stenosed carotid artery bifurcation. *Ultrasound in Medicine and Biology*, vol. 28, pp. 495-506.
- [30] D. W. Holdsworth, C. J. Norley, R. Frayne, *et al.* (1999), Characterization of common carotid artery blood-flow waveforms in normal human subjects. *Physiological Measurement*, vol. 20, pp. 219-40.

- [31] M. Y. Yousif, D. W. Holdsworth, and T. L. Poepping (2011), A blood-mimicking fluid for particle image velocimetry with silicone vascular models. *Experiments in Fluids*, vol. 50, pp. 769-774.
- [32] J. Zhou, R. J. Adrian, S. Balachandar, *et al.* (1999), Mechanisms for generating coherent packets of hairpin vortices in channel flow. *J. Fluid Mech.*, vol. 387, pp. 353-396.
- [33] N. Aubry, M. P. Chauve, and R. Guyonnet (1994), Transition to turbulence on a rotating flat disk. *Phys. Fluids*, vol. 6, pp. 2800-2814.
- [34] H. Telib, M. Manhart, and A. Iollo (2004), Analysis and low-order modeling of the inhomogeneous transitional flow inside a t-mixer. *Phys. Fluids*, vol. 16, pp. 2717-2731.
- [35] R. Bourguet, M. Braza, A. Sevrain, *et al.* (2009), Capturing transition features around a wing by reduced-order modeling based on compressible Navier-Stokes equations. *Phys. Fluids*, vol. 21, p. 11 pp.
- [36] A. S. Cruz, L. David, J. Pecheux, *et al.* (2005), Characterization by proper-orthogonal-decomposition of the passive controlled wake flow downstream of a half cylinder. *Exp. Fluids*, vol. 39, pp. 730-742.
- [37] D. A. Steinman, T. L. Poepping, M. Tambasco, *et al.* (2000), Flow patterns at the stenosed carotid bifurcation: Effect of concentric versus eccentric stenosis. *Annals of Biomedical Engineering*, vol. 28, pp. 415-23.
- [38] P. F. Fischer, F. Loth, S. E. Lee, *et al.* (2007), Simulation of high-Reynolds number vascular flows. *Computer Methods in Applied Mechanics and Engineering*, vol. 196, pp. 3049-3060.
- [39] E. Y. Wong, H. N. Nikolov, M. L. Thorne, *et al.* (2009), Clinical Doppler ultrasound for the assessment of plaque ulceration in the stenosed carotid bifurcation by detection of distal turbulence intensity: A matched model study. *European Radiology*, vol. 19, pp. 2739-49.
- [40] B. Knight and L. Sirovich (1990), Kolmogorov inertial range for inhomogeneous turbulent flows. *Phys. Rev. Lett.*, vol. 65, pp. 1356-1359.
- [41] R. D. Moser (1994), Kolmogorov inertial range spectra for inhomogeneous turbulence. *Phys. Fluids*, vol. 6, pp. 794-801.
- [42] J. R. Baltzer and R. J. Adrian (2011), Structure, scaling, and synthesis of proper orthogonal decomposition modes of inhomogeneous turbulence. *Physics of Fluids*, vol. 23,

- [43] M. L. Thorne, R. N. Rankin, D. A. Steinman, *et al.* (2010), In vivo Doppler ultrasound quantification of turbulence intensity using a high-pass frequency filter method. *Ultrasound in Medicine and Biology*, vol. 36, pp. 761-771.
- [44] D. H. Evans, J. A. Jensen, and M. B. Nielsen (2011), Ultrasonic colour Doppler imaging. *Interface Focus*, vol. 1, pp. 490-502.
- [45] P. P. Sengupta, G. Pedrizzetti, P. J. Kilner, *et al.* (2012), Emerging trends in cv flow visualization. *Jacc-Cardiovascular Imaging*, vol. 5, pp. 305-316.

Chapter 4

4 Turbulence Intensity Measurements Using Particle Image Velocimetry in Diseased Carotid Artery Models: Effect of Stenosis Severity, Plaque Eccentricity, and Ulceration*

4.1 Introduction

Atherothromboembolism accounts for about 50% of all ischemic strokes and transient ischemic attacks (TIA) [1]. In addition to primarily being regulated by blood agonists, thrombosis can also be regulated by hemodynamic factors introduced by altered flow patterns in the case of stenotic plaque [2]. Disturbed flow, particularly turbulent flow, has shown high correlation with thrombus formation [3-5]. Turbulent conditions also facilitate the exposure of blood components (i.e. platelets) to high temporal shear gradients, the transportation and deposition of atherogenic and prothrombotic materials to the vessel wall [6, 7], and possibly the release of blood-soluble agonists [8]. Moreover, under disturbed flow condition, the unstable thrombi are expected to mobilize [9], and vulnerable plaque to rupture [10]. Also, findings suggest that, due to a high concentration of red blood cells in blood, under turbulent conditions, viscous cell-cell interactions may result in shear-stress forces on the same order as turbulent (Reynolds) shear stresses [11]. Post-stenotic regions of recirculation, in which platelet agonists accumulate, also provide suitable environments for platelet activation and stabilization of aggregates [12].

Despite the extensive and increasing evidence that stenosis severity alone is not a sensitive predictor of stroke risk, it remains the main diagnostic indicator for the risk of TIA or stroke [13]. Major clinical trials, including the North American Symptomatic Carotid Endarterectomy Trial (NASCET) [14] and the European Carotid Surgery Trial

* A version of this chapter has been submitted to *Journal of Biomechanics* as an original article entitled “Turbulence intensity measurements using particle image velocimetry in diseased carotid artery models: effect of stenosis severity, plaque eccentricity, and ulceration” by S. Kefayati, D. W. Holdsworth, and T. L. Poepping.

(ECST) [15] showed that surgical removal the carotid artery plaque (i.e. a carotid endarterectomy) provides protection against stroke or crescendo TIA in symptomatic patients with severe stenosis. In a trial study by Ohara *et al.* [16] for patients with carotid-artery stenosis severity above 50% (as defined by NASCET criteria), eccentric (asymmetric) plaques showed significantly increased ipsilateral cerebrovascular events compared to concentric (symmetric) plaques and were independently related to the presence of a recent cerebrovascular incidence. Eccentric plaques have also been associated with larger content of lipid and increased calcification [17]. *In vitro* flow studies under steady [18] and pulsatile flow [19] have reported marked differences due to eccentricity in post-stenotic flow.

Plaque ulceration – commonly referred to as an irregularity in the plaque surface – is also associated with greater thromboembolic potential by exposing the necrotic core of the plaque to the blood flow [20]. Fisher *et al.* [21] reported more frequent thrombus in patients with ipsilateral symptoms and ulceration, thus suggesting higher risk of embolism for these patients leading to higher stroke risk. *In vitro* study by Wong *et al.* [22] showed the additional impact of ulceration – in various shapes and sizes – on flow disturbances introduced by stenosis.

Considerable promise exists in stroke-risk indicators that can be associated with thromboembolic activity level [23]. Plaque-associated indicators can be either morphology-dependent (e.g. plaque composition and vulnerability) or hemodynamic-dependent and thus be governed by certain geometrical features of the plaque.

The objective of the present work is to conduct a matched-model investigation to assess the effect of three geometrical variables of the plaque – namely stenosis severity, plaque eccentricity, and plaque ulceration – on the local hemodynamics of the diseased carotid artery bifurcation. As a hemodynamic factor with indirect association to thrombotic activity, and thus potential clinical significance, the level of turbulence intensity was quantified from the downstream elevated region.

4.2 Methods

4.2.1 Flow set-up

A family of eight carotid artery models was studied, incorporating three degrees of stenosis severity belonging to mild, moderate, and severe classification (i.e. 30%, 50%, and 70% respectively) based on NASCET criteria [24]. For each stenosis severity, two models with the two extremes of plaque symmetry, concentric and eccentric, were examined. Overall impact of ulceration was investigated through a single model with 50% eccentric stenosis and distally pointing ellipsoid ulcer [22]. A diseased-free model (i.e. normal) was also examined that provided the baseline understanding of the flow in the carotid artery bifurcation. PIV-compatible life-sized phantoms were manufactured using a lost-core casting technique [25, 26]. The models have an 8-mm inner diameter (ID) common carotid artery (CCA) which branches into the internal (ICA) and external (ECA) carotid arteries. Figure 4.1 depicts a silicone phantom (Figure 4.1a) incorporating a normal geometry (Figure 4.1b), with the geometry of the seven stenosed models shown in Figure 4.1c.

The working fluid was a PIV-compatible blood-mimicking fluid prepared according to the description given in Yousif *et al.* [27] and was composed of water (47.38% by weight), glycerol (36.94% by weight.), and sodium iodide (15.68% by weight). The fluid matched the refractive index of silicone phantoms, hence reducing the wall reflections, and achieved the dynamic viscosity of $\mu = 4.31$ cP and density of $\rho = 1.244$ g/ml matching those of blood. A computer-controlled pump [28] equipped with a synchronization signal generated a physiologically relevant cardiac-cycle flow waveform (Figure 3.1c) based on a previous *in vivo* characterization [29]. The cardiac-cycle period was $T = 920$ ms corresponding to the Womersley number ($0.5D\sqrt{2\pi\rho/\mu T}$) of 5.62 based on the CCA diameter. Downstream flow resistors achieved a ICA-ECA flow division of approximately 60:40 [30]. Flow rates were measured as follows: peak and mean CCA flow rates of 27.13 ± 0.30 and 6.29 ± 0.09 ml/s respectively, and peak and mean ICA flow rates of 12.22 ± 0.19 and 3.56 ± 0.02 ml/s respectively. Corresponding maximum and mean Reynolds numbers calculated based on the narrowest diameter of the ICA

stenosis were 1162 and 312 in the 30% models, 1627 and 473 in the 50% models, and 2712 and 789 in the 70% stenosed models.

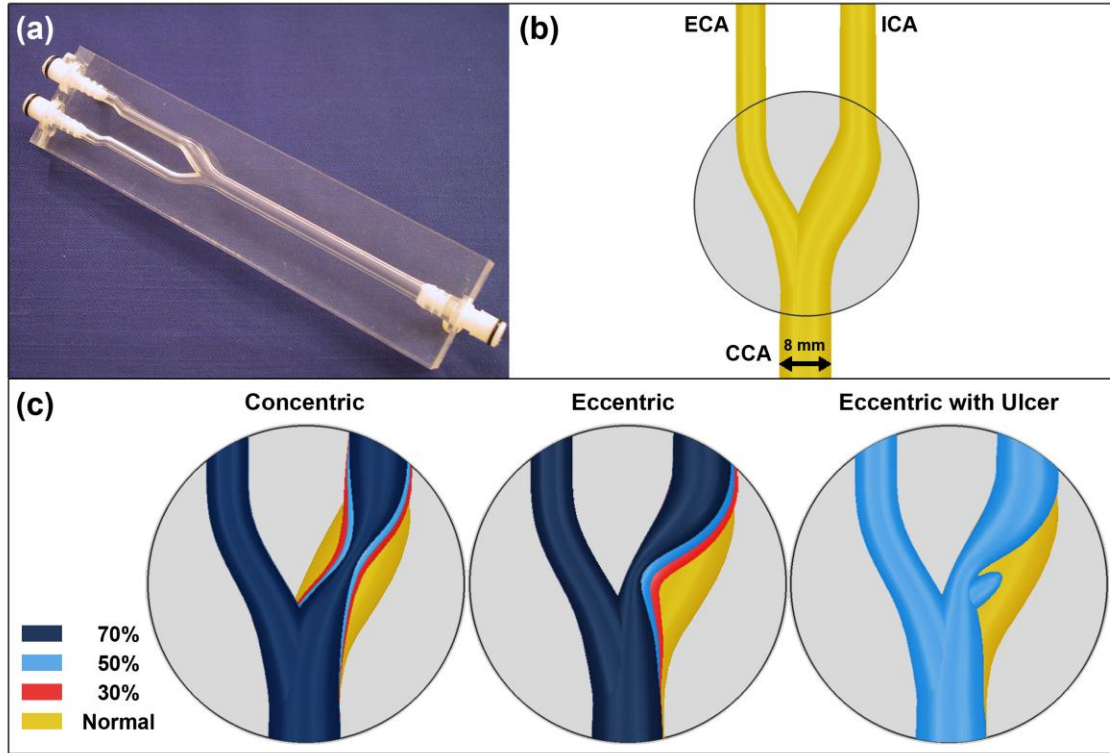


Figure 4.1: Geometry of the carotid artery bifurcation phantoms: (a) PIV compatible silicone phantom incorporating the normal (disease-free) geometry shown in (b); (c) outlines of the geometries with various stenosis severity superimposed on the normal geometry for the grey region indicated in (b) and for concentric, eccentric, and ulcerated plaques.

4.2.2 Data acquisition and analysis

The stereoscopic PIV system (LaVision Inc., Ipsilanti MI, USA) has been earlier described in detail in Chapter 3. Image acquisition was synchronized to the cardiac cycle through the pump synchronization pulse. From the full cardiac cycle (920 ms), the initial 870-ms portion was captured, which included all the significant phases, and the last 50 ms of nearly constant flow was neglected. Double-frame images of each plane were recorded at 100 Hz (10-ms temporal resolution), where the time interval between the two frames increased incrementally from 100 to 400 μ s from 70% stenosis to the normal

model. For volumetric acquisitions, the phantom was scanned with elevation increments of 0.5 mm covering the lumen volume in 15 planes of measurement.

PIV data processing was performed using *LaVision DaVis 7.2* software. Two-dimensional three-component (2D-3C) velocity vector maps were generated using the fast-Fourier-transform based cross-correlation algorithm, implemented with a multi-pass technique with an adaptive decreasing interrogation-window size; the window size ranged from 64 x 64 pixels down to 16 x 16 pixels in the last three passes, and a 50% overlap was used for all passes. Calibrated images had a scaling factor of $\sim 38 \mu\text{m}$ per pixel resulting in a velocity vector map with a grid resolution of $0.3022 \pm 0.0068 \text{ mm}$ (across all 8 phantoms). Velocity vector maps were post-processed once with a 3x3-smoothing kernel.

4.2.3 Turbulence intensity (TI) estimation

Flow in the stenosed carotid artery cannot generally be considered fully turbulent and can more accurately be described as unsteady or transitional, with the onset of turbulence for in moderate to severe stenosis (Chapter 1). However, for brevity, we refer to disturbed flow behavior as turbulent and quantify it using the metric turbulence intensity (TI) based on an ensemble-averaging method. For each time point of the cardiac cycle, t , the total estimate of TI ($TI_{tot}(t)$) was defined as follows:

$$TI_{tot}(t) = \sqrt{(TI_x(t))^2 + (TI_y(t))^2 + (TI_z(t))^2} \quad (4.1)$$

$$TI_i(t) = \sqrt{\frac{\sum_{n=1}^N v'_i(t, n) \cdot v'_i(t, n)}{N-1}}, \quad \begin{pmatrix} v'_i(t, n) = v_i(t, n) - V_i(t) \\ V_i(t) = \frac{1}{N} \sum_{n=0}^{N-1} v_i(t + nT) \end{pmatrix}, \quad i = \{x, y, z\}$$

where v' is the velocity fluctuation and V is the phase-averaged (ensemble-averaged) velocity derived for each component ($v_x, v_y, v_z \equiv u, v, w$) of velocity vector. The phase average is the average over the ensemble of data points – herein number of cardiac cycles (N) – having the same phase of the pulse over the period of T (920 ms). The phase-

averaged flow represents the coherent (i.e. deterministic) part of the flow and any deviation (i.e. fluctuation) from it can be associated with the turbulent (incoherent) characteristics. This type of flow decomposition was originally suggested by Reynolds and Hussain [31] and was later applied by Khalifa and Giddens [32] in the context of pulsatile arterial flows. In the current study, the phase correlation of cardiac cycles necessary for such treatment was facilitated through synchronized data acquisition triggered by the flow-pump signal. Based on a priori statistical convergence test, described in the following section, a minimum of $N = 15$ cardiac cycles was applied for TI estimation.

An uncertainty estimation for the velocities has been attempted using the recent method proposed by Timmins *et al.* [33], which they applied later for uncertainty-propagation estimation in statistical-based values of velocity mean and fluctuations. These calculations are shown in Appendix C.

A region of interest (ROI) downstream of the ICA stenosis, extending 5.5 mm wall to wall and axially 5 mm, was selected individually for each model, from which a ROI-averaged TI value (ROI – TI) was calculated. To test the sensitivity of the selected ROI, the ROI was shifted upstream and downstream by 50% of the ROI length, in 25% increments, resulting in a total of five repositioned ROIs used to calculate the mean of ROI – TI, herein referred to as $\overline{\text{ROI-TI}}$. For the volumetric ROI, this 2-D ROI was extended vertically to the off-center planes while excluding regions outside the lumen. Statistical evaluation was performed using a one-way analysis of variance (ANOVA) test with Bonferroni multiple-comparison post-hoc analysis (with $p < 0.05$ denoting significant difference). For the two cases of matched observations (i.e. central-plane versus volumetric ROI, and sequential versus non-sequential cardiac cycles), a two-way ANOVA test with Bonferroni multiple-comparison post-hoc analysis (with $p < 0.05$ denoting significant difference) was applied.

4.2.4 Convergence test for TI estimation

A statistical convergence test based on incrementally increasing subset of samples (i.e. number of cardiac cycles) was performed in order to determine the minimum required

number of samples yielding a converged TI value. The effect of cardiac-cycle sequentially and ROI size in the minimum required samples was also examined. Thirty sequential cardiac cycles of data were collected (in the 50% concentric model), and for statistical evaluation, the same acquisition was repeated six times. From these, six sets of 30 non-sequential iterations were created by mixing cardiac cycles. TI maps were generated using a minimum of $N = 3$ cardiac cycles up to a maximum of $N = 30$. To investigate the effect of ROI size, two ROI sizes were tested: $1.2 \times 1.2 \text{ mm}^2$ (similar to a single Doppler ultrasound sample volume, incorporating approximately 16 velocity vectors) and $5 \times 5.5 \text{ mm}^2$ (wall-to-wall ROI, ~ 270 velocity vectors). Maximum ROI-averaged TI values were derived by averaging over the 30-ms window of the systolic deceleration phase.

Figure 4.2 shows the maximum ROI – TI values from the 50% concentric model during systolic deceleration as a function of the number of cardiac-cycle iterations using the two ROIs. Error bars represent the standard deviation (SD) from the mean of six repeated measurements. No significant difference was seen across the 10 ROI – TI values from the smaller ROI for either series (sequential and non-sequential), nor any significant difference between corresponding TI pairs in the sequential versus non-sequential series. The larger ROI resulted in lower estimates of TI, due to averaging over a larger area, and smaller SD, due to smaller variability in the averaged TI. In overall, statistical analysis indicated that three cardiac-cycle iterations compared to higher iterations resulted in significantly lower TI values in both the sequential and non-sequential series for the larger ROI. Based on the post-hoc analysis, a minimum of six non-sequential iterations and 15 sequential iterations suffice for the convergence TI estimation when using a larger ROI. No significant difference was found between corresponding TI pairs in the sequential versus non-sequential series, except for the group of 6 iterations. Therefore, subsequent TI maps were generated using 15 sequential iterations. It is also worth noting, for the larger ROI, longitudinal expansion from 5 to 10 mm did not result in a different required number of cardiac-cycle iterations (results not shown).

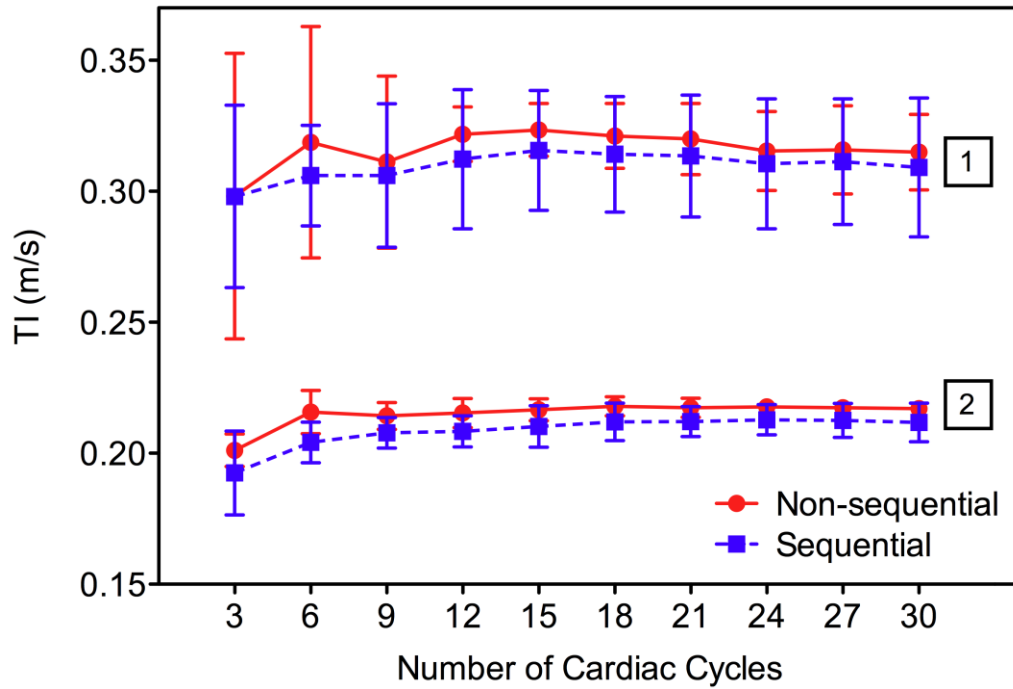


Figure 4.2: Dependency of turbulence intensity on the size of the ROI and on the number and sequencing of cardiac cycles incorporated in the ensemble averaging. Values are mean \pm SD based on 6 repeated measures of each TI map using a fixed ROI of $1.2 \times 1.2 \text{ mm}^2$ (upper set of lines, 1) or $5 \times 5.5 \text{ mm}^2$ (lower set of lines, 2) during systolic deceleration.

4.3 Results

4.3.1 Combined effect of stenosis severity and eccentricity on turbulence intensity

Figure 4.3 shows the flow patterns in the 50% stenosed models with concentric and eccentric plaque symmetry representing velocity magnitude at peak systole formed by averaging over 15 cardiac cycles. In both the eccentric and concentric models, flow in the ECA was well organized. In the concentric model (Figure 4.3a and Figure 4.3d), the ICA jet flowed along and detached from the outer wall, while in the eccentric model it crossed from the inner wall, impinging on the outer wall and detached downstream. This crossing pattern of the jet in the eccentric model generated two recirculation zones on either side

of the jet with the one adjacent to the outer wall being notably larger. In the concentric model and in the region located between the jet and the inner wall, a helical swirling motion (both above and below the central plane) was observed, as demonstrated by the volumetric streamlines (Figure 4.3d), as well as a counter-rotating pair of Dean-type vortices seen in the cross-sectional slice (Figure 4.3a). This pattern continued distally until flow relaminarized. Reversed flow also was detected along the inner wall of the ICA.

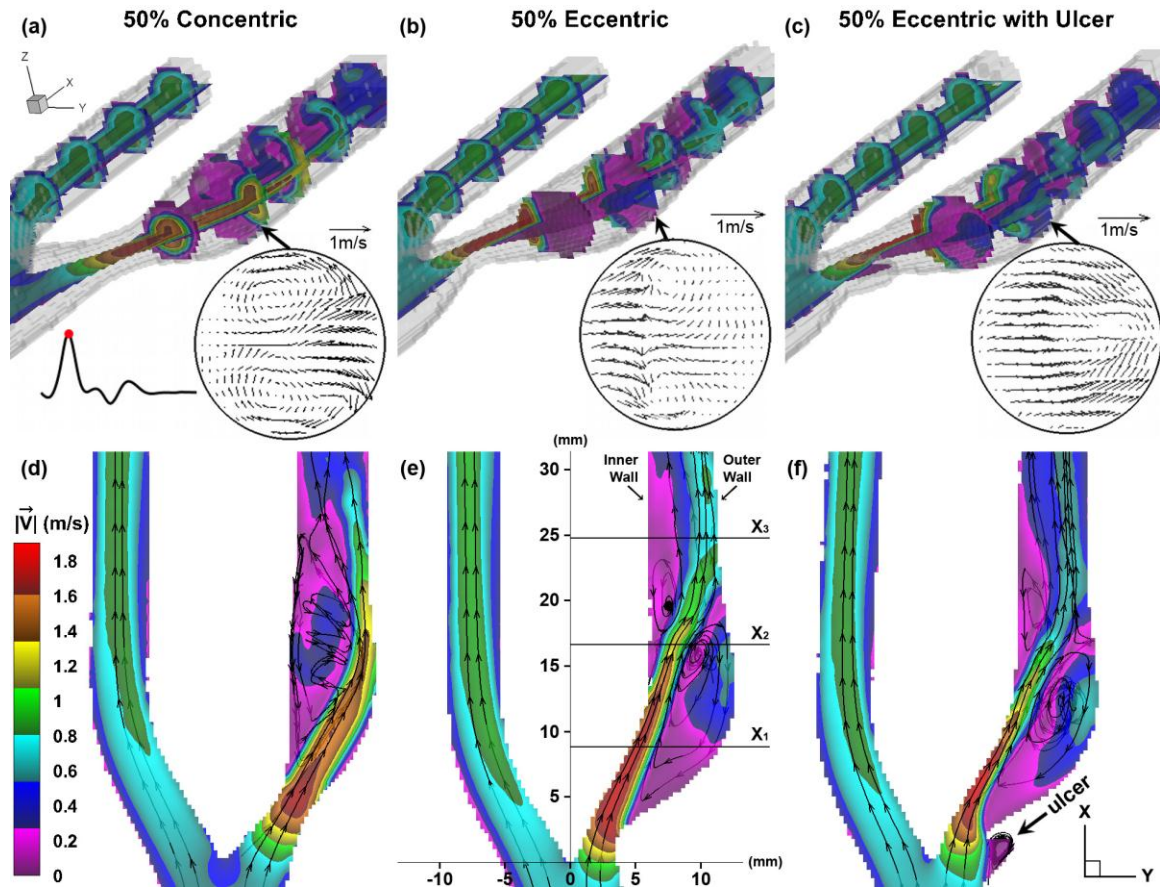


Figure 4.3: Flow pattern visualization at peak systole in carotid models with 50% concentric stenosis (a, d), 50% eccentric stenosis (b, e), and 50% eccentric stenosis with ulceration (c, f). Color-coded, central-plane, ensemble-averaged velocity maps (generated using 15 cardiac cycles) with imposed cross-sectional slices (set 6 mm apart) are shown in the top row (a-c) along with a vector map of the cross-sectional slice at 13 mm distal to the bifurcation apex (slice indicated by the arrow). Central-plane ensemble-averaged velocity maps, superimposed with sparse volumetric streamlines, are shown in the bottom row (d-f).

Figure 4.4, Figure 4.5, and Figure 4.6 show the velocity profiles of three examined in 50% stenosed models with concentric, non-ulcerated eccentric, and ulcerated eccentric plaque respectively. The remaining five models can be found in Appendix D. Mean and fluctuation (standard deviation, shown as error bars) of the three velocity components were extracted at three lateral lines in the ICA (indicated as X_1 to X_3 in Figure 4.3e) at five selected time points based on 15 cardiac cycles. For the 50% concentric model (Figure 4.4), at the most distal location X_3 , fluctuations (represented by error bars, with contribution from all three components) increased starting from peak systole and throughout the systolic deceleration phase. In the eccentric models (Figure 4.5 and Figure 4.6), during systole and systolic deceleration, a high level of fluctuation was observed for the middle (X_2) and downstream (X_3) profiles. In all three models, the velocity profile located most proximally to the apex (X_1) shows the lowest fluctuations compared to the other two locations for all three components at all five time points.

Figure 4.7 shows the TI map of the central-plane ICA branch for each of the eight models for the time point of maximum $\overline{ROI - TI}$ – simply referred to as $\overline{ROI - TI}_{Max}$. For each of the seven stenosed models, this time point of maximum was found during systolic deceleration phase (as denoted on the reference waveform on the bottom corner). For the normal model, however, the time point of maximum occurred at a different phase, thus an individual reference waveform depicting this time point is shown. TI values in the ECA (not shown) were similar for all models and never exceeded 0.05 m/s. The symmetry of the flow disturbance about the central plane is evident in the cross-sectional slices. The maximum TI value in the normal model was about 0.1 m/s, which occurred in the ICA bulb during recirculation in the deceleration phases. In general, TI values were more elevated in the eccentric models compared to their concentric counterparts, ranging from a maximum of 0.2 m/s in the 30% concentric to 0.8 m/s in the 70% eccentric model. Two marked distinctions can be noted between the concentric-eccentric pairs: in the concentric models, flow disturbance starts further downstream, and the elevated-TI region is mainly bounded by the outer wall of the ICA. Conversely, in the eccentric models, the elevated-TI region expands from the inner wall across the center of the lumen.

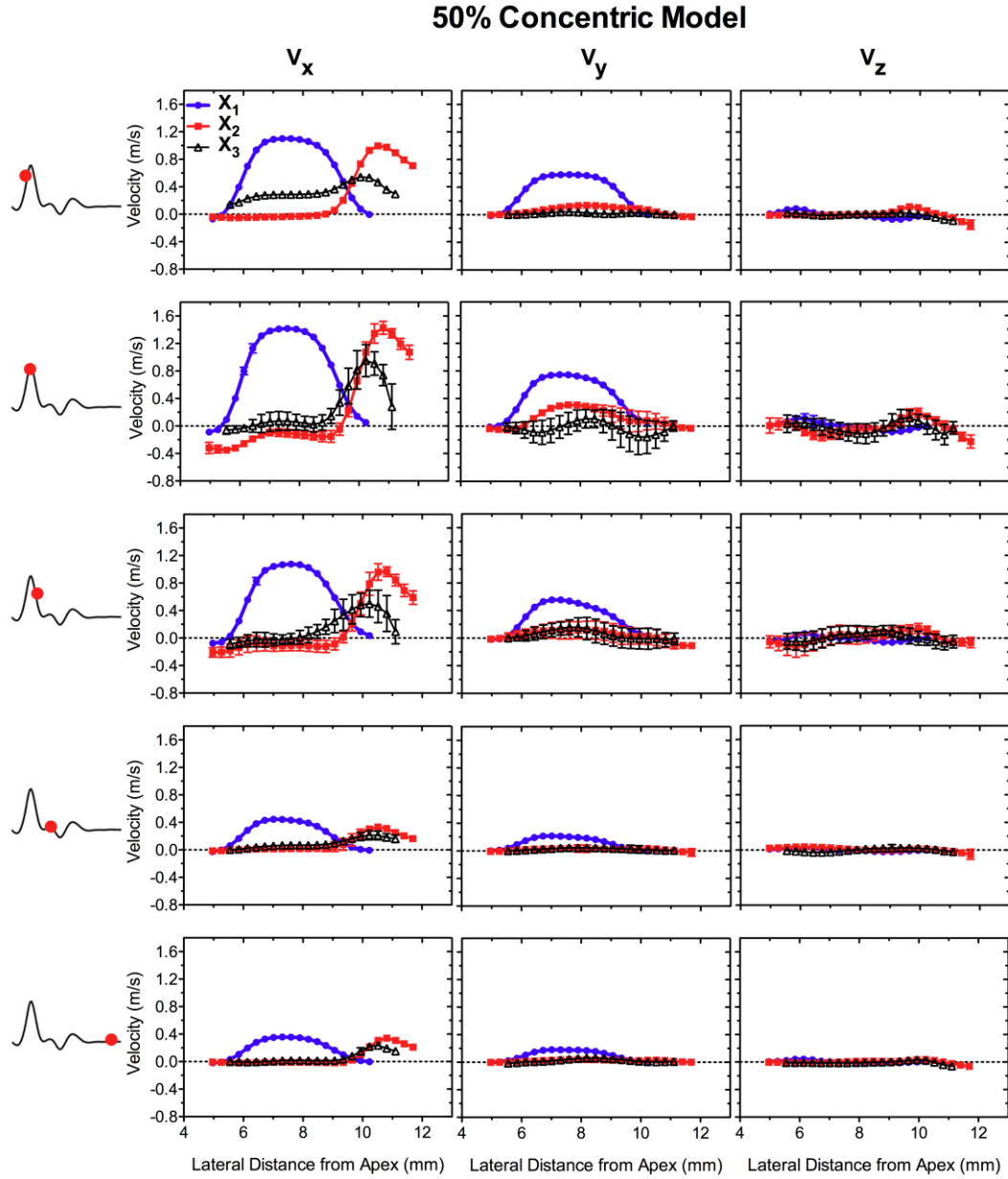


Figure 4.4: Profiles of velocity components (left to right V_x , V_y , and V_z) from 50% concentric stenosed carotid model. Values are mean \pm SD calculated based on 15 cardiac cycles and were extracted along three lateral lines (X_1 , X_2 , and X_3 shown in Figure 4.3e) located in the ICA at approximately 1, 2, and 3 CCA diameters, respectively, downstream from the bifurcation apex. The five time points (from top to bottom) correspond to 30 ms prior to peak systole, peak systole, and 40, 150, and 670 ms post peak systole.

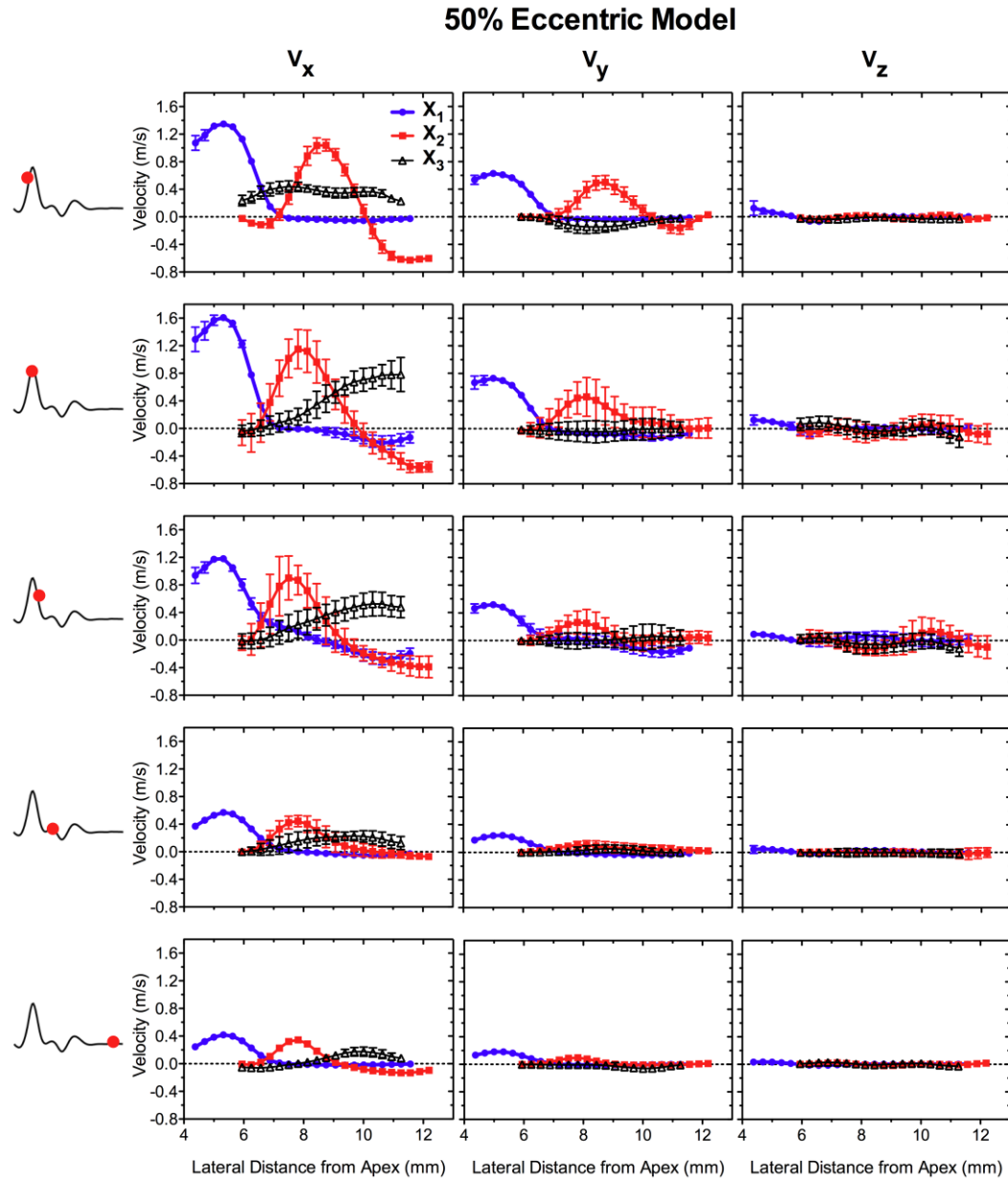


Figure 4.5: Profiles of velocity components (left to right V_x , V_y , and V_z) from 50% eccentric stenosed carotid model. Values are mean \pm SD calculated based on 15 cardiac cycles and were extracted along three lateral lines (X_1 , X_2 , and X_3 shown in Figure 4.3e) located in the ICA at approximately 1, 2, and 3 CCA diameters, respectively, downstream from the bifurcation apex. The five time points (from top to bottom) correspond to 30 ms prior to peak systole, peak systole, and 40, 150, and 670 ms post peak systole.

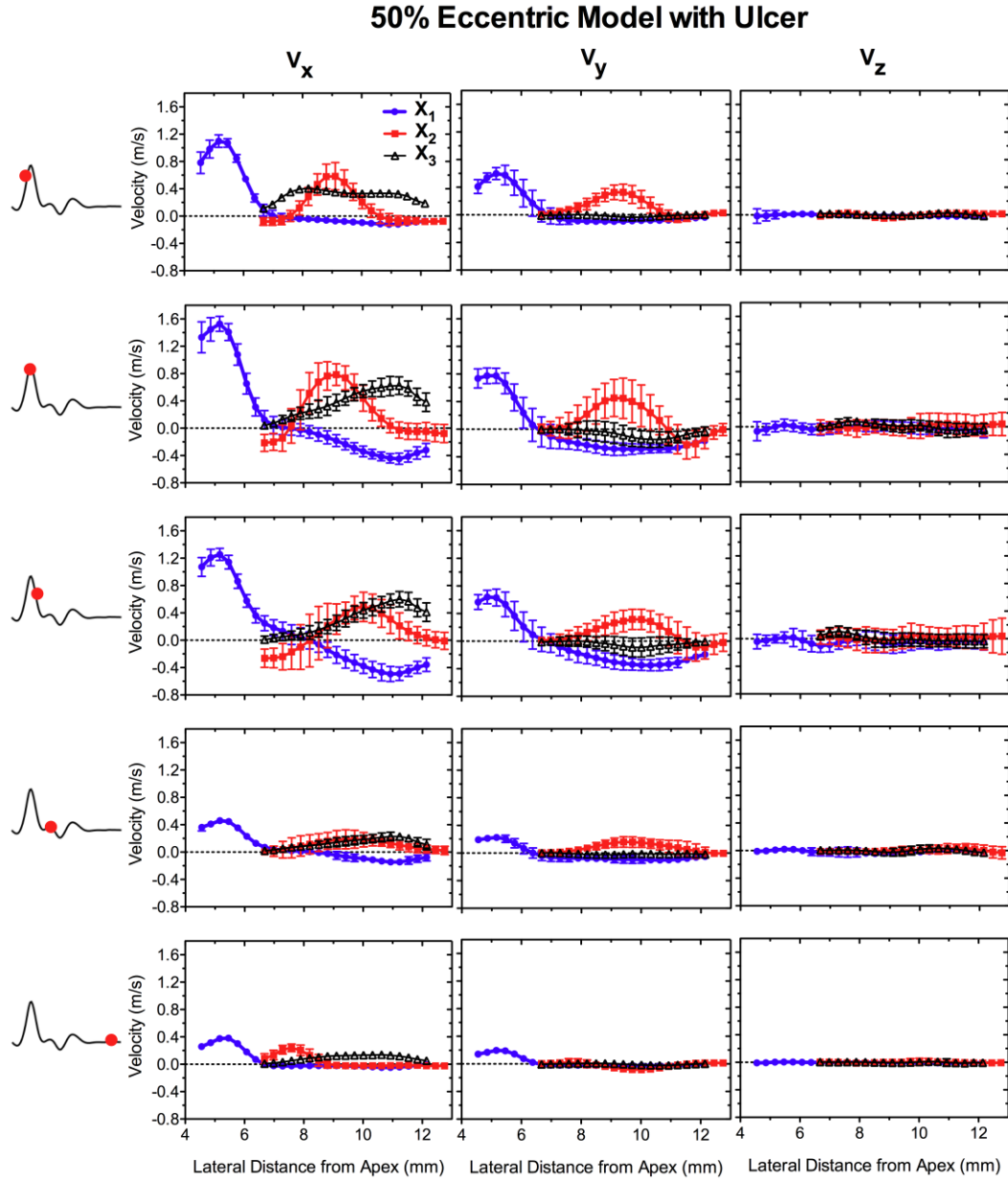


Figure 4.6: Profiles of velocity components (left to right V_x , V_y , and V_z) from 50% ulcerated eccentric model. Values are mean \pm SD calculated based on 15 cardiac cycles and were extracted along three lateral lines (X_1 , X_2 , and X_3 shown in Figure 4.3e) located in the ICA at approximately 1, 2, and 3 CCA diameters, respectively, downstream from the bifurcation apex. The five time points (from top to bottom) correspond to 30 ms prior to peak systole, peak systole, and 40, 150, and 670 ms post peak systole.

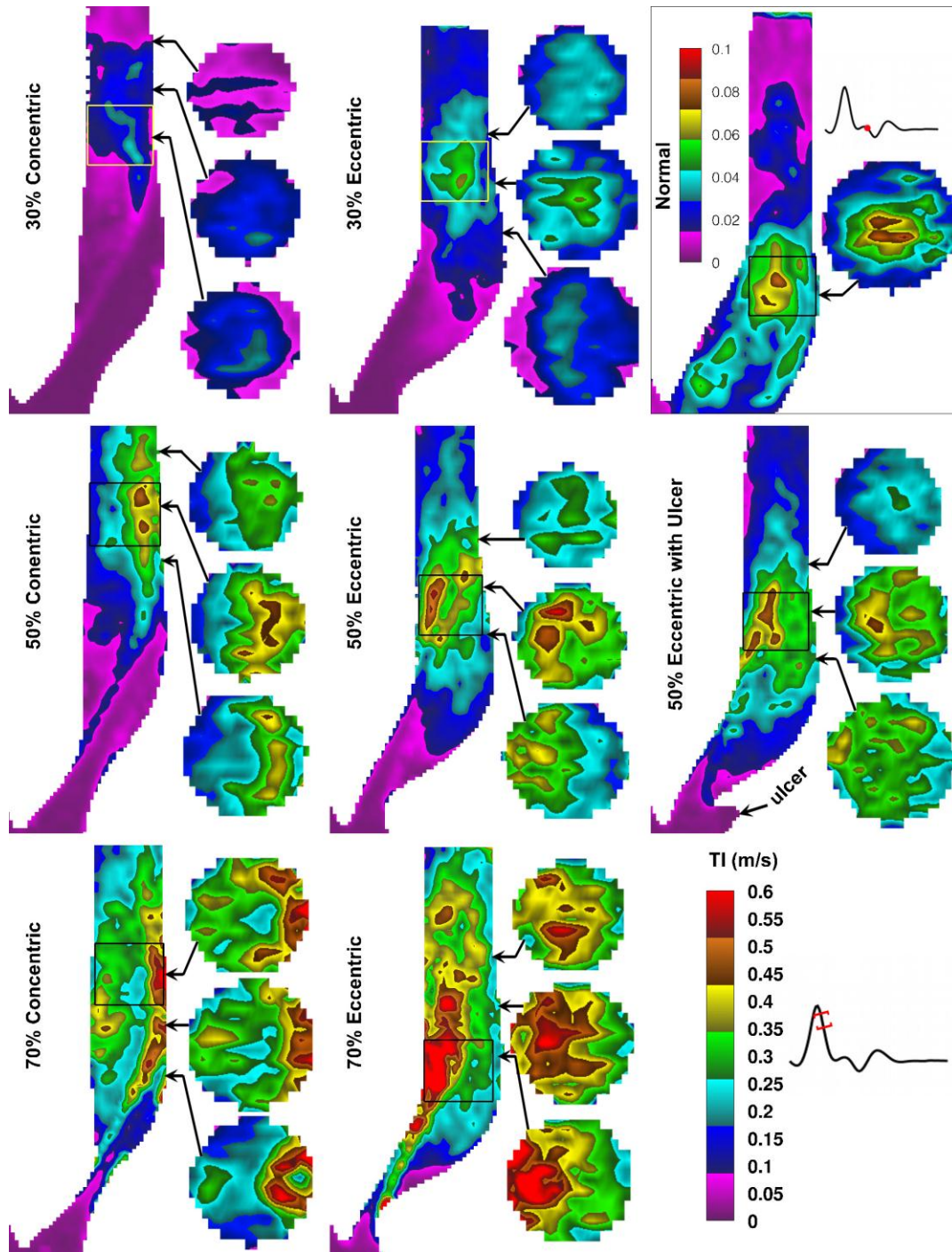


Figure 4.7: Turbulence intensity maps in the ICA of all 8 models at the time point of $\text{ROI-TI}_{\text{Max}}$ in the cardiac cycle. Cross-sectional slices are shown for the 3 specified locations set 4 mm apart. Boxed area shows the selected ROI, from which an additional 4 shifted ROIs were generated for calculation of ROI-TI. For the normal model, shown in the top right enclosure, a later time point and a color bar with smaller dynamic range were applied.

Figure 4.8 illustrates the cardiac-cycle evolution of TI based on the mean value of five repositioned ROIs (i.e. $\overline{\text{ROI} - \text{TI}}$) extracted from the central plane. The shaded area shows a scaled flow-rate waveform measured at the inlet of the CCA. It can be observed that for all of the stenosed models, the $\overline{\text{ROI} - \text{TI}}_{\text{Max}}$ occurs during systolic flow deceleration, varying slightly in time from 10 to 30 ms following peak systole (i.e. between 190-210 ms). The normal model, as expected, had the lowest values for which the maximum occurred later during a second deceleration phase, at 340 ms. In general, all models showed a rapid increase to $\overline{\text{ROI} - \text{TI}}_{\text{Max}}$ with a subsequent slower decay. Comparison between models showed an increase in TI with increasing stenosis severity at nearly all time points, which is also reflected in the cardiac-cycle averaged values shown in Table 4.1. It is interesting to note that statistical evaluation showed no significant difference ($p > 0.05$) between the cycle-averaged values for the pairs of 30% eccentric and 50% concentric, and 50% eccentric (both ulcerated and non-ulcerated) and 70% concentric.

Figure 4.9 shows a comparison of $\overline{\text{ROI} - \text{TI}}_{\text{Max}}$ values extracted using either a central-plane or volumetric ROI. In both the central-plane and volumetric cases, values were higher in an eccentric model compared to its concentric counterpart and increased as the degree of stenosis severity increased. Statistical evaluation (using five repositioned ROI - TI values) of the central-plane values revealed that all the pairs were significantly different ($p < 0.05$) except for the pairing of 50% eccentric (both ulcerated and non-ulcerated) with 70% concentric models. The $\overline{\text{ROI} - \text{TI}}_{\text{Max}}$ values extracted volumetrically showed a similar pattern as for the central plane; pairwise comparison between central-plane and matching volumetric values showed no significant difference except for the 70% eccentric model ($p < 0.001$).

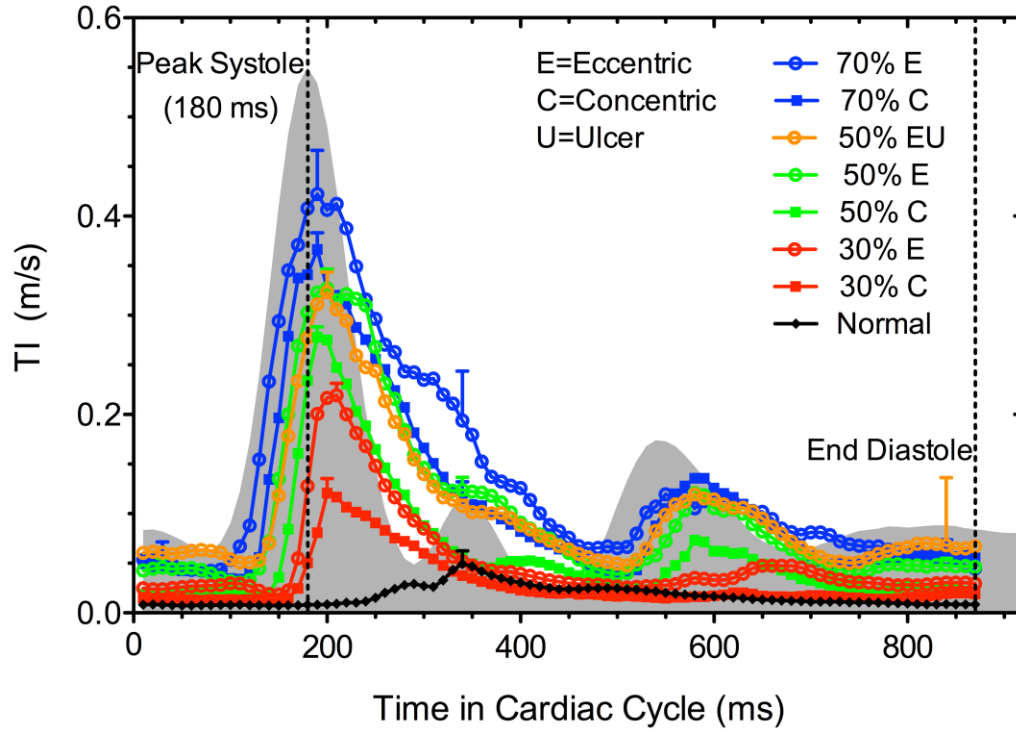


Figure 4.8: Cardiac-cycle evolution of turbulence intensity for all 8 carotid models. Values are $\overline{\text{ROI} - \text{TI}}$ calculated based on five repositioned $5 \times 5.5\text{-mm}^2$ ROIs extracted from ensemble-averaged central-plane TI map generated using an ensemble of 15 sequential cardiac cycles. Error bars represent SD shown, for clarity, in one direction and for selected time points (30 ms, time point of $\overline{\text{ROI} - \text{TI}}_{\text{Max}}$, 340 ms, and 840 ms) during the cardiac cycle. For cardiac-cycle phase reference, a scaled profile of the measured CCA flow-rate waveform is shown as the grey-shaded background.

Table 4.1: Cycle-averaged turbulence intensity (m/s). Values from all 8 models are given as mean \pm SD of ROI-TI averaged over the 87 cardiac-cycle time points shown in Figure 4.8.

Plaque	30% Stenosis	50% Stenosis		70% Stenosis	Normal
Concentric	0.029 ± 0.026	0.061 ± 0.061		0.109 ± 0.086	0.017± 0.010
Eccentric	0.052 ± 0.047	Non-ulcerated	Ulcerated	0.136 ± 0.105	
		0.101± 0.082	0.104 ± 0.069		

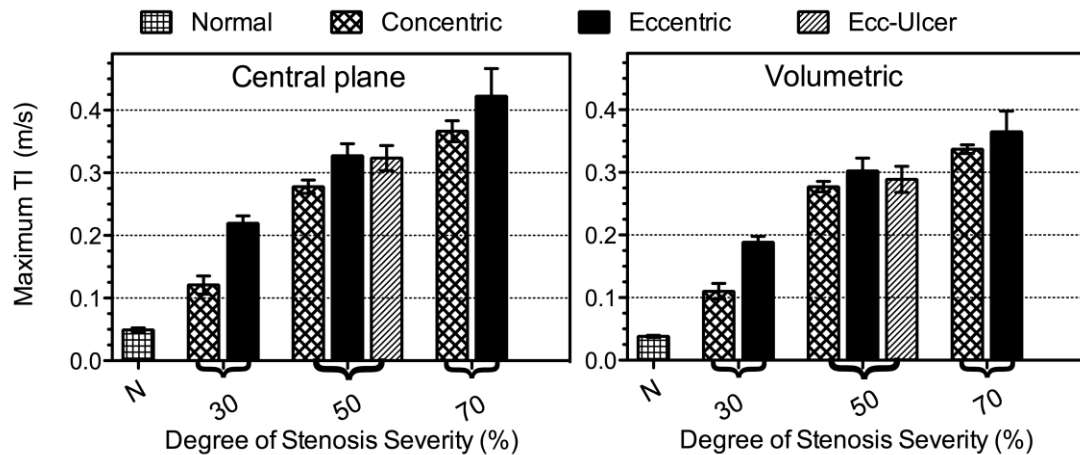


Figure 4.9: Maximum TI as a function of stenosis severity obtained from the central-plane (left) and volumetric (right) ROI. Values are mean \pm SD of ROI-TI calculated based on five repositioned $5 \times 5.5\text{-mm}^2$ ROIs. The time points of maximum were selected based on the central-plane ROI-TI values for each model (Figure 4.8) and carried over for volumetric values.

4.3.2 Effect of ulceration on turbulence intensity

The 50% ulcerated and non-ulcerated eccentric models demonstrated a similar governing pattern of the flow – crossing of the jet from the inner wall to the outer wall generating two distinct recirculation regions on either side (compare Figure 4.3e and Figure 4.3f). However, in the ulcerated model, a slightly narrower and higher velocity jet was observed, which also dissipated more quickly, thus resulting in a larger and more proximal recirculation zone. In the ulcer crater, a slow recirculating flow was present with no evidence of turbulence, as TI values did not exceed 0.03 m/s. Between the two models, similar expansions and ranges of downstream elevated TI were found resulting in statistically similar ROI-averaged TI values (Figure 4.8 and Table 4.1). By contrast, previous Doppler ultrasound (DUS) results showed significant increase in ROI-averaged TI values due to ulceration in the same geometries [34]. Thus, for a more sensitive comparison, a separate analysis shown in Figure 4.10 used five individual repeated measures of the central-plane TI map, and again similar values of ROI-TI were observed.

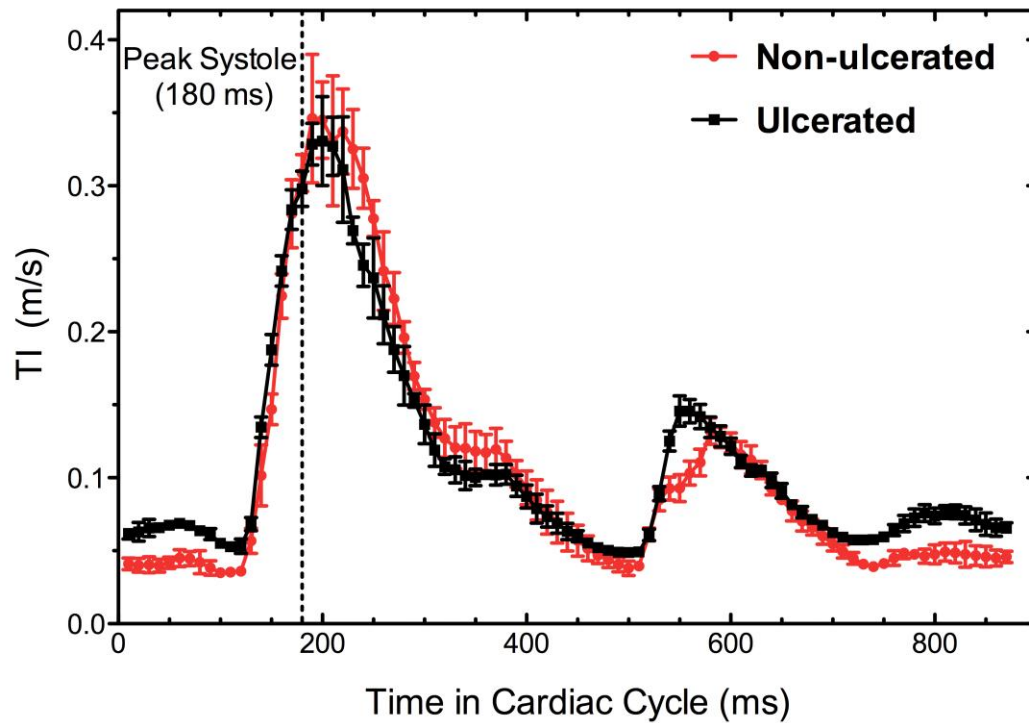


Figure 4.10: Cardiac-cycle evolution of turbulence intensity in the non-ulcerated and ulcerated models with 50% eccentric stenosis. For each model, mean \pm SD values were calculated based on 5 repeated measures of the TI maps each using an ensemble of six non-sequential iterations.

For the single examined ulcerated model, the major effect of ulceration on TI was found to be an expansion of the moderately elevated TI levels more proximal to the apex, as seen in the recirculation region of the TI map (Figure 4.7); this also was evident from comparatively higher velocity fluctuations across the X_1 profile (Figure 4.5 and Figure 4.6) during systolic deceleration. Figure 4.11 shows a histogram of all TI values accumulated over the full 35-mm length of the ICA lumen (starting from the bifurcation apex) and systolic deceleration phase. The ulcerated model shows an apparent increase around TI values of 0.1 m/s in both the central-plane and volumetric cases, reflecting the expanded proximal recirculation zone.

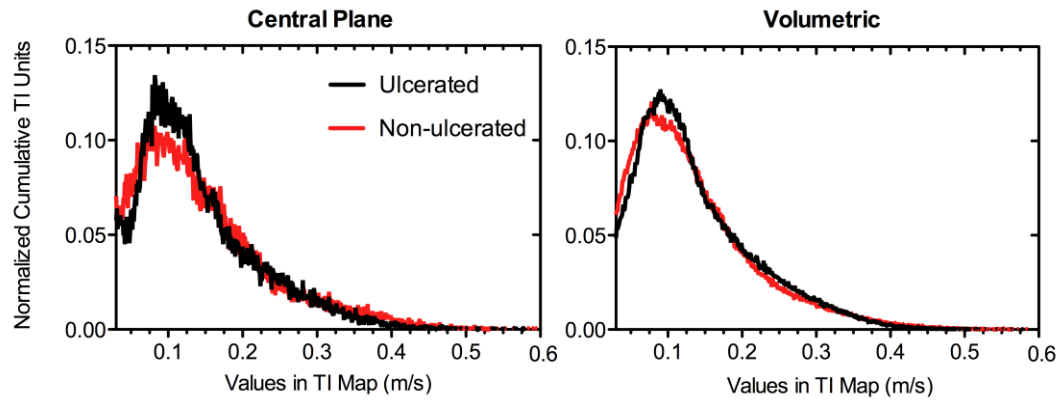


Figure 4.11: Distribution of values in the central-plane (left) and volumetric (right) TI maps for the ulcerated and non-ulcerated carotid models with 50% eccentric stenosis. For a specific TI value, the vertical axis corresponds to the total number of units in each TI map of the ICA branch and accumulated over the systolic deceleration phase (180-340 ms). For each model, the temporally and spatially accumulated TI units were normalized by the total number of non-zero units in the central-plane or volumetric TI map.

4.4 Discussion

The presented study demonstrated that eccentric plaque build-up (as opposed to concentric) resulted in an enhancement of the flow disturbances effected with increasing stenosis severity, where plaque eccentricity resulted in an increase in TI bringing it on par to the level found in the concentric plaque of the next higher category of stenosis severity (Figure 4.8, Figure 4.9, and Table 4.1). Varghese *et al.* [35] reported a similar observation where introducing as low as 5% eccentricity resulted in localized transition to turbulence in a 75% (i.e. 50% diameter reduction) stenotic tube under pulsatile flow. These results suggest that eccentricity independently affects the level of flow instability. While carotid endarterectomy is prescribed currently based on the degree of stenosis severity, this finding has potential clinical implications suggesting an additional categorization based on the factor of plaque eccentricity. Overall, volumetrically derived $\overline{ROI - TI}_{Max}$ values were not significantly different from those calculated from only the central plane, suggesting that central-plane metrics are sufficiently representative.

Assessment of TI as a function of the cardiac cycle (Figure 4.8) showed the greatest increase in TI in the systolic deceleration phase, which agrees with previous studies [36]. For both plaque symmetries, higher velocity fluctuations during this phase are attributed to the increased complexity and instability of the flow; the jet flow exhibits a flickering motion at its detachment points, recirculation zones break down into smaller vortices, and helical swirling motion in the concentric models becomes disordered. In both concentric and eccentric models, low turbulence levels were observed proximal to the apex (up to 1 CCA diameter) when compared to the downstream region (Figure 4.4 and Figure 4.5). In the concentric models turbulence started to peak beyond 2 CCA diameters. This is consistent with the work by Karri and Vlachos [37] who reported peak fluctuations occurring from 2-4 inlet diameters in the symmetric stenoses.

Compared to eccentric models, the elevated-TI region was found located further downstream in the concentric counterpart (Figure 4.7). This observation can be explained by the comparing the location of the downstream-jet detachment which, in turn, governs the location of peak turbulence; in each concentric model, the downstream point of jet detachment is located further downstream compared to the eccentric counterpart in which the downstream jet detachment occurs at the inner wall followed by the jet crossing to the outer wall.

Through examination of a 50% eccentrically stenosed model with plaque ulceration, the ulceration was found to contribute a proximal shift and expansion of the outer-wall recirculation zone (Figure 4.7) leading to an increased occurrence of moderate TI (~ 0.1 m/s) values (Figure 4.11). Previous DUS measurements also showed elevated TI (~ 0.2 - 0.3 m/s), which peaked in the area corresponding to the expanded outer-wall recirculation zone, leading to higher ROI-averaged TI in the ulcerated models compared to their non-ulcerated counterparts [34]. However, the highly elevated TI (>0.5 m/s) in the downstream ICA (~ 13 mm distal to apex) that was captured here using PIV does not appear to have been fully resolved and captured using DUS, likely due to the limitations in spatial and temporal resolution.

The ensemble-averaging method for turbulence quantification is a conventional method for repetitive pulsatile conditions [32], and previous studies have demonstrated its feasibility for *in vivo* applications [38, 39]. The method requires cyclic phase synchronization, such as the pump synchronization signal used here or an electrocardiogram (ECG) signal for clinical applications. Alternative methods of turbulence measurements in which cycle synchronization is not necessary have also been introduced previously [40-42].

Possible limitations of the present work include the simplicity of the examined models and the Newtonian blood-mimicking fluid. The carotid models use here incorporate idealized, planar-symmetric geometries and do not include vessel tortuosity and physiological compliance. However, the matched pairs and stenosis progression are ideally suited for controlled studies including the present objective of assessing geometrical variables of the plaque. The use of a Newtonian blood-mimicking fluid is typical given that blood in the larger arteries is typically considered to show Newtonian behavior [43]. Some studies have reported a significant difference by using a non-Newtonian model of blood [44]; in contrast, other studies have shown only minor variations [45].

In addition to the clinical implications, this work may provide a validation platform for numerical simulation methods including turbulent models [46, 47]. With recent capabilities in simulating transitional flow, more detailed features of the post-stenotic flow are achievable, as demonstrated in patient-specific stenosed models using direct numerical simulation, which have been able to capture the vortex shedding along the jet and helical Dean-type vortices [48, 49].

4.5 Conclusion

To our knowledge, the present work is the first experimental study of its kind conducted in a comprehensive series of carotid artery models. This work demonstrates the collective effects of stenosis severity, eccentricity and ulceration for increasing flow disturbances as quantified using turbulence intensity, which has potential clinical significance. However, the results indicate that improvements in DUS spatial and temporal resolution may be

necessary to capture the smaller scale flow disturbances. Current advancements in DUS, using parallel acquisition and processing of pre-beamformed acquired data, will enable higher temporal resolution (in the kilohertz range) for more detailed velocity maps and reduce discrete sample volume limitations [50].

4.6 References

- [1] C. Warlow, C. Sudlow, M. Dennis, *et al.* (2003), Stroke. *Lancet*, vol. 362, pp. 1211-1224.
- [2] W. S. Nesbitt, P. Mangin, H. H. Salem, *et al.* (2006), The impact of blood rheology on the molecular and cellular events underlying arterial thrombosis. *Journal of Molecular Medicine*, vol. 84, pp. 989-995.
- [3] R. L. Smith, P. D. Stein, J. Coalson, *et al.* (1972), Thrombus production by turbulence. *Journal of Applied Physiology*, vol. 32, pp. 261-264.
- [4] P. D. Stein and H. N. Sabbah (1974), Measured turbulence and its effect on thrombus formation. *Circulation Research*, vol. 35, pp. 608-614.
- [5] P. D. Stein and H. N. Sabbah (1980), Hemorheology of turbulence. *Biorheology*, vol. 17, pp. 301-319.
- [6] C. A. Skilbeck, P. G. Walker, T. David, *et al.* (2004), Disturbed flow promotes deposition of leucocytes from flowing whole blood in a model of a damaged vessel wall. *British Journal of Haematology*, vol. 126, pp. 418-427.
- [7] D. Bluestein, C. Gutierrez, M. Londono, *et al.* (1999), Vortex shedding in steady flow through a model of an arterial stenosis and its relevance to mural platelet deposition. *Annals of Biomedical Engineering*, vol. 27, pp. 763-73.
- [8] J. Vermynen, M. Verstraete, and V. Fuster (1986), Role of platelet activation and fibrin formation in thrombogenesis. *Journal of the American College of Cardiology*, vol. 8, pp. B2-B9.
- [9] E. Falk (1985), Unstable angina with fatal outcome - dynamic coronary thrombosis leading to infarction and or sudden-death - autopsy evidence of recurrent mural thrombosis with peripheral embolization culminating in total vascular occlusion. *Circulation*, vol. 71, pp. 699-708.
- [10] R. Virmani, E. R. Ladich, A. P. Burke, *et al.* (2006), Histopathology of carotid atherosclerotic disease. *Neurosurgery*, vol. 59, p. S219.

- [11] L. Antiga and D. A. Steinman (2009), Rethinking turbulence in blood. *Biorheology*, vol. 46, pp. 77-81.
- [12] S. P. Jackson, W. S. Nesbitt, and E. Westein (2009), Dynamics of platelet thrombus formation. *Journal of Thrombosis and Haemostasis*, vol. 7, pp. 17-20.
- [13] T. G. Brott, J. L. Halperin, and S. Abbara (2011), Guideline on the management of patients with extracranial carotid and vertebral artery disease: Executive summary. *Journal of Neurointerventional Surgery*, vol. 3, pp. 245-245.
- [14] North american symptomatic carotid endarterectomy trial (NASCET) investigators. (1991). Benefit of carotid endarterectomy for patients with high-grade stenosis of the internal carotid artery, *Stroke*, vol. 22, pp. 816-7.
- [15] European Carotid Surgery Trialists' (ECST) Collaborative Group (1998), Randomised trial of endarterectomy for recently symptomatic carotid stenosis: Final results of the MRC European Carotid Surgery Trial (ECST). *Lancet*, vol. 351, pp. 1379-1387.
- [16] T. Ohara, K. Toyoda, R. Otsubo, *et al.* (2008), Eccentric stenosis of the carotid artery associated with ipsilateral cerebrovascular events. *American Journal of Neuroradiology*, vol. 29, pp. 1200-1203.
- [17] F. Li, M. M. McDermott, D. Li, *et al.* (2010), The association of lesion eccentricity with plaque morphology and components in the superficial femoral artery: A high-spatial-resolution, multi-contrast weighted cmr study. *Journal of Cardiovascular Magnetic Resonance*, vol. 12,
- [18] D. L. Tang, C. Yang, S. Kobayasi, *et al.* (2003), Effect of stenosis asymmetry on blood flow and artery compression: A three-dimensional fluid-structure interaction model. *Annals of Biomedical Engineering*, vol. 31, pp. 1182-1193.
- [19] Q. Long, X. Y. Xu, K. V. Ramnarine, *et al.* (2001), Numerical investigation of physiologically realistic pulsatile flow through arterial stenosis. *Journal of Biomechanics*, vol. 34, pp. 1229-1242.
- [20] M. Sitzter, M. Siebler, G. Rose, *et al.* (1995), Cerebral microembolism in atherosclerotic carotid artery disease: Facts and perspectives. *Functional Neurology*, vol. 10, pp. 251-258.
- [21] M. Fisher, A. Paganini-Hill, A. Martin, *et al.* (2005), Carotid plaque pathology - thrombosis, ulceration, and stroke pathogenesis. *Stroke*, vol. 36, pp. 253-257.
- [22] E. Y. Wong, H. N. Nikolov, M. L. Thorne, *et al.* (2009), Clinical Doppler ultrasound for the assessment of plaque ulceration in the stenosed carotid bifurcation by detection of distal turbulence intensity: A matched model study. *European Radiology*, vol. 19, pp. 2739-49.

- [23] L. G. Spagnoli, A. Mauriello, G. Sangiorgi, *et al.* (2004), Extracranial thrombotically active carotid plaque as a risk factor for ischemic stroke. *Jama-Journal of the American Medical Association*, vol. 292, pp. 1845-1852.
- [24] R. F. Smith, B. K. Rutt, A. J. Fox, *et al.* (1996), Geometric characterization of stenosed human carotid arteries. *Academic Radiology*, vol. 3, pp. 898-911.
- [25] T. L. Poepping, R. N. Rankin, and D. W. Holdsworth (2010), Flow patterns in carotid bifurcation models using pulsed Doppler ultrasound: Effect of concentric vs. Eccentric stenosis on turbulence and recirculation. *Ultrasound in Medicine and Biology*, vol. 36, pp. 1125-1134.
- [26] R. F. Smith, B. K. Rutt, and D. W. Holdsworth (1999), Anthropomorphic carotid bifurcation phantom for MRI applications. *Journal of Magnetic Resonance Imaging*, vol. 10, pp. 533-44.
- [27] M. Y. Yousif, D. W. Holdsworth, and T. L. Poepping (2011), A blood-mimicking fluid for particle image velocimetry with silicone vascular models. *Experiments in Fluids*, vol. 50, pp. 769-774.
- [28] D. W. Holdsworth, D. W. Rickey, M. Drangova, *et al.* (1991), Computer-controlled positive displacement pump for physiological flow simulation. *Medical and Biological Engineering and Computing*, vol. 29, pp. 565-70.
- [29] D. W. Holdsworth, C. J. Norley, R. Frayne, *et al.* (1999), Characterization of common carotid artery blood-flow waveforms in normal human subjects. *Physiological Measurement*, vol. 20, pp. 219-40.
- [30] T. L. Poepping, H. N. Nikolov, R. N. Rankin, *et al.* (2002), An in vitro system for Doppler ultrasound flow studies in the stenosed carotid artery bifurcation. *Ultrasound in Medicine and Biology*, vol. 28, pp. 495-506.
- [31] W. C. Reynolds and A. K. M. F. Hussain (1972), The mechanics of an organized wave in turbulent shear flow. Part 3. Theoretical models and comparisons with experiments. *Journal of Fluid Mechanics*, vol. 54, pp. 263-288.
- [32] A. M. Khalifa and D. P. Giddens (1978), Analysis of disorder in pulsatile flows with application to poststenotic blood velocity measurement in dogs. *Journal of Biomechanics*, vol. 11, pp. 129-41.
- [33] B. H. Timmins, B. W. Wilson, B. L. Smith, *et al.* (2012), A method for automatic estimation of instantaneous local uncertainty in particle image velocimetry measurements. *Experiments in Fluids*, vol. 53, pp. 1133-1147.
- [34] E. Y. Wong, H. N. Nikolov, R. N. Rankin, *et al.* (2012), Evaluation of distal turbulence intensity for the detection of both plaque ulceration and stenosis grade in the carotid bifurcation using clinical Doppler ultrasound. *European Radiology*,

- [35] S. S. Varghese, S. H. Frankel, and P. F. Fischer (2007), Direct numerical simulation of stenotic flows. Part 2. Pulsatile flow. *Journal of Fluid Mechanics*, vol. 582, pp. 281-318.
- [36] P. A. J. Bascom, K. W. Johnston, R. S. C. Cobbold, *et al.* (1997), Relation of the flow field distal to a moderate stenosis to the Doppler power. *Ultrasound in Medicine and Biology*, vol. 23, pp. 25-39.
- [37] S. Karri and P. P. Vlachos (2010), Time-resolved DPIV investigation of pulsatile flow in symmetric stenotic arteries effects of phase angle. *Journal of Biomechanical Engineering*, vol. 132,
- [38] M. Casty and D. P. Giddens (1984), 25 + 1 channel pulsed ultrasound Doppler velocity meter for quantitative flow measurements and turbulence analysis. *Ultrasound in Medicine and Biology*, vol. 10, pp. 161-72.
- [39] K. Isaaz, J. F. Bruntz, A. Da Costa, *et al.* (2003), Noninvasive quantitation of blood flow turbulence in patients with aortic valve disease using online digital computer analysis of Doppler velocity data. *Journal of the American Society of Echocardiography*, vol. 16, pp. 965-974.
- [40] M. L. Thorne, R. N. Rankin, D. A. Steinman, *et al.* (2010), In vivo Doppler ultrasound quantification of turbulence intensity using a high-pass frequency filter method. *Ultrasound in Medicine and Biology*, vol. 36, pp. 761-71.
- [41] P. Dyverfeldt, A. Sigfridsson, J.-P. E. Kvitting, *et al.* (2006), Quantification of intravoxel velocity standard deviation and turbulence intensity by generalizing phase-contrast MRI. *Magnetic Resonance in Medicine*, vol. 56, pp. 850-858.
- [42] S. Kefayati and T. L. Poepping (2013), Transitional flow analysis in the carotid artery bifurcation by proper orthogonal decomposition and particle image velocimetry. *Medical Engineering and Physics*, vol. 35, pp. 898-909.
- [43] T. J. Pedley (1980), *The fluid mechanics of large blood vessels*. Cambridge University Press, Cambridge.
- [44] F. J. H. Gijsen, F. N. van de Vosse, and J. D. Janssen (1999), The influence of the non-newtonian properties of blood on the flow in large arteries: Steady flow in a carotid bifurcation model. *Journal of Biomechanics*, vol. 32, pp. 601-608.
- [45] K. Perktold, M. Resch, and H. Florian (1991), Pulsatile non-newtonian flow characteristics in a 3-dimensional human carotid bifurcation model. *ASME Journal of Biomechanical Engineering*, vol. 113, pp. 464-475.
- [46] D. Birchall, A. Zaman, J. Hacker, *et al.* (2006), Analysis of haemodynamic disturbance in the atherosclerotic carotid artery using computational fluid dynamics. *European Radiology*, vol. 16, pp. 1074-1083.

- [47] J. S. Stroud, S. A. Berger, and D. Saloner (2002), Numerical analysis of flow through a severely stenotic carotid artery bifurcation. *Journal of Biomechanical Engineering-Transactions of the ASME*, vol. 124, pp. 9-20.
- [48] L. Grinberg, A. Yakhot, and G. E. Karniadakis (2009), Analyzing transient turbulence in a stenosed carotid artery by proper orthogonal decomposition. *Annals of Biomedical Engineering*, vol. 37, pp. 2200-2217.
- [49] S. E. Lee, S.-W. Lee, P. F. Fischer, *et al.* (2008), Direct numerical simulation of transitional flow in a stenosed carotid bifurcation. *Journal of Biomechanics*, vol. 41, pp. 2551-2561.
- [50] D. H. Evans, J. A. Jensen, and M. B. Nielsen (2011), Ultrasonic colour Doppler imaging. *Interface Focus*, vol. 1, pp. 490-502.

Chapter 5

5 Effects of Plaque Geometry on *In Vitro* Shear Stress Measurements in a Family of Carotid Artery Models Using Particle Image Velocimetry*

5.1 Introduction

The association between shear stress and atherosclerosis-related complications is well established [1, 2]. Early stages of atherogenesis and plaque localization in the carotid artery are associated with regions of low or highly oscillatory wall shear stress (WSS), which affect and change the regular gene expression of the endothelium cells, while initially the regions with moderate to high shear stress are protected. Once stenotic plaque has formed and matured, shear stress forces – now altered due to the change in vessel geometry – play a role in plaque instability [3, 4]; plaque rupture and ulceration have been found to occur more frequently upstream (proximal) to the plaque where the shear stress is highest [5, 6].

Atherosclerotic plaques are particularly predisposed to thrombogenicity, which also can be promoted further by pathological shear stresses. Thrombosis is a complicated multi-step process that, under certain conditions, can occur either at the site of plaque or the vicinity of the vessel wall. Since the late 1970s, abundant investigations have been conducted, mainly under controlled conditions, to identify the underlying mechanism of shear-induced thrombus formation and mobilization. In an intriguing study by Nesbitt *et al.* [7], it was found that pathological WSS at the site of stenosis spatially regulates thrombus growth; when a shear-acceleration zone is followed by a shear-deceleration zone (dubbed shear microgradient [7]), platelet aggregation forms at the post-stenotic expansion zone initiating from the stenosis apex. This mechanism of aggregation – in

* A version of this chapter has been prepared for submission to *PLOS ONE* as an original article entitled “Effects of plaque geometry on *in vitro* shear stress measurements in a family of carotid artery models using particle image velocimetry” by S. Kefayati, J. S. Milner, D. W. Holdsworth, and T. L. Poepping.

which soluble agonists merely play a secondary role – is rheology dependent with platelets only at a low level of activation during the initial stage of aggregation. The intrinsic instability of these post-stenotic aggregates can contribute to thromboembolism and consequent cerebrovascular events [8].

For moderate and severe stenosis, turbulent (Reynolds) shear stress is expected distal to the stenosis throat where the jet flow becomes disturbed and turbulent. Blood components exposed to a higher level of shear stress compared to laminar flow can suffer damage. Under turbulent conditions, due to the high concentration of red blood cells in blood, viscous cell-cell interactions may give rise to increased shear-stress forces on the same order as Reynolds shear stresses [9]. An often-cited threshold of 400 Pa [10] is considered sufficient for lysis of red blood cells (and arguably considered to be an underestimation [11]). Platelets are much more sensitive to shear and their deformation starts at shear stress levels as low as 10-16.5 Pa [12]. It has also been established that shear-induced platelet activation has a cumulative effect, meaning it depends not only on the shear level, but also on the duration of exposure time [13-15]; at higher shear-stress levels, shorter exposure time is required. Turbulent stress levels of 10-100 Pa are considered to trigger platelet activation [16].

Through flow alteration, the dynamics of shear stress will be influenced by local geometrical features of the plaque. Greater stenosis severity, plaque eccentricity (symmetry) and plaque ulceration are among the plaque features that have been associated with more frequent cerebrovascular events based on clinical trials [17-19]. From a hemodynamic perspective, this may be due to an increased level of shear stress, such as due to a more severe stenosis, resulting in an increased probability of plaque rupture and larger growth of unstable thrombi formed at the post-stenotic region. Independent of stenosis severity, plaque eccentricity also can impact the local hemodynamics of the carotid artery. In a previous computational simulation study by Tambasco and Steinman [20], path-dependent hemodynamic factors associated with thrombotic activity were investigated in 30% concentrically and eccentrically stenosed models of a carotid bifurcation with identical geometry to that used in the present work. Using a trajectory scheme, the dynamic path histories of simulated blood elements (e.g.

platelets) were derived, from which the coupled effect of particle transit time and shear stress was obtained. Compared to the concentric model, the eccentric counterpart was found to be suggestive of a higher level of thrombotic activity owing to the larger percentage of particles experiencing maximum shear stress exposure, threshold activation, and mural deposition.

The widely recognized significance of hemodynamic factors of the carotid artery bifurcation with respect to stroke risk has encouraged numerous studies, mainly performed using computational techniques [21-23] with fewer *in vitro* studies [24, 25]. Regardless of the applied technique, the majority of these investigations have been conducted in a single patient-specific or idealized model of the carotid artery, and only a few computational studies have reported the effects due to changes in geometrical features of the stenotic plaques [20, 26, 27]. Assessment of the individual effect of each geometrical feature by performing a pooled comparison across these studies is difficult due to the variation in geometries, modalities, and flow conditions.

The objective of the present work was to conduct a comprehensive matched-model study to assess the shear stress (both laminar and turbulent) affected by three independent geometrical stenosis features (stenosis severity, plaque eccentricity, and plaque ulceration). Flow was characterized experimentally using particle image velocimetry (PIV) in a set of physiologically relevant carotid artery models covering a wide range of disease progression.

5.2 Methods

5.2.1 Experimental set-up

A family of eight carotid artery phantoms was examined consisting of six models with 30%, 50%, and 70% stenosis severity (as defined based on the NASCET criteria) each in either form of two extreme plaque symmetries (concentric or eccentric), as well as a normal (disease-free) model and a 50% eccentrically stenosed plaque incorporating an ulceration. The PIV-compatible life-sized phantoms [28] each incorporated a physiologically relevant geometry [29] based on an 8-mm inner diameter common carotid artery (CCA), 5.5-mm internal carotid artery (ICA), and 4.5-mm external carotid

artery (ECA). The flow loop included a phantom, downstream flow resistors (generating ~60:40 ICA:ECA flow division), and a programmable positive-displacement pump [30] equipped with a synchronization signal thus enabling gated data acquisition. The pump was programmed with an idealized carotid waveform [31] with a maximum flow rate at peak systole of $27.13 (\pm 0.30)$ ml/s and a mean of $6.29 (\pm 0.09)$ ml/s, as measured at the inlet of the CCA (Figure 3.1c). Local maximum and mean Reynolds numbers, respectively, derived from the narrowest diameter of the ICA stenosis were 1162 and 312 in the 30% models, 1627 and 473 in the 50% models, and 2712 and 789 in the 70% stenosed models. The phantoms were perfused with a blood-mimicking fluid, specifically developed to match the refractive index of the silicone PIV phantoms and the dynamic viscosity of blood [32], seeded with fluorescent microspheres with mean diameter of 15 μm .

Velocity maps were obtained using a stereoscopic PIV system (LaVision Inc. Ipsilanti MI, USA). The components of the system along with the applied arrangements have been described in detail earlier (Chapter 3). Briefly, the system consisted of a 5.5-W, 532-nm Nd:YAG laser creating a 1.5-mm thick horizontal illumination sheet through the phantom, which was viewed stereoscopically from above by two CMOS cameras fitted with Scheimpflug adapters and 550-nm filters suitable for the fluorescent microspheres. An overlying silicone prism was used to reduce astigmatism and was placed on top of the silicone phantom symmetrically between the two cameras, which each had an oblique viewing angle of 35°.

5.3 Data Acquisition and Analysis

Data acquisition and processing were performed using commercial software (*DaVis 7.2, LaVision*). From the full 920-ms cardiac-cycle period, the first 870-ms portion was acquired which included all phases of the cardiac cycle. Double-frame images were captured at a 100-Hz frame rate for multiple slices (from central and off-central planes) at 0.5 mm increments throughout the lumen volume. Calibration was performed for the central-plane view, and calibrated images had a scaling factor of ~38 μm per pixel. Two-dimensional, three-component (2D-3C) velocity vector maps were generated using the cross-correlation algorithm (based on a standard fast-Fourier-transform) applied in a

multi-pass mode with adaptive decreasing-size interrogation window. The window size decreased from 64 x 64 pixels to 16 x 16 pixels with a 50% overlap resulting in a velocity vector map with a grid resolution of 0.302 ± 0.007 mm (across all 8 phantoms). Velocity vector maps were then post-processed once with a 3x3-smoothing kernel. All further processing on the velocity maps was performed using custom MATLAB[®] programs. Shear stress parameters were estimated for a 180-ms sub-window corresponding to the systolic phase starting 20 ms before peak systole and continuing 160 ms post peak-systole (i.e. downstroke deceleration).

The 2D-3C velocity maps obtained from 15 repeated cardiac cycles were used to calculate ensemble (phase)-averaged velocity means. Using Reynolds decomposition ($v' = v - V$), velocity fluctuations (v') were then decomposed from the phase-averaged velocity means (V) [33]. At each time point of the cardiac cycle (t), the ensemble-averaged velocity maps were used to represent laminar flow behavior applied to the calculation of laminar shear stress (LSS) defined based on the strain tensor composed of averaged velocity components as follows:

$$\tau_{ij}(t) = \mu \left(\frac{\partial V_i(t)}{\partial x_j} + \frac{\partial V_j(t)}{\partial x_i} \right), \quad V_i(t) = \frac{1}{N} \sum_{n=0}^{N-1} v_i(t + nT), \quad i, j = 1, 2, 3 \quad (5.1)$$

where μ is the dynamic viscosity (4.31 ± 0.03 cP) of the blood-mimicking fluid, T is the period of the acquired cardiac cycle (920 ms), and N is the number of collected cardiac cycles (15 cycles). V_1 , V_2 , and V_3 correspond respectively to the ensemble-averaged velocity means (U , V , W) of the instantaneous velocity components u , v , and w in the x , y , and z direction (i.e. x_1 , x_2 , x_3). Velocity derivatives were calculated based on a central-difference scheme, which was found to be more representative of the boundary slope of velocity as opposed to a forward-difference scheme forces a misestimation of the wall position by assuming a linear velocity slope. Solving the eigenvalue problem for the shear-stress tensor yields three values representing normal stresses in the principal coordinates. The maximum shear stress was then defined as the half difference between the maximum and minimum eigenvalue. The maximum shear stress values at the wall boundaries were then used to represent wall shear stress (WSS). For improved

visualization of WSS, a smoothed-wall model and processing operations were carried out in the open-source Visualization Toolkit software (VTK, Clifton Park, NY, USA). Shear stress values greater than zero were retained via application of a threshold to eliminate the non-flow region of the data. Extraction of the outer polygonal surface produced a coarse wall model. Linear surface subdivision was used to increase triangle vertex density and to aid in smoothing during a volume-preserving geometric smoothing step that followed. Volumetric PIV data were then resampled onto the smoothed wall model producing surface maps of the data for visualization.

The turbulent shear stress tensor composed of Reynolds shear stress (RSS) components was formed from the covariance of the velocity fluctuations (u', v', w') calculated using multiple repeats of the cardiac cycle (i.e. $N = 15$):

$$\tau_{urb}(t) = -\rho \left(\overline{v'_i(t)v'_j(t)} \right), \quad \overline{v'_i(t)v'_j(t)} = \frac{\sum_{n=1}^N v'_i(t, n) \cdot v'_j(t, n)}{N-1}, \quad (5.2)$$

$$v'_i(t, n) = v_i(t, n) - V_i(t), \quad i, j = \{1, 2, 3\}$$

where ρ is the density (1244 kg/m^3) of the blood-mimicking fluid, v'_1, v'_2, v'_3 represent u', v', w' respectively and V_1, V_2, V_3 correspond respectively to the ensemble-averaged velocity means (U, V, W). The normal components of the covariance tensor (i.e. velocity variances) are commonly referred to as the components of the turbulence intensity (TI) (as in Chapter 4). The total of laminar (Equation (5.1)) and turbulent (Equation (5.2)) shear stresses was used to compose the tensor of the total shear stress (TSS), and similarly half of the difference between largest and smallest eigenvalue was used to represent the TSS principle value. Occurrence frequency of each TSS value was determined for the previously specified 180-ms time window over a downstream region expanding wall-to-wall laterally and 35 mm distally to the apex in both the central-plane and volumetric ICA branch.

Vortex identification was carried out using directional λ_{ci} -criterion method, which yielded 2D swirling-strength maps (Appendix B). This method is particularly suited for flow types with strong shear layers [34].

5.4 Results

5.4.1 Laminar shear stress

Figure 5.1 shows the ensemble-averaged velocity magnitude for the time point of peak systole in the eight models. In the normal model, the lowest velocities occur in the recirculating flow of the ICA bulb, while the highest velocities are seen in the ECA branch. In the stenosed models, the jet follows a different path in the eccentric versus concentric models, thus creating distinct recirculation areas. In the concentric models, a helical swirling motion (seen as a Dean-type vortex in the second cross-sectional slices) is observed in the jet-free region – located distal to the stenosis throat, medial to the jet, and along the inner (flow-divider) wall – as well as reversed flow along the inner wall forming the “inner-recirculation zone”. In the eccentric models, a large “outer-recirculation zone” and a smaller inner one are created on opposite sides of the jet as it crosses over from the inner wall to the outer (non-flow-divider) wall. Also, in an eccentric stenosis, the jet enters the bifurcation at a straighter angle and therefore, due to preservation of the path trajectory, the distal jet is narrower and thus has a higher maximum velocity. Regardless of the plaque symmetry, flow relaminarizes more distally with increasing stenosis severity resulting in a larger extent of the recirculation zones. The addition of ulceration to a 50% eccentric model resulted in an even narrower, and thus slightly faster, jet compared to its counterpart non-ulcerated model. As a result, a larger recirculation zone is created behind the jet. In the ulcer itself, very low velocities are present. Central-plane velocity maps of all eight models and for the entire cardiac cycle can be seen in the movie supplied with this thesis.

Laminar shear stress (LSS) profiles are shown in Figure 5.2 for the time point of peak systole. Intraluminal laminar shear stress, herein referred to as free shear stress (FSS) (i.e. not wall related), is governed by the pattern of the high-velocity jet. Notable differences can be seen between the FSS in the eccentric and concentric models; in the concentric models, immediately distal to the stenosis throat, a cylindrical lamina of FSS is present, which can be seen in the central-plane map as two parallel elevated-FSS streams. In the eccentric models, the shear-stress lamina is bounded on one side by the inner wall leading to elevated WSS.

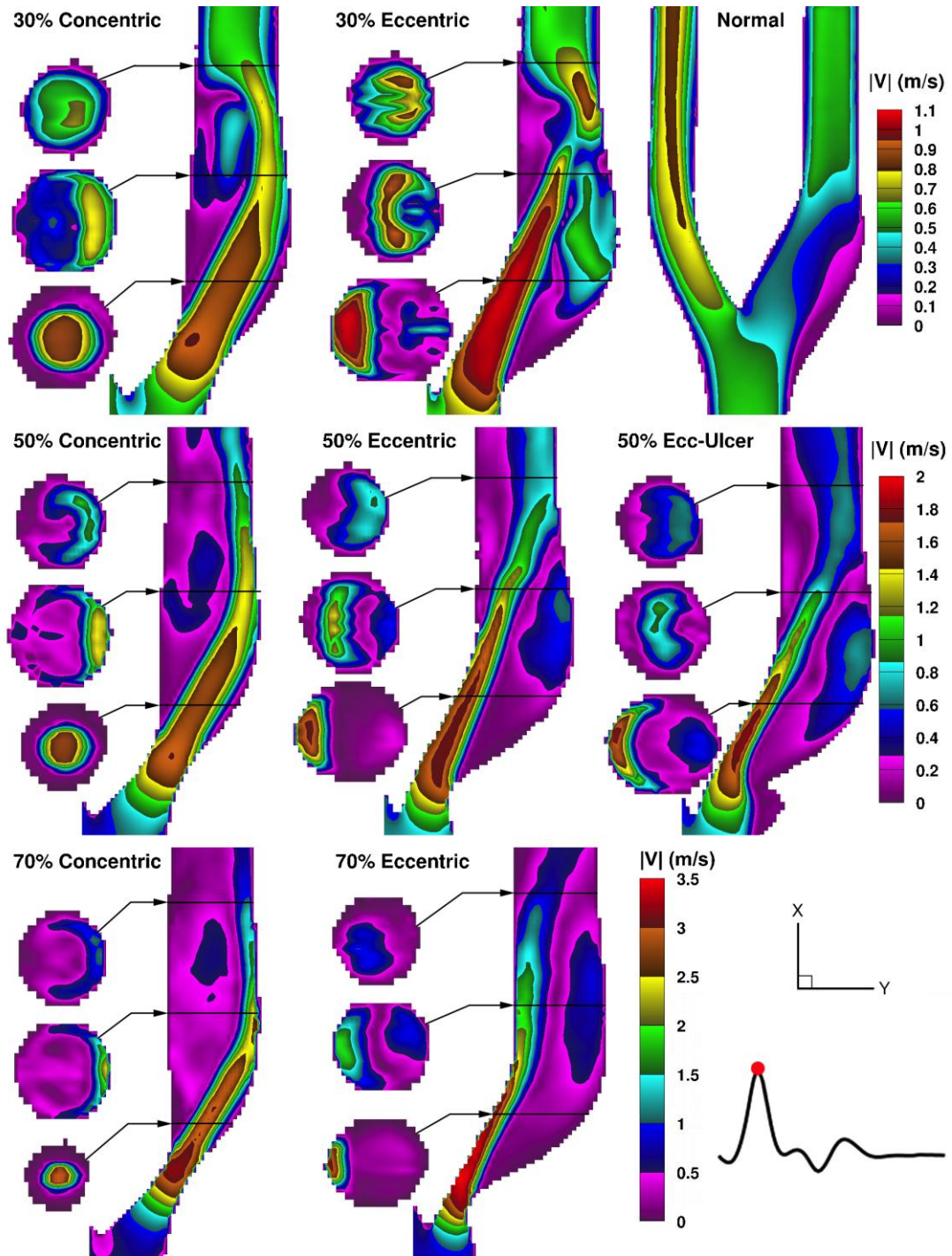


Figure 5.1: Color maps of ensemble-averaged velocity magnitudes shown for peak systole in a family of eight carotid models. Three cross-sectional slices are shown alongside the ICA lumen, for each stenosed model, at the locations indicated by the black lines at approximately 1, 2, and 3 CCA diameters downstream (i.e. ~8, 16, 24 mm). For scale, note the downstream ICA diameter is 5.5 mm. Note the range-appropriate color bar for each row of models.

Within each pair of models of matched stenosis severity, the detachment of the jet from the stenosis wall (i.e. outer wall in the eccentric models) occurs more distally in the concentric model compared to the eccentric one. The more distal detachment from the stenosis throat results in an extension of the elevated-FSS layer further downstream. The extension of the elevated-FSS layers also appears further downstream of the stenosis in the 50% non-ulcerated eccentric model compared to the ulcerated counterpart; however, the elevated-FSS layer forms earlier (upstream) in the stenosis throat for the ulcerated 50% eccentric model resulting from low circulating flow in the ulcer crater adjacent to the high-velocity jet and thus the high velocity gradients.

For a better assessment of spatial and temporal distribution of FSS, maximum-FSS values were extracted for the systolic phase in the ICA central plane extending 25 mm distal to the bifurcation apex, as shown in Figure 5.3. The apparent discontinuities mark the detachment of the jet from the wall, with elevated WSS thus converting to elevated FSS. As described in Figure 5.2, due to the more distal detachment of the jet from the stenosis throat in the concentric models, the onset of elevated-FSS values is shifted further downstream compared to their eccentric counterparts. Another marked difference noted between the eccentric and concentric models is that, as the stenosis severity increases, increasingly greater temporal extension is notable for an eccentric model compared to its concentric counterpart (e.g. note the 8-Pa isocontour in the 70% models). In the examined stenosed models, the maximum FSS peaks around peak systole. In overall, the maximum-FSS ranges were found to be similar in each group of stenosis severity reaching a peak value within 4-5 Pa in 30% models, within 7-8 Pa in 50% models (non-ulcerated ones), and within 16-17 Pa in the 70% models. Comparison between the ulcerated and non-ulcerated 50% eccentric models reveals multiple marked differences. In the ulcerated model, a region of elevated FSS is seen upstream of the stenosis throat (0-2 mm), as also noted in Figure 5.2, due to the presence of the ulcer. Although the non-ulcerated eccentric model shows slightly greater downstream spatial extension of the elevated FSS, the ulcerated model shows greater temporal extension later into the cardiac cycle (e.g. note the 3-Pa contour level) and a higher peak value (within 8-9 Pa). The pattern in the normal (disease-free) model is notably different where maximum FSS just exceeds 2 Pa.

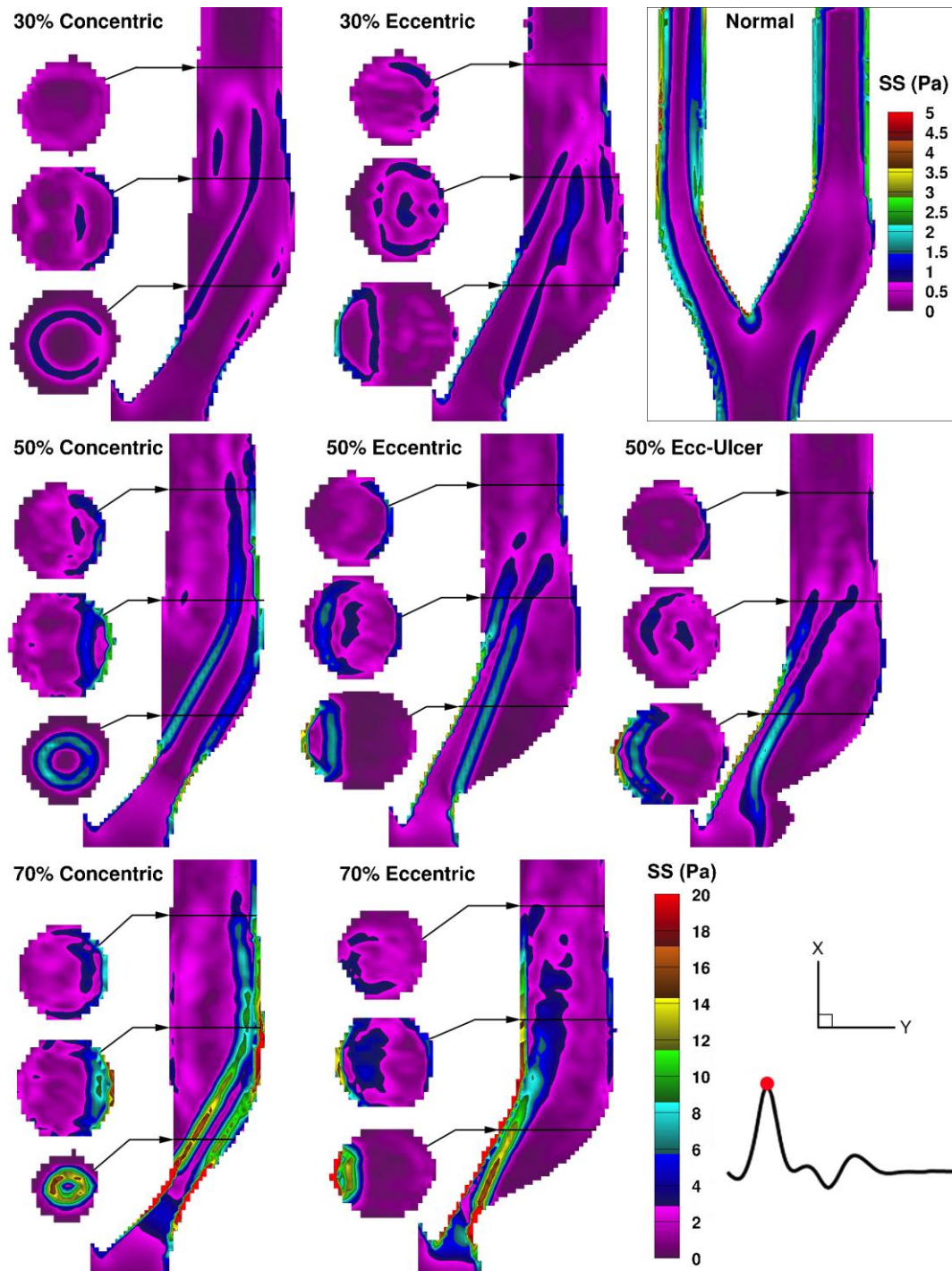


Figure 5.2: Color maps of the laminar shear stress shown for peak systole in a family of eight carotid models. Three cross-sectional slices are shown alongside the ICA lumen, for each stenosed model, at the locations indicated by the black lines at approximately 1, 2, and 3 CCA diameters downstream (i.e. $\sim 8, 16, 24$ mm). Note the bottom right color bar represents the 7 stenosed models and a separate color bar is used for the normal model shown in the enclosed box.

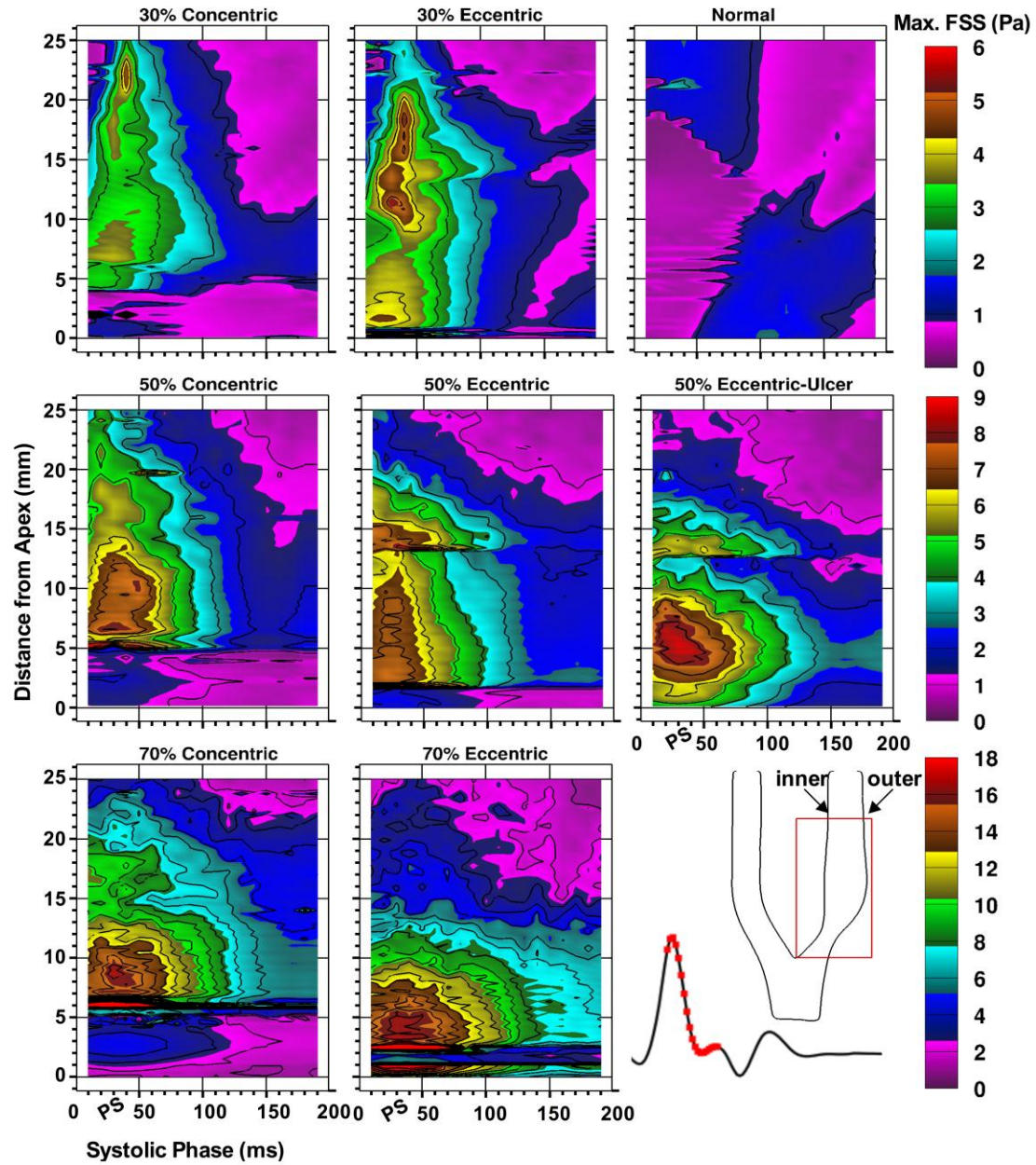


Figure 5.3: Spatial and temporal distribution of the maximum free (i.e. non wall) shear stress in a family of eight carotid models. For each time point, maximum FSS values were extracted across the entire ICA lumen along the 25-mm analyzed length. Data are shown for the 180-ms window, incorporating peak systole (PS), as shown on the reference cardiac-cycle waveform. Note the range-appropriate color bar associated with each row of models and the 1-Pa isocontour increments used for all maps.

Figure 5.4 shows laminar WSS at the time point of maximum shear stress (i.e. peak systole). The normal bifurcation bulb exhibits the lowest WSS area overall. In the normal model, a maximum WSS of about 6.5 Pa presents at the bend of the inner ECA wall; similar values were consistent in the ECA of all the examined models. Consistently in all the concentric models, elevated WSS appears at two disjointed regions: around the stenosis throat and at the outer ICA wall where the high-velocity jet impinges. The expansion and level in both regions increases with increasing stenosis severity. Minimal elevation of WSS was observed along the inner ICA wall distal to the stenosis in the concentric models. In the eccentric geometries, an elevated-WSS region appears in the stenosis throat extending distally along the inner wall. Downstream at the point of flow separation, a slight elevation of WSS is observed along the outer wall. In both the non-ulcerated and ulcerated 50% eccentric models, the inner ICA wall shows a similar pattern of WSS. However, elevated WSS observed in the non-ulcerated model proximal to the stenosis throat was replaced by elevated FSS at the mouth of the crater in the ulcerated model, which can be seen in the central plane in Figure 5.2.

Figure 5.5 shows the spatial (axial) and temporal distribution of WSS along the inner/flow-divider wall (a), and outer wall (b) derived from same region and cardiac phase used in Figure 5.3. Similar to FSS, WSS values peaked around peak systole. In the normal model, the maximum WSS is present at the inner wall and barely exceeds 4 Pa. Along both outer and inner wall, a consistent pattern is observed among the concentric models and likewise among the eccentric models. Assessing the outer-wall patterns (Figure 5.5b), two distinct regions of elevation are observed for both concentric and eccentric models (with exception of 50% ulcerated model). The first elevation arises due to WSS in the stenosis throat with the marked distinction of notably shorter extent in each eccentric model compared to its concentric counterpart. In the concentric models, the second WSS elevation occurs downstream where jet attaches to and flows along the outer wall before it detaches again. In each concentric model, this region has lower maximum values than elevation region at the stenosis throat, however, it extents longer. In the eccentric models, the downstream WSS elevation can be distinguished from two different shearing effects: one from the recirculation zone adjacent to the outer wall, followed by the shearing due to impact of the jet on this wall.

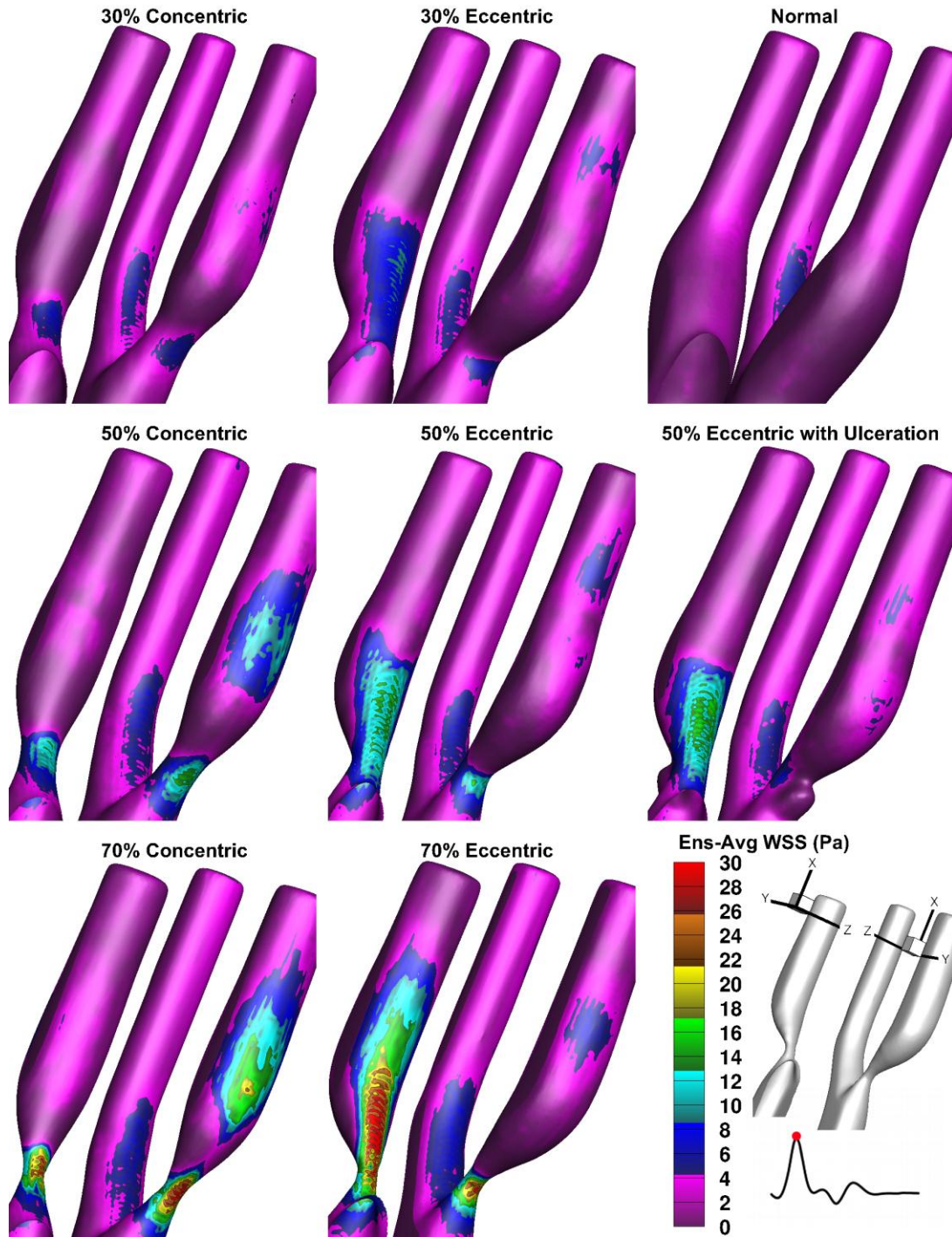
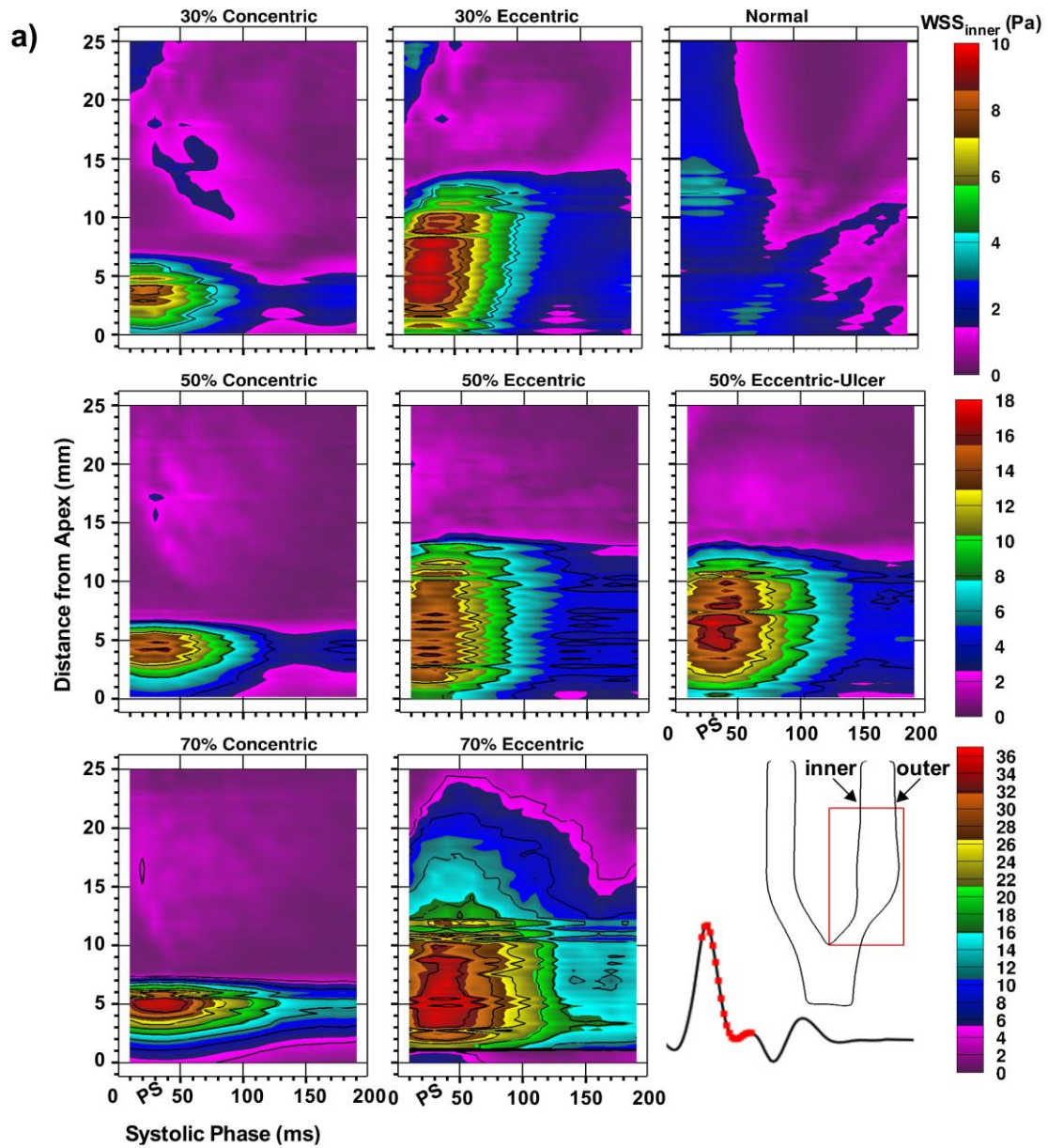


Figure 5.4: Ensemble-averaged wall shear stress shown for peak systole in a family of eight carotid models. For optimal display, the ICA is shown from 2 different perspectives, as indicated by the orientation schematic in the bottom right corner. The color bar represents all the models including the normal. For improved accommodation, the dynamic range of the color bar is reduced to a maximum of 30 Pa.

It is noted that in the 70% eccentric model only the shearing due to recirculation zone can be seen in outer-wall WSS patterns due to the fact that the jet impact on the outer wall occurs beyond the 25-mm analyzed distance from apex as shown in Figure 5.1. Due to the presence of ulcer, the elevated WSS at stenosis throat does not form in the ulcerated model. Despite the similar downstream patterns, the WSS region associated with recirculation zone (more proximal to apex) extends larger axially and temporally in the ulcerated model compared to the non-ulcerated counterpart.



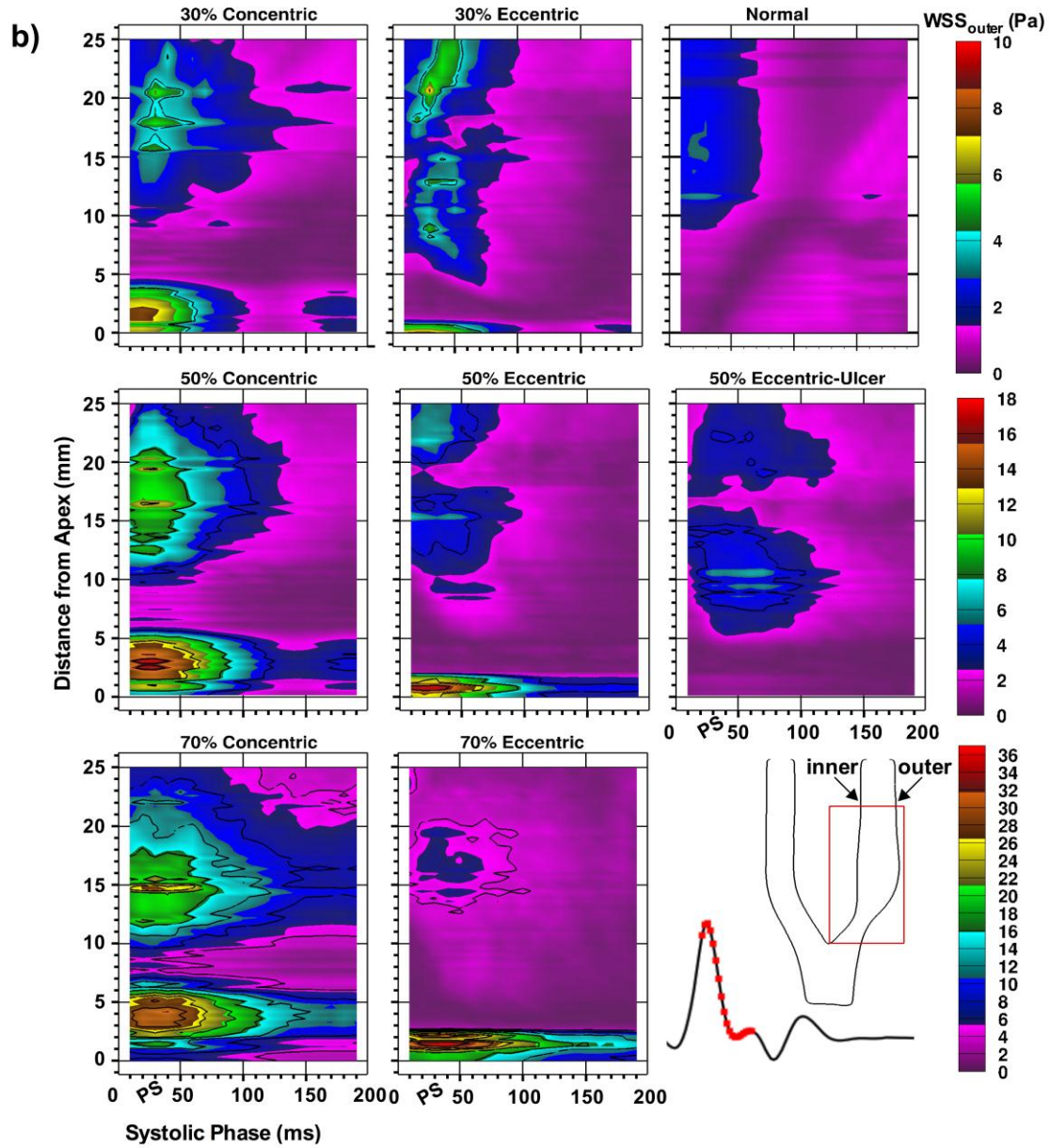


Figure 5.5: Spatial and temporal distribution of the wall shear stress along the inner wall (a) and outer wall (b) in a family of eight carotid models. For each time point, wall-bounded values were extracted along the 25-mm analyzed length. The analyzed 180-ms window (with peak systole denoted as PS) is highlighted on the reference cardiac-cycle waveform. Note the range-appropriate color bar associated with each row of the models and the 4-Pa contour level used for all the maps.

The WSS patterns along the inner wall (Figure 5.5a) are notably different from the outer-wall patterns; the proximal elevated region in the concentric models is again related to the stenosis throat and in the eccentric models is formed due to bounding and shearing of the jet on this non-stenosed wall. The extent of the WSS elevation in each eccentric model is about twice the extension in counterpart concentric one (up to 7 mm distal to apex). The elevated WSS at stenosis throat does not form in the ulcerated model due to the presence of ulcer. Compared to the non-ulcerated 50% eccentric model and similar to maximum-FSS pattern, the ulcerated model shows greater temporal sustention of inner-wall WSS in the depicted systolic phase (e.g. note the 8-Pa contour level) and a higher maximum value (within 16-18 Pa compared to 14-16 Pa in the non-ulcerated counterpart). In all stenosed models, by increasing stenosis severity in both concentric and eccentric groups, the peak value of maximum WSS at both inner and outer wall shifts more distal to the apex and the drop (decay) from this peak becomes notably sharper.

5.4.2 Turbulent shear stress

Figure 5.6 shows RSS distribution of $\overline{u'v'}$ component in the 50%-stenosed models at three different time points of the systolic phase: near peak systole (systolic acceleration), post peak systole (early deceleration), and near the dicrotic notch (late systolic phase). In the concentric model, RSS is skewed toward the outer wall, whereas it is more laterally distributed in the two eccentric models. In all three models, the spatial extent and level of RSS increases during deceleration. During deceleration in the eccentric models, RSS distribution expands into the large outer-wall recirculation zone, and it appears to have a wider distribution in the ulcerated model. The RSS distribution in the large recirculation zone persists during the entire deceleration phase, as evident by the third time point shown, although covering a lower range ($\pm 0.01 \text{ m}^2/\text{s}^2$). In the concentric model, spotted regions of elevated RSS are observed downstream during this phase. As expected RSS is governed by flow instabilities and coincides with the presence of vortices, which are shown explicitly in Figure 5.7.

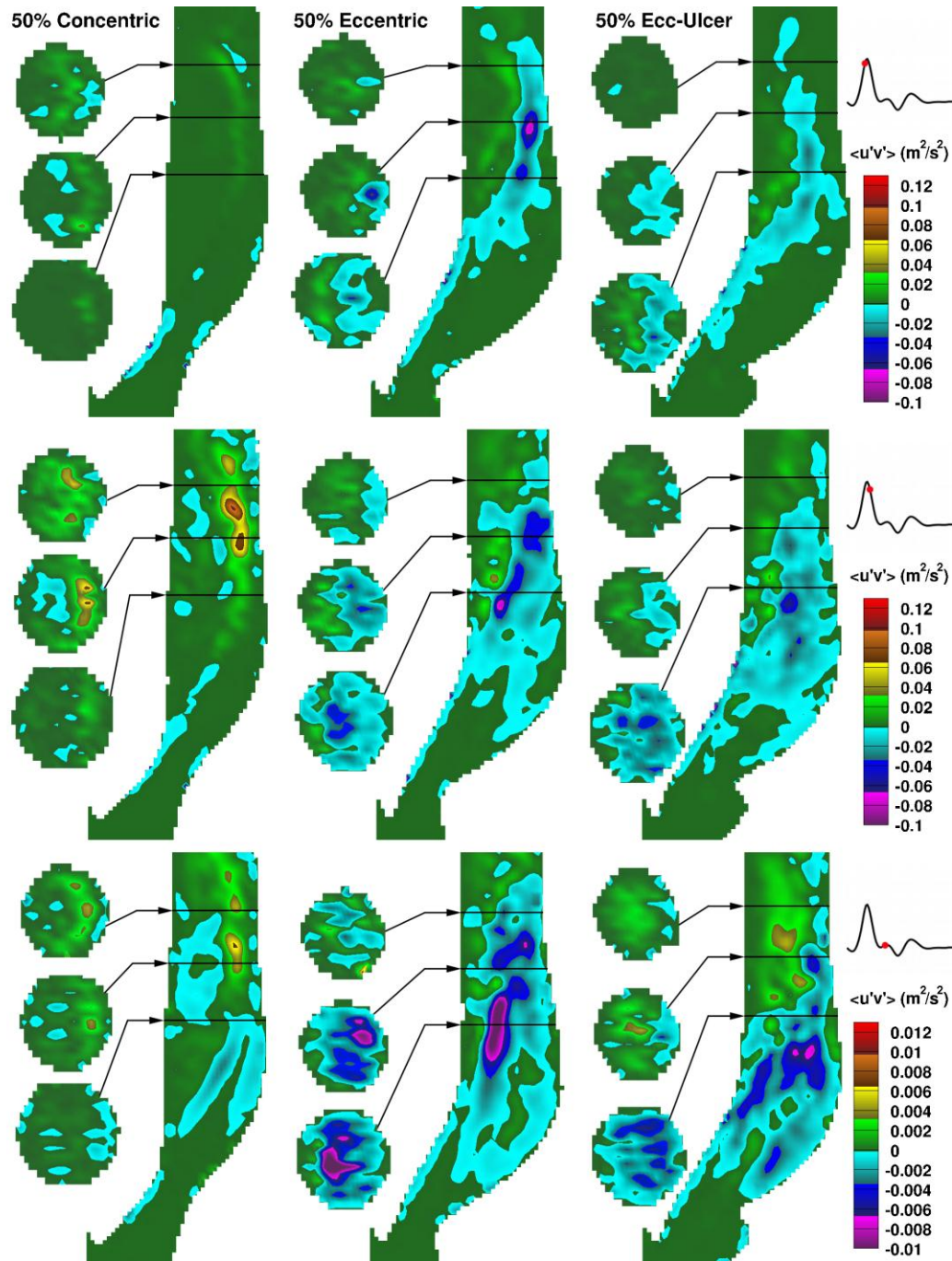


Figure 5.6: Reynolds shear stress $\overline{u'v'}$ shown as a function of time for the set of three 50%-stenosed models. Maps are shown at three time points: 20 ms before peak systole (top row), 20 ms after peak systole (middle), and 20 ms before the diastolic notch (bottom). Three cross-sectional slices are shown alongside the ICA lumen at the locations indicated by the black lines at approximately 2, 2.5, and 3 CCA diameters downstream (i.e. ~ 16, 20, 24 mm). Note the separate color bar used for the bottom row with the same zero-value color as for the upper rows.

Figure 5.7 shows central-plane vortices identified using swirling strength in the three 50% stenosed models derived, for comparison, based on an ensemble average of 15 cycles and based on instantaneous velocity from a single representative cycle. In the acceleration phase (top row), flow is well organized, with vortex shedding appearing along each side of the jet in all three models. Due to increasing flow instabilities during systolic deceleration (middle row), in addition to vortices along the jet, the large outer recirculation zone breaks down into small vortices. The dominant presence of these vortices is also evident in the ensemble-averaged map but appear as fewer large merged vortices of lesser strength. Destabilization of the helical flow in the concentric model can also be seen as some small instabilities in the region between the inner wall and the jet.

Figure 5.8 shows total shear stress (TSS) maps at the time point of maximum value for each model. For all the examined models, with the exception of the normal model, turbulent shear stress is most prominent early within the systolic deceleration. In all the stenosed models, the elevated region of TSS expands downstream of the stenosis throat starting from the point of jet detachment from the wall and, in general, contains higher values in the eccentric models to a maximum of approximately 300 Pa in the 70% eccentric stenosis. Notable from the cross-sectional slices, elevated-TSS region is mainly bounded to the outer wall in the concentric models, whereas in the eccentric models is more centrally distributed.

To further demonstrate the effect of geometrical factors on all the levels of shear stress (both laminar and turbulent), the combined spatial and temporal accumulation of TSS were investigated, indicating the frequency of occurrence for each value result is shown in Figure 5.9. Occurrence frequency of each TSS value was determined for the previously specified 180-ms time window over a downstream region expanding wall-to-wall laterally and 35 mm distally to the apex in both the central-plane and volumetric ICA branch. Notable differences can be seen between the eccentric and concentric models. In the 30% stenosed models, increased levels are seen across all TSS values in the eccentric model, indicating greater sustention over either time or space. In the 50% and, more pronouncedly, in the 70% eccentric stenosed models this increase was observed for higher-level shear stress (e.g. above 16 Pa in 70% models) which is attributed to the

elevated wall or turbulent shear stress. The ulcerated and non-ulcerated 50%-stenosed models were, in general, similar with greater accumulation found for low-level shear stress (below 8 Pa) in the ulcerated model.

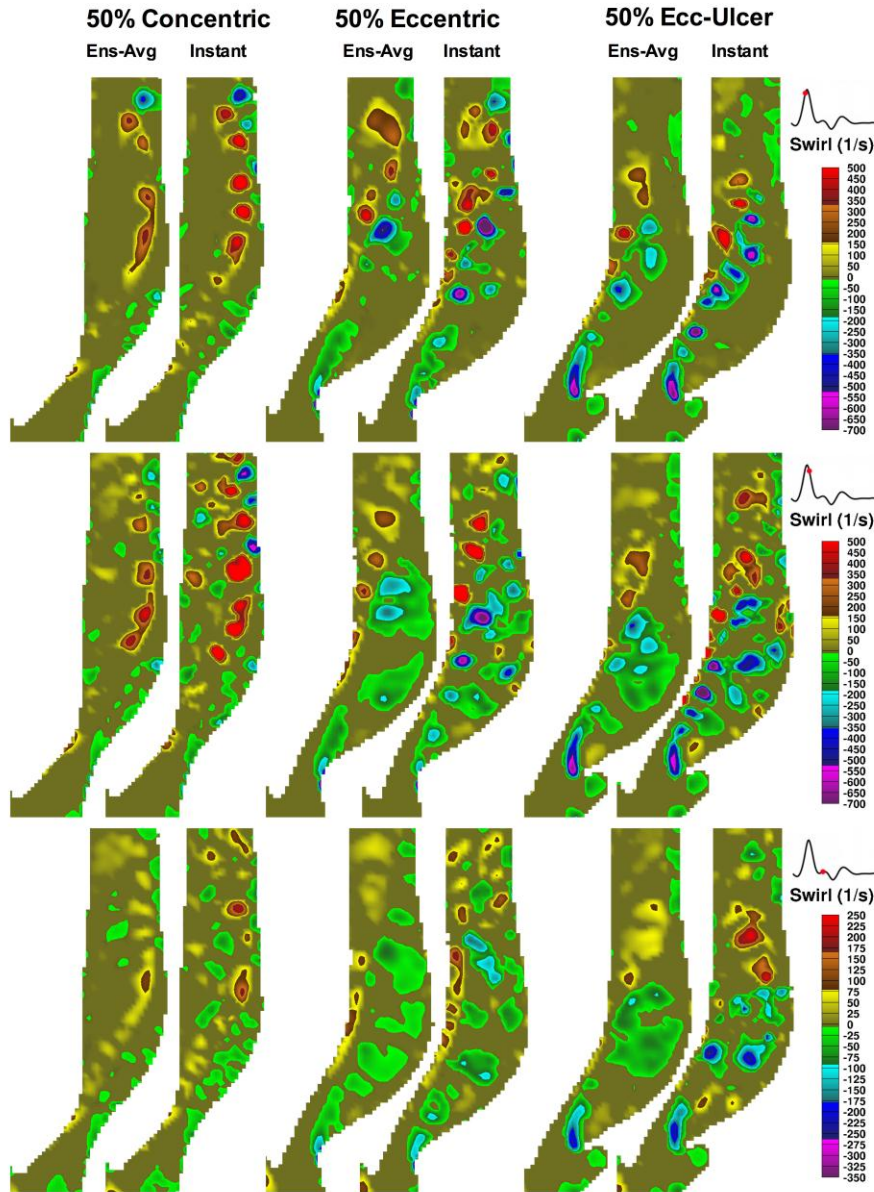


Figure 5.7: Color-encoded maps of orientation-dependent swirling strength (ω_z) shown for the ICA central plane in each of the set of three 50%-stenosed models at time points similar to those applied to Figure 5.6. Swirling strength maps were obtained from x and y components of the ensemble-averaged (left ICA of each column pair) and instantaneous (right ICA of each column pair) velocity maps. Note the different limits of the color bar used for the bottom row.

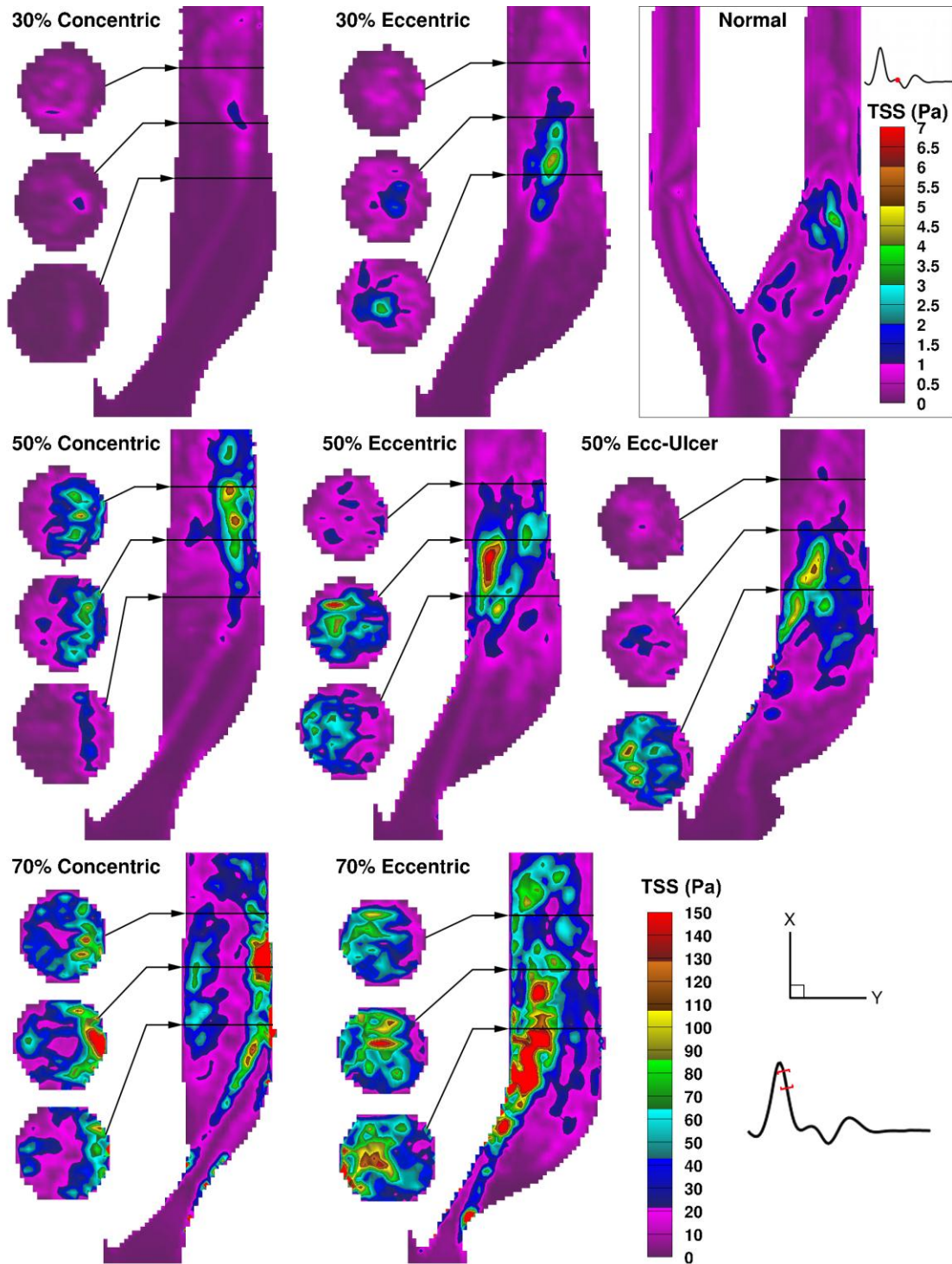


Figure 5.8: Color-encoded maps of total shear stress for the time point of maximum TSS in each of eight carotid models. Note the bottom right color bar (set to the maximum of 150 Pa) and indicated time point of maximum TSS (20 ± 10 ms post peak systole) represents the seven stenosed models; those associated with the normal model are shown in the enclosed box.

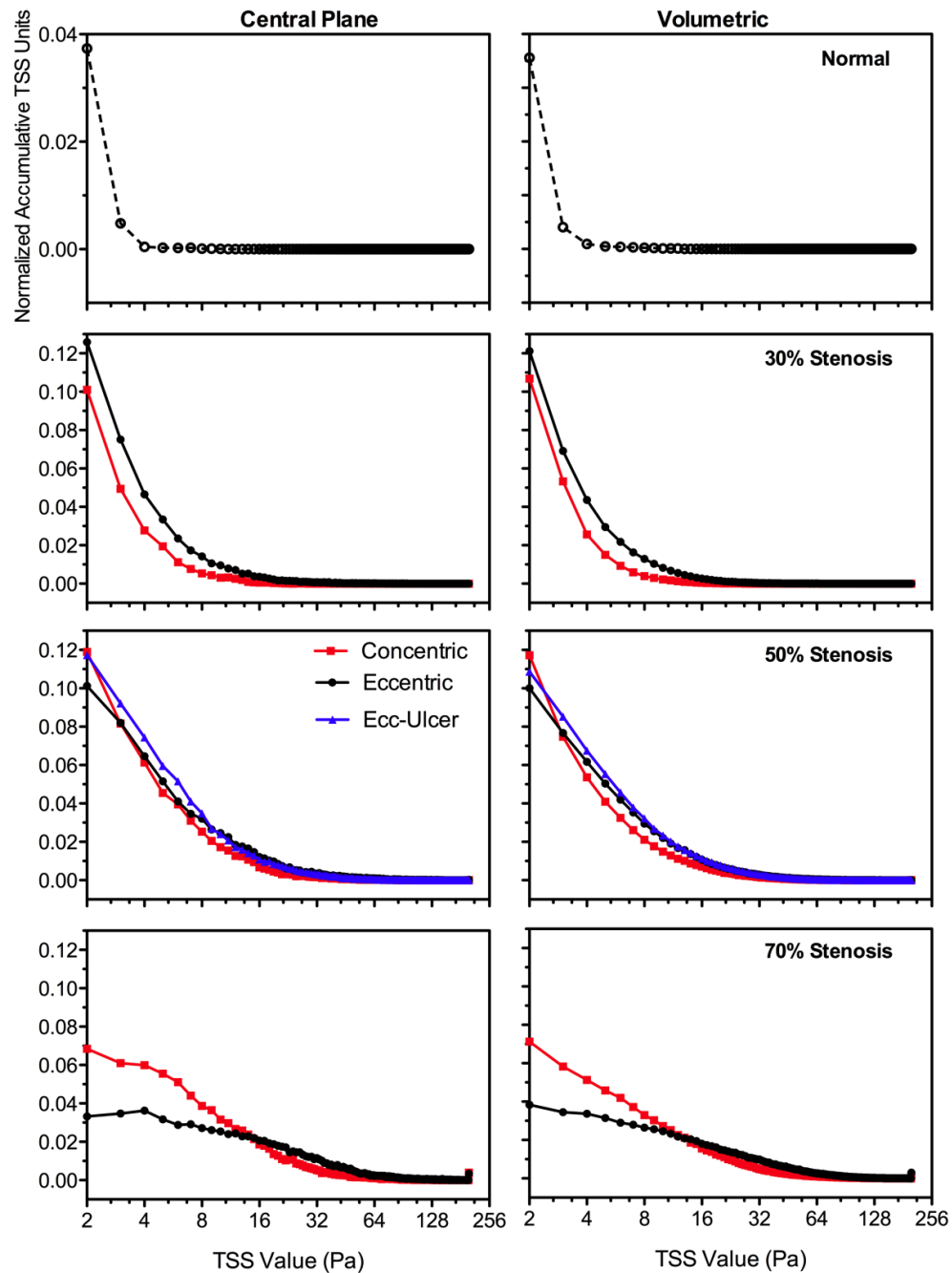


Figure 5.9: Combined spatial and temporal occurrence frequency of total shear stress values. The analyzed region extended wall-to-wall laterally and 35 mm distal to the apex in the ICA branch calculated both for the central-plane (left column) and volumetrically (right column). Values were accumulated over the systolic time window (180 ms). Horizontal axes are presented in log 2. Also, note the different range for the vertical axis of the plot associated with the normal model.

5.5 Discussion

Our findings demonstrated the marked differences in shear stress spatial distribution and time evolution induced by varying plaque geometry. Considering two equally stenosed concentric and eccentric models, although comparable maximum levels of FSS and WSS were found (Figure 5.3 and Figure 5.5), the marked difference was found in the spatial distribution pattern of the shear stress downstream of the stenosis (Figure 5.2 and Figure 5.4). Notable is the shorter extent of the elevated WSS at the outer wall of the stenosis throat in each eccentric model compared to its concentric counterpart (Figure 5.4). This finding translates to larger shear gradient (i.e. steeper decay of shear level) at the immediate post-stenotic expansion – the area that contains the large outer-wall recirculation zone with very low shear stress. From the aspect of thrombosis activity, this large recirculation zone with its adjacency to high WSS (at the throat) and FSS (along the jet stream) poses a favorable environment for thrombosis growth due to the steep shear drop-off and by facilitating the subsequent accumulation of soluble agonists [7]. It is important to recognize the different spatial distribution of WSS as it translates to different local WSS gradients, which are known to impact endothelial response [35]. The presence of recirculation also results in longer residence times and thus, higher platelet activation level [20]. As the stenosis severity increases, the level of shear stress – and the shear gradient – within the throat increases, which in turn promotes larger growth of post-stenotic platelet aggregates.

The WSS patterns observed in both the concentrically and eccentrically 30%-stenosed models matched those previously reported from computational simulation in the identical 30% stenosed models [27], however, the reported values were significantly larger compared to the finding in this study (>20 Pa vs. <10 Pa in this study) that can be due to the different methods applied to calculate the velocity derivatives.

Free shear layer is generated at the interface of the jet and separated flow regions (e.g. recirculation zones). During systolic phase when this sheared interface become unstable vortex shedding appears along sides of shear layers as seen in Figure 5.7. The significance of vortex shedding as a thrombosis mechanism was demonstrated in mechanical heart valves study by Bluestein *et al.* [36] in which particle paths showed the

platelets, after being exposed to high-level shear stress layers, were entrapped within the shed vortices past the leaflets. These potentially activated platelets can aggregate and form free emboli; subject to being convected downstream, these free thromboemboli can eventually lead to ischemic stroke.

During the systolic deceleration phase, in which flow becomes most disturbed [22, 37, 38], additional vortices appear due to the break down of the large recirculation zone (Figure 5.7) which were pronounced in eccentric models. It has been shown [39] that these post-stenotic vortices can enhance the local deposition and convection of the platelets near the wall (i.e. potentially near the site of plaque rupture). As was demonstrated, this region during the deceleration phase also was associated with the presence of elevated RSS (Figure 5.6), thus of potential significance with regards to platelet activation. Turbulent flow conditions promote high pathological shear stress level, suggesting shorter exposure times required for platelet activation. Although platelets can survive the damage from extremely short exposure time (in the order of 10^{-5} s) [15], it has been shown that a high level of shear stress can sensitize the platelets and prime them for activation under steadier flow conditions [40]. However, it has also been suggested that thrombosis under turbulent conditions may imply a different mechanism, as platelets need to form bonds very rapidly [41].

The patterns of elevated TSS (Figure 5.8) showed correlation to those of elevated TI previously studied [28, 42]; comparable to the TI maps, TSS elevations were most prominent during systolic deceleration and located at the point of the jet detachment.

Plaque ulceration has shown association with the presence of thrombus [43]. Based on our findings (in the ulcerated 50% eccentric model), ulceration potentially could contribute to a higher level of thrombosis activity due to the greater sustention of the elevated FSS and WSS (Figure 5.3 and Figure 5.5), larger expansion of RSS, and the presence of the shear stress lamina adjacent to the ulcer crater, in which low circulating flow is present.

As mentioned earlier, thrombosis at the plaque site can be regulated by high pathological shear stress in different ways, such as by promoting plaque rupture, thus exposing the

lipid core, and also by spatially regulating superimposed thrombus on the plaque surface. Thus, the differences in shear stress levels and patterns reported in the present work may explain how certain geometrical features of the plaque can be correlated with more frequent cerebrovascular events; however, it is important to note that, besides altering the local hemodynamics, geometrical features of the plaque are interlinked with plaque morphology. Eccentric plaques were reported to be strongly associated with higher content of lipid [44]. Plaque morphology has also shown correlation to the degree of stenosis severity and changes to more soft and haemorrhagic plaque as the degree of stenosis increases [45]. These findings suggest that a combination of physiological and hemodynamic factors can be involved in higher association with cerebrovascular events.

Potential limitations of the present works lies in the simplified examined models and Newtonian blood-mimicking fluid. The idealized carotid phantoms did not include vessel tortuosity and physiological compliance. However, the matched geometries of the examined models allowed controlled examination of each plaque variable. The use of Newtonian blood-mimicking fluid can be considered valid under the well-established and common assumption of Newtonian behavior of blood in larger arteries [46].

5.6 Conclusion

While the significance of stenosis severity is undeniable, alone and especially for moderate cases, it is not a sensitive predictor of stroke risk [47]. In the quest for more sensitive risk assessment, additional factors, such as plaque vulnerability [48] and the level of thrombosis activity [49] have been suggested for consideration as risk factors. The association of shear stress and level of thrombosis activity has inspired trajectory-based hemodynamic studies [20, 50-53] to measure more directly related indices. The notable differences in shear-stress levels and patterns found in the present work would be expected to translate to different levels of thrombosis activity. With the provided experimental knowledge and validation base, more trajectory-based studies are encouraged for enabling clinically compatible quantifications of the thrombosis-activity levels based on geometrical features of the stenosis.

5.7 References

- [1] A. M. Malek, S. L. Alper, and S. Izumo (1999), Hemodynamic shear stress and its role in atherosclerosis. *Journal of the American Medical Association*, vol. 282, pp. 2035-2042.
- [2] J. J. Wentzel, Y. S. Chatzizisis, F. J. H. Gijsen, *et al.* (2012), Endothelial shear stress in the evolution of coronary atherosclerotic plaque and vascular remodelling: Current understanding and remaining questions. *Cardiovascular Research*, vol. 96, pp. 234-243.
- [3] C. J. Slager, J. J. Wentzel, F. J. H. Gijsen, *et al.* (2005), The role of shear stress in the destabilization of vulnerable plaques and related therapeutic implications. *Nature Clinical Practice Cardiovascular Medicine*, vol. 2, pp. 456-464.
- [4] F. J. H. Gijsen, J. J. Wentzel, A. Thury, *et al.* (2008), Strain distribution over plaques in human coronary arteries relates to shear stress. *Am J Physiol Heart Circ Physiol*, vol. 295, pp. H1608-H1614.
- [5] H. C. Groen, F. J. H. Gijsen, A. van der Lugt, *et al.* (2007), Plaque rupture in the carotid artery is localized at the high shear stress region - a case report. *Stroke*, vol. 38, pp. 2379-2381.
- [6] J. K. Lovett and P. M. Rothwell (2003), Site of carotid plaque ulceration in relation to direction of blood flow: An angiographic and pathological study. *Cerebrovascular Diseases*, vol. 16, pp. 369-375.
- [7] W. S. Nesbitt, E. Westein, F. J. Tovar-Lopez, *et al.* (2009), A shear gradient-dependent platelet aggregation mechanism drives thrombus formation. *Nature Medicine*, vol. 15, pp. 665-U146.
- [8] S. P. Jackson, W. S. Nesbitt, and E. Westein (2009), Dynamics of platelet thrombus formation. *Journal of Thrombosis and Haemostasis*, vol. 7, pp. 17-20.
- [9] L. Antiga and D. A. Steinman (2009), Rethinking turbulence in blood. *Biorheology*, vol. 46, pp. 77-81.
- [10] A. M. Sallam and N. H. C. Hwang (1984), Human red blood-cell hemolysis in a turbulent shear-flow - contribution of Reynolds shear stresses. *Biorheology*, vol. 21, pp. 783-797.
- [11] P. C. Lu, H. C. Lai, and J. S. Liu (2001), A reevaluation and discussion on the threshold limit for hemolysis in a turbulent shear flow. *Journal of Biomechanics*, vol. 34, pp. 1361-1364.

- [12] T. C. Hung, R. M. Hochmuth, J. H. Joist, *et al.* (1976), Shear-induced aggregation and lysis of platelets. *Transactions - American Society for Artificial Internal Organs*, vol. 22, pp. 285-291.
- [13] J. M. Ramstack, L. Zuckerman, and L. F. Mockros (1979), Shear-induced activation of platelets. *Journal of Biomechanics*, vol. 12, pp. 113-125.
- [14] G. Colantuoni, J. D. Hellums, J. L. Moake, *et al.* (1977), Response of human platelets to shear-stress at short exposure times. *Transactions - American Society for Artificial Internal Organs*, vol. 23, pp. 626-631.
- [15] J. D. Hellums (1994), 1993 Whitaker lecture- biology in thrombosis research. *Annals of Biomedical Engineering*, vol. 22, pp. 445-455.
- [16] L. J. Wurzinger, R. Opitz, P. Blasberg, *et al.* (1985), Platelet and coagulation parameters following millisecond exposure to laminar shear-stress. *Thrombosis and Haemostasis*, vol. 54, pp. 381-386.
- [17] North American Symptomatic Carotid Endarterectomy Trial (NASCET) Investigators (1991), Clinical alert: Benefit of carotid endarterectomy for patients with high-grade stenosis of the internal carotid artery. *Stroke*, vol. 22, pp. 816-7.
- [18] T. Ohara, K. Toyoda, R. Otsubo, *et al.* (2008), Eccentric stenosis of the carotid artery associated with ipsilateral cerebrovascular events. *American Journal of Neuroradiology*, vol. 29, pp. 1200-1203.
- [19] P. M. Rothwell, R. Gibson, and C. P. Warlow (2000), Interrelation between plaque surface morphology and degree of stenosis on carotid angiograms and the risk of ischemic stroke in patients with symptomatic carotid stenosis. *Stroke*, vol. 31, pp. 615-621.
- [20] M. Tambasco and D. A. Steinman (2003), Path-dependent hemodynamics of the stenosed carotid bifurcation. *Annals of Biomedical Engineering*, vol. 31, pp. 1054-1065.
- [21] J. S. Stroud, S. A. Berger, and D. Saloner (2002), Numerical analysis of flow through a severely stenotic carotid artery bifurcation. *Journal of Biomechanical Engineering-Transactions of the ASME*, vol. 124, pp. 9-20.
- [22] S. E. Lee, S.-W. Lee, P. F. Fischer, *et al.* (2008), Direct numerical simulation of transitional flow in a stenosed carotid bifurcation. *Journal of Biomechanics*, vol. 41, pp. 2551-2561.
- [23] L. Grinberg, A. Yakhot, and G. E. Karniadakis (2009), Analyzing transient turbulence in a stenosed carotid artery by proper orthogonal decomposition. *Annals of Biomedical Engineering*, vol. 37, pp. 2200-2217.

- [24] N. A. Buchmann, C. Atkinson, M. C. Jeremy, *et al.* (2011), Tomographic particle image velocimetry investigation of the flow in a modeled human carotid artery bifurcation. *Experiments in Fluids*, vol. 50, pp. 1131-1151.
- [25] J. Vetel, A. Garon, and D. Pelletier (2009), Lagrangian coherent structures in the human carotid artery bifurcation. *Experiments in Fluids*, vol. 46, pp. 1067-1079.
- [26] D. Birchall, A. Zaman, J. Hacker, *et al.* (2006), Analysis of haemodynamic disturbance in the atherosclerotic carotid artery using computational fluid dynamics. *European Radiology*, vol. 16, pp. 1074-1083.
- [27] D. A. Steinman, T. L. Poepping, M. Tambasco, *et al.* (2000), Flow patterns at the stenosed carotid bifurcation: Effect of concentric versus eccentric stenosis. *Annals of Biomedical Engineering*, vol. 28, pp. 415-423.
- [28] T. L. Poepping, R. N. Rankin, and D. W. Holdsworth (2010), Flow patterns in carotid bifurcation models using pulsed Doppler ultrasound: Effect of concentric vs. Eccentric stenosis on turbulence and recirculation. *Ultrasound in Medicine and Biology*, vol. 36, pp. 1125-1134.
- [29] R. F. Smith, B. K. Rutt, and D. W. Holdsworth (1999), Anthropomorphic carotid bifurcation phantom for MRI applications. *Journal of Magnetic Resonance Imaging*, vol. 10, pp. 533-44.
- [30] D. W. Holdsworth, D. W. Rickey, M. Drangova, *et al.* (1991), Computer-controlled positive displacement pump for physiological flow simulation. *Medical and Biological Engineering and Computing*, vol. 29, pp. 565-70.
- [31] D. W. Holdsworth, C. J. D. Norley, R. Frayne, *et al.* (1999), Characterization of common carotid artery blood-flow waveforms in normal human subjects. *Physiological Measurement*, vol. 20, pp. 219-240.
- [32] M. Y. Yousif, D. W. Holdsworth, and T. L. Poepping (2011), A blood-mimicking fluid for particle image velocimetry with silicone vascular models. *Experiments in Fluids*, vol. 50, pp. 769-774.
- [33] W. C. Reynolds and A. K. M. F. Hussain (1972), The mechanics of an organized wave in turbulent shear flow. Part 3. Theoretical models and comparisons with experiments. *Journal of Fluid Mechanics*, vol. 54, pp. 263-288.
- [34] R. J. Adrian, K. T. Christensen, and Z. C. Liu (2000), Analysis and interpretation of instantaneous turbulent velocity fields. *Experiments in Fluids*, vol. 29, pp. 275-290.
- [35] L. Rouleau, M. Farcas, J.-C. Tardif, *et al.* (2010), Endothelial cell morphologic response to asymmetric stenosis hemodynamics: Effects of spatial wall shear stress gradients. *Journal of Biomechanical Engineering*, vol. 132,

- [36] D. Bluestein, E. Rambod, and M. Gharib (2000), Vortex shedding as a mechanism for free emboli formation in mechanical heart valves. *Journal of Biomechanical Engineering-Transactions of the ASME*, vol. 122, pp. 125-134.
- [37] P. A. J. Bascom, K. W. Johnston, R. S. C. Cobbold, *et al.* (1997), Relation of the flow field distal to a moderate stenosis to the Doppler power. *Ultrasound in Medicine and Biology*, vol. 23, pp. 25-39.
- [38] S. Kefayati and T. L. Poepping (2013), Transitional flow analysis in the carotid artery bifurcation by proper orthogonal decomposition and particle image velocimetry. *Medical Engineering and Physics*, vol. 35, pp. 898-909.
- [39] D. Bluestein, C. Gutierrez, M. Londono, *et al.* (1999), Vortex shedding in steady flow through a model of an arterial stenosis and its relevance to mural platelet deposition. *Annals of Biomedical Engineering*, vol. 27, pp. 763-773.
- [40] J. Sheriff, D. Bluestein, G. Girdhar, *et al.* (2010), High-shear stress sensitizes platelets to subsequent low-shear conditions. *Annals of Biomedical Engineering*, vol. 38, pp. 1442-1450.
- [41] D. L. Bark, Jr. and D. N. Ku (2010), Wall shear over high degree stenoses pertinent to atherothrombosis. *Journal of Biomechanics*, vol. 43, pp. 2970-2977.
- [42] E. Y. Wong, H. N. Nikolov, R. N. Rankin, *et al.* (2012), Evaluation of distal turbulence intensity for the detection of both plaque ulceration and stenosis grade in the carotid bifurcation using clinical Doppler ultrasound. *European Radiology*,
- [43] M. Fisher, A. Paganini-Hill, A. Martin, *et al.* (2005), Carotid plaque pathology - thrombosis, ulceration, and stroke pathogenesis. *Stroke*, vol. 36, pp. 253-257.
- [44] F. Li, M. M. McDermott, D. Li, *et al.* (2010), The association of lesion eccentricity with plaque morphology and components in the superficial femoral artery: A high-spatial-resolution, multi-contrast weighted cmr study. *Journal of cardiovascular magnetic resonance*, vol. 12,
- [45] R. J. Holdsworth, P. T. McCollum, J. S. Bryce, *et al.* (1995), Symptoms, stenosis and carotid plaque morphology. Is plaque morphology relevant? *European Journal of Vascular and Endovascular Surgery*, vol. 9(1), pp. 80-85.
- [46] T. J. Pedley (1980), *The fluid mechanics of large blood vessels*. Cambridge : Cambridge University Press, 1980.
- [47] L. B. Goldstein (2003), Extracranial carotid artery stenosis. *Stroke*, vol. 34, pp. 2767-2773.
- [48] N. Nighoghossian, L. Derex, and P. Douek (2005), The vulnerable carotid artery plaque - current imaging methods and new perspectives. *Stroke*, vol. 36, pp. 2764-2772.

- [49] L. G. Spagnoli, A. Mauriello, G. Sangiorgi, *et al.* (2004), Extracranial thrombotically active carotid plaque as a risk factor for ischemic stroke. *Journal of the American Medical Association*, vol. 292, pp. 1845-1852.
- [50] Y. Alemu and D. Bluestein (2007), Flow-induced platelet activation and damage accumulation in a mechanical heart valve: Numerical studies. *Artificial Organs*, vol. 31, pp. 677-88.
- [51] S. Raz, S. Einav, Y. Alemu, *et al.* (2007), DPIV prediction of flow induced platelet activation - comparison to numerical predictions. *Annals of Biomedical Engineering*, vol. 35, pp. 493-504.
- [52] S. Shadden and S. Hendabadi (2012), Potential fluid mechanic pathways of platelet activation. *Biomechanics and Modeling in Mechanobiology*, pp. 1-8.
- [53] D. Massai, G. Soloperto, D. Gallo, *et al.* (2012), Shear-induced platelet activation and its relationship with blood flow topology in a numerical model of stenosed carotid bifurcation. *European Journal of Mechanics B-Fluids*, vol. 35, pp. 92-101.

Chapter 6

6 Summary, Conclusion, and Future Work

6.1 Summary of Studies

6.1.1 Summary of Chapter 3

Chapter 3 detailed the *in vitro* study performed using stereoscopic PIV in three models of carotid bifurcations including healthy (normal) geometry, a moderate stenosis, and a severe stenosis. The level of flow complexity was assessed via proper orthogonal decomposition (POD). The volumetrically reconstructed velocity maps obtained from multiple measurement planes throughout the lumen enabled the assessment of 3D flow patterns. The dominant characteristics of flow in both stenosed models was the helical swirling motion generated immediately downstream of the jet persisting to a further extent with a severe stenosis. The instantaneous velocity maps depicted the presence of vortex shedding along the shear layers. The vortex shedding was the main smaller coherent feature present in intermediate eigenmodes, with larger vortices associated more with the severe stenosis compared to the moderate one. This vortex shedding may be the underlying contributor to the inertial range in which energy was sustained with a flatter spectrum associated with the severe stenosis. The slope of exponential decay in the inertial sub-range of the energy spectrum, as well as the entropy values clearly reflected the stage of stenosis severity, hence the progression of disease. These two metrics were thus introduced as two clinically applicable indices indicative of the level of flow complexity and instabilities. To assess the potential performance of these parameters with clinical modalities for which lower temporal resolutions are expected, POD analysis was applied to velocity measurements acquired with various temporal resolutions ranging from 100 to 500 Hz. Based on the convergence test it was shown that the first two modes adequately capture the dominate energy content of the flow for all temporal resolutions indicating the sufficiency of 100 Hz. However, the entropy value was found to require a minimum of 400 Hz for convergence. This study provided detailed information of stenotic flow, which generally is just understood as flow separation regions and downstream instabilities. The metrics introduced in this study are applicable to clinical

diagnosis without the necessity of ECG gating as required for statistical-based analysis of flow disturbances. This work has been published in *Medical Engineering and Physics* [1].

6.1.2 Summary of Chapter 4

Chapter 4 detailed the *in vitro* study performed to investigate the individual and combined effects of stenosis severity, plaque eccentricity, and ulceration on the downstream flow disturbances in the carotid models. For this purpose, a comprehensive series of eight carotid bifurcation models, representing various stages of disease progression, were examined. The series included a healthy (normal) model, two 30% (concentric and eccentric), three 50% (concentric, eccentric, and ulcerated), and two 70% (concentric and eccentric) stenosed models of the carotid bifurcation. Initially, a detailed analysis of flow features and velocity profiles was performed through which the effect of geometry was clearly demonstrated. Different to the concentric models' dominant feature of helical swirling motion, eccentric models showed two regions of recirculation zones created on either side of the jet. In the ulcerated model, the size of the outer-wall recirculation zone was found to be larger compared to the non-ulcerated eccentric model. The statistical metric of turbulence intensity (TI) was employed as the quantifiable parameter derived based on an ensemble-averaging method and derived throughout the entire volume for each model. Different patterns of downstream TI elevation were observed when comparing the counterpart pairs of concentric and eccentric models, and TI elevation was located at the downstream region of flow separation, which occurred further downstream in the concentric models. The elevated downstream TI region was averaged over a defined region of interest. The progression of TI level over the course of the cardiac cycle showed an apparent peak at the flow deceleration phase (i.e. systolic downstroke) for all stenosed models. Comparison across the eight models revealed that, besides the increase with increasing stenosis severity, plaque eccentricity also enhances the turbulence level. No significant difference was found between TI values in an eccentric plaque and the concentric plaque of the next group of stenosis severity (e.g. TI in 50% eccentric model matched that of the 70% concentric). For the single 50% ulcerated eccentric model, ulceration was associated with a larger recirculation zone thus a larger area or volume of TI within this zone. This study showed that the quantifiable

metric of turbulence intensity may provide a clinical index capable of reflecting the more detailed plaque geometry such as plaque eccentricity. This work is under final review for the *Journal of Biomechanics* [2].

6.1.3 Summary of Chapter 5

As an extension of the work described in Chapter 4, Chapter 5 aimed specifically at the investigation of shear stress detailing, comparatively, its levels and patterns under the effect of varying plaque geometry. The phased-averaged flow provided a means for evaluating the laminar shear stress, both for the free (non-wall) shear layers and at the wall (WSS). Specific to each group of concentric and eccentric models, different extents and regions of FSS and WSS were recognized. In concentric models, two WSS regions were identified along the outer wall, while no elevated-WSS region was found downstream of the stenosis throat along the inner wall. In the eccentric models, however, WSS was significantly elevated along both walls, with the outer wall showing additional WSS regions associated with the recirculation zone. Along the outer wall for which both plaque symmetries showed significant WSS, the decay from the maximum WSS at the stenosis throat was found to be notably steeper in the eccentric model. The adjacency of this region to the low-WSS recirculation zone may promote a favorable environment for thrombosis, as described earlier. Assessment of the time progression of the laminar shear-stress levels revealed a longer sustention of the same range of values were associated with an eccentric model as compared to the concentric counterpart. In the examined 50% eccentric model, ulceration resulted in both higher levels and longer sustention of laminar shear stress compared to the matched non-ulcerated model. The fluctuations from phase-averaged means were applied towards calculation of Reynolds and total shear stress values. Assessing the in-plane map of RSS in models of concentric, eccentric, and ulcerated eccentric revealed a larger expansion of RSS in the eccentric models, which was associated with the breakdown of vortices in the larger recirculation zone during the deceleration phase when flow is most unstable. Furthermore, levels of total shear stress were found to be quite different for changes in both stenosis severity and plaque symmetry. This study aimed to provide qualitative and quantitative bases for future application of particle-trajectory calculations for deriving metrics representative of the

cumulative level of thrombotic activity. This work is under preparation for submission to *PLOS ONE*.

6.2 Conclusion

The incidence of thrombosis leading to a higher risk of ischemic stroke and the association of thrombosis with the hemodynamic factors of turbulence and shear stress motivated the current work. Based on the previously proven increased risk of stroke for patients with higher degree of stenosis severity, eccentric plaques, and ulcerated plaques, the hypothesis was formed that these plaque features can lead to a higher level of turbulence and shear stress. This hypothesis was proven as increased level of turbulence was observed with increasing stenosis severity and eccentricity. Although an increase in turbulence was seen with increasing stenosis severity regardless of plaque type, the percent increase of TI from mild to moderate to severe stenosis was found to be higher for the concentric models (133% increase from 30% to 50% stenosis and 32% increase from 50% to 70% stenosis) compared to the increase observed for eccentric stenoses (50% TI increase from 30% to 50% stenosis and 27% from 50% to 70% stenosis). It can already be postulated that the classification of stenosis ‘*severity*’ based only on lumen diameter may not be the optimal metric, and eccentricity of the plaque should also be included in the grading and categorization of the stenosis. In fact, for any given degree of stenosis severity, an increased turbulence level was observed for the eccentric form of plaque symmetry compared to the concentric counterpart. The highest level of increase was observed for the mild stenosis pair with increasing TI by 83% from concentric 30% to eccentric 30% stenosis. TI increased by 18% in the moderate eccentric stenosis (i.e. 50% diameter reduction) and by 13.5% in the severe eccentric stenosis (70%) compared to their concentric counterparts. Statistical analysis, showed that the TI level measured in the 50% eccentric model was not significantly different from the TI level in the 70% concentric stenosis. This finding suggests that independent of the degree of stenosis, eccentric plaques may pose the same level of stroke risk as may be expected for the next higher category of stenosis constriction. Again, this emphasizes the need for a more sensitive classification of stenosis ‘*severity*’ that is also reflective of plaque symmetry rather than only being based on lumen reduction.

The findings from both the turbulence analysis and shear stress analysis are complementary in providing insight on how increasing degree of stenosis severity, eccentric versus concentric plaque, and ulcerated plaques are more suggestive of increased risk of cerebrovascular events. In fact, in order to understand the hemodynamic-induced mechanism of thrombosis, it is essential to study the effect of both turbulence and shear stress in combination; by investigating the laminar shear stress, regions of elevated free shear layers were recognized along the jet path in both concentric and eccentric models. The platelets that come into contact with this layer can potentially be activated. During the systolic deceleration phase when prominent flow turbulence is expected, the activated platelets can be convected from the disturbed recirculation, which includes small vortices, towards the wall and thus promote thrombosis. The activated platelets can also be trapped in the vortices shed along the jet, thus forming free emboli and then convected distally by the downstream flow disturbance. Although a similar range of elevated free shear stress was found for concentric and eccentric plaque of the same stenosis severity, the adjacency of the free shear layer and the large recirculation zone, which contains elevated TI, in the eccentric model may potentially translate to higher thrombotic activity when both shear stress and turbulence effects are considered. By increasing the stenosis severity, maximum free shear stress approximately doubled with each increase of stenosis severity from 30% to 50% to 70%. The potentially higher thrombogenicity of eccentric plaques can be postulated due to the steeper decay of post-stenotic wall shear stress, which – as described previously – is linked to larger platelet aggregation formed at this region. With the presence of elevated TI in the recirculation zone, which is located further upstream of the stenosis compared to each counterpart concentric, the unstable thrombus may break loose and be transported downstream resulting in an acute clot clogging incident.

One of the goals of this study was to explore alternative methods of turbulence quantification beside the conventional ensemble-averaging method of turbulence intensity, which is based on the level of velocity fluctuations induced by cycle-to-cycle variability. The advantage of TI analysis is that it enables quantified 3D mapping of flow disturbances for each time point of the cardiac cycle, which can be beneficial in locating the regions of elevated turbulence or flow instability. For instance, by comparing the TI

maps for the ulcerated and non-ulcerated 50% eccentric models, the subtle differences in turbulence distribution between the two models was revealed with the ulcerated model showing larger distribution of turbulence in the recirculation zone. The elevated TI in the recirculation zone in the ulcerated model seems to be what contributed to the captured maximum TI in the ulcerated model when previously assessed with Doppler ultrasound, which did not appear to be capable of resolving the smaller scales of turbulence occurring downstream at the tail of the jet.

The turbulence intensity method, however, is an ensemble-averaging method requiring acquisition of multiple cardiac cycles, which need to be correlated in time for phase averaging. This can impose a limitation for clinical assessment in which the multiple acquisition of cardiac cycle may not be possible due to potential patient movement as well as inaccessibility of the ECG signal necessary for synchronized acquisition of each cardiac cycle. Additionally, once the TI map are acquired, certain criteria, such as averaging over a region of interest, are required to quantify the level of turbulence in a single value. The result of this thesis showed that a model-specific ROI should be selected based on plaque geometry, which again can be a tedious task in a clinical situation. To overcome this limitation the method of POD analysis was employed in which the level of flow instability was quantified using the energy content of all modes. Examined for the three models of normal, 50% and 70% concentric model, this method clearly demonstrated benefits over the conventional TI method by eliminating the requirement of ECG gating, ROI selection, and multiple cardiac cycle acquisition. Moreover, via acquisition of the single cardiac cycle with varying temporal resolutions, the conducted convergence test revealed that a temporal resolution of 100 Hz, which is an achievable recording rate with clinical Doppler ultrasound, would be sufficient for application of POD analysis. For future studies, it would be of interest to assess the capability of this technique in capturing the energy content differences that were revealed via the TI analysis in the eccentric and ulcerated models. Also, it would be of interest to investigate how sufficient signal-to-noise ratio (SNR) can be obtained using POD for a single cardiac cycle, as used in the study of this thesis, versus the improvement of the SNR level by using multiple cardiac cycles in POD analysis.

6.3 Future Directions

6.3.1 Turbulence quantification using high-frame-rate DUS

Future work will be directed towards the quantification of turbulence using the clinical modality of DUS. As discussed earlier, ultrasound offers a cost-effective and non-invasive diagnostic tool and is currently used for front-line examination before patients go through more elaborate and costly methods, such as MRI. TI has previously been quantified employing a conventional DUS system based on ensemble averaging of the mean velocity derived from spectral DUS [3-5], similar to the PIV ensemble-averaging method described in Chapter 4. Since only a single velocity measurement in the assigned sample volume is possible with DUS, the FOV was raster scanned to build TI maps in the above DUS studies. Comparison between the DUS and PIV TI maps of matched models shows qualitative agreement, and similarly eccentric plaques were found to be associated with higher amounts of turbulence. However, in DUS only the magnitude velocity in the direction of the transducer is captured thus contributing to an underestimation in TI compared to stereo-PIV, which provides all three components of the velocity.

Although the ensemble-averaging and raster-scanning methods can readily be applied to *in vitro* DUS studies, in clinical situations they can prove to be cumbersome owing to the considerably long acquisition time for multiple cardiac cycles or raster scanning and the need for cardiac (i.e. ECG) gating for phase synchronization, which are not part of a typical clinical protocol.

To circumvent these limitations, an alternative ultrasound method is sought that can provide full-field velocity maps thus eliminating the raster-scanning requirement. As discussed earlier, a new class of ultrafast ultrasound enables full-field acquisition of velocity maps with up to two in-plane components with frame rates in the order of kilohertz. We propose employing high-frame-rate color Doppler imaging methods, such as shown by Yiu and Yu [6] in a carotid artery with 25% stenosis. In their described method, three new additions (as opposed to conventional color Doppler) will result in significant improvement in the number of frame per second: plane-wave transmission, parallel receiving of pre-beamformed (raw) data from all channels, and parallel

beamforming. Our experiments are at preliminary stage and will be carried out in a recently fabricated vertical carotid artery model with 50% stenosis. A SonixRP ultrasound system will be used and is equipped with a multi-channel data acquisition module (SonixDAQ) that enables parallel acquisition (128 channels) of pre-beamformed data [7]. Plane waves will be transmitted with maximum pulse repetition frequency (PRF) of 10 kHz. Post-processing steps will be carried out in MATLAB-based programs. To achieve a high-resolution image, angular compounding of multiple (e.g. five) frames will be used yielding a lesser frame rate (e.g. 2 kHz) than the original PRF. Once the color maps are generated for multiple cardiac cycles, TI maps can be generated and compared to PIV measurements. Current limitations of this method, beside the single-component velocity measurements as mentioned above, is to incorporate ECG gating and also improve the signal-to-noise ratio by perhaps modifying the applied band-pass filter.

The implementation of POD-based turbulence quantification, as described in Chapter 3, overcomes the ECG-gating requirement. Moreover, our proposed POD-based turbulence quantification only requires a single cardiac acquisition. Two metrics – (1) exponential slope of inertial sub-range (i.e. intermediate modes) of the energy spectrum and (2) global entropy value – were demonstrated for quantifying turbulence. In order to obtain an approximate assessment of the effect of single-component velocity on the shape of the energy spectrum, a fractional energy spectrum derived from original 2D-3C velocity maps in a 70% concentric model is compared to a DUS-simulated energy spectrum as shown in Figure 6.1. The DUS-simulated velocity maps were obtained from original PIV velocity maps by only including the magnitude of the in-plane velocity component in the direction of an assumed Doppler angle of 65° (i.e. with the transducer lying in the x-y plane and a 65° steering angle relative to the x axis).

Figure 6.1a shows a comparison of the described energy spectra acquired with a 500-Hz frame rate. Compared to the first energy mode of the PIV spectrum ($\sim 72\%$ of energy), the first mode in the DUS-simulated energy spectrum contains higher energy (82%) indicating that less of the turbulent energy is captured in the DUS-simulated velocity maps. However, comparison of the inertial sub-range shows close proximity between the two energy spectra resulting in similar decay slopes. In the DUS-simulated spectrum,

faster dissipation is observed, which compensates for the higher first-mode energy, thus conserving the total energy under the spectrum and making it equal to that of PIV. The faster dissipation in the DUS-simulated spectrum can be attributed to the lack of an out-of-plane component resulting in less sustention of turbulent energy.

Also, similar to the observation in the PIV-based POD energy spectrum in Chapter 3, lower temporal resolution does not result in notable change in the slope of the energy decay in the inertial range, as shown in Figure 6.1b for 100 and 500-Hz DUS-simulated spectra. A first mode energy of about 82% was captured in both cases. A larger velocity grid spacing of 0.6 mm – as typical of conventional DUS – resulted in a higher energy of the first mode (~85%); however, the overall shape of the energy spectrum was preserved by the lower energy levels in the remaining modes.

Future work will assess the possibility of POD-based turbulence quantification using high-frame-rate color Doppler ultrasound and validation with PIV measurements. Similar geometries of carotid artery models will be employed allowing direct comparison with our previous studies. It is expected that POD-based turbulence quantification could be further facilitated if ECG-gating was available, in which case only the portion of the cardiac cycle associated with the highest level of turbulence could be acquired for POD assessment as proposed by Grinberg *et al.* [8]. In this case, only the window containing the systolic deceleration phase of the cardiac cycle would need to be analyzed.

6.3.2 Compliant carotid artery models

Complexity of the carotid artery flow is governed by vessel geometry, especially in the presence of stenosis, and flow pulsatility. To a lesser degree wall compliance can also impact the flow pattern [9]. In this current work, the carotid artery bifurcation phantoms used can be considered as rigid walled. One of the future directions is to incorporate compliance in the carotid artery bifurcation phantoms. Arterial compliance – an index of elasticity – degrades due to several risk factors including aging or diseases such as atherosclerosis and diabetes.

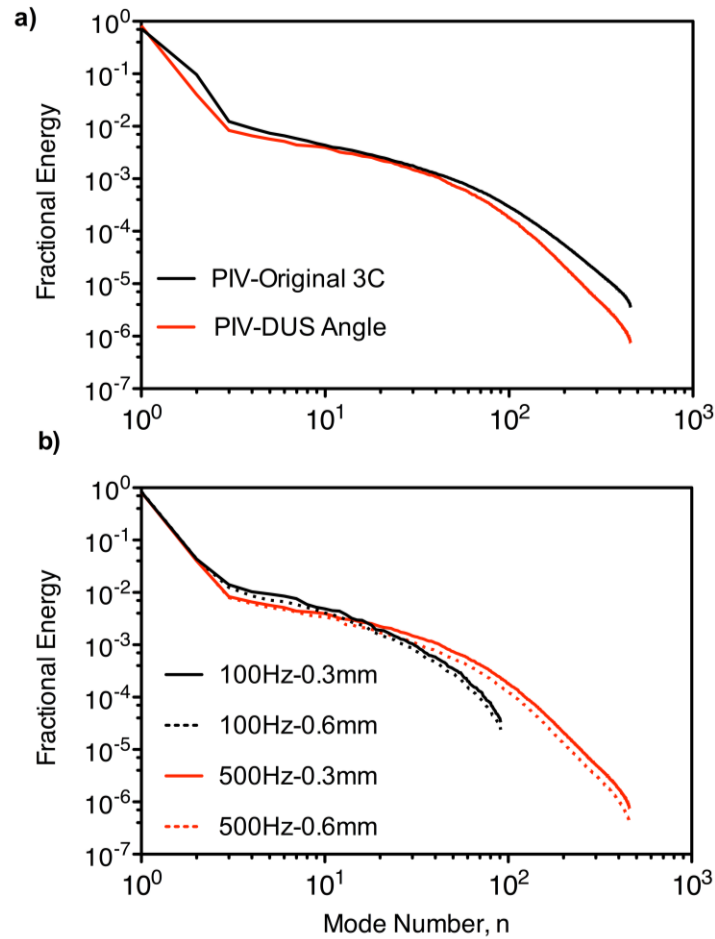


Figure 6.1: DUS-simulated POD energy spectra derived from PIV velocity measurements. Comparison of (a) PIV and DUS-simulated energy spectra obtained in a 70% concentric model of the carotid artery, and (b) DUS-simulated POD energy spectra using two different temporal resolutions and two different sample volumes in the same carotid artery model.

A limited number of previous studies have focused on the effect of compliance in flow patterns through comparisons with matched rigid arteries. Reneman *et al.* [10] characterized flow in the normal carotid arteries of two groups of younger and older volunteers using multigate DUS. At the sinus bulb, flow separation and recirculation was found to be less pronounced and less frequent in older subjects in which vessel compliance was lower compared to the younger group. However, the velocity and flow patterns in the younger group (i.e. compliant cases) were reported to be similar to those characterized *in vitro* in a non-compliant glass model of the normal carotid artery [11]. In

contrary, in the *in vitro* study by Liepsch *et al.* [12], wall compliance was found to eliminate the occurrence of flow reversal along the lateral walls of the femoral bifurcation.

Anayiotos *et al.* [13] performed a LDA study under pulsatile inlet flow in a compliant model of a normal carotid artery bifurcation and compared the shear-stress measurements to that of an identical rigid model. Along various locations in the ICA, a reduction of about 30% in mean WSS and 100% in peak WSS was observed in the compliant model. The separation point was also shifted upstream in the compliant model suggesting an axially larger recirculation zone.

Perktold and Rappitsch [14] conducted a numerical simulation using a finite-element method coupled with fluid-structure interactions to model the flow in a compliant and rigid-walled normal carotid artery bifurcation. Overall, similar flow patterns in both models were observed. The reported differences were associated with axial velocity magnitude and changed by the phase of the cardiac cycle. During systolic acceleration, axial velocity in the internal branch was lower in the compliant model owing to higher pressure. In the deceleration phase, when pressure decreased and the vessel contracted, the axial velocity in the compliant model increased. In this phase, both models showed flow separation and the presence of recirculation in the sinus bulb; however, the reversed flow was found to be slower in the compliant model compared to the rigid wall. Alternatively, at the flow-divider side, flow was faster in the compliant model. Furthermore, as compliance decreased, it resulted in a decrease in WSS level by 25% compared to the rigid wall.

Based on the evidence from the previous studies in various bifurcation sites, it can be concluded that arterial compliance affects the WSS levels and patterns. The majority of these studies, however, were conducted in the normal human carotid bifurcation. It would be of interest to investigate the compliance effect on stenotic flows which have significantly higher shear-stress levels at the throat followed by post-stenotic low-WSS regions. Compliance has been shown to affect levels of WSS differently by lowering the level in regions of low WSS and resulting in an increase in regions with high WSS [15].

Future work will consider the effect of compliance incorporated in the modeling of carotid bifurcations with similar geometries as used in the current work. The new PIV-compatible compliant phantoms are manufactured using the same silicone material as here but in a manner similar to thin-walled DUS phantoms as described in Poepping *et al.* [16] without the surrounding ultrasound tissue-mimicking materials. Employing the same geometries, as those used in this thesis, will allow for direct assessment of the compliance effect on hemodynamic parameters such as shear stress and downstream disturbances. It will also be of interest to investigate the change in flow features such as the length of the recirculation zone, helical swirling motion, and pattern of downstream vortex shedding.

It should also be noted that in compliant arteries, pressure and flow are out of phase as the consequence of vessel elasticity. It is estimated that in large or medium-sized arteries this phase angle is about 45° [17]. In future work, the phase angle can also be quantified in the diseased carotid artery models, similar to the study by Karri and Vlachos [18] in simple compliant stenosed tubes.

6.3.3 Numerical simulations

Numerical simulations can assist with studies that are difficult to implement experimentally. Numerical simulations facilitate the modeling of patient-specific arterial geometries (e.g. [8, 19] among many others), the non-Newtonian blood behaviors (e.g. [20, 21] among many others), and compliant arteries (e.g. [22, 23] among many others). Future work will also be directed at employing numerical simulations of the flow in stenosed carotid artery models that are also affected by peripheral factors, such as aging, and other systemic diseases, such as diabetes. Various degrees of arterial compliance will be simulated, as well as varying flow-waveform pulsatility and downstream flow resistance, mimicking different stages of local and systemic disease. Modeling the patient-specific geometries and inclusion of turbulent models are also considered. The first stage of study will include validation with PIV measurements by utilizing the same geometries.

Numerical simulations can also enable virtual particle tracking to extract more directly associated thrombotic activity factors through residence times and level of shear-stress

exposure. Under steady-inlet flow conditions it is estimated that a residence time of about 10 s is required for platelets to be activated significantly [24]. In less than this critical time, 99% of platelets are expected to be washed out as reported by Cao and Rittgers [25] and Tambasco and Steinman [26]. Both studies also reported that the residence time of platelets is insensitive to the severity of stenosis. Also, in their studied models of 30% eccentric and concentric stenosed carotid arteries with similar geometries as used in the current work, Tambasco and Steinman [26] reported no significant difference between the residence times of the two models. Of interest will be assessing the effect of plaque eccentricity with higher stenosis severity, as well as the effect of ulceration on platelet residence time. Although no significant difference was found in the residence time alone, the shear-stress associated residence time, such as maximum shear-stress exposure, was found to be significantly higher in the eccentric model. Of interest will be quantifying these levels based on various degrees of stenosis severity and different shapes of plaque symmetries with the long-term objective of introducing this factor as a clinical assessment of thrombotic activity level.

6.4 References

- [1] S. Kefayati and T. L. Poepping (2013), Transitional flow analysis in the carotid artery bifurcation by proper orthogonal decomposition and particle image velocimetry. *Medical Engineering & Physics*, vol. 35, pp. 898-909.
- [2] S. Kefayati, D. W. Holdsworth, and T. L. Poepping (2013), Turbulence intensity measurements using particle image velocimetry in diseased carotid artery models: Effect of stenosis severity, plaque eccentricity, and ulceration. *Journal of Biomechanics*, vol. under revision,
- [3] T. L. Poepping, R. N. Rankin, and D. W. Holdsworth (2010), Flow patterns in carotid bifurcation models using pulsed Doppler ultrasound: Effect of concentric vs. Eccentric stenosis on turbulence and recirculation. *Ultrasound in Medicine and Biology*, vol. 36, pp. 1125-1134.
- [4] E. Y. Wong, H. N. Nikolov, R. N. Rankin, *et al.* (2013), Evaluation of distal turbulence intensity for the detection of both plaque ulceration and stenosis grade in the carotid bifurcation using clinical Doppler ultrasound. *European Radiology*, vol. 23, pp. 1720-1728.

- [5] E. Y. Wong, H. N. Nikolov, M. L. Thorne, *et al.* (2009), Clinical Doppler ultrasound for the assessment of plaque ulceration in the stenosed carotid bifurcation by detection of distal turbulence intensity: A matched model study. *European Radiology*, vol. 19, pp. 2739-2749.
- [6] B. Y. S. Yiu and A. C. H. Yu (2013), High-frame-rate ultrasound color-encoded speckle imaging of complex flow dynamics. *Ultrasound in Medicine and Biology*, vol. 39, pp. 1015-1025.
- [7] f. IEEE transactions on ultrasonics, and frequency control Cheung, Chris C. P., A. C. H. Yu, N. Salimi, *et al.* (2012), Multi-channel pre-beamformed data acquisition system for research on advanced ultrasound imaging methods. *IEEE Transactions on Ultrasonics Ferroelectrics and Frequency Control*, vol. 59, pp. 243-253.
- [8] L. Grinberg, A. Yakhot, and G. E. Karniadakis (2009), Analyzing transient turbulence in a stenosed carotid artery by proper orthogonal decomposition. *Annals of Biomedical Engineering*, vol. 37, pp. 2200-2217.
- [9] A. I. Barakat and D. K. Lieu (2003), Differential responsiveness of vascular endothelial cells to different types of fluid mechanical shear stress. *Cell Biochemistry and Biophysics*, vol. 38, pp. 323-343.
- [10] R. S. Reneman, T. Vanmerode, P. Hick, *et al.* (1985), Flow velocity patterns in and distensibility of the carotid-artery bulb in subjects of various ages. *Circulation*, vol. 71, pp. 500-509.
- [11] D. N. Ku and D. P. Giddens (1983), Pulsatile flow in a model carotid bifurcation. *Arteriosclerosis*, vol. 3, pp. 31-39.
- [12] D. Liepsch and S. Moravec (1984), Pulsatile flow of non-newtonian fluid in distensible models of human arteries. *Biorheology*, vol. 21, pp. 571-586.
- [13] A. S. Anayiotos, S. A. Jones, D. P. Giddens, *et al.* (1994), Shear-stress at a compliant model of the human carotid bifurcation. *Journal of Biomechanical Engineering*, vol. 116, pp. 98-106.
- [14] K. Perktold and G. Rappitsch (1995), Computer-simulation of local blood-flow and vessel mechanics in a compliant carotid-artery bifurcation model. *Journal of Biomechanics*, vol. 28, pp. 845-856.
- [15] D. D. Duncan, C. B. Barger, S. E. Borchardt, *et al.* (1990), The effect of compliance on wall shear in casts of a human aortic bifurcation. *Journal of Biomechanical Engineering-Transactions of the ASME*, vol. 112, pp. 183-188.
- [16] T. L. Poepping, H. N. Nikolov, M. L. Thorne, *et al.* (2004), A thin-walled carotid vessel phantom for Doppler ultrasound flow studies. *Ultrasound in Medicine and Biology*, vol. 30, pp. 1067-1078.

- [17] Y. C. Qiu and J. M. Tarbell (2000), Numerical simulation of pulsatile flow in a compliant curved tube model of a coronary artery. *Journal of Biomechanical Engineering-Transactions of the ASME*, vol. 122, pp. 77-85.
- [18] S. Karri and P. P. Vlachos (2010), Time-resolved DPIV investigation of pulsatile flow in symmetric stenotic arteries effects of phase angle. *Journal of Biomechanical Engineering-T. ASME*, vol. 132,
- [19] S. E. Lee, S.-W. Lee, P. F. Fischer, *et al.* (2008), Direct numerical simulation of transitional flow in a stenosed carotid bifurcation. *Journal of Biomechanics*, vol. 41, pp. 2551-2561.
- [20] M. M. Molla, B.-C. Wang, and D. C. S. Kuhn (2012), Numerical study of pulsatile channel flows undergoing transition triggered by a modelled stenosis. *Physics of Fluids*, vol. 24,
- [21] A. Leuprecht and K. Perktold (2001), Computer simulation of non-newtonian effects on blood flow in large arteries. *Computer Methods in Biomechanics and Biomedical Engineering*, vol. 4, pp. 149-63.
- [22] S. Tada and J. M. Tarbell (2005), A computational study of flow in a compliant carotid bifurcation-stress phase angle correlation with shear stress. *Annals of Biomedical Engineering*, vol. 33, pp. 1202-1212.
- [23] Y.-H. Kim, J.-E. Kim, Y. Ito, *et al.* (2008), Hemodynamic analysis of a compliant femoral artery bifurcation model using a fluid structure interaction framework. *Annals of Biomedical Engineering*, vol. 36, pp. 1753-1763.
- [24] P. Y. Huang and J. D. Hellums (1993), Aggregation and disaggregation kinetics of human blood-platelets .2. Shear-induced platelet-aggregation. *Biophysical Journal*, vol. 65, pp. 344-353.
- [25] J. Cao and S. E. Rittgers (1998), Particle motion within in vitro models of stenosed internal carotid and left anterior descending coronary arteries. *Annals of Biomedical Engineering*, vol. 26, pp. 190-199.
- [26] M. Tambasco and D. A. Steinman (2003), Path-dependent hemodynamics of the stenosed carotid bifurcation. *Annals of Biomedical Engineering*, vol. 31, pp. 1054-1065.

Appendix A

Proper Orthogonal Decomposition (POD)

Formulation

While snapshot POD has been described in the past [1], we have adopted the formalism of Meyer *et al.* [2] who categorized the required steps of POD calculations in a series of simple steps described briefly in the equations below. The first step is to create the velocity matrix of U :

$$U = \begin{bmatrix} u^1 & u^2 & \cdots & u^N \end{bmatrix} = \begin{bmatrix} u_1^1 & u_1^2 & \cdots & u_1^N \\ \vdots & \vdots & \vdots & \vdots \\ u_M^1 & u_M^2 & \cdots & u_M^N \\ v_1^1 & v_1^2 & \cdots & v_1^N \\ \vdots & \vdots & \vdots & \vdots \\ v_M^1 & v_M^2 & \cdots & v_M^N \\ w_1^1 & w_1^2 & \cdots & w_1^N \\ \vdots & \vdots & \vdots & \vdots \\ w_M^1 & w_M^2 & \cdots & w_M^N \end{bmatrix}, \quad (\text{A.1})$$

where u , v , and w represent the three velocity components, N represents the number of the snapshots (i.e. possible maximum number of modes), and M is the total number of vector positions in each velocity field. Note that the above arrangement of the velocity matrix is independent of the positions of the vectors. From the velocity matrix, the $N \times N$ auto-correlation matrix C can then be created as:

$$C = U^T U. \quad (\text{A.2})$$

The corresponding eigenvalue problem can be solved by:

$$CA^i = \lambda^i A^i, \quad (\text{A.3})$$

where λ is the eigenvalue (also referred to as the mode energy) and A is the eigenvector.

Eigenvalues are then arranged and numbered in decreasing order of size as follows:

$$\lambda^1 > \lambda^2 > \dots > \lambda^N = 0. \quad (\text{A.4})$$

The above arrangement of the eigenvalues is to ensure that the modes are also arranged in decreasing order in terms of their energy content. The POD spatial modes (i.e. eigenfunctions), $\phi^i(\vec{x})$, can then be generated based on the calculated eigenvectors:

$$\phi^i = \frac{\sum_{n=1}^N A_n^i \mathbf{u}^n}{\left\| \sum_{n=1}^N A_n^i \mathbf{u}^n \right\|}, \quad i = 1, \dots, N, \quad (\text{A.5})$$

where A_n^i is the n^{th} component of the i^{th} eigenvector corresponding to λ^i , and $\|, \|$ represents the 2-norm defined as:

$$\|y\| = \sqrt{y_1^2 + y_2^2 + \dots + y_M^2}. \quad (\text{A.6})$$

The POD coefficients, a_i , are then calculated by projecting the velocity field onto the POD spatial modes:

$$a_i^n = \phi^i \mathbf{u}^n, \quad \text{or} \quad \mathbf{a}^n = \Phi^T \mathbf{u}^n, \quad (\text{A.7})$$

where $\Phi = [\phi^1 \quad \phi^2 \quad \dots \quad \phi^N]$. Each snapshot of the velocity field can be reconstructed from the first N^{th} POD spatial modes and corresponding temporal coefficients as follows:

$$\mathbf{u}^n = \sum_{i=1}^N a_i^n \phi^i = \Phi \mathbf{a}^n. \quad (\text{A.8})$$

It can be shown [3] that the total kinetic energy of the flow is:

$$E = \sum_{i=1}^N \lambda^i, \quad (\text{A.9})$$

with the fractional (or relative) energy contribution of each mode being:

$$E^i = \frac{\lambda^i}{E}. \quad (\text{A.10})$$

When POD is applied to instantaneous velocity fields, the first spatial mode represents the time-averaged flow; in this case turbulent kinetic energy is normally defined [4] by deducting the first eigenvalue – which is the energy within the first eigenfunction – from the total energy content. This is intuitively similar to statistical measures of turbulence intensity, which correspond to fluctuations about the mean flow. More information on POD analysis and its theoretical background can be found elsewhere [1, 3].

Spatio-temporal complexity of the flow can be described by the energy distribution over the POD eigenfunctions. Aubry *et al.* [5] suggested the concept of global entropy in order to quantitatively describe the level of the complexity in the flow. In this concept, entropy provides a probability value that varies between the extremes of 0 and 1, with the former referring to the hypothetical case that all the energy content of the flow is contained within the first mode, and the latter referring to the case that the total energy of the flow is distributed evenly across all the modes. For transitional flow states – a mixture between laminar and turbulent flow – the energy of the eigenfunctions spreads more uniformly across the intermediate modes resulting in a plateau in the energy spectrum, and thus an increase in the entropy. The normalized global entropy is defined as follows [5]:

$$H = -\frac{1}{\ln N} \sum_{n=1}^N \frac{\lambda_n}{\lambda_{tot}} \ln \frac{\lambda_n}{\lambda_{tot}}. \quad (\text{A.11})$$

References

- [1] D. Hilberg, W. Lazik, and H. E. Fiedler (1994), The application of classical pod and snapshot pod in a turbulent shear-layer with periodic structures. *App. Sci. Res.*, vol. 53, pp. 283-290.
- [2] K. E. E. Meyer, J. M. Pedersen, and O. Ozcan (2007), A turbulent jet in crossflow analysed with proper orthogonal decomposition. *J. Fluid Mech.*, vol. 583, pp. 199-227.

- [3] P. Holmes, J. L. Lumley, and G. Berkooz (1998), *Turbulence, coherent structures, dynamical systems and symmetry*. Cambridge University Press, Cambridge.
- [4] A. S. Cruz, L. David, J. Pecheux, *et al.* (2005), Characterization by proper-orthogonal-decomposition of the passive controlled wake flow downstream of a half cylinder. *Exp. Fluids*, vol. 39, pp. 730-742.
- [5] N. Aubry, R. Guyonnet, and R. Lima (1991), Spatiotemporal analysis of complex signals - theory and applications. *J. Stat. Phys.*, vol. 64, pp. 683-739.

Appendix B

Vortex Identification

The λ_{ci} -criterion method of vortex identification is based on the velocity gradient tensor, which – in the case of 2D PIV velocity fields – is generated from the u and v velocity components corresponding to x and y directions, respectively, as follows:

$$D = \begin{bmatrix} \frac{\partial u}{\partial x} & \frac{\partial u}{\partial y} \\ \frac{\partial v}{\partial x} & \frac{\partial v}{\partial y} \end{bmatrix}. \quad (\text{B.1})$$

The two eigenvalues of the gradient tensor are either a pair of real eigenvalues or two complex eigenvalues. As has been shown by Zhou *et al.* [1], the strength of the local swirling motions present in the flow field can be quantified by the imaginary part of the complex eigenvalues referred to as λ_{ci} or the “swirling strength”. A vortex is present when $\lambda_{ci} > 0$ [2]. Once the tensor is generated, in the case of existing complex eigenvalues, λ_{ci} is computed as follows:

$$\lambda_{ci} = \frac{1}{2} \sqrt{\left(\frac{\partial u}{\partial x} - \frac{\partial v}{\partial y} \right)^2 + 4 \left(\frac{\partial u}{\partial y} \times \frac{\partial v}{\partial x} \right)}. \quad (\text{B.2})$$

By nature, all the calculated λ_{ci} are positive values, and therefore no information about the rotational direction of the swirling motion can be extracted from the above calculation.

Clockwise and counter-clockwise rotation were distinguished using the approach suggested by Christensen *et al.* [3], where a modified swirling strength, based on the calculated vorticity (ω_z), was defined as follows:

$$\lambda_{ci}^* = \lambda_{ci} \frac{\omega_z}{|\omega_z|}, \quad \omega_z = \frac{\partial u}{\partial x} - \frac{\partial v}{\partial y}. \quad (\text{B.3})$$

which includes a rotation sign – negative for clockwise and positive for counter-clockwise in our case. It should also be noted that swirling strength does not uniquely refer to closed swirling motion (i.e. a vortex) as it includes open-bending type motions, but avoids shearing gradients.

References

- [1] J. Zhou, R. J. Adrian, S. Balachandar, *et al.* (1999), Mechanisms for generating coherent packets of hairpin vortices in channel flow. *J. Fluid Mech.*, vol. 387, pp. 353-396.
- [2] R. J. Adrian, K. T. Christensen, and Z. C. Liu (2000), Analysis and interpretation of instantaneous turbulent velocity fields. *Exp. Fluids*, vol. 29, pp. 275-290.
- [3] K. T. Christensen and Y. Wu (2005), Visualization and characterization of small-scale spanwise vortices in turbulent channel flow. *J. Vis.*, vol. 8, pp. 177-185.

Appendix C

Uncertainty Estimation

PIV has some associated sources both systematic (bias) and random error. The bias errors are associated with inefficiency of statistical cross-correlation method for particular cases. The bias errors can therefore be reduced or eliminated by using a different or modified cross-correlation analysis, such as recent advancement of window deformation to account for velocity gradients within the interrogation window. The main factors contributing to PIV uncertainties, as described in Chapter 5 of the book by Raffel *et al.*[1], are considered particle image diameter, particle image displacement, particle image density, background noise, displacement gradients, and out-of-plane motion. The uncertainties in the estimated instantaneous velocities can propagate into statistical values, such as turbulence intensity, as well as velocity derivatives, such as shear stress, varying also depending on the applied differential scheme.

Recently, estimation of PIV uncertainty has gained much attention among researchers, and many techniques have been developed. The most recent trend is to introduce techniques that can estimate uncertainties using the actual experimental particle images and velocity maps. This category of technique is referred to as posterior methods, and the most recent proposals, each based on different techniques, are given by Charonko and Vlachos [2], Sciacchitano *et al.* [3], and Timmins *et al.* [4]. Each of the proposed methods has their own advantages and limitations, mainly specific to the type of the flow and the PIV algorithm.

As an exploration to the field of PIV uncertainty, we took interest in the method proposed by Timmins *et al.* (herein simply referred to as the Timmins' method), and critically evaluated the estimated uncertainties for our PIV results. Two of the main advantages of this method are that it is developed specifically for the PIV algorithm in the *DaVis 7* software, which was the software employed for this thesis, and that it automatically generates uncertainty maps for velocity maps in a way that each velocity vector is associated with its own uncertainty value. One of the current limitations of this technique

(although it is being addressed in the recent updates) is that it is only applicable to uncertainty estimation for in-plane velocities, and the out-of-plane component is not included in the method. Below, a description of this method and how it is applied to the experimental results is given.

Timmins' method considers four major contributing sources of PIV errors – namely particle image size, particle-seeding density, shear rate, and displacement – for which an uncertainty surface is calculated. The processing steps are as follows: a set of synthetic images bearing various ranges of the aforementioned four parameters are processed for vector-field estimations using input parameters identical to those used to process the velocity maps from the actual experimental data. The uncertainty is then computed for the asymmetric distribution of the errors (both bias and random) and is formed into a surface. The next step is to estimate the range of the four parameters for the experimental data, followed by applying the previously derived uncertainty surface in order to estimate the uncertainty value for each vector. These steps yield an uncertainty estimation for the instantaneous 2D-2C velocity maps. Once the instantaneous uncertainties are calculated, the uncertainties of the mean and fluctuating components of velocity (variances and covariances) can also be estimated from the propagation of instantaneous uncertainties based on their described method using Taylor-series expansion for uncertainty propagation [5, 6]. A detailed description of the uncertainty method and the open-source uncertainty codes can be found in [7].

The most challenging model for our study was considered the 70%-stenosed models in which a wide dynamic range of velocities are expected, varying from ~ 3.5 m/s at peak systole in the stenosis jet to approximately zero in the recirculation zone for the same time point. Also, strong shear layers are created in this model at the interface of the jet and separated flow. Thus, uncertainty estimations were considered for a 70% stenosed model, for all time points of the cardiac cycle, in order to present the maximum expected uncertainty ranges. Two critical time points – peak systole and end diastole – were selected to be shown based on maximal shear stress in the former and minimal displacements in the latter, which are two major error-contributing sources. Figure C.1 shows uncertainty-band maps for the peak-systole time point depicted side-by-side to an

instantaneous in-plane velocity magnitude map (Figure C.1a) and ensemble-averaged (15 cycles) velocity magnitude (Figure C.1c). It should be noted that values of uncertainties are shown as uncertainty bandwidth, which spans from the lower to upper limit of an asymmetric distribution of expectation values. Therefore, uncertainty band presented here can be roughly interpreted as twice the common (i.e. \pm) uncertainty representation; for example, for a symmetric distribution, the bandwidth would be equivalent to 2σ or twice the standard deviation. For the instantaneous uncertainties, as expected, the greatest contribution is from the shear layers with the maximum values not exceeding 0.2 m/s. In other regions of the ICA as well as in the CCA and ECA, values are nearly zero.

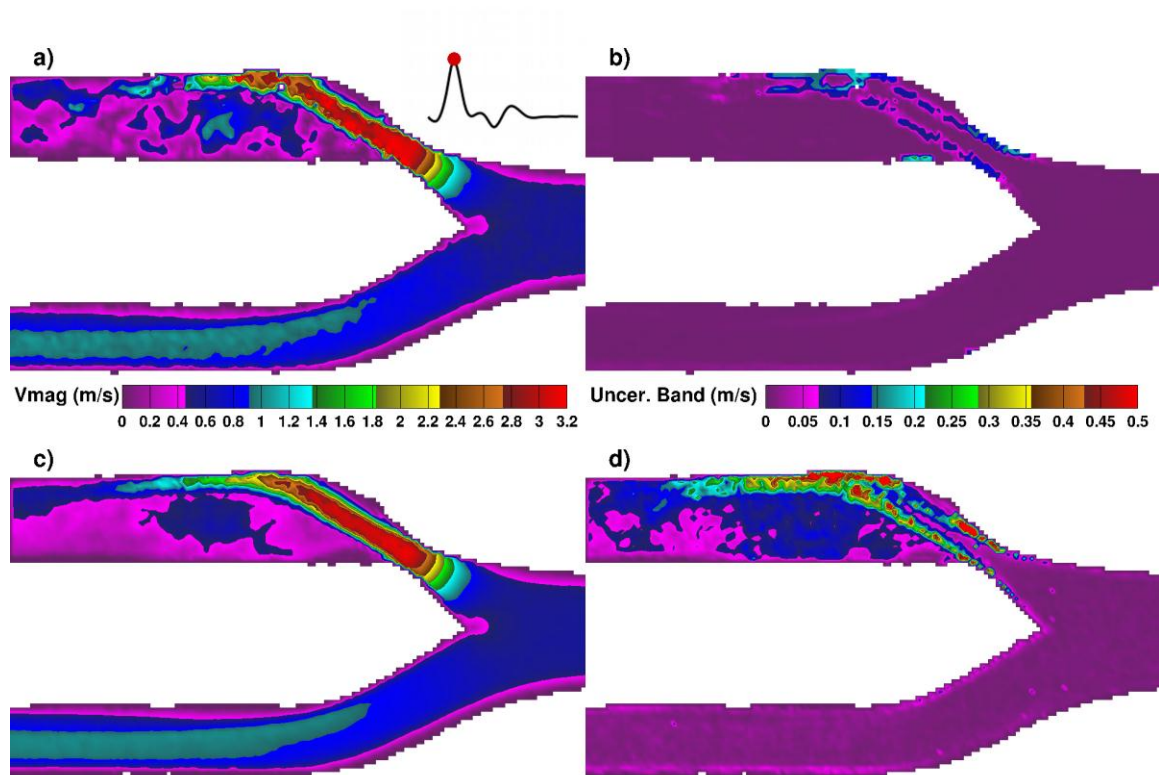


Figure C.1: Color-coded maps of instantaneous (a) and ensemble-averaged (c) velocity magnitude, alongside the corresponding maps for uncertainty bandwidth (b, d) for the time point of peak systole. The respective color bars are shown between the relevant panels.

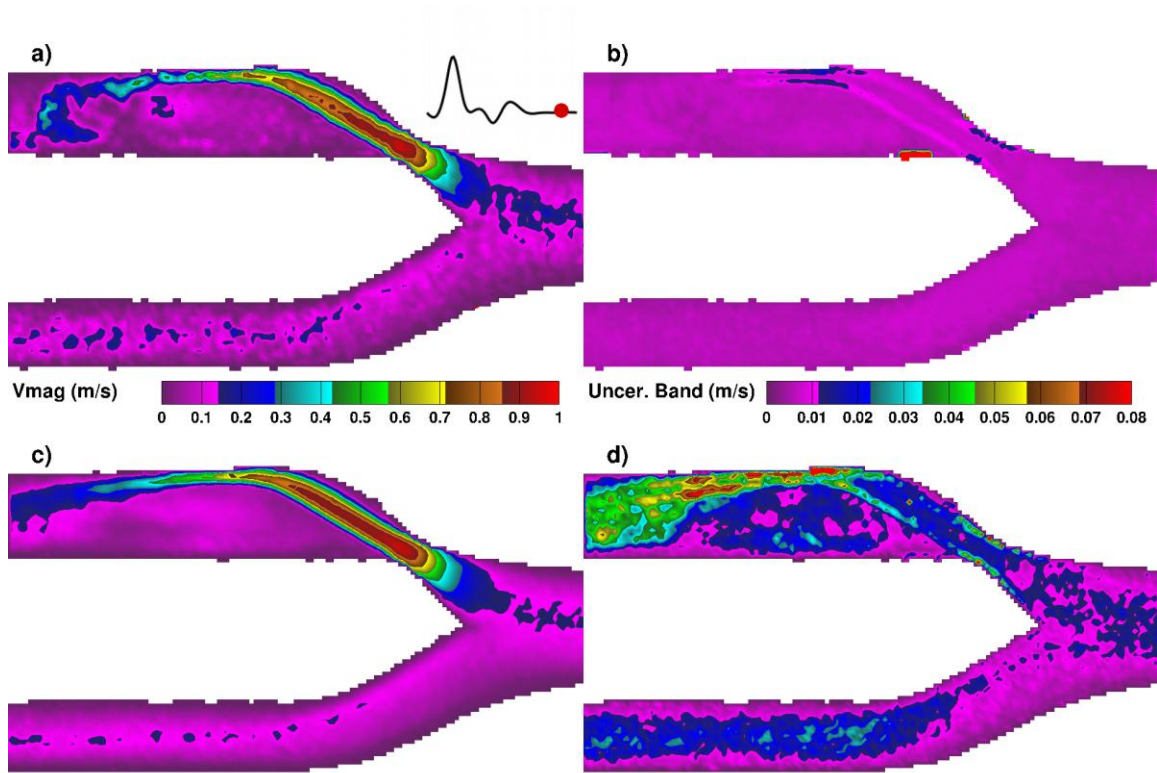


Figure C.2: Color-coded maps of instantaneous (a) and ensemble-averaged (c) velocity magnitude, alongside the corresponding maps for uncertainty bandwidth (b, d) for the time point of end diastole. The respective color bars are shown between the relevant panels.

Similarly, in the uncertainty map associated with the ensemble-averaged velocity magnitude, the shear layers are the dominant contributor to the uncertainty, with maximum values of ~ 0.5 m/s now increased due to propagation of error for the 15 cycles. In the other parts of the ICA, the downstream region located around the detachment point of the jet, as well as the recirculation region, contain notable uncertainty values associated with velocity fluctuations located in these regions as essentially reflected in our TI maps. Similar observations can be made for the maps associated with a time point from end diastole shown in Figure C.2. In the instantaneous map, the greatest contribution is again from the shear layers but with significantly lower values (maximum of ~ 0.02 m/s) compared to peak systole. In the ensemble-averaged map, however, it

appears the effect of shear layer is slightly diminished compared to the high uncertainty value arising downstream of the detached jet.

Table C.1 summarizes the ranges of measured parameter values and associated uncertainties corresponding to each branch of the CCA, ICA, and ECA, shown as mean \pm SD, for peak systole, and likewise in Table C.2 for end diastole.

For the first three rows associated with the instantaneous variables, small uncertainty bands are obtained. For both time points and in all three branches, larger values and uncertainty bands are associated with the streamwise velocity component (u) compared to the spanwise (v) component. In the ICA, where the u velocity range is the largest, the mean of the uncertainty band did not exceed 0.02 m/s compared to the velocity mean value of 0.5 m/s at peak systole, and likewise was about 0.005 m/s compared to the velocity mean value of 0.16 m/s at end diastole.

An important observation was derived by assessing the statistical values of mean, variance, covariance variables, and TI variable in which uncertainty values were found to be significantly larger compared to the instantaneous counterparts. This is due to the fact that in the uncertainty estimation of these variables, velocity fluctuations are incorporated as an estimate of uncertainty. From the Taylor-series equations of uncertainty propagation [5], a component of uncertainty (i.e. precision uncertainty) is defined based on the standard deviation of the velocities. As the result, high cycle-to-cycle fluctuations (i.e. ensemble-averaged TI) yield a high level of standard deviation, thus velocity fluctuations will dominate the estimation of the uncertainty. In our case, where pulsatile flow in a severe stenosis results in a high level of fluctuations, reflected in the derived TI estimations, the corresponding values of uncertainty also reflects the level of flow instabilities. This will impose a limitation for the estimation of uncertainty propagation in the turbulent flows based on a Taylor-series expansion as used in the current applied method.

Table C.1: Uncertainty and measured values at peak systole time point for the specified variables. Values are mean and standard deviation over the range of values present in the corresponding branch of bifurcation.

	CCA		ICA		ECA	
Variable	Value (Mean \pm SD)	Uncertainty Band (Mean \pm SD)	Value (Mean \pm SD)	Uncertainty Band (Mean \pm SD)	Value (Mean \pm SD)	Uncertainty Band (Mean \pm SD)
u (m/s)	0.5180 \pm 0.1409	0.0056 \pm 0.0007	0.5138 \pm 0.9995	0.0195 \pm 0.0356	0.7049 \pm 0.2648	0.0062 \pm 0.0030
v (m/s)	-0.0161 \pm 0.0274	0.0041 \pm 0.0009	0.3245 \pm 0.4681	0.0065 \pm 0.0132	-0.1103 \pm 0.1322	0.0045 \pm 0.0021
$uv_{(mag)}$ (m/s)	0.5193 \pm 0.1396	0.0071 \pm 0.0007	0.8766 \pm 0.9049	0.0220 \pm 0.0371	0.7266 \pm 0.2623	0.0079 \pm 0.0033
U (m/s)	0.5116 \pm 0.1489	0.0111 \pm 0.0047	0.5050 \pm 0.8986	0.1370 \pm 0.1052	0.6784 \pm 0.2959	0.0185 \pm 0.0151
V (m/s)	-0.0157 \pm 0.0255	0.0043 \pm 0.0014	0.3068 \pm 0.4341	0.0778 \pm 0.0537	-0.1069 \pm 0.1316	0.0075 \pm 0.0076
$UV_{(mag)}$ (m/s)	0.5128 \pm 0.1481	0.0110 \pm 0.0047	0.8239 \pm 0.8428	0.1202 \pm 0.1103	0.6997 \pm 0.2956	0.0184 \pm 0.0152
$\overline{u'u'}$ (m ² /s ²)	0.0006 \pm 0.0008	0.0008 \pm 0.0012	0.1164 \pm 0.2089	0.1725 \pm 0.3094	0.0022 \pm 0.0077	0.0033 \pm 0.0114
$\overline{v'v'}$ (m ² /s ²)	0.0001 \pm 0.0001	0.0001 \pm 0.0001	0.0349 \pm 0.0517	0.0517 \pm 0.0766	0.0004 \pm 0.0029	0.0007 \pm 0.0043
$\overline{u'v'}$ (m ² /s ²)	0.0000 \pm 0.0001	0.0003 \pm 0.0002	0.0114 \pm 0.0767	0.0853 \pm 0.1326	-0.0001 \pm 0.0014	0.0012 \pm 0.0051
$\overline{(uv)'(uv)'}$ (m ² /s ²)	0.0006 \pm 0.0008	0.0008 \pm 0.0012	0.1039 \pm 0.2289	0.1540 \pm 0.3392	0.0022 \pm 0.0079	0.0033 \pm 0.0117
$\mathbf{TI}_{(m^2/s^2)}^{(2C)}$	0.0236 \pm 0.0093	0.0153 \pm 0.0069	0.3168 \pm 0.2258	0.1901 \pm 0.1447	0.0401 \pm 0.0326	0.0259 \pm 0.0217

Table C.2: Uncertainty and measured values at end diastole time point for the specified variables. Values are mean and standard deviation over the range of values present in the corresponding branch of bifurcation.

	CCA		ICA		ECA	
Variable	Value (Mean \pm SD)	Uncertainty Band (Mean \pm SD)	Value (Mean \pm SD)	Uncertainty Band (Mean \pm SD)	Value (Mean \pm SD)	Uncertainty Band (Mean \pm SD)
u (m/s)	0.0937 \pm 0.0538	0.0058 \pm 0.0020	0.1564 \pm 0.2425	0.0052 \pm 0.0021	0.0730 \pm 0.0457	0.0048 \pm 0.0006
v (m/s)	0.0004 \pm 0.0091	0.0033 \pm 0.0005	0.0667 \pm 0.1318	0.0051 \pm 0.0065	-0.0160 \pm 0.0199	0.0041 \pm 0.0009
$uv_{(mag)}$ (m/s)	0.0949 \pm 0.0525	0.0068 \pm 0.0019	0.2111 \pm 0.2459	0.0076 \pm 0.0066	0.0778 \pm 0.0448	0.0064 \pm 0.0008
U (m/s)	0.0917 \pm 0.0472	0.0106 \pm 0.0039	0.1552 \pm 0.2497	0.0253 \pm 0.0172	0.0716 \pm 0.0432	0.0127 \pm 0.0063
V (m/s)	0.0002 \pm 0.0039	0.0041 \pm 0.0012	0.0693 \pm 0.1260	0.0146 \pm 0.0103	-0.0153 \pm 0.0169	0.0049 \pm 0.0020
$UV_{(mag)}$ (m/s)	0.0928 \pm 0.0461	0.0104 \pm 0.0041	0.2166 \pm 0.2483	0.0238 \pm 0.0170	0.0762 \pm 0.0430	0.0121 \pm 0.0063
$\overline{u'u'}$ (m ² /s ²)	0.0005 \pm 0.0003	0.0007 \pm 0.0005	0.0036 \pm 0.0058	0.0054 \pm 0.0086	0.0008 \pm 0.0007	0.0012 \pm 0.0011
$\overline{v'v'}$ (m ² /s ²)	0.0001 \pm 0.0000	0.0001 \pm 0.0001	0.0012 \pm 0.0019	0.0019 \pm 0.0029	0.0001 \pm 0.0002	0.0002 \pm 0.0003
$\overline{u'v'}$ (m ² /s ²)	0.0000 \pm 0.0001	0.0003 \pm 0.0001	-0.0001 \pm 0.0016	0.0028 \pm 0.0038	0.0001 \pm 0.0001	0.0004 \pm 0.0004
$\overline{(uv)'(uv)'}$ (m ² /s ²)	0.0005 \pm 0.0003	0.0007 \pm 0.0005	0.0033 \pm 0.0057	0.0049 \pm 0.0084	0.0007 \pm 0.0007	0.0011 \pm 0.0011
$\mathbf{TI}_{(m^2/s^2)}^{(2C)}$	0.0225 \pm 0.0077	0.0146 \pm 0.0056	0.0588 \pm 0.0379	0.0361 \pm 0.0252	0.0270 \pm 0.0126	0.0176 \pm 0.0091

References

- [1] M. Raffel, C. E. Willert, S. T. Wereley, *et al.* (2007), *Particle image velocimetry: A practical guide*. Springer-Verlag Berlin Heidelberg.
- [2] J. J. Charonko and P. P. Vlachos (2013), Estimation of uncertainty bounds for individual particle image velocimetry measurements from cross-correlation peak ratio. *Measurement Science & Technology*, vol. 24,
- [3] A. Sciacchitano, B. Wieneke, and F. Scarano (2013), PIV uncertainty quantification by image matching. *Measurement Science & Technology*, vol. 24,
- [4] B. H. Timmins, B. W. Wilson, B. L. Smith, *et al.* (2012), A method for automatic estimation of instantaneous local uncertainty in particle image velocimetry measurements. *Experiments in Fluids*, vol. 53, pp. 1133-1147.
- [5] B. M. Wilson and B. L. Smith (2013), Taylor-series and monte-carlo-method uncertainty estimation of the width of a probability distribution based on varying bias and random error. *Measurement Science & Technology*, vol. 24,
- [6] B. M. Wilson and B. L. Smith (2013), Uncertainty on PIV mean and fluctuating velocity due to bias and random errors. *Measurement Science & Technology*, vol. 24,
- [7] PIV Uncertainty Open-source Codes <http://efdl.neng.usu.edu/EFDL/Code.html>

Appendix D

Velocity Profiles

The following five figures depict the velocity profiles of normal, 30% stenosed (concentric and eccentric), and 70% stenosed (concentric and eccentric) models. The remaining, out of total eight examined models, three models of 50% stenosis are shown in Figure 4.4, Figure 4.5, and Figure 4.6.

Values are mean \pm SD calculated based on 15 cardiac cycles and were extracted along three lateral lines (X_1 , X_2 , and X_3 shown in Figure 4.3e) located in the ICA at approximately 1, 2, and 3 CCA diameters, respectively, downstream from the bifurcation apex. The five time points (from top to bottom) correspond to 30 ms prior to peak systole, peak systole, and 40, 150, and 670 ms post peak systole.

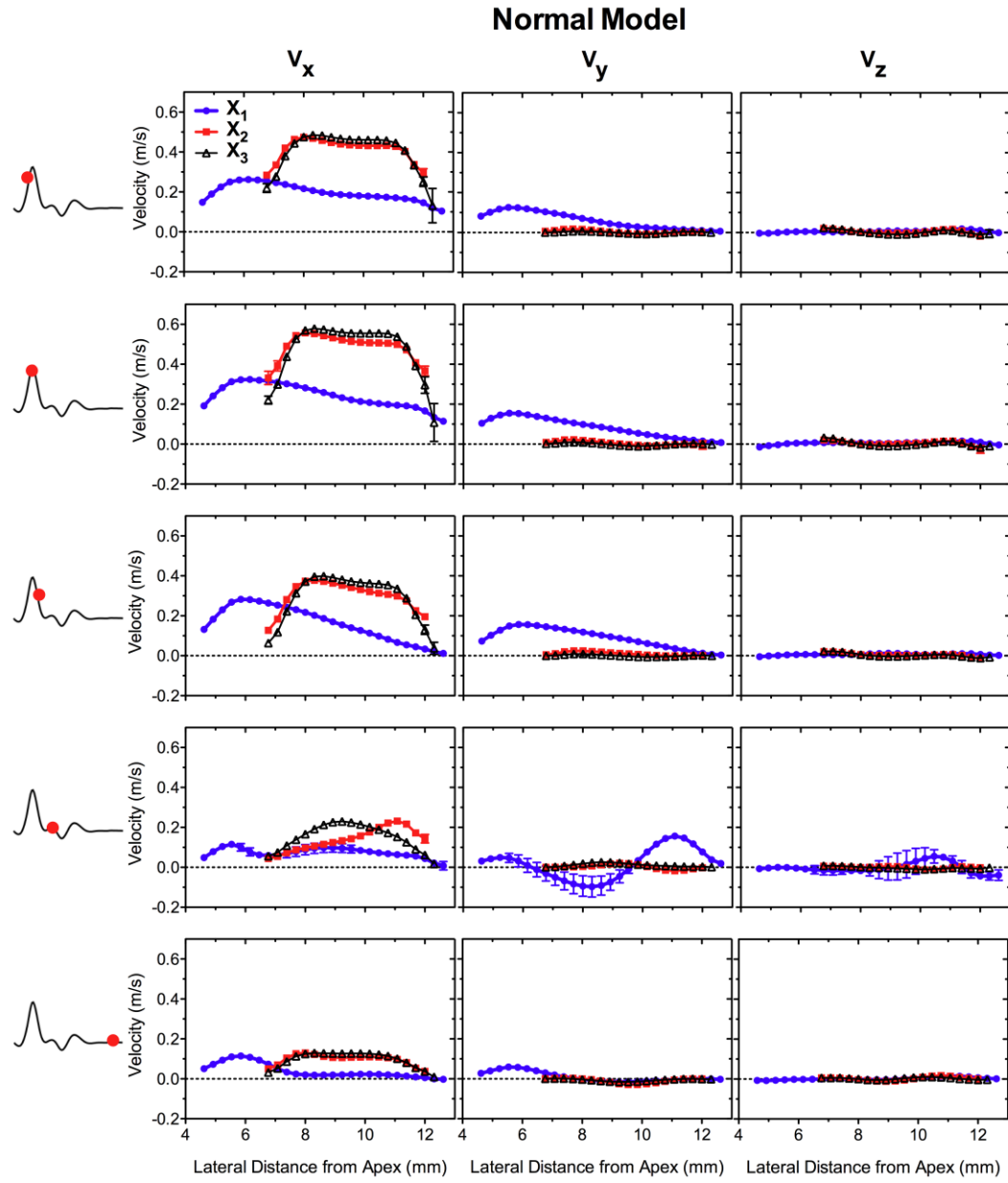


Figure D.1: Profiles of velocity components (left to right V_x , V_y , and V_z) for normal model.

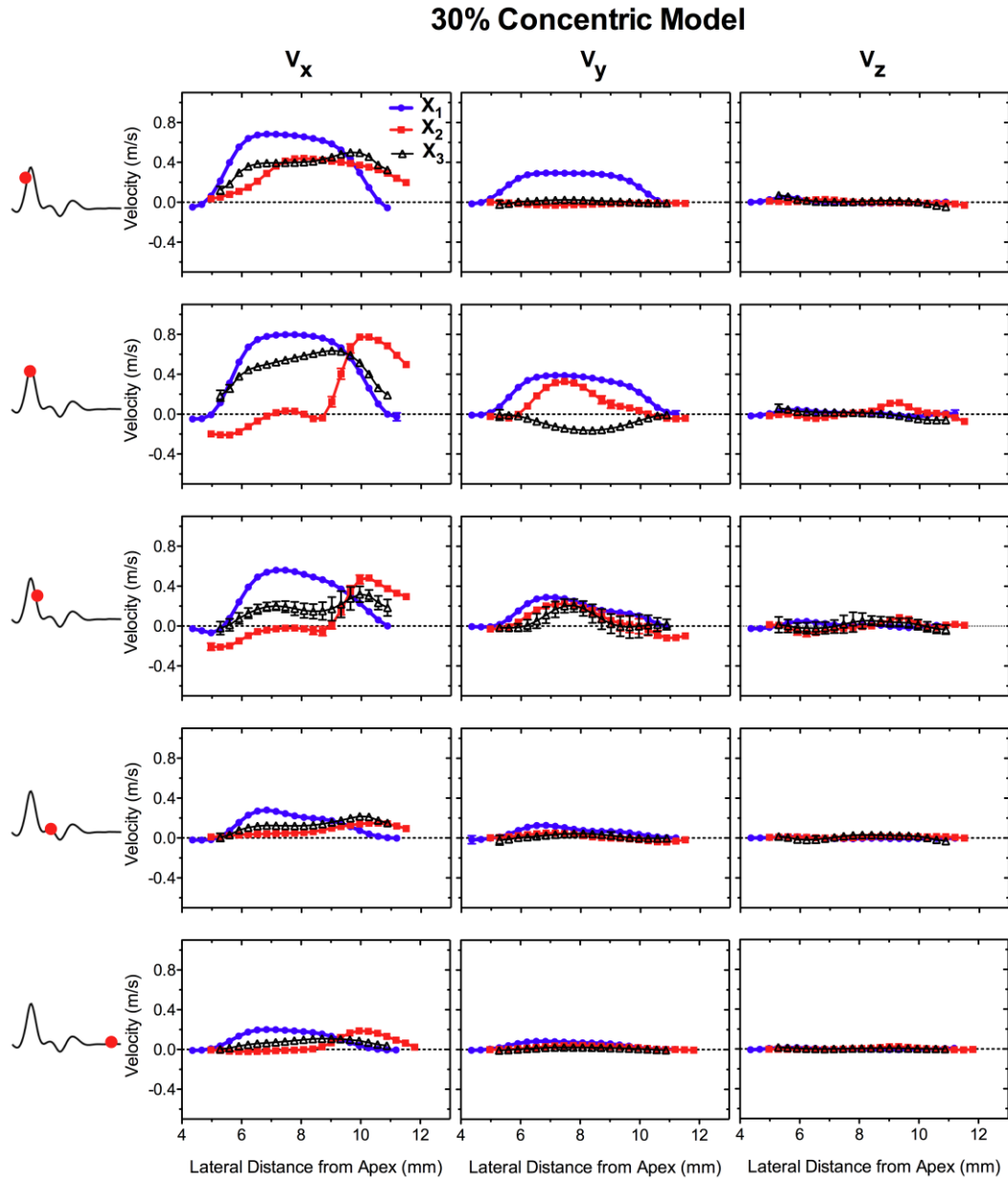


Figure D.2: Profiles of velocity components (left to right V_x , V_y , and V_z) for 30% concentric model.

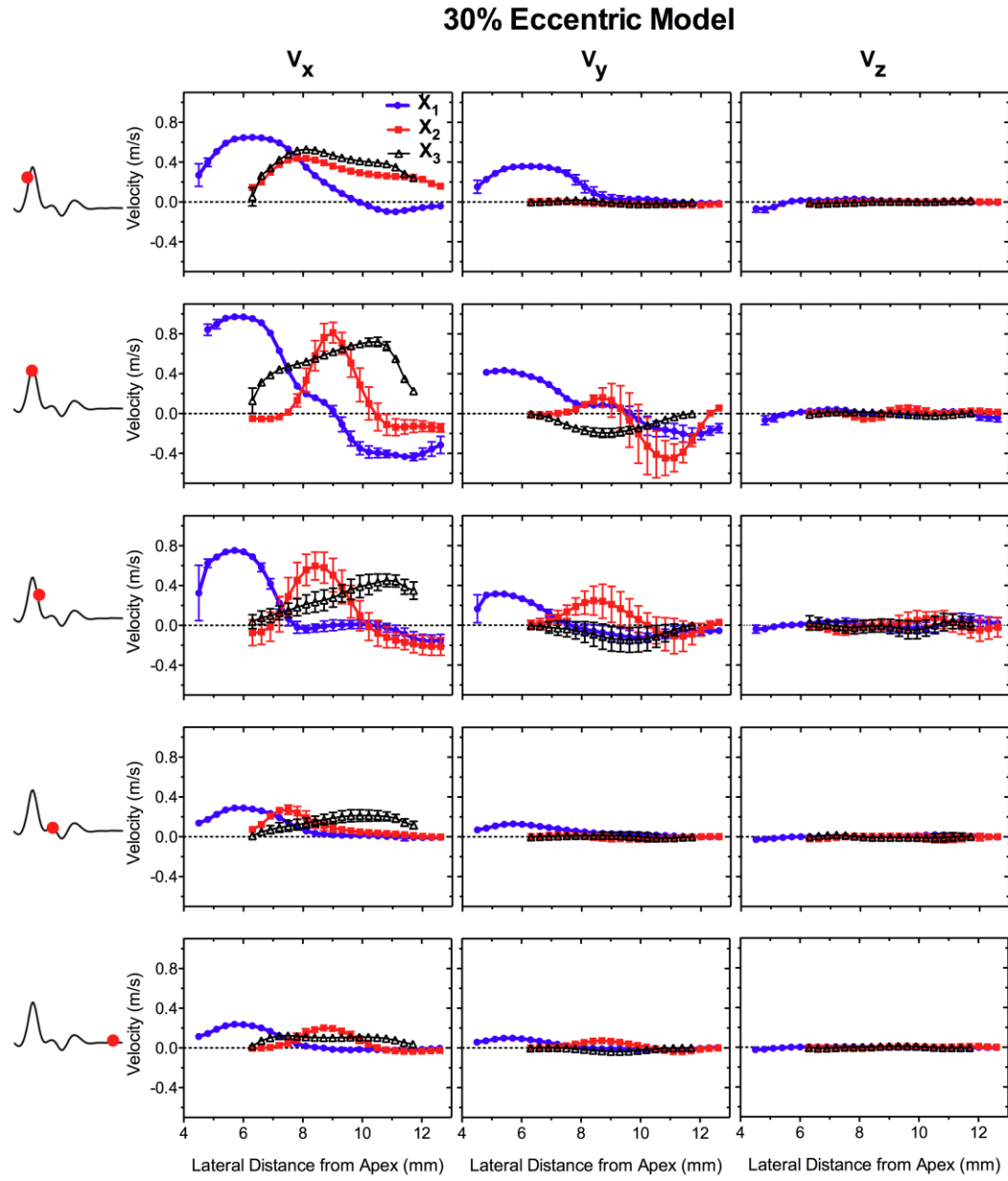


Figure D.3: Profiles of velocity components (left to right V_x , V_y , and V_z) for 30% eccentric model.

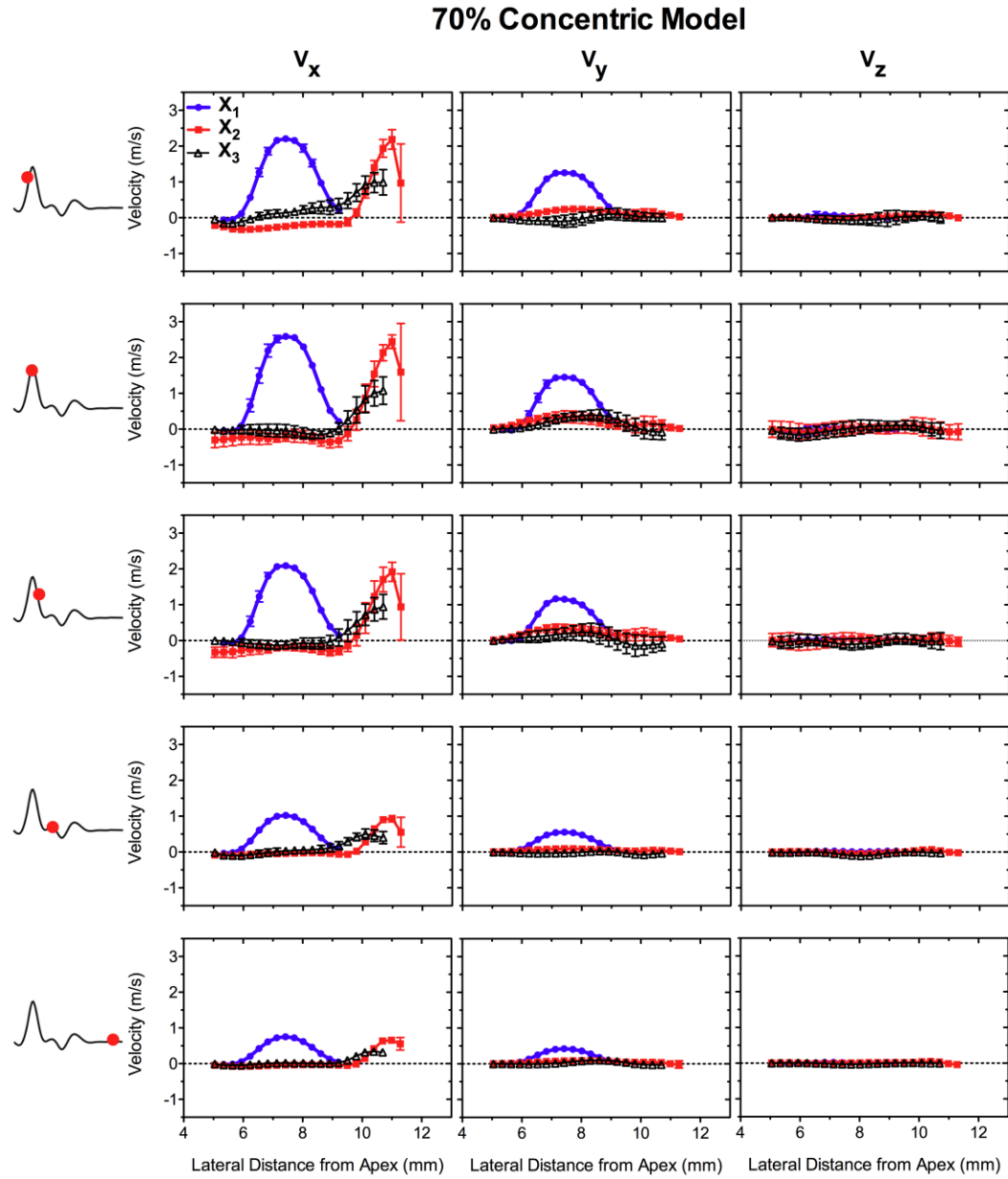


Figure D.4: Profiles of velocity components (left to right V_x , V_y , and V_z) for 70% concentric model.

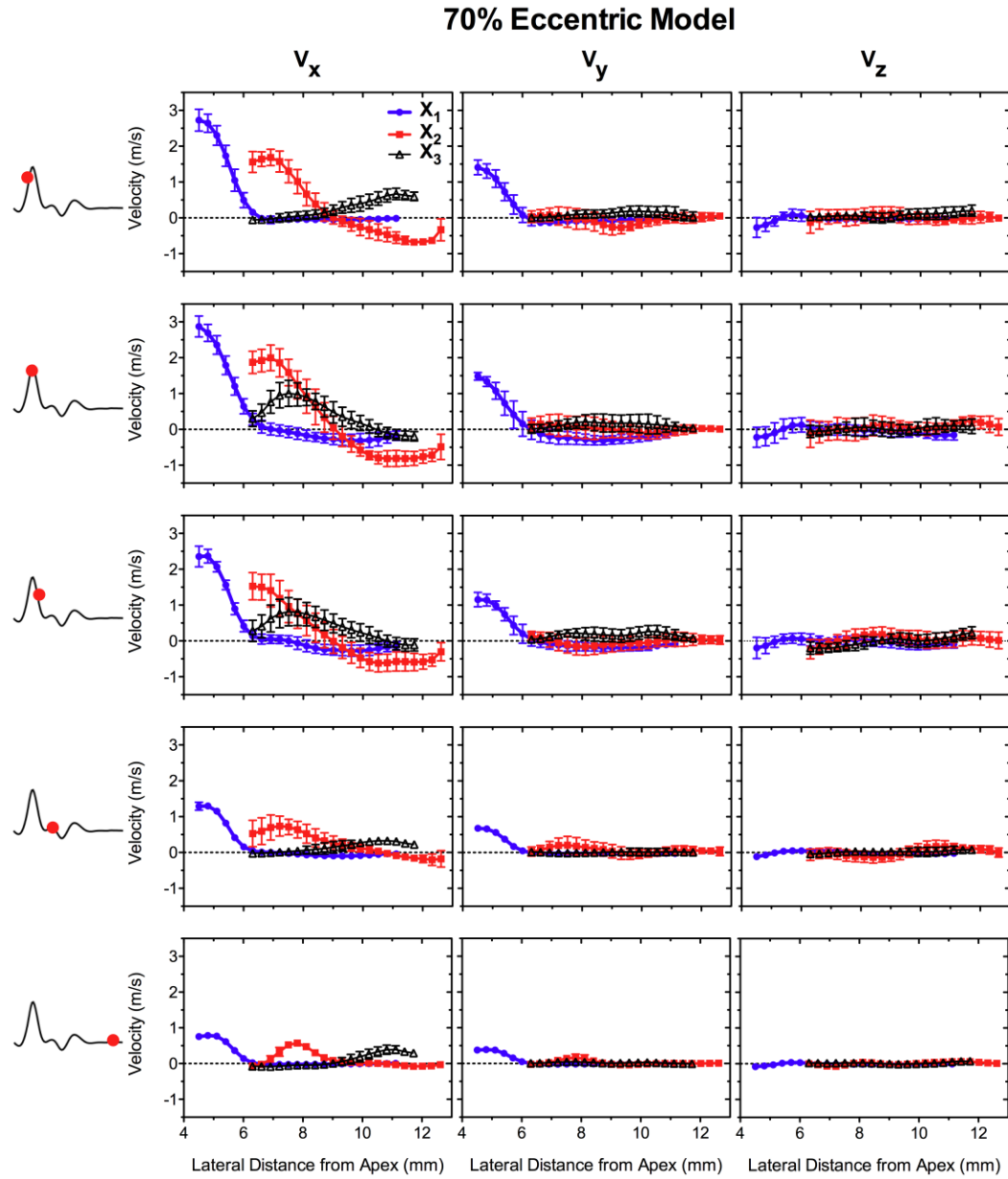


Figure D.5: Profiles of velocity components (left to right V_x , V_y , and V_z) for 70% eccentric model.

Appendix E

Copyright Permissions

RightsLink – Your Account

2013-07-18 7:21 AM

ELSEVIER LICENSE TERMS AND CONDITIONS

Jul 18, 2013

This is a License Agreement between Western University ("You") and Elsevier ("Elsevier") provided by Copyright Clearance Center ("CCC"). The license consists of your order details, the terms and conditions provided by Elsevier, and the payment terms and conditions.

All payments must be made in full to CCC. For payment instructions, please see information listed at the bottom of this form.

Supplier	Elsevier Limited The Boulevard, Langford Lane Kidlington, Oxford, OX5 1GB, UK
Registered Company Number	1982084
Customer name	Western University
Customer address	The Department of Physics and Astronomy London, ON N6A 3K7
License number	3191880514953
License date	Jul 18, 2013
Licensed content publisher	Elsevier
Licensed content publication	Medical Engineering & Physics
Licensed content title	Transitional flow analysis in the carotid artery bifurcation by proper orthogonal decomposition and particle image velocimetry
Licensed content author	Sarah Kefayati, Tamie L. Poepping
Licensed content date	July 2013
Licensed content volume number	35
Licensed content issue number	7
Number of pages	12
Start Page	898
End Page	909
Type of Use	reuse in a thesis/dissertation
Portion	full article
Format	both print and electronic
Are you the author of this Elsevier article?	Yes
Will you be translating?	No
Order reference number	1
Title of your thesis/dissertation	PIV-based investigation of hemodynamic factors in the diseased carotid artery bifurcations with

	varying plaque geometries
Expected completion date	Aug 2013
Estimated size (number of pages)	150
Elsevier VAT number	GB 494 6272 12
Permissions price	0.00 USD
VAT/Local Sales Tax	0.00 USD
Total	0.00 USD
Terms and Conditions	

INTRODUCTION

1. The publisher for this copyrighted material is Elsevier. By clicking "accept" in connection with completing this licensing transaction, you agree that the following terms and conditions apply to this transaction (along with the Billing and Payment terms and conditions established by Copyright Clearance Center, Inc. ("CCC"), at the time that you opened your Rightslink account and that are available at any time at <http://myaccount.copyright.com>).

GENERAL TERMS

2. Elsevier hereby grants you permission to reproduce the aforementioned material subject to the terms and conditions indicated.
 3. Acknowledgement: If any part of the material to be used (for example, figures) has appeared in our publication with credit or acknowledgement to another source, permission must also be sought from that source. If such permission is not obtained then that material may not be included in your publication/copies. Suitable acknowledgement to the source must be made, either as a footnote or in a reference list at the end of your publication, as follows:

"Reprinted from Publication title, Vol /edition number, Author(s), Title of article / title of chapter, Pages No., Copyright (Year), with permission from Elsevier [OR APPLICABLE SOCIETY COPYRIGHT OWNER]." Also Lancet special credit - "Reprinted from The Lancet, Vol. number, Author(s), Title of article, Pages No., Copyright (Year), with permission from Elsevier."

4. Reproduction of this material is confined to the purpose and/or media for which permission is hereby given.

5. Altering/Modifying Material: Not Permitted. However figures and illustrations may be altered/adapted minimally to serve your work. Any other abbreviations, additions, deletions and/or any other alterations shall be made only with prior written authorization of Elsevier Ltd. (Please contact Elsevier at permissions@elsevier.com)

6. If the permission fee for the requested use of our material is waived in this instance, please be advised that your future requests for Elsevier materials may attract a fee.

7. Reservation of Rights: Publisher reserves all rights not specifically granted in the combination of (i) the license details provided by you and accepted in the course of this licensing transaction, (ii) these terms and conditions and (iii) CCC's Billing and Payment terms and conditions.

8. License Contingent Upon Payment: While you may exercise the rights licensed immediately upon issuance of the license at the end of the licensing process for the transaction, provided that you have disclosed complete and accurate details of your proposed use, no license is finally effective unless and until full payment is received from you (either by publisher or by CCC) as provided in CCC's Billing and Payment terms and conditions. If full payment is not received on a timely basis, then any license preliminarily granted shall be deemed automatically revoked and shall be void as if never granted. Further, in the event that you breach any of these terms and conditions or any of CCC's Billing and Payment terms and conditions, the license is automatically revoked and shall be void as if never granted. Use of materials as described in a revoked license, as well as any use of the materials beyond the scope of an unrevoked license, may constitute copyright infringement and publisher reserves the right to take any and all action to protect its copyright in the materials.

9. Warranties: Publisher makes no representations or warranties with respect to the licensed material.

10. Indemnity: You hereby indemnify and agree to hold harmless publisher and CCC, and their respective officers, directors, employees and agents, from and against any and all claims arising out of your use of the licensed material other than as specifically authorized pursuant to this license.

11. No Transfer of License: This license is personal to you and may not be sublicensed, assigned, or transferred by you to any other person without publisher's written permission.

12. No Amendment Except in Writing: This license may not be amended except in a writing signed by both parties (or, in the case of publisher, by CCC on publisher's behalf).

13. Objection to Contrary Terms: Publisher hereby objects to any terms contained in any purchase order, acknowledgment, check endorsement or other writing prepared by you, which terms are inconsistent with these terms and conditions or CCC's

Billing and Payment terms and conditions. These terms and conditions, together with CCC's Billing and Payment terms and conditions (which are incorporated herein), comprise the entire agreement between you and publisher (and CCC) concerning this licensing transaction. In the event of any conflict between your obligations established by these terms and conditions and those established by CCC's Billing and Payment terms and conditions, these terms and conditions shall control.

14. **Revocation:** Elsevier or Copyright Clearance Center may deny the permissions described in this License at their sole discretion, for any reason or no reason, with a full refund payable to you. Notice of such denial will be made using the contact information provided by you. Failure to receive such notice will not alter or invalidate the denial. In no event will Elsevier or Copyright Clearance Center be responsible or liable for any costs, expenses or damage incurred by you as a result of a denial of your permission request, other than a refund of the amount(s) paid by you to Elsevier and/or Copyright Clearance Center for denied permissions.

LIMITED LICENSE

The following terms and conditions apply only to specific license types:

15. **Translation:** This permission is granted for non-exclusive world **English** rights only unless your license was granted for translation rights. If you licensed translation rights you may only translate this content into the languages you requested. A professional translator must perform all translations and reproduce the content word for word preserving the integrity of the article. If this license is to re-use 1 or 2 figures then permission is granted for non-exclusive world rights in all languages.

16. **Website:** The following terms and conditions apply to electronic reserve and author websites:

Electronic reserve: If licensed material is to be posted to website, the web site is to be password-protected and made available only to bona fide students registered on a relevant course if:

This license was made in connection with a course,

This permission is granted for 1 year only. You may obtain a license for future website posting,

All content posted to the web site must maintain the copyright information line on the bottom of each image,

A hyper-text must be included to the Homepage of the journal from which you are licensing at

<http://www.sciencedirect.com/science/journal/xxxxx> or the Elsevier homepage for books at <http://www.elsevier.com> , and

Central Storage: This license does not include permission for a scanned version of the material to be stored in a central repository such as that provided by Heron/XanEdu.

17. **Author website** for journals with the following additional clauses:

All content posted to the web site must maintain the copyright information line on the bottom of each image, and the permission granted is limited to the personal version of your paper. You are not allowed to download and post the published electronic version of your article (whether PDF or HTML, proof or final version), nor may you scan the printed edition to create an electronic version. A hyper-text must be included to the Homepage of the journal from which you are licensing at

<http://www.sciencedirect.com/science/journal/xxxxx> . As part of our normal production process, you will receive an e-mail notice when your article appears on Elsevier's online service ScienceDirect (www.sciencedirect.com). That e-mail will include the article's Digital Object Identifier (DOI). This number provides the electronic link to the published article and should be included in the posting of your personal version. We ask that you wait until you receive this e-mail and have the DOI to do any posting.

Central Storage: This license does not include permission for a scanned version of the material to be stored in a central repository such as that provided by Heron/XanEdu.

18. **Author website** for books with the following additional clauses:

Authors are permitted to place a brief summary of their work online only.

A hyper-text must be included to the Elsevier homepage at <http://www.elsevier.com> . All content posted to the web site must maintain the copyright information line on the bottom of each image. You are not allowed to download and post the published electronic version of your chapter, nor may you scan the printed edition to create an electronic version.

Central Storage: This license does not include permission for a scanned version of the material to be stored in a central repository such as that provided by Heron/XanEdu.

19. **Website** (regular and for author): A hyper-text must be included to the Homepage of the journal from which you are licensing at <http://www.sciencedirect.com/science/journal/xxxxx> . or for books to the Elsevier homepage at <http://www.elsevier.com>

20. **Thesis/Dissertation:** If your license is for use in a thesis/dissertation your thesis may be submitted to your institution in either print or electronic form. Should your thesis be published commercially, please reapply for permission. These requirements include permission for the Library and Archives of Canada to supply single copies, on demand, of the complete thesis and include permission for UMI to supply single copies, on demand, of the complete thesis. Should your thesis be published commercially, please reapply for permission.

21. **Other Conditions:** Permission is granted to submit your article in electronic format. This license permits you to post this Elsevier article online if it is embedded within your thesis. You are also permitted to post your Author Accepted Manuscript online

however posting of the final published article is prohibited. Please refer to Elsevier's Posting Policy for further information:
<http://www.elsevier.com/wps/find/authors.authors/postingpolicy>

v1.6

If you would like to pay for this license now, please remit this license along with your payment made payable to "COPYRIGHT CLEARANCE CENTER" otherwise you will be invoiced within 48 hours of the license date. Payment should be in the form of a check or money order referencing your account number and this invoice number RLNK501068952. Once you receive your invoice for this order, you may pay your invoice by credit card. Please follow instructions provided at that time.

Make Payment To:
Copyright Clearance Center
Dept 001
P.O. Box 843006
Boston, MA 02284-3006

For suggestions or comments regarding this order, contact RightsLink Customer Support: customercare@copyright.com or +1-877-622-5543 (toll free in the US) or +1-978-646-2777.

Gratis licenses (referencing \$0 in the Total field) are free. Please retain this printable license for your reference. No payment is required.

Curriculum Vitae

Name: Sarah Kefayati

Post-secondary Education and Degrees: Western University
London, Ontario, Canada
2008-2013 Ph.D. Medical Physics

Brock University
St. Catharines, Ontario, Canada
2006-2008 M.Sc. Biophysics

Iran University of Science and Technology
Tehran, Iran
2001-2005 B.Sc. Atomic & Molecular Physics

Honours and Awards

2012	Travel Stipend Award for the 2012 IEEE International Ultrasonics Symposium
2010	First Place Prize for Poster Presentation in London Imaging Discovery
2008 – 2012	Western Graduate Research Scholarship
2008 – 2010	CIHR Strategic Training Fellowship in Vascular Research
2006 – 2008	Graduate Research Fellowship, Brock University
2006 – 2008	International Graduate Student Fellowship, Brock University
2005	Distinguished Student Graduated in Physics, 2nd Position, Iran University of Science & Technology

Related Work Experience Teaching Assistant
Western University
2008-2012

Teaching Assistant
Brock University
2006-2008

Publications:

Peer-Reviewed Journal Publications:

Kefayati, S., and Poepping, T. L., *Transitional Flow Analysis in the Carotid Artery Bifurcation by Proper Orthogonal Decomposition and Particle Image Velocimetry*. Medical Engineering & Physics, 2013 Vol:35 pp: 898-909.

Kefayati, S., Holdsworth, D. W., and Poepping, T. L., *Turbulence Intensity Measurements using Particle Image Velocimetry in Diseased Carotid Artery Models: Effect of Stenosis Severity, Plaque Eccentricity, and Ulceration*. Journal of Biomechanics.

Kefayati, S., Milner, J. S., Holdsworth, D. W., and Poepping, T. L., *Effects of Plaque Geometry on In Vitro Shear Stress Measurements in a Family of Carotid Artery Models Using Particle Image Velocimetry*. (to be submitted)

Refereed Conference Proceedings:

Kefayati, S., Holdsworth D. W., Poepping T. L., *Application of Stereoscopic PIV for hemodynamic studies of life-sized carotid artery models under pulsatile flow conditions*. Proceedings of PIV13 Conference, Delft, Netherlands, 2013.

Kefayati, S., Powell J. L., Wong E. Y., and Poepping, T. L., *Investigation of the effect of geometrical features of carotid artery plaque on turbulence intensity using Doppler ultrasound and particle image velocimetry*. Proceedings of IEEE International Ultrasonics Symposium: Blood Flow Measurements, Dresden, Germany, 2012.

Kefayati, S., and Poepping, T. L., *3-D Flow Characterization and Shear Stress in a Stenosed Carotid Artery Bifurcation Model using Stereoscopic PIV Technique*. Proceedings of Annual International Conference of the IEEE Engineering in Medicine and Biology Society, Buenos Aires, Argentina, 2010.

Other Conference Presentations:

Kefayati, S., and Poepping, T. L., “Hemodynamics of the Carotid Bifurcation using Stereoscopic PIV”, *Artimino Doppler Conference*, Artimino, Italy, June 26 – 29, 2011.

Kefayati, S., and Poepping, T. L., “Turbulence Measurements of Diseased Carotid Artery Bifurcation using Stereoscopic PIV Technique”, *London Image Discovery (LID)*, London, Canada, June 23, 2011.

Kefayati, S., and Poepping, T. L., “Stereoscopic PIV Measurements to Characterize 3D Flow and Shear Stress in a Stenosed Carotid Artery Bifurcation Model”, *London Image Discovery (LID)*, London, Canada, June 23, 2010.

Kefayati, S., and Poepping, T. L., “Stereoscopic PIV Measurements to Characterize 3D Flow and Shear Stress in a Stenosed Carotid Artery Bifurcation Model”, *CAP, Toronto, Canada*, June 7, 2010.

Kefayati, S., Vassiliev, S., Harroun, T. A., and Bruce, D. H., “The Accurate Measurement of Point Spread Function using *In Situ* Approach over Commonly Used Experimental Methods in Two-Photon Microscopy for Arabidopsis Tissue”, *Chemical Biophysics Symposium*, Toronto, Canada, April 2008.